To the Graduate Council:

I am submitting herewith a dissertation written by Tina Morina Rice entitled "Effect of Unsteady Combustion on the Stability of Rocket Engines." I have examined the final electronic copy of this dissertation for form and content and recommend that it be accepted in partial fulfillment of the requirements for the degree of Doctor of Philosophy, with a major in Aerospace Engineering.

Gary A. Flandro
Major Professor

We have read this dissertation
and recommend its acceptance:

Basil Antar

Trevor Moeller

Christian Parigger

Accepted for the council:

Dr. Carolyn R. Hodges
Vice Provost and
Dean of the Graduate School

(Original signatures are on file with official student records.)

Effect of Unsteady Combustion on the Stability of Rocket Engines

A Dissertation
Presented for the
Doctor of Philosophy in Science
Degree
The University of Tennessee, Knoxville

Tina Morina Rice
May 2011

DEDICATION

This dissertation is dedicated to my many loved ones for all of their support and belief in me throughout this effort and my prior endeavors, including the much-extended Rice family. Most especially, this is dedicated to my precious mother, Morina Rice, and my loving husband, Richard Lewis, for all of their never ending love and care.

ACKNOWLEDGEMENTS

I would like to express my sincere gratitude to all members of my thesis committee: Dr. Gary A. Flandro, Dr. Basil Antar, Dr. Trevor Moeller, and Dr. Christian Parriger. I would also like to extend thanks to Paul Gloyer and Richard Lewis for their assistance and much appreciated support when needed. The author is especially thankful for the never-ending support of her mother, Morina Rice, without whose love and support this success could have not been achieved. Thanks are also extended to the University of Tennessee Space Institute for its financial support during much of this endeavor. Thanks are also due to the fellows at the Vanderbilt Space Grant Consortium for the last year's support.

ABSTRACT

Combustion instability is a problem that has plagued the development of rocket-propelled devices since their conception. It is characterized by the occurrence of high-frequency nonlinear gas oscillations inside the combustion chamber. This phenomenon degrades system performance and can result in damage to both structure and instrumentation.

The goal of this dissertation is to clarify the role of unsteady combustion in the combustor instability problem by providing the first quantified estimates of its effect upon the stability of liquid rocket engines. The combination of this research with a new system energy balance method, accounting for all dynamic interactions within a system, allows for the isolation of combustion effects for this study. These effects are quantified through use of classical linear stability analysis to calculate the unsteady combustion heat release growth rate.

Since combustion modeling can become very involved, including the mixing process and multiple reactions concerned, for this initial evaluation the model is limited to a one-dimensional flame analysis for a one-step premixed chemical reaction. Using classical analysis of oscillatory burning, the governing combustion equations are expanded into sets of steady and unsteady equations adapted for premixed liquid rockets. From this expansion process, the first real treatment of the effects of unsteady combustion in a rocket system is presented, and the first quantified values of the unsteady heat release in a rocket system are computed. Finally, the corresponding linear heat release growth rate for the system is then calculated for the first quantified effects of unsteady combustion on the overall system stability.

The mechanism of unsteady combustion is shown to behave as a driving mechanism, serving as one of the more important stability mechanisms comparable to the magnitude of the nozzle damping mechanism. This analysis confirms that unsteady combustion is an important stability mechanism that warrants further investigation. This study also creates a firm foundation upon which to extend the analysis of this important mechanism to fully understand all of its effects within a rocket system.

TABLE OF CONTENTS

CHAPTER 1 – INTRODUCTION TO INSTABILITY 1

1.1 – Objective 3

1.2 – Background 4

1.3 – Common Features of Instability 4

1.3.1 – Forced Versus Self-Excited Oscillations 5

1.3.2 – Acoustic Modeling 6

1.3.3 – Transverse and Longitudinal Waveforms 6

1.3.4 – Limit Cycle 9

1.3.5 – The DC Shift 11

1.4 – Historical Treatment of Instability in Practice 14

CHAPTER 2 – MODELING OF COMBUSTION INSTABILITY 26

2.1 – Traditional Analytical Approach 26

2.2 – Stability Analysis 29

2.3 – The Need for Nonlinear Calculations 34

CHAPTER 3 – WHAT IS THE ENERGY METHOD? 37

3.1 – Historical Development 38

3.2 – Introduction to the Energy Corollary Method 44

3.3 – Overview of Nomenclature 49

3.4 – Analytical Development 52

3.5 – Energy Corollary Balance 57

3.5.1 – Zeroth Order Corollary Proof 57

3.5.2 – First Order Corollary Proof 59
3.5.3 – Second Order Expansion Process 60
3.6 – Incorporation of Heat Release Terms 65
3.7 – Integral Formulation 66
3.8 – Overview of Nonlinear Analysis 68
CHAPTER 4 – VOLUMETRIC COMBUSTION ANALYSIS 75
4.1 – Rocket Combustion 75
4.2 – Combustion Model 80
4.3 – Mathematical Technique 83
4.4 – Role of the Stoichiometrically Weighted Mass Fraction 88
4.5 – Derivation of the Steady and Unsteady Governing Equations 90
4.5.1 – Steady Equations 91
4.5.1.1 – Conservation of Mass Equation 92
4.5.1.2 – Conservation of Energy and Species Equations 93
4.5.2 – Unsteady Equations 96
4.5.2.1 – Derivation of the Unsteady Conservation of Mass Equation 97
4.5.2.2 – Derivation of the Unsteady Conservation of Energy Equation 98
4.5.2.3 – Derivation of the Unsteady Conservation of Species Equation 100
4.5.2.4 – Expansion of the Unsteady Equations Into Real and Imaginary Form 101
CHAPTER 5 – NUMERICAL TECHNIQUE 105
5.1 – Steady Solution 106
5.2 – Unsteady Solution 111
5.3 – Heat Release Calculation 122

5.4 – Heat Release Linear Growth Rate 124

CHAPTER 6 – ANALYSIS OF PROGRAM RESULTS 130

6.1 – Discussion of Setup 130

6.2 – Comparison to Tien's Results 132

6.3 – Initial Baseline Liquid Rocket Results 136

6.4 – Sensitivity Analysis 142

6.5 – Analysis of Dimensional Results 166

CHAPTER 7 – RECOMMENDATIONS AND FUTURE WORK 173

CHAPTER 8 – CONCLUSIONS 176

REFERENCES 179

APPENDICES 189

APPENDIX A 190

APPENDIX B 202

APPENDIX C 218

VITA 222

LIST OF FIGURES

Figure 1. Example of Sinusoidally Oscillating Longitudinal Waveform 7

Figure 2. Example of Standing Tangential Waveform [2] 8

Figure 3. Illustration of Traveling Tangential Waveform [2] 8

Figure 4. Example of Oscillating Radial Waveform 9

Figure 5. Frequency Spectrum for Rijke Tube [38] 10

Figure 6. Example of Limit Cycle Behavior (JPL Corporal) [39] 12

Figure 7. Example of Energy Cascade [40] 12

Figure 8. Example of DC Shift (Tactical Motor Test) [41] 14

Figure 9. Minuteman III Pressure Data [48] 18

Figure 10. Minuteman III Propellant Grain Configuration [48] 18

Figure 11. Image of Propellant Removal To Eliminate Oscillations [48] 18

Figure 12. Pressure Data After Propellant Removal [48] 19

Figure 13. Aft End View of Injector Face Damage Due To Transverse Waves [12] 20

Figure 14. F-1 Engine Pressure Data [12] 21

Figure 15. F-1 Injector Face After Addition Of Baffles To Reduce Oscillations [12] 21

Figure 16. Corporal Pressure Data recorded At Various Chamber Locations [44] 23

Figure 17. Behavior Of Oscillation Amplitude Based Upon Growth Rate 30

Figure 18. Nonlinear System Behavior 35

Figure 19. Historical Development of the Energy Corollary Method 40

Figure 20. Diagrams Showing Combustion Of Liquid/Solid Rocket 77

Figure 21. Flowchart For Overall Energy Method 107

Figure 22. Program Flow Chart For Calculation of Heat Release Growth Rate 107

Figure 23. Flow Chart For Unsteady Program 108

Figure 24. Tien's Oscillatory Results for Solid Rocket Motor [75] 134

Figure 25. Results of Steady State Temperature For Liquid Rocket Engine 135

Figure 26. Results of Oscillatory Components For Liquid Rocket Engine 135

Figure 27. Fuel Species Profile (Y_f) for T_i=0.2, γ=1.17 137

Figure 28. Reaction Rate Profile (w) for T_i=0.2, γ=1.17 137

Figure 29. Steady State Heat Release Profile ($\mathscr{H}_0$) for T_i=0.2, γ=1.17 139

Figure 30. Steady State Temperature Profile (T_0) for T_i=0.2, γ=1.17 139

Figure 31. Unsteady Temperature Amplitude Profile (τ) for T_i=0.2, γ=1.17, ω=1 140

Figure 32. Unsteady Heat Release Amplitude Profile ($\mathscr{H}_1$) for T_i=0.2, γ=1.17, ω=1 ... 140

Figure 33. Unsteady Temperature (peak) Change with Frequency for T_i=0.2, γ=1.17 .. 141

Figure 34. Unsteady Heat Release (peak) Change with Frequency for T_i=0.2, γ=1.17.. 141

Figure 35. Dimensionless Growth Rate (α_{UC}) for T_i=0.2, γ=1.17 143

Figure 36. Reaction Rate Profile (w) Varying Initial Temperature (γ=1.17) 145

Figure 37. Steady Heat Release ($\mathscr{H}_0$) Varying Initial Temperature (γ=1.17) 145

Figure 38. Steady Temperature Profile (T_0) Varying Initial Temperature (γ=1.17) 146

Figure 40. Real Unsteady Temperature Component ($\tau^{(r)}$) Varying Initial Temperature (γ=1.17, ω=1) 148

Figure 41. Imaginary Unsteady Temperature Component ($\tau^{(i)}$) Varying Initial Temperature (γ=1.17, ω=1) 148

Figure 42. Unsteady Temperature Amplitude (τ) Varying Initial

Temperature (γ=1.17, ω=1) 149

Figure 44. Real Unsteady Heat Release Component ($\mathscr{H}^{(r)}$) for Varying Initial Temperature (γ=1.17, ω=1) 151

Figure 45. Imaginary Unsteady Heat Release Component ($\mathscr{H}^{(i)}$) Varying Initial Temperature (γ=1.17, ω=1) 151

Figure 46. Unsteady Heat Release Amplitude ($\mathscr{H}_1$) Varying Initial Temperature (γ=1.17, ω=1) 152

Figure 47. Dimensionless Growth Rate (α_{UC}) Varying Initial Temperature (γ=1.17) 152

Figure 48. Dimensionless Growth Rate (α_{UC}) for Varying Gamma (T_i=0.35) 153

Figure 49. Dimensionless Growth Rate (α_{UC}) Varying Gamma (T_i=0.05) 155

Figure 50. Dimensionless Growth Rate (α_{UC}) Varying Gamma (T_i=0.1) 155

Figure 51. Dimensionless Growth Rate (α_{UC}) Varying Gamma (T_i=0.15) 156

Figure 52. Dimensionless Growth Rate (α_{UC}) Varying Gamma (T_i=0.2) 156

Figure 53. Dimensionless Growth Rate (α_{UC}) Varying Gamma (T_i=0.25) 157

Figure 54. Dimensionless Growth Rate (α_{UC}) Varying Gamma (T_i=0.3) 157

Figure 55. Dimensionless Growth Rate (α_{UC}) Varying Gamma (T_i=0.35) 158

Figure 56. Dimensionless Growth Rate (α_{UC}) Varying Gamma (T_i=0.4) 158

Figure 57. Change in Dimensionless Growth Rate (α_{UC}) over Varying Temperature for γ=1.1 and γ=1.667 159

Figure 58. Dimensionless Growth Rate (α_{UC}) for Nitrous Oxide Decomposition 160

Figure 59. Dimensionless Growth Rate (α_{UC}) for LOX/CH_4 160

Figure 60. Dimensionless Growth Rate (α_{UC}) for LOX/RP-1 161

Figure 61. Comparison of Dimensionless Growth Rate (α_{UC}) for Different Propellant Combinations 162

Figure 62. Comparison of Dimensionless Growth Rate (α_{UC}) for Different Gamma Over Varying Initial Temperature (ω=0.001) 165

Figure 63. Comparison of Dimensionless Growth Rate (α_{UC}) for Different Chamber Frequency Over Initial Temperature (γ=1.1) 165

Figure 64. Phase Comparison of Oscillatory Temperature (T) and Pressure (P) (ω=0.01) 167

Figure 66. Phase Comparison of Dimensionless Oscillatory Heat Release ($\mathscr{H}$) and Pressure (P) (ω=0.01) 168

Figure 67. Phase Comparison of Dimensionless Oscillatory Heat Release ($\mathscr{H}$) and Temperature (T) (ω=0.01) 168

Figure 68. Dimensional Growth Rate (α_{UC}) over Longitudinal Frequency for L=0.5 meters (Noting Modes for a System with γ=1.2) 169

Figure 69. Dimensional Growth Rate (α_{UC}) over Longitudinal Frequency for L=3.0 meters (Noting Modes for a System with γ=1.2) 170

Figure 70. Nozzle Damping Growth Rate (α_{ND}) Over Changing Chamber Pressure 172

Figure 71. Dimensional Growth Rate (α_{UC}) for L=3.0 meters Over Changing Chamber Pressure 172

Figure A-1. Real Unsteady Species Component ($Y^{(r)}$) Varying Initial 203

Temperature (γ=1.17, ω=1) 203

Figure A-2. Imaginary Unsteady Species Component $Y^{(i)}$ Varying Initial Temperature

(γ=1.17, ω=1)..... 203

Figure A-3. Unsteady Species Amplitude Y for Varying Initial Temperature

(γ=1.17, ω=1)..... 204

Figure A-4. Real Unsteady Velocity Component $v^{(r)}$ for Varying Initial Temperature

(γ=1.17, ω=1)..... 204

Figure A-5. Imaginary Unsteady Velocity Component $v^{(i)}$ for Varying Initial

Temperature (γ=1.17, ω=1) 205

Figure A-6. Unsteady Velocity Amplitude v for Varying Initial Temperature

(γ=1.17, ω=1)..... 205

Figure A-7. Reaction Rate Profile (w) for Varying Gamma (T_i=0.35) 206

Figure A-8. Steady Temperature Profile (T_0) for Varying Gamma (T_i=0.35) 206

Figure A-9. Real Unsteady Temperature Component ($\tau^{(r)}$) Varying Gamma

(T_i=0.35, ω=1)..... 207

Figure A-10. Imaginary Unsteady Temperature Component ($\tau^{(i)}$) for Varying Gamma

(T_i=0.35, ω=1)..... 207

Figure A-11. Unsteady Temperature Component (τ) Varying Gamma

(T_i=0.35, ω=1)..... 208

Figure A-12. Real Unsteady Species Component ($Y^{(r)}$) Varying Gamma (T_i=0.35, ω=1) 208

Figure A-13. Imaginary Unsteady Species Component ($Y^{(i)}$) Varying Gamma (T_i=0.35, ω=1) 209

Figure A-14. Unsteady Species Amplitude (Y) Varying Gamma (T_i=0.35, ω=1) 209

Figure A-15. Real Unsteady Velocity Component ($v^{(r)}$) Varying Gamma (T_i=0.35, ω=1) 210

Figure A-16 Imaginary Unsteady Velocity Component ($v^{(i)}$) Varying Gamma (T_i=0.35, ω=1) 210

Figure A-17. Unsteady Velocity Component (v) Varying Gamma (T_i=0.35, ω=1) 211

Figure A-18. Real Unsteady Heat Release Component ($\mathscr{H}^{(r)}$) Varying Gamma (T_i=0.35, ω=1) 211

Figure A-19. Imaginary Unsteady Heat Release Component ($\mathscr{H}^{(i)}$) Varying Gamma (T_i=0.35, ω=1) 212

Figure A-20. Unsteady Heat Release Component ($\mathscr{H}_1$) Varying Gamma (T_i=0.35, ω=1) 212

Figure A-21. Comparison of Dimensionless Growth Rate for Different Gamma Over Varying Initial Temperature (ω=0.01) 213

Figure A-22. Comparison of Dimensionless Growth Rate for Different Gamma Over Varying Initial Temperature (ω=0.1) 213

Figure A-23. Comparison of Dimensionless Growth Rate for Different Gamma Over

Varying Initial Temperature (ω=1) 214
Figure A-24. Comparison of Dimensionless Growth Rate for Different Gamma Over Varying Initial Temperature (ω=10) 214
Figure A-25. Comparison of Dimensionless Growth Rate for Different Chamber Frequency Over Initial Temperature (γ=1.2) 215
Figure A-26. Comparison of Dimensionless Growth Rate for Different Chamber Frequency Over Initial Temperature (γ=1.3) 215
Figure A-27. Comparison of Dimensionless Growth Rate for Different Chamber Frequency Over Initial Temperature (γ=1.4) 216
Figure A-28. Comparison of Dimensionless Growth Rate for Different Chamber Frequency Over Initial Temperature (γ=1.5) 216
Figure A-29. Comparison of Dimensionless Growth Rate for Different Chamber Frequency Over Initial Temperature (γ=1.6) 217
Figure A-30. Comparison of Dimensionless Growth Rate for Different Chamber Frequency Over Initial Temperature (γ=1.667) 217

LIST OF TABLES

Table 1. Notable Instability Cases 23

Table 2. Dimensionless Variable Values 136

Table 3. Propellant Combination Data..... 164

Table 4. Dimensionalizing Variable Values 169

LIST OF SYMBOLS

A	Admittance, Mode/Geometry Weighting Function
a	Speed of Sound
B	Reaction Coefficient, Boundary Location, Eigenvalue
b	Boundary Surface
Cp	Specific Heat at Constant Pressure
E	System Energy, Modal Energy, Activation Temperature
e	Internal Energy
F	Body Forces
f	Chamber Longitudinal Frequency, Random Function
h	Enthalpy
H	Enthalpy
i	Mode Number
j	Mode Number, Reaction Dependant Quantity
k	Wave Number
L	Chamber Length
M	Boundary Value
m	Mass Flux, Mode Number
N	Nozzle Plane
n	Surface Normal, Mode Number, Order of Reaction
p	Pressure
Q	Heat
q	Heat Flux, Combustion Heat per Unit Mass
R	Universal Gas Constant, Oscillation Amplitude
r	Position Vector
S	Surface Area, Vector Potential
s	Entropy
T	Temperature
t	Time
u	Velocity
V	Volume
W	Energy Flux Vector
w	Reaction Rate
x	Position Unit
Y	Unsteady Species
Y_o	Oxidizer Species
Y_p	Propellant Species
Y_f	Fuel Species

Non-Roman Symbols:

$\mathscr{D}$	Source Function
$\mathscr{E}$	Energy Density
$\mathscr{H}$	Volumetric Heat Release
α	Growth Rate, Thermal Diffusivity

γ	Ratio of Specific Heats
δ	Kronecker Delta Function
∂	Reaction Rate Temperature Exponent
ε	Perturbation Parameter
λ	Thermal Conductivity
η	Bulk Viscosity, Periodic Time Function
μ	Viscosity
ρ	Density
Φ	Energy Dissipation, Phase Angle
ν	Unsteady Velocity
σ	Stoichiometrically Weighted Mass Ratio of Species
τ	Unsteady Temperature, Period
ω	Vorticity, Circular Frequency
ξ	Perturbation Parameter
ψ	Mode shape, Volumetric Forces
ζ	Perturbation Parameter

Super and Sub Scripts:

Re{}	Real part
Im{}	Imaginary part
‘	Oscillatory Part
^	Over variable - irrotational (acoustic)
~	Over variable – rotational
–	Over bar – steady (heat release model)
*	Dimensional Value
Subscript 0	Steady term
Subscript 1	Unsteady term
Subscript 2	Second order term

LIST OF ABBREVIATIONS

1-D	One-Dimensional
AFRL	Air Force Research Laboratory
DC	Direct Current
CFD	Computational Fluid Dynamics
ECM	Energy Corollary Method
ETM	Engineering Test Motor
GTL	Gloyer-Taylor Laboratories
JPL	Jet Propulsion Laboratories
LRE	Liquid Rocket Engine
NASA	National Aeronautics and Space Administration
NAWC	Naval Air Warfare Center
O/F Ratio	Oxidizer to Fuel Ratio
RSRM	Reusable Solid Rocket Motor
UTSI	University of Tennessee Space Institute

CHAPTER 1 – INTRODUCTION TO INSTABILITY

The phenomenon of combustion instability in propulsion devices has been a source of great concern for over six decades. It occurs in all combustion devices, including rockets (liquid, hybrid, and solid), turbojets (combustors and augmenters), ramjets, scramjets, and others [1]. It is characterized by the occurrence of organized pressure oscillations inside the combustion chamber during the firing (combustion) process.

The presence of these disturbances can have numerous undesirable effects on a mission. It can significantly degrade system performance, making completion of a mission impossible due to lack of necessary thrust. It can also inflict vibration-induced damage to vehicle guidance systems leading to loss of control and, hence, possible destruction. These vibrations can also lead to cargo damage or vehicle structural damage.

Obtaining a sufficiently complete understanding of combustion instability has been difficult. Too often instability is not typically dealt with until it appears in a development program. Then, focus is often placed on finding one specific design feature believed responsible for observed oscillations. This simplistic view of the situation often misses the fact that the instability process actually involves an interaction of multiple processes occurring within the system. It is not necessarily the effect of one feature in the system that imposes the observed pressure disturbance.

The name “combustion instability” actually originates from focus on one such mechanism, unsteady combustion effects [1]. Due to early experiences with oscillation issues, it was believed that since instability occurred during engine firing, the oscillations

must be a result of the actual combustion process itself [2]. This led to the original assumption that the oscillations must be the result of an unsteady combustion process through which the distributed effects of the burning must interact with the chamber acoustics. While this overly simplistic viewpoint is still held by many analysts, the actual effect of the combustion process itself on the stability of a system has not been successfully quantified. Until the development of the Extended Energy Corollary Method (ECM), no model or measurement technique provided the means to isolate the effects of unsteady combustion and quantify its energy feedback. This left its significance open to speculation and contributed to the often-held view that addressing combustion instability was a black art and it could not be solved.

Gaining insight into instability has not been easy due not only to the extreme complexity of the physical processes involved but also due to the non-linear behavior of the system. For this reason, many researchers have focused on individual mechanisms [1], depended on over simplified models [1], or applied computational fluid dynamic [1] tools to try to understand the problem. Until recently, none of these methods have been able to produce a reliable means to predict or characterize instability.

However, a recent breakthrough in stability analysis has produced a sophisticated process that incorporates a full suite of physical processes to provide reliable predictions of the onset of instability, the amplitude of the pressure oscillations, and detailed stability characteristics [1]. After forty years of iterative research by Culick [3-11], Yang [8-9, 12], Cantrell [13], Hart [13-15], and many others, Flandro successfully distilled the combustion instability research into a rigorous, self-consistent analytical framework using the concept of the unsteady energy corollary [1].

In Flandro's analytical framework, sub-models for the different stability mechanisms, such as unsteady combustion, are integrated to describe the energy balance for the system. Each of these sub-models yields a contribution to the stability characteristics of the system. Still an evolving work in progress, this technique's ability to predict the occurrence and severity of oscillations within a system is constantly being improved. Regular revision and inclusion of the effects of newly understood mechanisms improves the reliability of the model. It is desired to improve the fidelity of this method through the inclusion of a model for the unsteady combustion heat release effects within the system. Since the combustion effects within a system have never been quantified in a stability analysis, this is a vital component that needs to be investigated.

1.1 – Objective

It is the objective of this dissertation to enhance the understanding of unsteady combustion and its effects within a combustor system, namely a liquid rocket system. Through analysis of the combustion process in a distributed combustion zone, the interaction of a burning region with a superimposed acoustic wave can be examined. It is the intent of this research to quantify the effects of unsteady combustion on the stability of a rocket system through calculation of the heat release linear growth rate. This investigation will also seek to understand what system parameters affect this mechanism as well as determine the relative importance of unsteady combustion heat release compared to other established combustion instability mechanisms. This understanding will be incorporated into the new energy method for predicting combustion instability.

1.2 – Background

A presentation of the phenomenon of "combustion instability" is described in the following sub-section along with an introduction to the key features that are observed during rocket motor operation. This is followed by a historical discussion of the occurrence of instability in practice. The following chapter describes the historical approach used in predicting the occurrence of oscillations. A brief discussion of other important driving and damping mechanisms is also given. The limited amount of information presented in theses chapters along with other excellent work of many investigators has formed a solid foundation for the new nonlinear method described in Chapter 3.

1.3 – Common Features of Instability

Combustion instability involves a vast array of both physical and chemical interactions that are not yet fully understood. This leads to an extremely complicated nonlinear system that cannot be solved simply. This difficulty has led many researchers in the field to believe that no solution to combustion instability would ever be found, while others viewed it as a black art. This has left engine developers with little choice but to use costly and time-consuming trial-and-error methods and the hope that serious instability would not be experienced.

However, recent advances [1, 16-19] have shown that the key to understanding combustion instability is to recognize that all systems undergoing instability display common physical features and that it is a system dynamics problem involving the

interaction of dozens of physical mechanisms. The following subsections describe some of the key features and provide an overview of the physical mechanisms.

1.3.1 – Forced Versus Self-Excited Oscillations

There are two types of oscillations that can be seen inside of unstable rocket systems, forced oscillations and self-excited oscillations. When a system experiences forced oscillations, some outside force is acting upon it. A classic example of this is the spring mass damper system. While forced oscillations can occur within a rocket chamber (e.g. valve cycling or actuator pumping), the resulting amplitudes tend to be low because they require an external source of energy. High amplitudes tend to occur only when an unsteady energy feedback mechanism is present. In other words, unless the forced oscillation interacts with a self-excited oscillation it tends to be of little interest. Furthermore, in a forced system, when the driving disturbance disappears, so do its effects upon the system.

Typically, a system experiencing combustion instability can be referred to as a self-excited system. A self-excited system is one in which feedback mechanisms exist between the gas motions themselves and the driving or damping mechanism. In other words, the gas dynamics store the unsteady energy briefly then release it back into the system in a way that amplifies the oscillation. For example, an acoustic wave moving over a burning solid propellant can introduce additional unsteady mass flow into the system that reinforces the acoustic wave (i.e. pressure coupling mechanism). In this type of system, the feedback mechanisms can drive the chamber oscillations even after the original disturbance has ceased to have an influence.

1.3.2 – Acoustic Modeling

A notable feature of instability is that the system oscillation frequencies are very close to the acoustic modes for a given chamber geometry. This has led many researchers [3-15, 19-25] to model the chamber fluctuations using standard acoustic wave theory as shown in the following equation. This formulation calculates the oscillating pressure for a particular mode of excitation.

$$p'_m = a_m \sin\left(w_m t\right) \sin\left(k_m t\right) \tag{1}$$

This will be discussed further in Chapter 2.

While acoustic theory provides a good prediction of the oscillatory frequency, just modeling instability in this way does not truly represent the oscillations experienced during instability. Rather than being a simple sine wave, instability oscillations tend to be steepened in form [1, 27-29]. It must be realized that the fluctuating pressure is actually a superposition of all of the acoustic mode pressure contributions.

1.3.3 – Transverse and Longitudinal Waveforms

There are two main types of acoustic waveforms used to represent oscillations within a rocket chamber: longitudinal and transverse waves. Longitudinal waves involve gas motions parallel to the axis of symmetry, usually in the direction of the flow. Oscillations are expressed in the above form for each mode representing an acoustic sinusoidal standing waveform, as seen in Figure 1.

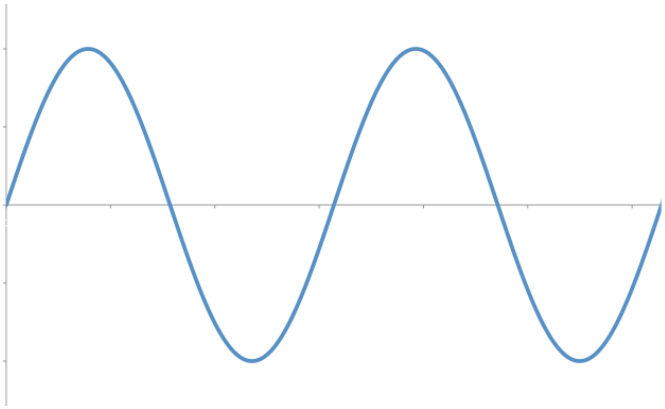

Figure 1. Example of Sinusoidally Oscillating Longitudinal Waveform

The frequency for a given mode can be determined based upon chamber quantities of length, L, and the speed of sound, a, as shown, where n is the mode number.

$$f = \frac{na}{2L} \tag{2}$$

Transverse waves involve gas motions that oscillate normal to the long axis of the chamber, generally perpendicular to direction of flow. There are two types of transverse waveforms, tangential and radial. Tangential waves occur in the traditional sense of a waveform across the chamber diameter, as seen in Figure 2 in standing form, with high-pressure and low-pressure antinodes occurring on opposite sides. While standing waveforms can occur for tangential modes, the tangential nodes can move around the chamber perimeter leading to traveling forms of such waves, as shown in Figure 3. Radial modes are centered about the radius with the peak amplitude fluctuating back and forth along the centerline, as seen in Figure 4.

While all waveforms can occur in any rocket chamber, certain wave types are more common in particular systems due to typical geometric features. For instance, long solid rocket motors tend to display longitudinal modes. In contrast, short and stubby

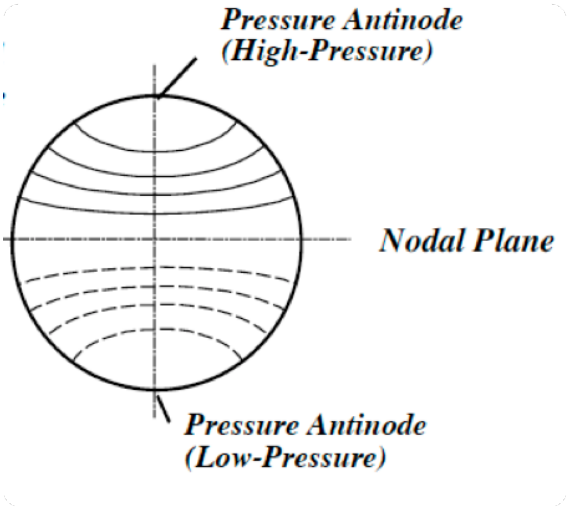

Figure 2. Example of Standing Tangential Waveform [2]

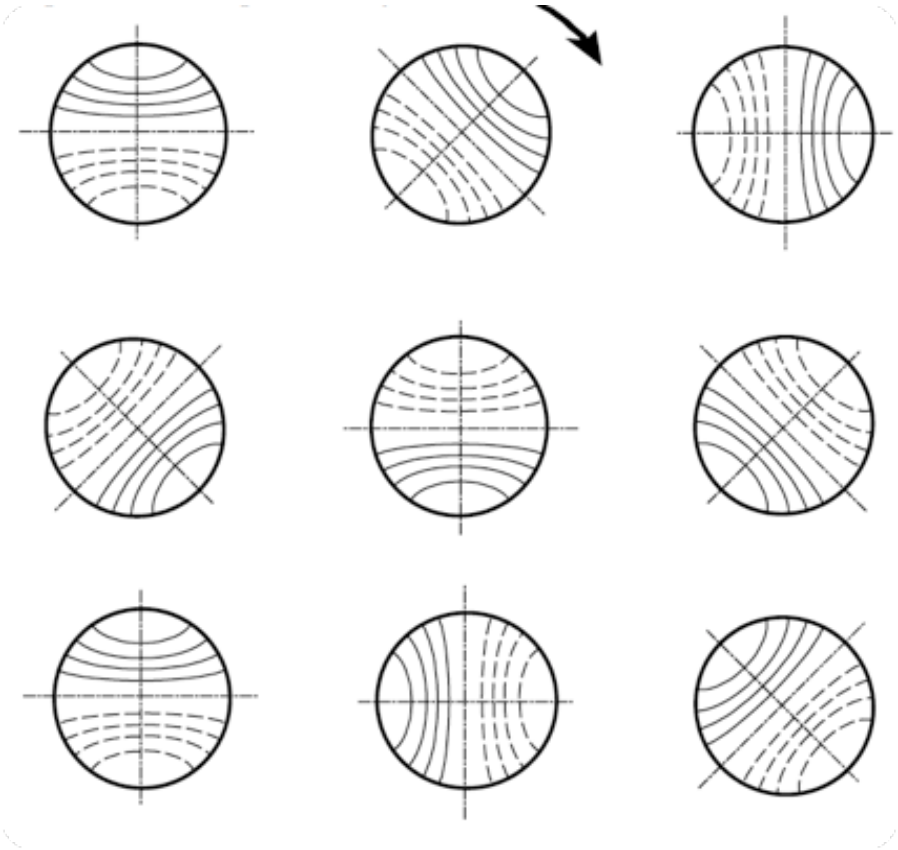

Figure 3. Illustration of Traveling Tangential Waveform [2]

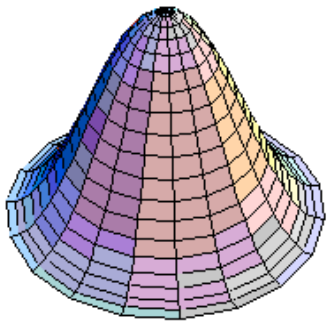

Figure 4. Example of Oscillating Radial Waveform

liquid rocket engines tend to experience tangential modes, while radial modes are seldom dominant in any device. Furthermore, while there are cases where higher modes may dominate, in general, the modes with the lowest frequencies are typically of greatest concern [2]. This is due to the fact that the lower frequency modes require a relatively less intense energy source for their excitation.

1.3.4 – Limit Cycle

Another important feature of instability is that oscillation amplitudes can be observed to grow exponentially at very low amplitude then transition to limiting amplitude in what is referred to as a limit cycle oscillation [1, 4, 30-37]. This is an effect captured in the nonlinear analysis. While this partly comes about from the natural damping of the each acoustic mode, this does not account for the strong limiting effect seen in test data. A clue to this damping source can be seen in the pressure frequency spectrum for various engines. Figure 5 shows the frequency spectrum diagram for a Rijke tube from testing conducted by Devarakonda [38], revealing harmonics at integer multiples of the excited first mode.

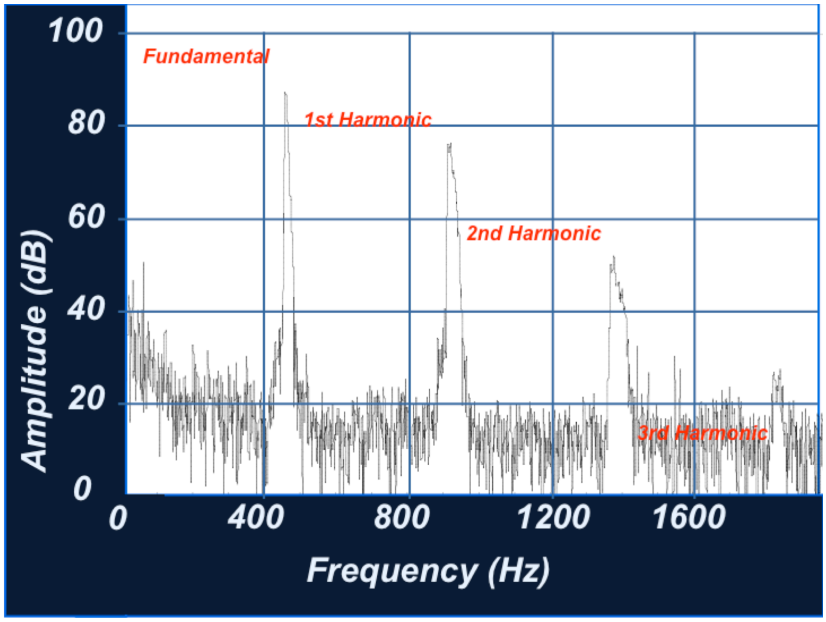

Figure 5. Frequency Spectrum for Rijke Tube [38]

The presence of these multiple harmonics of the excited mode of oscillation can be seen in practically every unstable engine test data [1, 37]. Since these harmonics are integer multiples of the unstable mode of oscillation, they tend to align with the natural modes in the case of longitudinal oscillations. However, in the case of tangential oscillations, the natural modes are defined by Bessel functions, which are not integer multiples; therefore, the harmonics and modes do not align.

The appearance of these harmonics is the result of a cascading of energy from the excited mode to higher frequencies [1, 16]. This process removes unsteady energy from the primary mode and transfers it to modes that have enhanced damping from viscous effects, thereby accelerating the dissipation of the unsteady energy. This provides a natural process to limit the growth of the primary mode of oscillation, producing what is known as a limit cycle. This common feature can be readily seen in rocket test data where the oscillations grow to fixed amplitude and then remain constant from theorem.

An example of the limit cycle effect can be seen in Figure 6, while Figure 7 displays the energy cascade effect to higher modes. Figure 6 shows recorded pressure data over time for the JPL Corporal liquid rocket engine. In this data, an initial pulse is introduced to start the oscillations. This disturbance rapidly dissipates as the higher mode oscillations are damped. However, the residual unsteady energy at the unstable (i.e. first tangential) mode then grows in amplitude due to the energy feedback until the energy cascade process limits its amplitude. This process causes the harmonic modes to increase in amplitude as they dissipate the energy and transfer it to even higher modes. Thus, this process tends to produce a series of harmonic oscillations with reduced amplitude at higher frequencies, as seen in the simulation data run by Flandro for a corporal rocket sized chamber, shown in Figure 7.

This process leading to limit cycle amplitude can also be described as wave steepening. When all of the acoustic modal waveforms are combined and allowed to progress, it is seen that the motion develops into a steep fronted traveling wave, akin to a weak shock wave. One way to look at this is that various parts of the wave are traveling at different local speeds of sound; this occurs because the absolute pressure at the wave peaks is higher than at the wave troughs. As a result, the tips of the waves pile into one another causing a build up, with the front of the steep wave at slightly higher speed than the average.

1.3.5 – The DC Shift

A subject of great practical importance is the so-called "DC" mean pressure shift. This occurs when the oscillatory gas motion is accompanied by a shift in mean chamber

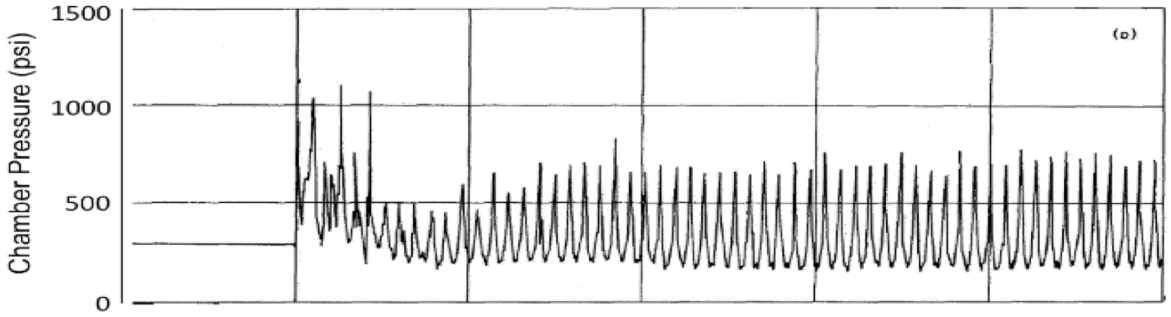

Figure 6. Example of Limit Cycle Behavior (JPL Corporal) [39]

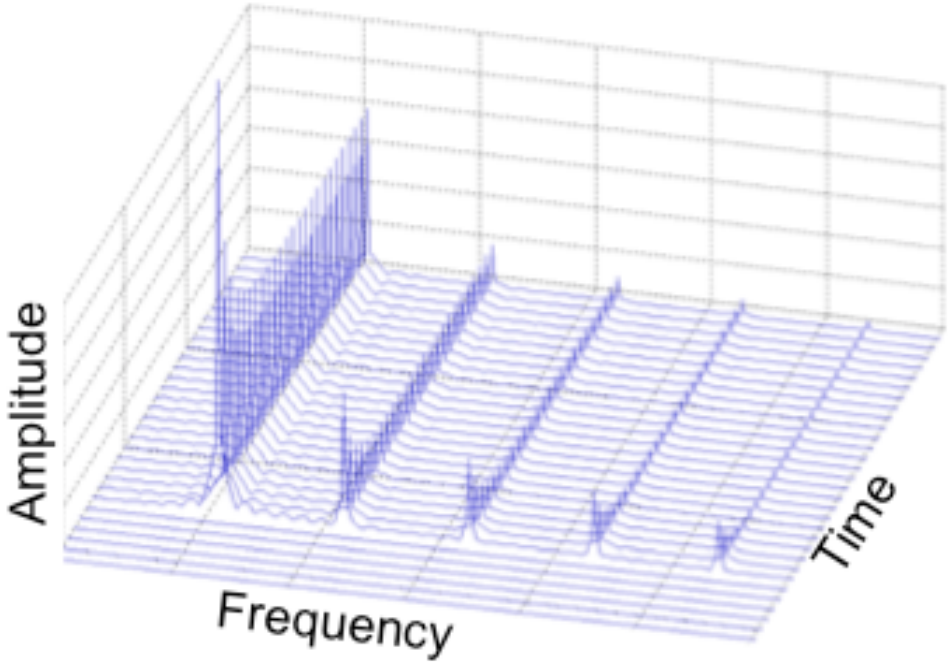

Figure 7. Example of Energy Cascade [40]

pressure and temperature. This was in fact, the first known symptom of combustion instability, often referred to as "irregular burning" [39, 30-37]. This has historically been acknowledged as a rise in mean chamber pressure, only recently having been recognized that a temperature and heat flux shift can also occur [2, 18].

The DC shift occurrence to this day is one of the most feared features of combustion instability in solid rockets. In addition to altering motor performance, a significant DC shift in chamber pressure may threaten the structural integrity and possibly lead to explosive failure of the motor case. An example of this DC shift can be seen in Figure 8 [41]. This figure shows experimental results by Blomshield, discussed in references [41-43]. In this tactical motor test, the mean chamber pressure clearly increases once the oscillations begin, at about one second into the burn. Prior to that, the mean chamber pressure is at about 750 psi and is gradually increasing as the solid propellant burns. However, just after one second, the motor begins to oscillate and rapidly reaches a limit cycle. This limit cycle starts at about 300 psi peak to peak and then grows to over 600 psi peak to peak due to motor geometry changes.

Along with this, the mean chamber pressure abruptly shifts from 750 psi to approximately 1100 psi then continues to grow as the propellant burns until it reaches approximately 1750 psi, whereupon the motor fails and shuts down. Under normal (i.e non-oscillating) conditions the mean chamber pressure would only have reached about 1000 psi at the end of the burn. The difference between the nominal mean pressure and the oscillating mean pressure is the DC shift. In this case, the initial DC shift is about 350 psi and then grows to around 750 psi, clearly showing that the DC shift can change over time as the operating conditions change.

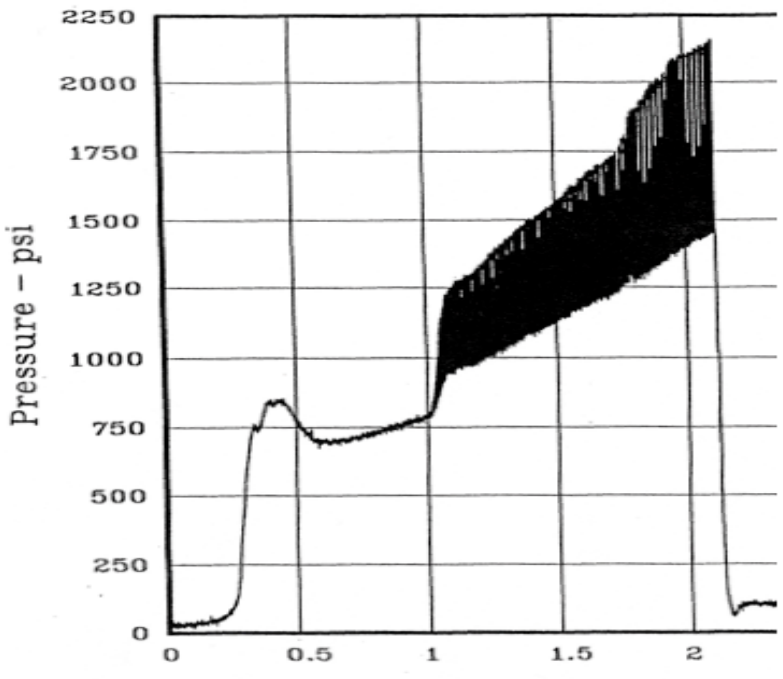

Figure 8. Example of DC Shift (Tactical Motor Test) [41]

While solid rockets tend to be at risk for DC pressure shift, this feature is seldom seen in liquid rockets [44]. The reason is that the propellant burning rate in solid rockets tends to increase when chamber pressure increases, producing a reinforcing effect by adding additional mass to the chamber in phase with the oscillations. In contrast, the mass flow into a liquid rocket is controlled by the propellant pumps and feed system [44]; thus, as chamber pressure increases, mass flow into a liquid rocket chamber decreases due to the reduction in injection pressure drop driving the liquid propellant flow.

1.4 – Historical Treatment of Instability in Practice

Problems with instability first appeared in the 1930's when rocket propulsion was in its beginnings, arising in programs like the German V2 liquid engine (1938) and in

solid rocket development studies under Poole (1937) [2]. For example, when Germany tried to simplify the injector design in the V2 to reduce cost and speed production, they encountered severe pressure oscillations [40]. This appearance of what is now known to be combustion instability during testing was just the first step in the process of understanding this complex phenomenon.

In the 1940's, studies in both the United Kingdom and in the United States at Caltech during World War II pointed to acoustic oscillatory combustion as an important factor even though oscillations could not be measured at the time [2]. Propellant charges ejected during over pressure led to the suggestion that there must be a dissipation of vibration energy in the solid. Initially only thought of as occurring in longitudinal modes of vibration, it was later determined that transverse oscillatory modes can also occur [2]. This was the result of testing by Hickman in which the inclusion of support rods in protruding propellant charges was able to reduce observed oscillations. Upon hearing of this, researchers at Caltech inserted longitudinal rods into the cavity of solid propellants and were able to reduce oscillations. Since such a rod was unlikely to interfere with longitudinal modes, it was thought that there must also be transverse modes present. The presence of these oscillations was only theoretical at the time, as there were no means to measure them until it was confirmed in 1948 [2].

During the 1950's, there was a great deal of experimental research into instability as more rocket development programs experienced oscillations [2]. It was something to cope with and 'fix'. Often, it could take hundreds if not thousands of iterations and tests to identify an approach that reduced the oscillation amplitude to acceptable levels. These included such things as modifying the geometry of the propellant in the case of solid

rockets or modifications to the chamber and injector features in the case of a liquid system. Modifications were also made to the propellant, such as mixture ratio and particulates. Multiple techniques for damping were also incorporated such as rods, cavities and baffles. Since handling instability was pretty much a black art at this time, even with these preventative techniques, rockets often went into service with some small oscillation, deemed as nonthreatening to the system [2].

This approach was initially acceptable for small rockets but as the missile and space programs began to produce larger rockets, the oscillations tended to get worse [2]. Arriving upon a suitable fix for larger systems could become quite costly and time-consuming, resulting in much of the program budget being spent on correction of this problem. At the time during which this phenomenon was being understood, this was an acceptable price to pay. With the Cold War well in motion and Russia's increasing propulsive and spaceflight capabilities, with a rising economy, the United States was willing to pay any price necessary to ensure military and scientific superiority.

During this time, some of the experimental studies conducted included the comprehensive study conducted by Brownlee [45-47]. Data collected in these investigations of solid propellant rocket motors have been extensively studied in the development of instability prediction theory. The most recent effort aimed at understanding the nonlinear effects displayed in the Brownlee data is the 2006 effort of Flandro, Perry, and French [37].

An example of a system that went into service with a known oscillation deemed to be non-threatening was the Minuteman II Stage III solid rocket [2]. The system was originally sent into service with a ten percent mean pressure oscillation at a non-resonant

frequency. However, halfway through service, flights began to have failures. The frequency of oscillation had shifted to one that created a system resonance, leading to failure of the thrust direction control system. This change occurred because the manufacturer of the aluminum powder in the propellant had changed [2]. This resulted in different combustion characteristics in the propellant, which altered its damping characteristics at lower frequencies making it susceptible to oscillations at those modes.

Oscillatory problems were also experienced in the later Minuteman III stage III. However, these were experienced for a different reason. Figure 9 shows data recorded during firing of the Minuteman III third stage. In this case, the oscillations can be seen to gradually shift to lower frequency over time then rapidly shift back to higher frequencies in a repeating pattern. This "locking-in" phenomenon is now known to be a characteristic of a motor with vortex shedding and a changing geometry [39]. The oscillation frequency shifts in order to maintain an integer number of vortex cells within the primary geometrical feature. The locking-in shifts occur when the geometrical gap has grown enough to sustain an additional vortex cell [39].

While not understood during service, it was later found that the oscillations could be easily eliminated with a slight contour change to reduce the driving mechanism caused by shedding of vortices. Figure 10 shows the propellant geometry inside of the motor; it can be seen that the major sources of vortex shedding are the steps near the middle of the motor. Figure 11 shows the change in the grain geometry that was employed by Flandro [48] to reduce the intensity of the vortex shedding. It can be seen in Figure 12 that this modification reduced the overall driving of the system, thereby eliminating the complex pressure oscillation signature seen in the previous test data. However, at the time of

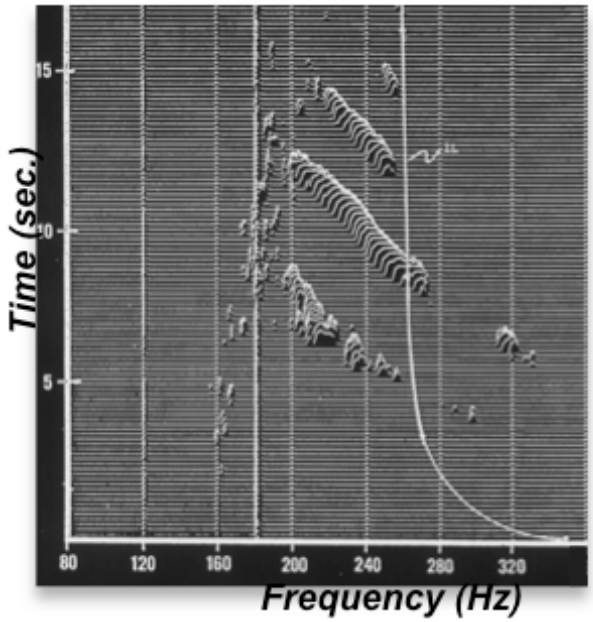

Figure 9. Minuteman III Pressure Data [48]

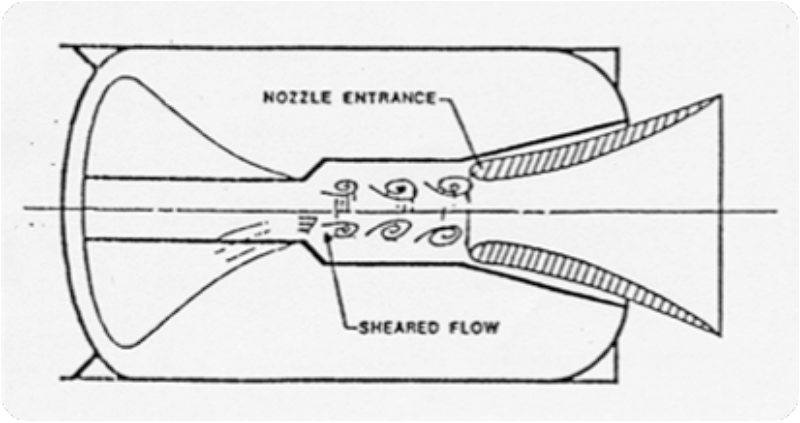

Figure 10. Minuteman III Propellant Grain Configuration [48]

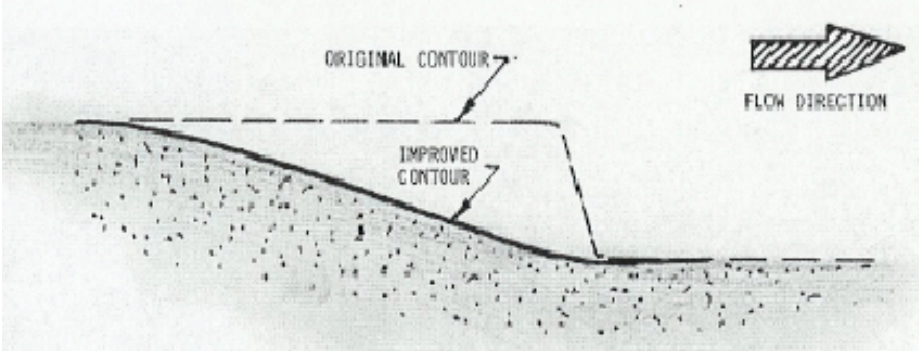

Figure 11. Image of Propellant Removal To Eliminate Oscillations [48]

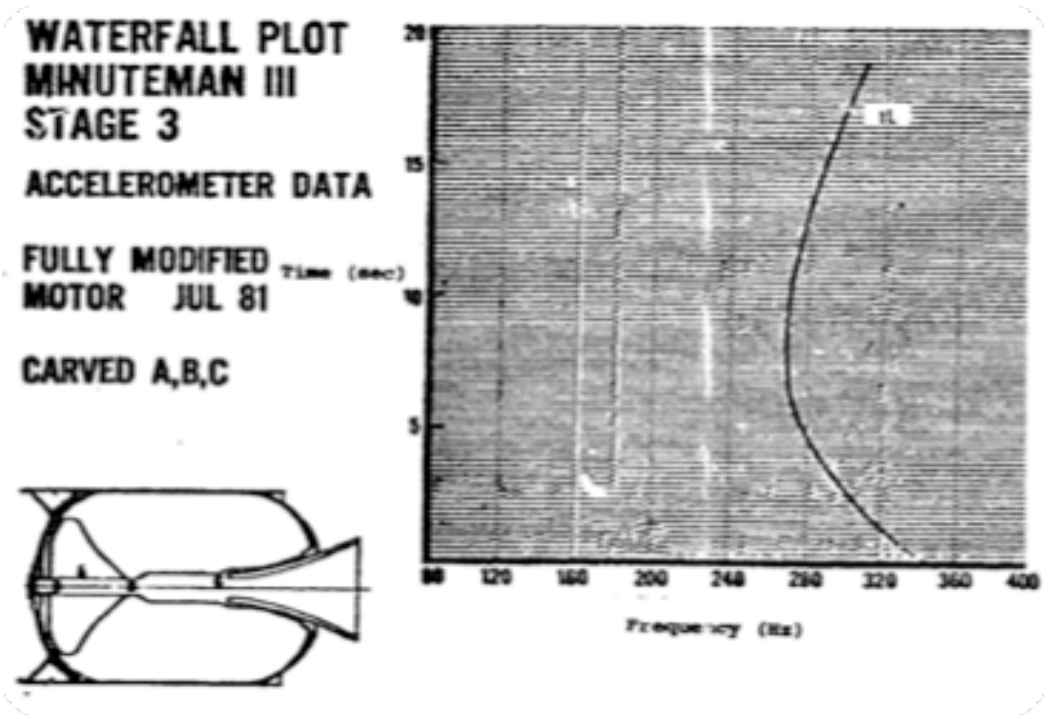

Figure 12. Pressure Data After Propellant Removal [48]

service, an incomplete understanding of combustion instability instead led engineers to reinforce the guidance system to withstand the oscillations. Rather than trying to understand and eliminate the oscillations, it was deemed easier to live with the oscillations and pay the performance penalties.

In the sixties, a very well known program that experienced damaging oscillations during its development was the Saturn V program, the launch vehicle for the Apollo moon exploration missions [12, 40, 44]. This system experienced severe oscillations in the first stage F-1 liquid rocket engine during the testing phase of development. An oscillation with extremely high amplitude, comparable to the chamber pressure, occurred at a frequency of the first tangential acoustic mode. The oscillations resulted in severe damage to the injector face, as shown in Figure 13. The recorded oscillations that

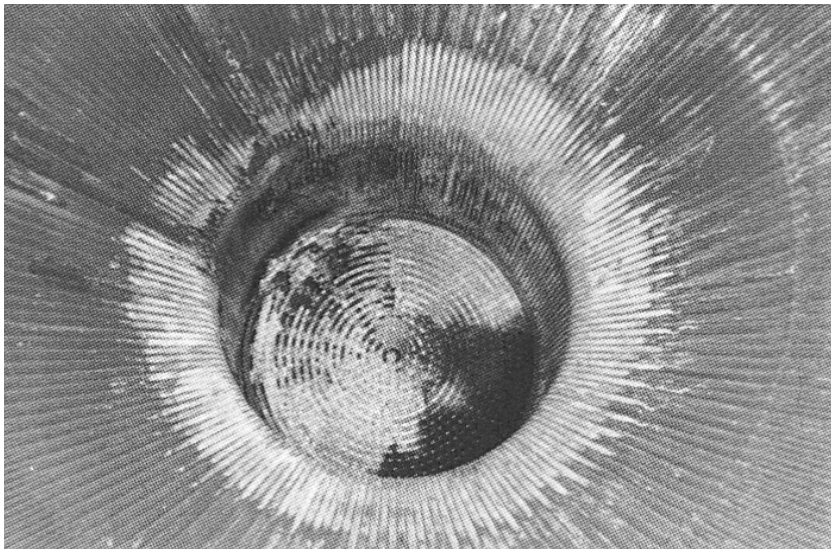

Figure 13. Aft End View of Injector Face Damage Due To Transverse Waves [12]

occurred within the engine are shown in Figure 14. Since it was not understood what was causing this oscillation, developers conducted over 2500 full-scale tests in order to reduce the amplitude of the chamber oscillations [12, 40, 44]. The resulting fix was the attachment of a baffle configuration to the injector facing. Figure 15 shows an image of the injector face with the baffle configuration used to reduce the oscillations. Though not understood how these baffles reduced oscillations, their use resulted in an oscillation that was only ten percent of the chamber pressure.

During testing of the F-1 engine, NASA enlisted the assistance of several outside agencies to aid in understanding the phenomenon [40]. This was an attempt not only to determine a way to reduce the extreme amplitude of observed oscillations but also to understand the exact behavior of transverse waves within a system. A series of extensive experiments were conducted at the Caltech Jet Propulsion Laboratory (JPL) using hardware from the Corporal liquid rocket engine with very comprehensive instrumentation [44]. While the data recorded were not fully utilized during the F-1

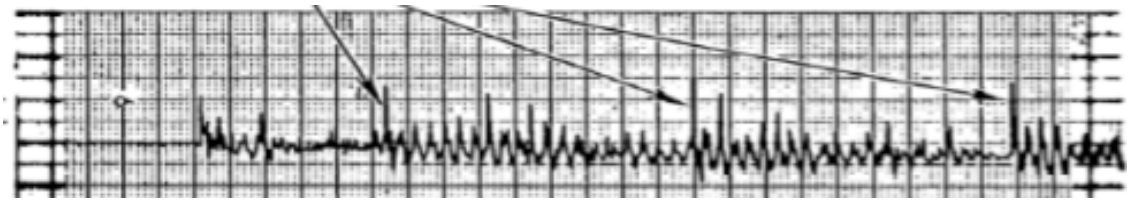

Figure 14. F-1 Engine Pressure Data [12]

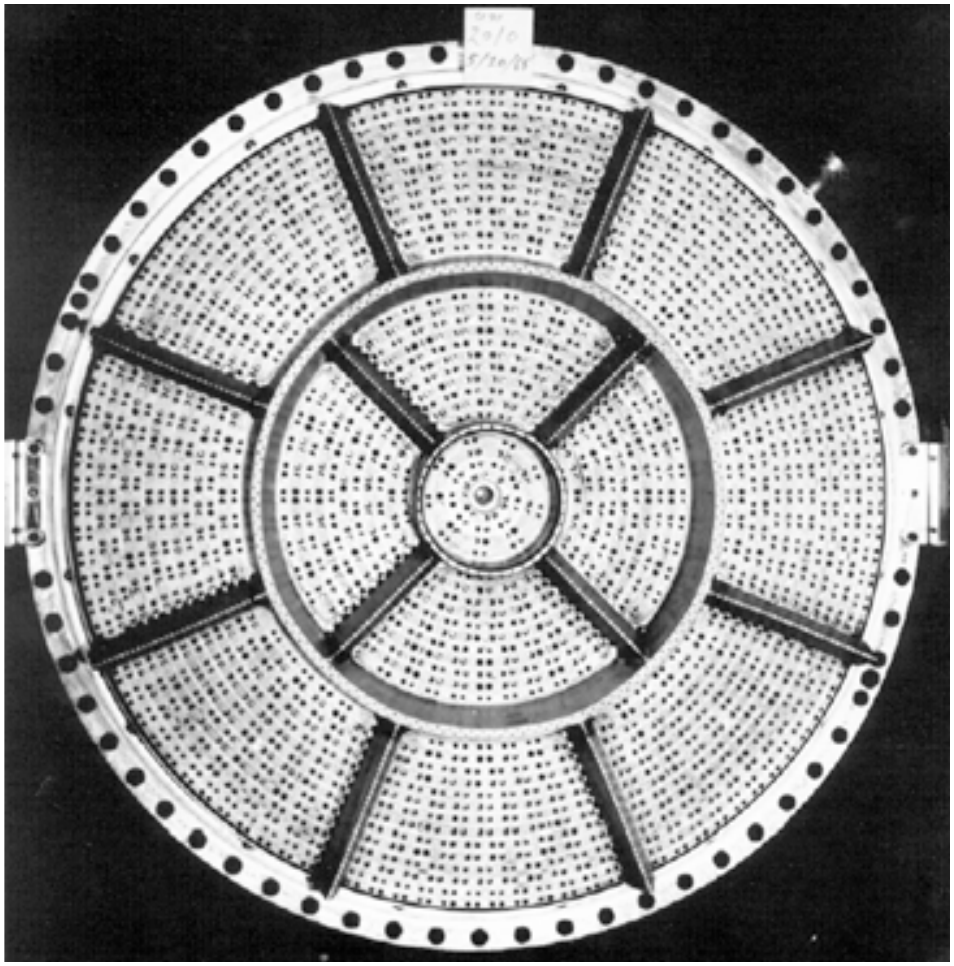

Figure 15. F-1 Injector Face After Addition Of Baffles To Reduce Oscillations [12]

development crisis, they provide critical insight that has been very beneficial in verifying the analytical methods described herein. A sample of this data is shown in Figure 16, which corresponds to the pressure time history data shown earlier in Figure 6 for the Corporal. The figure clearly shows the steep fronted waveform, as measured at several points along the chamber radius. This data is the result of important experimental study of the Corporal conducted by Clayton [49-50] and Sotter [50-51]. Data obtained from this study has proved extremely valuable in continuous analytic development endeavors. During this study, it is worthy to note that Sotter film documented high amplitude rotating transverse waves within the rocket [49-51].

This historical discussion gives a very brief introduction to rocket systems that have experienced oscillatory behavior. There are just far too many systems that have encountered problems with instability to provide a comprehensive list. Table 1 shows a list of those rockets discussed as well as other notable instability examples, along with the excited mode that was of concern in each system [40]. As seen in this list, instability is experienced in all types and sizes of rocket systems.

As a result of this experience, some of the corrective procedures employed over the years have become design standards used to deal with instability. For example, Helmholtz and quarter-wave resonator cavities are commonly used in liquid rocket engines to damp oscillations [2]. Application of these procedures sometimes gives designers a false sense that they have the risk under control and that they can deal with instability. While designers often incorporate these fixes during the design stage of development, much effort is usually required during testing to adjust or tune them to the actual conditions encountered. However, even then, many times the engine dynamics are

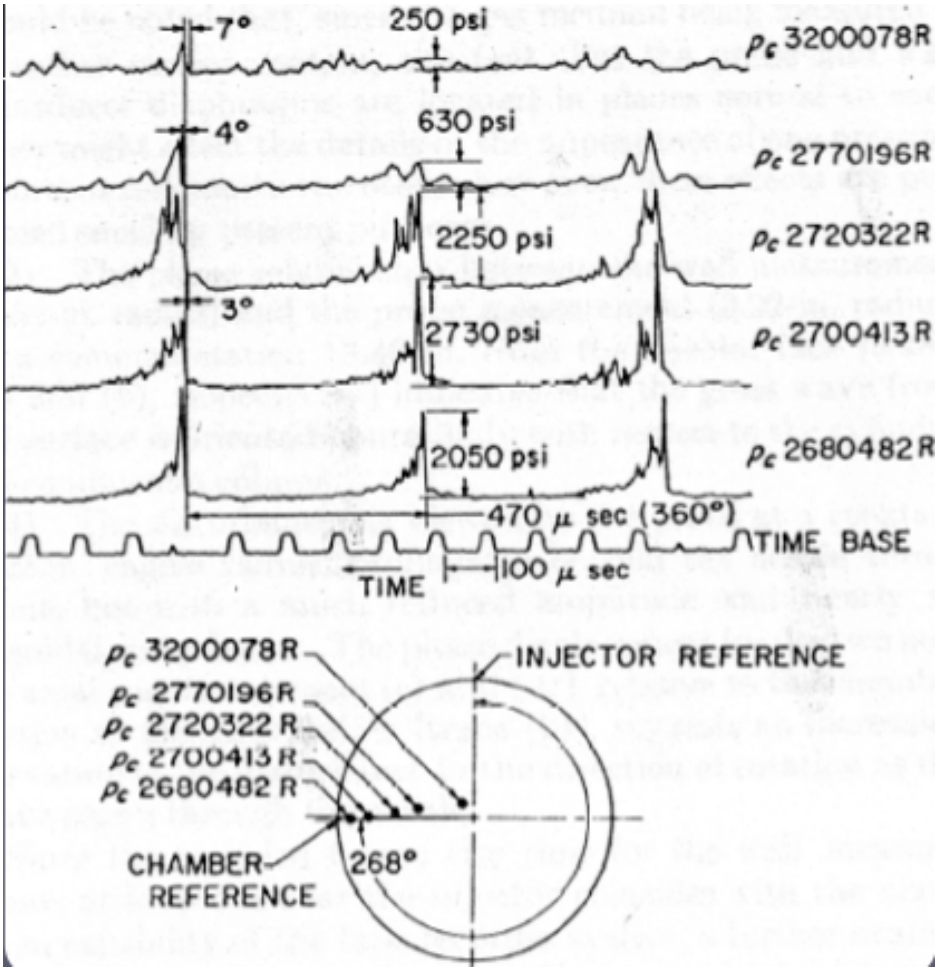

Figure 16. Corporal Pressure Data recorded At Various Chamber Locations [44]

Table 1. Notable Instability Cases

Engine/Motor	Issue
Minuteman II - Stage 3 [2]	Axial Modes
Minuteman III - Stage 3 [48]	Axial Modes
Corporal Liquid Rocket Engine [44]	Tangential Modes
Titan Solid Rocket Booster [2]	Axial Modes
JPL 6" Motors [31]	Transverse Modes
NAWC 6" Tactical Rocket Series [41]	Axial Modes
F-1 Liquid Rocket Engine [12]	First-Tangential Mode
RSRM & ETM3 [16,17]	Longitudinal Modes

so complex that the fixes are ineffective, or the oscillatory behavior changes in unexpected ways and renders them useless.

As previously mentioned, these fixes do not always eliminate oscillations, if they have any affect at all. It is still often necessary to accept an oscillation that is some small percentage of the chamber pressure amplitude, deemed to be nonthreatening. This leads into a common misconception in liquid rocket development, in which it is thought that an oscillation amplitude of ten percent of the mean pressure is an acceptable design standard to eliminate harmful oscillations. This is merely an artifact from the Saturn V program; there is little real basis for this common stability metric. In reality, if there are any organized pressure oscillations, then the engine is technically unstable, or at best, neutrally stable.

Since, at the present time, there is no standard way to predict the possibility of instability, engine development teams tend to ignore or downplay the risk of combustion instability. The problem that arises is that instability may still occur unexpectedly, often late in the development cycle, without a clear-cut approach to its solution. The appearance of instability in an engine development program can prove disastrous and may result in program cancellation.

It is clear that the use of such trial and error techniques and settling for an acceptable oscillation amplitude is not acceptable engineering practice. What is needed is a full physical understanding of what is actually occurring within the engine system, one in which all of the observed features of combustion instability are explained. It will be shown that a new technique known as the Energy Corollary Method leads to a powerful method for predicting instability. It can be used in a new system at the design

stage or used to diagnose experimental data, and it can be used to devise useful corrective strategies to eliminate combustion instability problems.

It is the focus of this dissertation to examine the effects of unsteady combustion heat release and then incorporate them into this new combustion stability prediction algorithm. This will enhance the fidelity of the predictions of the method and make it possible to avoid problems early in the development cycle.

CHAPTER 2 – MODELING OF COMBUSTION INSTABILITY

2.1 – Traditional Analytical Approach

To model the dynamics of combustion instability, it is assumed that there is an oscillatory acoustic pressure fluctuation superimposed on a chamber mean flow. The governing equations that result are nonlinear and therefore cannot be solved directly using classical methods of analysis. The oscillatory effects add a great deal of complexity to the problem. Therefore, attempts to create successful computational procedures based on conventional CFD techniques have been unsuccessful [1, 52].

To make the problem manageable, the classical method used to simplify the equations has been application of perturbation methods [2]. The solution must be able to reproduce results seen in test data as well as promote an understanding of those results. As a result, the tool that has become the foundation of combustion stability research is the asymptotic perturbation method [2].

This technique focuses on the relative smallness (or largeness) of key parameters in the formulation. Perturbation methods can be employed in this case since it is assumed that the amplitude of the oscillatory gas motion relative to the steady mean flow is typically small. As an example, it is assumed that the oscillatory pressure is a combination of steady and unsteady parts, as shown in equation 3, where m represents the mode number. The oscillatory pressure is shown to be a sinusoidally oscillating function of time as well as position.

$$p = \bar{P} + p' = \bar{P} + a_m \sin(\omega_m t)\sin(k_m x) \tag{3}$$

It can then be assumed that the mean flow properties are influenced by changes in a small amplitude parameter referred to as ε. It is the result of dividing the oscillatory pressure amplitude by the mean pressure, thus resulting in the following value,

$$\varepsilon = \frac{a_m}{\bar{P}} \tag{4}$$

where a_m is the amplitude of the wave.

Since it is assumed that the wave amplitude is very small compared to the mean flow, it is clear that this is an extremely small parameter. As with pressure, other unsteady system parameters, such as velocity, density, etc., can also be scaled by the wave amplitude parameter, ε. The expansions of each parameter can then be expressed in a regular perturbation series:

$$a = a_0 + \varepsilon a_1 + \varepsilon^2 a_2 + \varepsilon^3 a_3 + ... \tag{5}$$

Each of the subscripts denotes the relative order of the term, as do the powers of the ε multipliers. The first term represents the quasi-steady or mean flow value of the parameter of interest. The other terms represent perturbations of first order in ε, second order in ε, and so on. Since ε is assumed to be a small value, increasing orders of ε become smaller and smaller.

A useful attribute of perturbation techniques is that the principle of superposition can be used to group functions that are of the same order [2]. Each of their effects upon the system can then be isolated and, in some cases, be treated independently of the other orders.

The order of terms retained in the expansion process depends on the level of precision that is desired in understanding the solution. Retention of only first order terms

results in a linear system of equations to be solved for system behavior. In nature, deviation from linear behavior is often small so that a linear solution may at times be acceptable to explain system behavior. The majority of models for combustion instability in current use are based on such linearization [2]. However, combustion instability is known to exhibit important nonlinear behavior. In fact, several of the most important practical features of combustion instability are known to be symptoms of its inherent nonlinearity, such as limit amplitude, wave steepening, and the DC shift [1, 35-36]. Therefore, system behavior cannot be fully represented through linear analysis alone. If the higher order terms in the perturbation expansion process are retained, it will be shown in Chapter 3 that the nonlinear features of the system can be represented. The mathematics required in solving the equations increases with increasing order. Fortunately, most of the important nonlinearities are accommodated by retention of terms of second order.

Much effort in understanding rocket combustion instability has been devoted to the linear analysis since retention of the leading first-order terms give rise to a linear set of the equations to be solved. Due to the vastly decreased level of complexity in solving linearized equations, this has led to focus on understanding the linear behavior of stability. That is, the problem was reduced to a "stability" analysis in which system behavior near a low amplitude stability boundary is analyzed to determine whether the system would tend to oscillate or not.

However, actually understanding the behavior of real rocket engines and constructing representations for all of the stability mechanisms makes solution to the linear equations an extremely difficult task as well. The tendency has been to neglect this

important part of the problem and to focus on only a small number of linear driving and damping mechanisms. Correct treatment of the linear part of the problem is the key to predicting instability, as discussed in Section 2.2. For emphasis, this important part of the problem can only be useful if all driving and damping effects are correctly included. In this dissertation, focus is placed on one such component that has not been treated correctly in the past, namely the coupling between unsteady combustion effects and the acoustic wave structure.

2.2 – Stability Analysis

Historically, the linear model has served as a basis for predicting whether a system will be stable or unstable. Based upon the closeness of the oscillatory frequency to those of acoustic waves within the chamber, to analyze the governing equations the theory of acoustics was utilized. Oscillatory properties such as unsteady velocity and pressure can be expressed as shown below exponential form of the oscillatory pressure presented in equation 3, where m represents the mode number. [2]

$$p' = p_m e^{\alpha t} e^{i\omega t} \tag{6}$$

To aid in determination of stability, what is known as the net system linear growth rate is calculated. The exponent, α, represents this linear growth rate. Based upon linear theory, for an arbitrary pressure amplitude, R_m, a given growth rate can be used to determine the change in pressure oscillation amplitude over time, as expressed below [1]. This can be determined for each mode of oscillation, m, usually one of the acoustic modes for the chamber.

$$\frac{dR_m}{dt} = \alpha_m R_m \tag{7}$$

Correct determination of this growth rate defines a system that is stable vis-a'-vis one that is unstable. A mode, m, with a positive growth rate value will experience a growth in pressure oscillation amplitude and is said to be linearly unstable. A mode, m, with a negative growth rate represents decaying oscillation amplitude, or a stable mode. It is possible for a system to experience what is known as neutral stability, which results from a growth rate of zero or one that is nearly zero. This behavior is demonstrated in Figure 17.

Therefore, in order for oscillations to persist in a system, a system must have a positive (or near zero) growth rate for at least one mode of oscillation. It is important to note here that systems often referred to as "stable" if they experience oscillations lower than a specified percentage (such as the 10% rule that was devised during the Apollo, Saturn V F-1 engine crisis) are still technically unstable. If the system is truly stable, (negative linear growth rate), organized oscillations will damp out if given enough time.

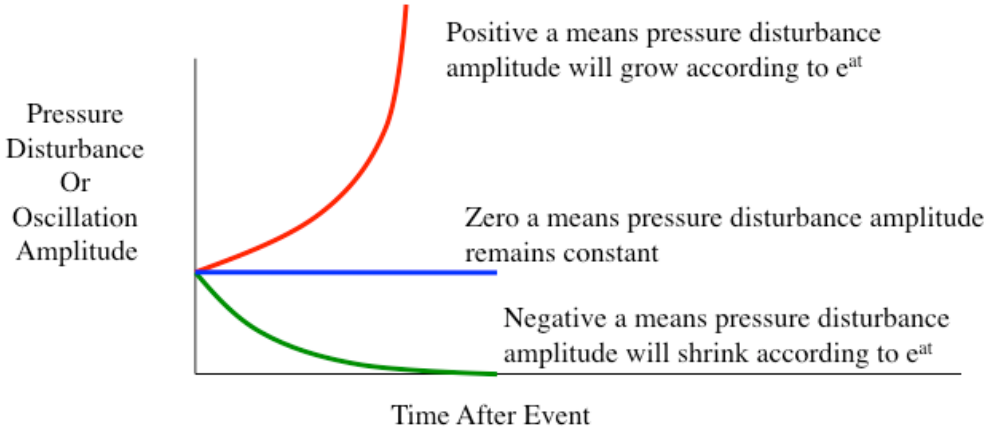

Figure 17. Behavior Of Oscillation Amplitude Based Upon Growth Rate

Thus, the key to determining the stability of the system is to determine the linear growth rate for each mode of oscillation. It requires knowledge of the linear growth rate contributions of all of the mechanisms occurring within a system. This process is very involved and will be discussed in further detail in the Chapter 3. It will be shown that upon extensive work with the governing equations, the following expansion for alpha results [1]:

$$\alpha_m = \left[\begin{array}{l} \underbrace{\frac{1}{2E_m^2}\iint_{S_{inj}} M_{inj}\left(A_{inj}^{(r)}+1\right)\psi_m^2 dS}_{\text{Pressure Coupling}} - \underbrace{\frac{1}{2E_m^2}\iint_{S_N} M_N\left(A_N^{(r)}+1\right)\psi_m^2 dS}_{\text{Nozzle Damping}} \\ \underbrace{+\frac{1}{2E_m^2}\iint_{S_{injll}} M_{inj}B_{inj}^{(r)}\psi_m^2 dS}_{\text{Acoustic Boundary Layer Pumping (ABL)}} \underbrace{-\frac{1}{2E_m^2}\iint_{S_{injll}}\left(\frac{\delta}{2\gamma M_{inj}}\right)^2\left\langle \nabla\psi_m\cdot\nabla\psi_m\right\rangle dS}_{\text{Viscous Damping at Injection Surfaces}} \\ \underbrace{-\frac{1}{2\gamma P_0 E_m^2}\iiint_V \rho_0\boldsymbol{u}_0\cdot\left\langle \boldsymbol{u}_1\times\boldsymbol{\omega}_1\right\rangle dV - \frac{1}{2\gamma P_0 E_m^2}\iiint_V \rho_1\boldsymbol{u}_1\cdot\left\langle \boldsymbol{u}_0\times\boldsymbol{\omega}_0\right\rangle dV}_{\text{Vortex Shedding Effects and Flow Turning Loss}} \\ \underbrace{+\frac{1}{2\gamma P_0 E_m^2}\iiint_V \left\langle \frac{\mathscr{H}_1 T_1}{T_0} - \frac{\mathscr{H}_0 T_1^2}{T_0^2}\right\rangle dV + other\ sources}_{\text{Distributed Combustion Heat Release}} \end{array} \right] \quad (8)$$

This expression represents a summation of growth rate contributions due to all of the various mechanisms occurring within the system for a given acoustic mode, denoted by the subscript m. The net overall growth rate for mode m results from the summation of individual rate contributions from various mechanisms occurring within the system. Note the volume integral that represents the contribution due to volumetric heat release, the focus of this research, is shown on the last line of this equation. This term has only recently been discovered [1] and will be evaluated for the first time in this dissertation to

determine its importance relative to the other gain and loss mechanisms shown in equation 8.

The terms calculated in this extremely complex analysis can be broken into two categories: damping terms and excitation terms. The damping terms include mechanisms such as nozzle damping, flow turning, particle damping, and viscous wall damping. The excitation terms include mechanisms such as pressure coupling, boundary layer pumping, and vortex shedding. As previously mentioned, the unsteady combustion heat release growth rate, to be determined in this research, is anticipated (based on much conjecture) to be an excitation term. The behavior of this effect, its dependence on all of the system parameters, and its importance relative to the other growth rate terms will be examined in detail.

Since these terms are linear in nature, the total growth rate of the system can be determined by adding them together, as above. These terms merit a short explanation to give an overall depiction of the internal dynamics occurring within an unstable system [16-17].

Damping terms:

Nozzle Damping: This term represents the amount of the acoustic energy that is convected out of the combustion chamber through the nozzle. Factors such as the nozzle throat size relative to the time varying chamber port area, the throat erosion rate and how much the throat is submerged in the chamber have a major effect on this term. Additionally, nozzle damping is largest for axial modes and is small for tangential and

radial modes [16-17]. Recently, a method to directly compute the nozzle damping has been developed by French [53].

Flow Turning: This term represents the energy interaction between the gas traveling parallel with a burning surface and the gas emitted from the surface, which is a function of the acoustic velocity at the surface. This term tends to be significant for axial modes when there is side-wall burning or for tangential modes when there is head end injection [16-17].

Particle Damping: This term is a volumetric integral that determines how much energy is transferred from the acoustic motion of the gas to particulates, such as slag or propellant drops. The amount of particle damping is directly related to the relative size of the particles to the acoustic wavelength. For low frequency oscillations, the particles must be very large to produce significant damping. However, small particles or drops can be significant in small devices with high frequencies [16-17].

Wall Damping: This term represents the frictional removal of energy due to acoustic motions. This term is directly proportional to the non-burning, non-injecting surface area that is exposed to viscous flow [16-17].

Excitation terms:

Pressure Coupling: This term represents the amount of energy added to the system due to the response of the propellant's burn rate or mass injection to an acoustic wave. This term is directly proportional to the solid propellant burning surface area, or, the amount of liquid injection area. In liquid rockets, the reflection of pressure waves inside the liquid feed system controls this parameter [16-17].

Boundary Layer Pumping: This term (discovered by Flandro in 1995 [24]) represents the addition of energy to the system resulting from the perturbation level maintenance of the no-slip acoustic boundary condition, which is a function of the local acoustic pressure at the surface. This term is maximized, or least stable, when the burning surface area or liquid injection area is large [16-17].

Vortex Shedding: This term represents the amount of energy added to the system from the creation of vortices at vortex shedding sites in the motor or engine. The magnitude of this term for a specific vortex-shedding site depends upon the location in the motor, and the shear layer characteristics, including maximum velocity, momentum thickness and other parameters. In general, this term is maximized, or least stable, when there are strong shear layers (large velocity gradients) in the motor or engine [16-17]. This term has recently been quantified for use in rocket motor stability computations and led to the successful prediction of the Ares I thrust roughness problem. That problem resulted from axial mode oscillations in the combustion chamber of the rocket caused by vortex shedding [16-17].

2.3 – The Need for Nonlinear Calculations

The challenge with linear stability models is that they only predict the onset of instability, in other words, determining whether an oscillation damps, grows, or remain constant. While this is helpful to some degree, engine developers are much more interested in the physical impact of the oscillations. Specifically, what are the amplitudes of the pressure oscillations, what are the thermal loads, and so on. This insight can only be obtained through the inclusion of nonlinear terms in the analysis [1, 2, 36].

If instability were really characterized by linear behavior, experienced oscillations would grow to infinity. However, as mentioned earlier, the oscillation amplitude in a real system is limited by the nonlinear energy cascade and cannot grow without bounds. This is shown nicely in Figure 18. This figure is a useful aid in understanding this important nonlinear behavior. The royal blue line indicates an initially exponential growth in oscillations that settles off to set amplitude, which is the limit cycle amplitude. The dashed royal blue line indicates the infinite growth that would be observed if instability were governed by linear behavior. Also, the cascading effect energy to higher modes can be seen by the amplitude growth of the first, second, and third harmonics, a contributing factor to the production of the limit amplitude, as discussed earlier. This figure displays a process that is still under much investigation and shows that there is clearly a need to take the analysis of instability beyond that of just a linear stability approach.

Although a great deal of analytical effort has been spent on linear techniques throughout the decades, it is indeed a necessary step. For progress in the complete

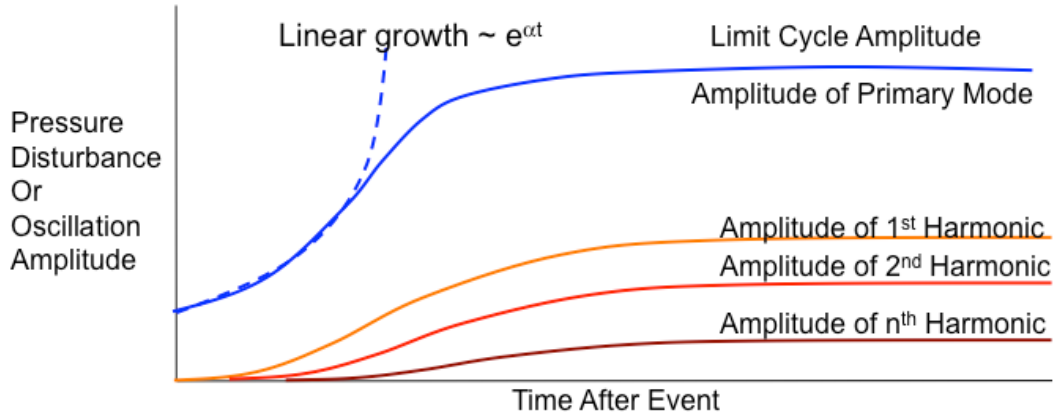

Figure 18. Nonlinear System Behavior

nonlinear problem, it is first a necessity that the linear problem be fully implemented and verified. Essentially, the linear part of the problem serves as a foundation upon which the nonlinear effects are built in order to complete the model. Then the higher order terms can be used as nonlinear corrections in a natural progression.

The following chapter presents the newly devised analytical methodology [1] based upon the energy balance within the system. It will be shown how the well-known expression for growth rate is developed for incorporation of unsteady combustion mechanisms effects. Also, the inclusion of higher order terms will be shortly discussed, in which all of the common nonlinear features that are experienced with instability are accounted.

CHAPTER 3 – WHAT IS THE ENERGY METHOD?

The research conducted in this dissertation is possible due to the efforts of Flandro in developing a generalized combustion instability framework referred to as the Extended Energy Balance Corollary Method [1]. Through implementation of a system energy balance approach to understanding instability, this method enables the representation of flow inside a combustion system through superposition of waves of compressibility, vorticity, and entropy upon a mean flow field. Through manipulation of the governing equations into an overall system energy balance, the effects of different flow features within a system can be described in terms of first order linear effects, second order nonlinear effects and so on. Thus, classic linear stability theory is accounted for, and the problem can then be extended to second order to include nonlinear effects upon the system.

Thus, after decades of ongoing research and occasional debate, extensive progress has been made towards an all-encompassing analytical model to aid in predicting the occurrence, as well as understanding the features, of instability in propulsion systems. Using this model, it is now possible to isolate different mechanisms of interest within a combustion system and then reincorporate their determined effects into the overall theory. Keeping with classic linear stability theory, a system energy balance comprised of first order terms can be arranged into an expression representing the system linear growth rate. This growth rate is comprised of the individual growth rate contributions from various mechanisms within the system, as previously discussed.

Through use of the extended ECM, this dissertation's contribution to stability theory is focused, then, upon isolating the effects of the unsteady combustion mechanism. Because the different system contributions can be combined in a linear summation, the mechanism of unsteady combustion can now be isolated from other system mechanisms and looked at as a separate problem. Upon determining its growth rate contribution, it can easily be added back into the calculation for determination of the total system growth rate. Then, through inclusion of nonlinear effects into the system, the full system dynamics can be represented - including the effects due to the unsteady combustion mechanism.

Before discussing this unsteady combustion analysis, it is essential that a detailed discussion of the energy balance method be given. Since this is still a work in progress, and although this dissertation's focus is placed upon investigation of the determination of the linear heat release growth rate, it is necessary to present the history and a seemingly long but much streamlined presentation of the development and use of the Extended Energy Balance Corollary Method in solving the problem of combustion instability. Through presentation of this development, the reader will be given full insight into the overall picture of how the unsteady combustion heat release growth rate contribution fits into the overall theory for prediction of instability.

3.1 – Historical Development

The development of the Extended Energy Corollary Method is the result of over forty years of research into the field of combustion instability by many researchers. During this time, three very distinct paths of understanding instability developed. These

three models are known as time-lag theory, energy balance theory, and acoustic wave theory. These three different avenues of study followed relatively independent paths until the last decade when Flandro, having contributed much to the field of instability research, concluded that each of the theories added information to the overall understanding of the phenomenon of combustion instability. Through the inclusion of features from all three theories, he developed what is known as the Extended Energy Balance Corollary Method. Figure 19 shows the historical development over time of these three independent theories. The three theories can be seen to combine together at the bottom of the center column, representing the development of the energy method, into the Extended Energy Corollary Method. The following discussion gives a brief discussion of the development of these three theories until culminating into the Extended Energy Corollary Method.

The column on the left of Figure 19 shows the development of the time-lag theory. This theory is derived from early liquid rocket development and attempts to model stability as a type of feedback system. Building off of initial work due to Von Karman, Crocco, and Cheng at Penn State University, this theory has been developed based largely on analysis of liquid rocket engines [54]. Throughout the decades other researchers from this group have attempted to carry this theory forward to aid in prediction of instability (but with little success [54-58]). Though useful information has been gained through this endeavor, this method of investigation is essentially a curve-fitting technique. While attempts have been made to predict instability based upon stability criterion referred to as n and τ, the lack of connection to physical processes has limited its effectiveness.

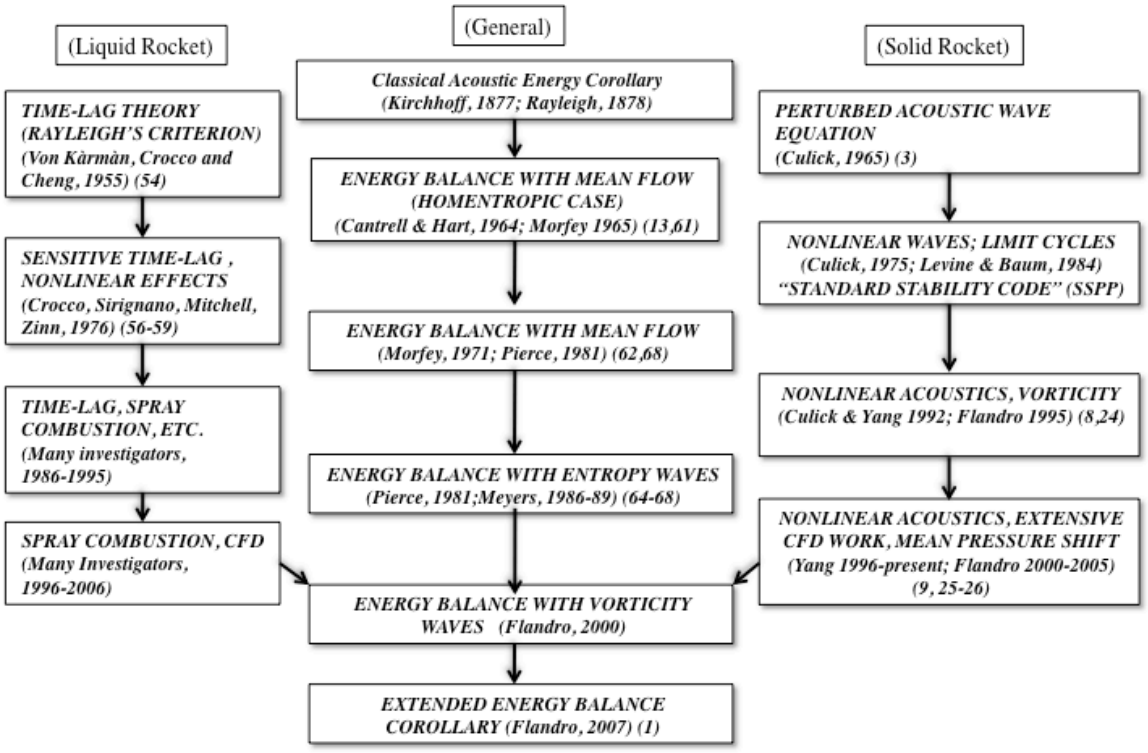

Figure 19. Historical Development of the Energy Corollary Method

The column on the right of Figure 19 shows the development over time of the acoustic wave theory, derived primarily from solid rocket research. Initially developed by Culick [3] to model instability, this theory forms the foundation for current instability theory as discussed in Section 2.1. It is from this theory that representation of stability through use of the linear growth rate was developed.

This theory has been extended through the efforts of Culick and others at Caltech to include various driving and damping mechanisms that may occur within a rocket system [3-12, 20-37, 39]. Most of these efforts have been focused upon the prediction of instability within solid rocket motors. Thus, not all of the disturbance mechanisms that may occur in other systems, such as liquid rockets, are represented.

Also, this theory only accounts for the presence of acoustic pressure wave disturbances. It was first proposed by Chu and Kovasznay [60] in 1958 that the full flow field would actually include effects due to waves of vorticity and entropy in addition to acoustic disturbances.

Efforts by Culick and Yang (1992) in nonlinear acoustics attempted to extend this model beyond a simple stability prediction scheme to include nonlinear effects seen in test data [8]. Flandro first attempted to include effects due to vorticity into the theory (1995) [24]. Until recently, further efforts to fully represent the behavior of unstable systems with this methodology were still being made. Further incorporation of the nonlinear effects was developed as well as representation of the mean DC pressure shift [29-37, 39].

After spending better part of the last twenty years trying to incorporate all of the expected flow field disturbances into the established acoustic theory, in 2007, Flandro made extensive efforts for inclusion of the knowledge gained from both of the above theories into the energy balance theory [1]. This theory development over time is shown in the center column of Figure 19. These efforts were not conducted by those in the field of rocket science, but by physicists and acousticians interested in representing the transport of energy associated disturbances in flow fields. The following is a brief history of how certain research contributed to the current theory.

Cantrell and Hart [13] proposed initial investigation into the use of energy-balance techniques in 1964 and form the initial motivation for this approach. They were focusing their efforts upon solid rocket combustion instability. The approach used in the current effort is an extension of the formulation that they originally introduced

generalized to any combustion system. It may be known to some readers that many people in the research community have criticized this formulation. However, with a little justification, it is shown that this powerful analytical technique is fully capable of supporting mainstream combustion instability research. The concern in their approach can be assuaged when it is made clear that Cantrell and Hart made some simple assumptions that must be expanded to represent a full system.

Cantrell and Hart computed an energy-balance based on a mean flow that was assumed to be a linear irrotational homentropic case. This approach came under much criticism by experts such as Culick [1, 5]. He showed that their approach was able to replicate the main results of his analysis. However, he also found their technique to be extremely lacking; he questioned that their implementation of an energy balance was appropriate for investigation of combustion instability. However, based upon their original assumption of irrotational, homentropic flow, their published results were correct. This can be shown upon explanation of the method employed herein. They did not commit any errors in either their modeling of fluid dynamic or their mathematical strategies.

Their insightful work was generalized by later researchers, through efforts carried on in the following decades by researchers such as Morfey who incorporated acoustic energy in nonuniform flows [61-63]. These efforts were continued by Myers [64-66]. Myers' initial interest was sparked by the research conducted by Cantrell and Hart for the case of homentropic flow. However, unlike the method used originally by Cantrell and Hart, who directly manipulated the total energy equation, these researchers employed the other conservation equations to arrive at an expression for a system energy balance. This

method avoids some of the pitfalls and difficulties in directly manipulating the energy equation that Cantrell and Hart dealt with.

The very useful analysis due to Myers extended the case of irrotational homentropic flow for inclusion of disturbances due to acoustic as well as entropy waves. Myers demonstrates that his method leads to an exact representation of the unsteady system energy balance. The Extended Energy Corollary directly employs this technique developed by Myers for representation of combustion system dynamics. Myers' analysis provides valuable guidance in generalizing the computations and adapting them to the special case of a generalized flow field. Although he made great strides at representation of a fully general flow-field with inclusion of these disturbances, the Extended ECM develops the first system energy balance that fully includes effects from all of these disturbances. The Extended ECM also incorporates effects due to vorticity disturbances as a result of Flandro's continuing efforts to include effects due to vorticity into the combustion instability understanding [22-26].

This presentation of representing system dynamics through manipulation of the other governing equations for determination of a system energy balance has led to much debate. However, other researchers besides Flandro have found use in this method of arriving at a system energy balance. Pierce [67-68] found use of representing fluid dynamic systems through implementing an acoustic corollary balance in his research efforts and also gives a discussion into its formulation and applications in his book on acoustic theory. Also, Rienstra and Hirschberg [69], state in their book on introduction to acoustics that starting from the linearized energy conservation law is an ad-hoc procedure resulting in an energy expression of the approximation and not an approximation of the

total energy. This follows along with some of the problems other researchers have seen in Cantrell and Hart's direct manipulation of the total energy equation, in that some terms may be left out in their direct perturbation expansion of this conservation law. They also state that this balance can only be used properly for the case of irrotational homentropic flow, the study performed by Cantrell and Hart. They then base their use of a system energy balance for representation of system energy off of Myers' initial investigations into homentropic flow and his extensions to nonuniform flows. So although the use of representation generalized flow dynamics may be under debates by some, there are others besides Flandro that have found value in it.

Flandro's research into energy balance methods led to the eventual combination of these works into the Extended Energy Corollary Method [1]. This method makes use of representing the system behavior through utilization of a full energy balance [1]. This is useful in stability analysis, because it aids in clarification of the flow of energy between the wave disturbances and the vast set of physical and chemical mechanisms required in describing the complex dynamics within a combustion system. This approach will be introduced here with formulation details that in no way represent a full presentation of the approach. It is merely discussed to give an understanding of this groundbreaking approach and to explain precisely the manner in which the later heat release results come into use in the formulation.

3.2 – Introduction to the Energy Corollary Method

The outcome of the Energy Corollary Method is an entirely general approach, capable of application to any flow. This formulation is the first instability method to

account not only for disturbances due to acoustic compressibility waves but to also include the effects of disturbances due to vorticity and entropy waves [1].

It is intended that this methodology will provide the ability to handle all energy sources and sinks that may occur within a system, i.e. excitation and damping terms. This general approach allows for easy inclusion of contributions of additional mechanisms once their behavior is understood. An example of this is the inclusion of the effects of unsteady combustion heat release, once a sufficient model is developed in the work of the following chapters.

To achieve system generality, use of limiting assumptions in this methodology is minimized. There is no limit to the mean flow Mach number, as in most theories. Mean properties are allowed to undergo response change depending upon growth or decay of the wave system. Also, the flow is not assumed to be isentropic, therefore entropy is retained as a variable. The only assumption placed on the system is that the gas is ideal.

Through use of the Energy Corollary Method, it can be shown that the expression for the classic growth rates is a natural result of the mathematics when taken to higher order. In this approach, it can be shown how simply the nonlinear model can be added to the linear theory. In Section 3.4, the mathematical process to obtain this expression for the linear growth will be developed. Since the focus of this work is contained within this expression for linear growth rate, only a brief overview of the nonlinear affects will be presented for completeness of the theory in Section 3.7.

The process employed in this analysis involves gaining a complete understanding of the system energy behavior. All mechanisms that could possibly occur within the system can be represented in a simple, concise equation for the system energy. The

unsteady system energy balance can be expressed as follows [1], which can be interpreted as a conservation law for acoustic energy.

$$\frac{\partial \mathscr{E}}{\partial t} + \nabla \cdot \mathbf{W} = \mathscr{D} \tag{9}$$

Credit is often given to Kirchhoff [70] for development of this formulation, as in the works of Pierce [68] as well as Rienstra and Hirschberg [69] in their books on acoustics. The latter authors show nicely how Kirchhoff developed an expression for the energy balance for a non-conducting quiescent flow through use of the conservation of mass and momentum equations; they showed that this expression could then be placed in the form of the energy corollary. Rayleigh also makes reference to this analysis by Kirchhoff in his book on the theory of sound [71].

In this equation, the unsteady energy, or energy density, E, signifies the system energy. The energy flux vector, **W**, represents a balance of all energy gain and loss mechanisms through boundaries, such as heat transfer and flow work. The source function, D, results from the addition or subtraction of energy due to effects such as heat release, vorticity, friction, body forces, etc.

It can be noted that equation 9 is not in the exact form used by Pierce, Rienstra and Hirschberg, and others; it does not include the negative sign in front of the source function, D. The inclusion of this sign is really a choice of the analyst, as, for example, in the work of Rienstra and Hirschberg [69]. Working only with an acoustic energy balance, they express a negative sign in this term, because they expect it to act as an energy dissipater due to effects such as diffusivity and thermal conduction [68]; it is actually referred to as the "dissipation" in their work. However, in this dissertation, it is

taken to be a source term, because energy sources such as combustion heat release and certain interactions between unsteady vorticity and the acoustic field are accommodated. Any positive or negative signs for the different terms in function D are included and accounted for within the D term itself; in this case, it makes no sense to place a sign in front of this term, because its overall effect may be a gain or loss term depending upon what sources have the largest effect in the system of interest.

It will be shown that once a representation of the system energy in the form of equation 9 is developed, an expression that includes all the linear growth rate integral contributions can be developed in the form of equation 10. For a chamber with flow due to combustion, the energy density can be integrated over the control volume representing the chamber to find the rate of change of the system energy, E:

$$\frac{dE}{dt} = \iiint_V \frac{\partial \mathscr{E}}{\partial t} dV = -\iint_S \mathbf{n} \cdot \mathbf{W}\, dS + \iiint_V \mathscr{D}\, dV \tag{10}$$

This expression states that the rate of change of the system total energy equals the net energy transfer by flux through the boundaries and the rate at which energy is produced or dissipated.

To arrive at the above representation for the total system energy, historically, focus has been placed upon the use of direct manipulation of the energy equation. In this analysis, direct manipulation of the energy equation is avoided, and, in place of the classical total energy equation, the remaining classical conservation equations are manipulated to yield the above unsteady energy balance. The familiar equations of conservation of mass, momentum, energy, and entropy, are shown below for a general flow case [40].

$$\begin{cases} \dfrac{\partial \rho}{\partial t} + \nabla \cdot \boldsymbol{m} = 0 \\ \dfrac{\partial u}{\partial t} + (\boldsymbol{\omega} \times \boldsymbol{u}) + \nabla H - T\nabla s = \boldsymbol{\psi} \\ \dfrac{\partial}{\partial t}\left[\rho\left(e + \dfrac{1}{2}\boldsymbol{u}\cdot\boldsymbol{u}\right)\right] + \nabla \cdot \left[\rho \boldsymbol{u}\left(e + \dfrac{p}{\rho} + \dfrac{1}{2}\boldsymbol{u}\cdot\boldsymbol{u}\right)\right] = (\boldsymbol{m}\cdot\boldsymbol{\psi}) + (QT) \\ \dfrac{\partial(\rho s)}{\partial t} + \nabla \cdot (\boldsymbol{m} s) = Q \end{cases} \tag{11}$$

Through development of the system energy through use of the extended energy balance corollary, it is shown that greater insight into system behavior can be obtained through inclusion of the entropy equation into this process rather than the direct manipulation of the energy equation. Through inclusion of the entropy equation, this allows direct incorporation of entropy waves into the analysis framework. The equations for conservation of mass, momentum, and entropy thus represent the disturbance of the mean flow field due to waves of compressibility (acoustics), vorticity, and entropy, respectively. Manipulation of these equations yields insight into the dynamic effects these disturbances impose upon the flow for a given chamber geometry.

With inclusion of the entropy equation, it will be shown that the conservation equations are not independent of one another. In this analysis, the energy equation can be thought of as a corollary to the set of equations, consisting of the conservation of mass, momentum, and entropy equations, hence the name Energy Corollary Method. This means that the energy equation can naturally be inferred from the others with no additional proof; it is a natural result upon manipulation of the set. The following sections detail the analytical process by which the energy corollary can be reached.

It will be shown in Section 3.4 from the results of the zeroth and first order expansions that, for those orders, the energy equation can be considered an identity for

any mean flow that satisfies the three other equations. An identity is an equality that remains true regardless of the values of any variables that appear within it. It will be shown in the following sections that expansion of the governing equations into ordered sets reveals that the above unsteady energy corollary balance in equation 9 results due to those terms from the second order set of equations.

3.3 – Overview of Nomenclature

Before presenting the methodology, for the benefit of the reader it is first necessary to discuss some important variables and equations to aid in understanding the development process. To better understand the form in which the above conservation equations are presented, some terms that may not be immediately familiar, or seem out of place, are discussed.

The governing equations of conservation of mass, momentum, and entropy are presented in the forms shown in equation 11 in order to capture the effects on the flow field due to waves of compressibility (acoustics), vorticity, and entropy. Thus the momentum equation has been adjusted to represent effects due to both vorticity and entropy. Also, the thermodynamic energy equation, which can be expressed in several common forms, is expressed in terms of entropy to capture effects due to entropy waves.

The momentum equation can be placed into the above form (equation 11) through application of the following expressions in equations 12, 13, and 14. For more detailed information, the reader should consult reference books by Enflo, et al [72] and Landau, et al [73].

The enthalpy of a system, h, is a total measure of the thermodynamic energy, usually expressed as a change in enthalpy. It can be represented as:

$$\mathrm{h} = \mathrm{e} + \frac{\mathrm{p}}{\rho} \tag{12}$$

The total enthalpy of a flow at a stagnation point is known as the stagnation enthalpy can be represented in the following form.

$$\mathrm{H} = \mathrm{h} + \frac{1}{2}\mathbf{u}\cdot\mathbf{u} \tag{13}$$

Through use of Crocco's theroem, expressed below, the momentum equation can then be placed into the form seen in equation 11.

$$\frac{1}{\rho}\nabla p = \nabla h - T\nabla s \tag{14}$$

The nomenclature **m** in equation set 11 symbolizes the mass flux, written as,

$$\boldsymbol{m} = \rho\boldsymbol{u} \tag{15}$$

representing the flow of mass across a surface.

The psi term on the right-hand side of both the momentum and energy equations is the vector sum of the volumetric forces. This term includes the viscous shear and dilatational stresses along with body forces, expressed as follows.

$$\boldsymbol{\psi} = \frac{1}{\rho}\left[-\mu\nabla\times\nabla\times\boldsymbol{u} + \left(\eta + \frac{4}{3}\mu\right)\nabla\left(\nabla\cdot\boldsymbol{u}\right) + \boldsymbol{F}\right] \tag{16}$$

To refresh the reader, it can be noted here that the first term can be slightly simplified through using the following substitution.

$$\boldsymbol{\omega} = \nabla\times\boldsymbol{u} \tag{17}$$

This is known as the vorticity, as seen in the momentum equation. This vorticity term is one of the previously mentioned disturbances being accounted for in this analysis; effects due to vorticity can play a very important role in the instability of certain systems.

The term, Q, on the right hand side of the energy and entropy equations is expanded as follows.

$$Q = \frac{\Phi - \nabla \cdot \boldsymbol{q} + \mathscr{H}}{T} \tag{18}$$

It represents the total heat change due to energy dissipation, heat transfer, and combustion, respectively. The first term is the energy dissipation due to effects of viscosity, which, when fully expanded, is written as:

$$\Phi = -\mu\left[\boldsymbol{\omega}\cdot\boldsymbol{\omega} - \boldsymbol{u}\cdot\nabla\times\boldsymbol{\omega}\right] + \left(\eta + \frac{4}{3}\mu\right)\left[\left(\nabla\cdot\boldsymbol{u}\right)^2 + \boldsymbol{u}\cdot\nabla\left(\nabla\cdot\boldsymbol{u}\right)\right] \tag{19}$$

The second term is the divergence of the heat flux vector, shown below.

$$\boldsymbol{q} = -\lambda\nabla T \tag{20}$$

The third term, $\mathscr{H}$, represents the rate of volumetric combustion heat release. This term represents the focus of this current research and will be discussed in greater detail in later sections.

In order to fully account for the effects of compressibility, vorticity, and entropy, these and other thermodynamic variables, such as temperature, T, and pressure, p, can be expressed in terms of entropy and density. The following relations aid in this endeavor; these and other useful thermodynamic expressions can be found in the gas dynamics book by Liepmann and Roshko [74].

$$
\begin{aligned}
de &= Tds + \frac{p}{\rho^2} d\rho \\
dp &= a^2 \left(\frac{\rho}{C_P} ds + d\rho \right) \\
dT &= \frac{1}{C_P} \left(\gamma T ds + \frac{a^2}{\rho^2} d\rho \right) \\
Tds &= dh - \frac{dp}{\rho}
\end{aligned}
\tag{21}
$$

The following derivation requires a tremendous deal of mathematical manipulation. As a result, only steps deemed necessary for understanding of the process are presented.

3.4 – Analytical Development

The first step in this development is to expand the dynamic equations in a regular perturbation series as discussed in Section 2.1. This assumes that the mean flow properties are influenced by changes in a small amplitude parameter called ε. The general form of a perturbed parameter is shown again as follows.

$$a = a_0 + \varepsilon a_1 + \varepsilon^2 a_2 + \varepsilon^3 a_3 + ... \tag{22}$$

Expansion of different system parameters in this form allows for determination of influence of the afore mentioned waveforms upon them.

Once the equations have been expanded through substitution of their perturbed properties, sets of governing equations are obtained for each order of perturbation. Each ordered sets of equations governs the system flow for a given order of e. For example, the equations obtained representing the mean flow can be seen as follows. Presented here so that the reader has foreknowledge of where the derivation is proceeding, it will be

shown in the following pages, the steps and manipulation necessary to obtain these equations.

$$\begin{cases} \dfrac{\partial \rho_0}{\partial t} + \nabla \cdot \boldsymbol{m}_0 = 0 \\ \dfrac{\partial \boldsymbol{u}_0}{\partial t} + (\boldsymbol{\omega} \times \boldsymbol{u})_0 + \nabla H_0 - T_0 \nabla s_0 = \boldsymbol{\psi}_0 \\ \dfrac{\partial}{\partial t}\left[\rho \left(e + \dfrac{1}{2}\boldsymbol{u} \cdot \boldsymbol{u} \right) \right]_0 + \nabla \cdot \left[\rho \boldsymbol{u} \left(e + \dfrac{p}{\rho} + \dfrac{1}{2}\boldsymbol{u} \cdot \boldsymbol{u} \right) \right]_0 = (\boldsymbol{m} \cdot \boldsymbol{\psi})_0 + (QT)_0 \\ \dfrac{\partial (\rho s)_0}{\partial t} + \nabla \cdot (\boldsymbol{m}_0 s_0) = Q_0 \end{cases} \tag{23}$$

For clarity, the equations shown do not display the expansions for the heat transfer and body force effects. These are normally small and not critical to the current investigation, but are readily included when required. The equations for the first order and second order disturbances are shown below.

$$\begin{cases} \dfrac{\partial \rho_1}{\partial t} + \nabla \cdot \boldsymbol{m}_1 = 0 \\ \dfrac{\partial u_1}{\partial t} + (\boldsymbol{\omega} \times \boldsymbol{u})_1 + \nabla H_1 - T_1 \nabla s_1 = \boldsymbol{\psi}_1 \\ \dfrac{\partial}{\partial t}\left[\rho \left(e + \dfrac{1}{2}\boldsymbol{u} \cdot \boldsymbol{u} \right) \right]_1 + \nabla \cdot \left[\rho \boldsymbol{u} \left(e + \dfrac{p}{\rho} + \dfrac{1}{2}\boldsymbol{u} \cdot \boldsymbol{u} \right) \right]_1 = (\boldsymbol{m} \cdot \boldsymbol{\psi})_1 + (QT)_1 \\ \dfrac{\partial (\rho_0 s_1 + \rho_1 s_0)}{\partial t} + \nabla \cdot (\boldsymbol{m}_0 s_1 + \boldsymbol{m}_1 s_0) = Q_1 \end{cases} \tag{24}$$

$$\begin{cases} \dfrac{\partial \rho_2}{\partial t} + \nabla \cdot \boldsymbol{m}_2 = 0 \\ \dfrac{\partial \boldsymbol{u}_2}{\partial t} + (\boldsymbol{\omega} \times \boldsymbol{u})_2 + \nabla H_2 - T_0 \nabla s_2 - T_1 \nabla s_1 - T_2 \nabla s_0 = \boldsymbol{\psi}_2 \\ \dfrac{\partial}{\partial t}\left[\rho \left(e + \dfrac{1}{2}\boldsymbol{u} \cdot \boldsymbol{u} \right) \right]_2 + \nabla \cdot \left[\rho \boldsymbol{u} \left(e + \dfrac{p}{\rho} + \dfrac{1}{2}\boldsymbol{u} \cdot \boldsymbol{u} \right) \right]_2 = (\boldsymbol{m} \cdot \boldsymbol{\psi})_2 + (QT)_2 \\ \dfrac{\partial (\rho_0 s_2 + \rho_1 s_1 + \rho_2 s_0)}{\partial t} + \nabla \cdot (\boldsymbol{m}_0 s_2 + \boldsymbol{m}_1 s_1 + \boldsymbol{m}_2 s_0) = Q_2 \end{cases} \tag{25}$$

3.4.1 – Variable Expansions

To obtain these ordered above sets of equations, it is first necessary to develop the series expansions for each of the participating variables. The density and the entropy are employed as the main thermodynamic variables throughout the analysis since it includes wave disturbances not only due to compressibility effects but also due to entropy. Therefore, to achieve this, each of the variables is expanded using double Taylor series expansions with entropy, s, and density, ρ, as the reference variables.

The first expansions to be done are those for enthalpy, h, pressure, p, and the product of density and internal energy, ρe, into the form of equation 22. To obtain an equation for enthalpy of the form

$$h = h_0 + \varepsilon h_1 + \varepsilon^2 h_2 + \mathbf{...} \tag{26}$$

it is first written in double Taylor series as [19, 74]:

$$h = h_0 + \left\{ \begin{array}{l} \left.\frac{\partial h}{\partial \rho}\right|_0 (\rho - \rho_0) \\ + \left.\frac{\partial h}{\partial s}\right|_0 (s - s_0) \end{array} \right\} + \left\{ \begin{array}{l} \left.\frac{\partial^2 h}{\partial \rho^2}\right|_0 \frac{(\rho - \rho_0)^2}{2!} \\ + \left.\frac{\partial^2 h}{\partial \rho \partial s}\right|_0 (\rho - \rho_0)(s - s_0) \\ + \left.\frac{\partial^2 h}{\partial s^2}\right|_0 \frac{(s - s_0)^2}{2!} \end{array} \right\} + \left\{ \begin{array}{l} \left.\frac{\partial^3 h}{\partial \rho^3}\right|_0 \frac{(\rho - \rho_0)^3}{3!} \\ + \left.\frac{\partial^3 h}{\partial \rho^2 \partial s}\right|_0 \frac{(\rho - \rho_0)^2 (s - s_0)}{2!} \\ \left.\frac{\partial^3 h}{\partial \rho^2 \partial s}\right|_0 \frac{(\rho - \rho_0)(s - s_0)^2}{2!} \\ + \left.\frac{\partial^2 h}{\partial s^2}\right|_0 \frac{(s - s_0)^2}{3!} \end{array} \right\} + \ldots \tag{27}$$

The necessary derivatives in this expansion can then be calculated from the help of the thermodynamic relationships (equation 21). After some manipulation and collection of terms, the following expansion for enthalpy results.

$$h = h_0 + \varepsilon\left(a_0^2 \rho_1 + \gamma T_0 s_1\right) + \varepsilon\left(\frac{a_0^2}{\rho_0}\rho_2 + \frac{(\gamma - 2)a_0^2}{\rho_0}\rho_1^2 + \frac{a_0^2}{C_V \rho_0}\rho_1 s_1 + \frac{\gamma T_0}{C_V}s_1^2 + \gamma T_0 s_2\right) + \ldots \tag{28}$$

Similar expansions can be calculated for the pressure and ρe terms.

The next step is to expand each of the other individual terms to be inserted into the governing equations. The expansion of mass flux is as follows:

$$\begin{aligned} \boldsymbol{m} = \rho_0 \boldsymbol{u}_0 + \varepsilon\left(\rho_0 \boldsymbol{u}_1 + \rho_1 \boldsymbol{u}_0\right) + \varepsilon^2\left(\rho_0 \boldsymbol{u}_2 + \rho_1 \boldsymbol{u}_1 + \rho_2 \boldsymbol{u}_0\right) \\ + \varepsilon^3\left(\rho_0 \boldsymbol{u}_3 + \rho_1 \boldsymbol{u}_2 + \rho_2 \boldsymbol{u}_1 + \rho_3 \boldsymbol{u}_0\right) + \ldots \end{aligned} \tag{29}$$

The same steps can be taken with other terms such as the inner product of the velocity used in the momentum and energy equations. This product and its multiplication by density follow as shown.

$$\begin{aligned} \frac{1}{2}\boldsymbol{u}\cdot\boldsymbol{u} &= \frac{1}{2}\left(\boldsymbol{u}_0 + \varepsilon\boldsymbol{u}_1 + \varepsilon^2\boldsymbol{u}_2 + \varepsilon^3\boldsymbol{u}_3 + \ldots\right)\cdot\left(\boldsymbol{u}_0 + \varepsilon\boldsymbol{u}_1 + \varepsilon^2\boldsymbol{u}_2 + \varepsilon^3\boldsymbol{u}_3 + \ldots\right) \\ &= \frac{1}{2}\boldsymbol{u}_0^2 + \varepsilon\left(\boldsymbol{u}_0\cdot\boldsymbol{u}_1\right) + \varepsilon^2\left[\left(\boldsymbol{u}_1\cdot\boldsymbol{u}_1\right) + \boldsymbol{u}_0\cdot\boldsymbol{u}_2\right] + \varepsilon^3\left[\boldsymbol{u}_1\cdot\boldsymbol{u}_2 + \boldsymbol{u}_0\cdot\boldsymbol{u}_3\right]\ldots \end{aligned} \tag{30}$$

$$\begin{aligned} &\frac{1}{2}\rho\boldsymbol{u}\cdot\boldsymbol{u} = \frac{1}{2}\rho_0\boldsymbol{u}_0^2 + \varepsilon\left(\rho_0\left(\boldsymbol{u}_0\cdot\boldsymbol{u}_1\right) + \frac{1}{2}\rho_0\boldsymbol{u}_0^2\right) \\ &+\varepsilon^2\left[\rho_0\left(\frac{1}{2}\left(\boldsymbol{u}_1\cdot\boldsymbol{u}_1\right) + \boldsymbol{u}_0\cdot\boldsymbol{u}_2\right) + \rho_1\left(\boldsymbol{u}_0\cdot\boldsymbol{u}_1\right) + \frac{1}{2}\rho_2\boldsymbol{u}_0^2\right] \\ &+\varepsilon^3\left[\rho_0\left(\boldsymbol{u}_1\cdot\boldsymbol{u}_2 + \boldsymbol{u}_0\cdot\boldsymbol{u}_3\right) + \frac{1}{2}\rho_1\left(\boldsymbol{u}_1\cdot\boldsymbol{u}_1\right) + \rho_1\left(\boldsymbol{u}_0\cdot\boldsymbol{u}_2\right) + \rho_2\left(\boldsymbol{u}_0\cdot\boldsymbol{u}_1\right) + \frac{1}{2}\rho_3\boldsymbol{u}_0^2\right] + \ldots \end{aligned} \tag{31}$$

All of the terms in equations 23 must be expanded in this form, requiring various mathematical simplifications, not discussed further here. These and other expanded terms can then be inserted into the governing system of equations. While equations 27-31 are shown expanded to third order, the following discussion is limited to second order for clarity. Expansion of the equations to second order is sufficient to capture the linear behavior, which is the focus of this research. For more details on the third order expansion see Jacob [19].

Upon substitution of the expanded terms, the resulting forms of the equations can then be split into sets depending upon order [2]. This is shown for conservation of mass, momentum, entropy, and energy equations as follows. These are shown for the zeroth, first, and second orders of epsilon equations [39].

$$\begin{aligned}
&\mathrm{O}(1): \quad \frac{\partial \rho_0}{\partial t} + \nabla \cdot \boldsymbol{m}_0 = 0 \\
&\mathrm{O}(\varepsilon): \quad \frac{\partial \rho_1}{\partial t} + \nabla \cdot \boldsymbol{m}_1 = 0 \\
&\mathrm{O}(\varepsilon^2): \quad \frac{\partial \rho_2}{\partial t} + \nabla \cdot \boldsymbol{m}_2 = 0
\end{aligned} \tag{32}$$

$$\begin{aligned}
&\mathrm{O}(1): \quad \frac{\partial \boldsymbol{u}_0}{\partial t} + \nabla\left(h_0 + \frac{1}{2}\boldsymbol{u}_0^2 \right) - T_0 \nabla s_0 = \boldsymbol{u}_0 \times \boldsymbol{\omega}_0 + \boldsymbol{\psi}_0 \\
&\mathrm{O}(\varepsilon): \quad \frac{\partial \boldsymbol{u}_1}{\partial t} + \nabla\left(h_1 + \boldsymbol{u}_0 \cdot \boldsymbol{u}_1 \right) - \left(T_0 \nabla s_1 - T_1 \nabla s_0 \right) = \left(\boldsymbol{u}_0 \times \boldsymbol{\omega}_1 + u_1 \times \boldsymbol{\omega}_0 \right) + \boldsymbol{\psi}_1 \\
&\mathrm{O}(\varepsilon^2): \quad \frac{\partial \boldsymbol{u}_2}{\partial t} + \nabla\left(h_2 + \frac{1}{2}\left(\boldsymbol{u}_1 \cdot \boldsymbol{u}_1 \right) + \boldsymbol{u}_0 \cdot \boldsymbol{u}_2 \right) - \left(T_0 \nabla s_2 - T_1 \nabla s_1 - T_2 \nabla s_0 \right) \\
&\qquad\qquad = \left(\boldsymbol{u}_0 \times \boldsymbol{\omega}_2 + \boldsymbol{u}_1 \times \boldsymbol{\omega}_1 + \boldsymbol{u}_2 \times \boldsymbol{\omega}_0 \right) + \boldsymbol{\psi}_2
\end{aligned} \tag{33}$$

$$\begin{aligned}
&\mathrm{O}(1): \quad \nabla \cdot \left(\boldsymbol{m}_0 s_0 \right) = Q_0 \\
&\mathrm{O}(\varepsilon): \quad \frac{\partial}{\partial t}\left(\rho_0 s_1 + \rho_1 s_0 \right) + \nabla \cdot \left(\boldsymbol{m}_0 s_1 + \boldsymbol{m}_1 s_0 \right) = Q_1 \\
&\mathrm{O}(\varepsilon^2): \quad \frac{\partial}{\partial t}\left(\rho_0 s_2 + \rho_1 s_1 + \rho_2 s_0 \right) + \nabla \cdot \left(\boldsymbol{m}_0 s_2 + \boldsymbol{m}_1 s_1 + \boldsymbol{m}_1 s_0 \right) = Q_2
\end{aligned} \tag{34}$$

$$
\begin{aligned}
&\mathrm{O}(1): \quad \frac{\partial}{\partial t}\left[\left(\left(\rho e\right)_0+\left(\frac{1}{2}\rho \boldsymbol{u}\cdot\boldsymbol{u}\right)_0\right)\right]+\nabla\cdot\left[\boldsymbol{m}_0\left(h_0+\frac{1}{2}\boldsymbol{u}_0^2\right)\right]_2=\boldsymbol{m}_0\cdot\boldsymbol{\psi}_0+T_0Q_0\\
&\mathrm{O}(\varepsilon): \quad \frac{\partial}{\partial t}\left[\left(\left(\rho e\right)_1+\left(\frac{1}{2}\rho \boldsymbol{u}\cdot\boldsymbol{u}\right)_1\right)\right]+\nabla\cdot\begin{bmatrix}\boldsymbol{m}_0\left(h_1+\left(\frac{1}{2}\boldsymbol{u}\cdot\boldsymbol{u}\right)_1\right)\\+\boldsymbol{m}_1\left(h_0+\frac{1}{2}\boldsymbol{u}_0^2\right)\end{bmatrix}=\begin{pmatrix}\boldsymbol{m}_0\cdot\boldsymbol{\psi}_1\\+\boldsymbol{m}_1\cdot\boldsymbol{\psi}_0\end{pmatrix}+\begin{pmatrix}T_0Q_1\\+T_1Q_0\end{pmatrix} \qquad (35)\\
&\mathrm{O}(\varepsilon^2): \quad \frac{\partial}{\partial t}\left[\left(\left(\rho e\right)_2+\left(\frac{1}{2}\rho \boldsymbol{u}\cdot\boldsymbol{u}\right)_2\right)\right]+\nabla\cdot\begin{bmatrix}\boldsymbol{m}_0\left(h_2+\left(\frac{1}{2}\boldsymbol{u}\cdot\boldsymbol{u}\right)_2\right)+\boldsymbol{m}_1\left(h_1+\left(\frac{1}{2}\boldsymbol{u}\cdot\boldsymbol{u}\right)_1\right)\\+\boldsymbol{m}_2\left(h_0+\frac{1}{2}\boldsymbol{u}_0^2\right)\end{bmatrix}\\
&\qquad\qquad =\left(\boldsymbol{m}_0\cdot\psi_2+\boldsymbol{m}_1\cdot\psi_1+\boldsymbol{m}_2\cdot\psi_0\right)+\left(T_0Q_1+T_1Q_1+T_2Q_0\right)
\end{aligned}
$$

3.5 – Energy Corollary Balance

Now that the equations have been presented in their expanded forms, it will be shown that the energy equation is a natural result of the manipulation of the other three governing equations for the zeroth and first orders. The linear energy balance is shown to be the result of expansion of the second order governing equations [19, 40].

3.5.1 – Zeroth Order Corollary Proof

The first task is to show the relation of the zeroth-order of epsilon energy equation with the other mean flow equations. This order is classically referred to in perturbation nomenclature as O(1). Since it is assumed that there is a quasi-steady mean flow field upon which oscillations are being imposed, this assumes that the mean, or base, flow properties are slowly changing with time, essentially remaining constant. The time derivative of these properties can therefore be assumed to be zero.

$$\frac{\partial \rho_0}{\partial t} = \frac{\partial \boldsymbol{u}_0}{\partial t} = \frac{\partial (\rho s)_0}{\partial t} = 0 \tag{36}$$

The mean flow energy equation then reduces to:

$$\nabla \cdot \left[\boldsymbol{m}_0 \left(h_0 + \frac{1}{2} \boldsymbol{u}_0 \right) \right] = \boldsymbol{m}_0 \cdot \boldsymbol{\psi}_0 + T_0 Q_0 \tag{37}$$

Likewise, the other mean flow equations reduce to the following:

$$\begin{aligned} &\nabla \cdot \boldsymbol{m}_0 = 0 \\ &\nabla \left(h_0 + \frac{1}{2} \boldsymbol{u}_0^2 \right) - T_0 \nabla s_0 = \boldsymbol{u}_0 \times \boldsymbol{\omega}_0 + \boldsymbol{\psi}_0 \\ &\nabla \cdot (\boldsymbol{m}_0 s_0) = Q_0 \rightarrow s_0 \nabla \cdot \boldsymbol{m}_0 + \boldsymbol{m}_0 \cdot \nabla s_0 = Q_0 \end{aligned} \tag{38}$$

Inserting these equations into the energy equation results in some of the following manipulations:

$$\begin{aligned} &\left(h_0 + \frac{1}{2} \boldsymbol{u}_0 \right) \nabla \cdot \boldsymbol{m}_0 + \boldsymbol{m}_0 \cdot \nabla \left(h_0 + \frac{1}{2} \boldsymbol{u}_0 \right) = \boldsymbol{m}_0 \cdot \boldsymbol{\psi}_0 + T_0 Q_0 \\ &\Rightarrow \boldsymbol{m}_0 \cdot \nabla \left(h_0 + \frac{1}{2} \boldsymbol{u}_0 \right) = \boldsymbol{m}_0 \cdot \boldsymbol{\psi}_0 + T_0 Q_0 \\ &\Rightarrow \boldsymbol{m}_0 \cdot \left[T_0 \nabla s_0 + \boldsymbol{u}_0 \times \boldsymbol{\omega}_0 + \boldsymbol{\psi}_0 \right] = \boldsymbol{m}_0 \cdot \boldsymbol{\psi}_0 + T_0 Q_0 \\ &\Rightarrow T_0 \boldsymbol{m}_0 \cdot \nabla s_0 + \boldsymbol{m}_0 \cdot (\boldsymbol{u}_0 \times \boldsymbol{\omega}_0) + \boldsymbol{m}_0 \cdot \boldsymbol{\psi}_0 = \boldsymbol{m}_0 \cdot \boldsymbol{\psi}_0 + T_0 Q_0 \end{aligned} \tag{39}$$

Since the inner product of two orthogonal vectors is zero, the following term is eliminated, because the cross product term in the parenthesis is perpendicular to the velocity.

$$\boldsymbol{m}_0 \cdot (\boldsymbol{u}_0 \times \boldsymbol{\omega}_0) = \rho_0 \boldsymbol{u}_0 \cdot (\boldsymbol{u}_0 \times \boldsymbol{\omega}_0) = 0 \tag{40}$$

Thus, the following equality results.

$$T_0 Q_0 + \boldsymbol{m}_0 \cdot \boldsymbol{\psi}_0 = \boldsymbol{m}_0 \cdot \boldsymbol{\psi}_0 + T_0 Q_0 \tag{41}$$

This result essentially means that the zeroth-order energy equation can be considered an identity for any mean flow that satisfies the three other equations. In other

words, any variable values that satisfy the conservation of mass, momentum, and entropy also satisfy the energy equation [19, 40, 74].

3.5.2 – First Order Corollary Proof

A similar process is performed for manipulation of the first order energy equation. This order is referred to in perturbation nomenclature as O(ε), pronounced order epsilon.

$$\frac{\partial}{\partial t}\left[\left(\left(\rho e\right)_1+\left(\frac{1}{2}\rho \boldsymbol{u}\cdot\boldsymbol{u}\right)_1\right)\right]+\nabla\cdot\begin{bmatrix}\boldsymbol{m}_0\left(h_1+\left(\frac{1}{2}\boldsymbol{u}\cdot\boldsymbol{u}\right)_1\right)\\+\boldsymbol{m}_1\left(h_0+\frac{1}{2}\boldsymbol{u}_0^2\right)\end{bmatrix}=\begin{pmatrix}\boldsymbol{m}_0\cdot\boldsymbol{\psi}_1\\+\boldsymbol{m}_1\cdot\boldsymbol{\psi}_0\end{pmatrix}+\begin{pmatrix}T_0Q_1\\+T_1Q_0\end{pmatrix} \tag{42}$$

The following first order forms of the other flow equations are used in this analysis.

$$\begin{aligned}&\nabla\cdot\boldsymbol{m}_1=\frac{\partial\rho_1}{\partial t},\quad \nabla\cdot\boldsymbol{m}_0=0\\&\frac{\partial\boldsymbol{u}_1}{\partial t}+\nabla\left(h_1+\boldsymbol{u}_0\cdot\boldsymbol{u}_1\right)-\left(T_0\nabla s_1-T_1\nabla s_0\right)=\left(\boldsymbol{u}_0\times\boldsymbol{\omega}_1+\boldsymbol{u}_1\times\boldsymbol{\omega}_0\right)+\boldsymbol{\psi}_1\\&\frac{\partial}{\partial t}\left(\rho_0 s_1+\rho_1 s_0\right)+\nabla\cdot\left(\boldsymbol{m}_0 s_1+\boldsymbol{m}_1 s_0\right)=Q_1\end{aligned} \tag{43}$$

Expanding the ε order energy equation, equation 42, and making use of the following useful known quantities from term expansions

$$\begin{aligned}&\boldsymbol{m}_1=\rho_0\boldsymbol{u}_1+\rho_1\boldsymbol{u}_0,\quad \boldsymbol{m}_0=\rho_0\boldsymbol{u}_0\\&h_1=\frac{a_0^2}{\rho_0}\rho_1+\gamma T_0 s_1\\&\left(\rho e\right)_1=h_0\rho_1+\rho_0 T_0 s_1\\&\left(\frac{1}{2}\boldsymbol{u}\cdot\boldsymbol{u}\right)_1=\boldsymbol{u}_0\cdot\boldsymbol{u}_1\\&\left(\frac{1}{2}\rho\boldsymbol{u}\cdot\boldsymbol{u}\right)_1=\rho_0\left(\boldsymbol{u}_0\cdot\boldsymbol{u}_1\right)+\frac{1}{2}\rho_1\boldsymbol{u}_0^2\end{aligned} \tag{44}$$

and simplifying, yields the following equation.

$$\rho_0 T_0 \frac{\partial s_1}{\partial t} + \boldsymbol{m}_1 \cdot \left[T_0 \nabla s_0 + \boldsymbol{u}_0 \times \boldsymbol{\omega}_0 \right] + \boldsymbol{m}_0 \cdot \begin{bmatrix} \left(T_0 \nabla s_1 + T_1 \nabla s_0 \right) \\ + \left(\boldsymbol{u}_0 \times \boldsymbol{\omega}_1 + \boldsymbol{u}_1 \times \boldsymbol{\omega}_0 \right) \end{bmatrix} = T_0 Q_1 + T_1 Q_0 \quad (45)$$

Employment and manipulation of the entropy equation yields the following.

$$\begin{aligned} & T_0 Q_1 - \boldsymbol{m}_0 \cdot T_0 \nabla s_1 - \boldsymbol{m}_1 \cdot T_0 \nabla s_0 + \left[T_0 \boldsymbol{m}_1 \cdot \nabla s_0 + \boldsymbol{m}_1 \cdot \boldsymbol{u}_0 \times \boldsymbol{\omega}_0 \right] \\ & + \left[\left(T_0 \boldsymbol{m}_0 \cdot \nabla s_1 + T_1 \boldsymbol{m}_0 \cdot \nabla s_0 \right) + \boldsymbol{m}_0 \cdot \left(\boldsymbol{u}_0 \times \boldsymbol{\omega}_1 + \boldsymbol{u}_1 \times \boldsymbol{\omega}_0 \right) \right] = T_0 Q_1 + T_1 Q_0 \end{aligned} \quad (46)$$

Upon reduction of this expression, the following equality results.

$$\begin{aligned} \boldsymbol{m}_1 \cdot \boldsymbol{u}_0 \times \boldsymbol{\omega}_0 + \boldsymbol{m}_0 \left(\boldsymbol{u}_0 \times \boldsymbol{\omega}_1 + \boldsymbol{u}_1 \times \boldsymbol{\omega}_0 \right) = 0 \\ \left(\rho_0 \boldsymbol{u}_1 + \rho_1 \boldsymbol{u}_0 \right) \cdot \boldsymbol{u}_0 \times \boldsymbol{\omega}_0 + \rho_0 \boldsymbol{u}_0 \left(\boldsymbol{u}_0 \times \boldsymbol{\omega}_1 + \boldsymbol{u}_1 \times \boldsymbol{\omega}_0 \right) = 0 \end{aligned} \quad (47)$$

Upon elimination of terms, it can be seen, as in the zeroth order case, that the energy equation reduces to zero. The following formula shows that even with vorticity and entropy included, they cancel so that the energy equation is still satisfied [40].

$$\rho_0 \boldsymbol{u}_0 \cdot \boldsymbol{u}_1 \times \boldsymbol{\omega}_0 + \rho_0 \boldsymbol{u}_1 \cdot \boldsymbol{u}_0 \times \boldsymbol{\omega}_0 = \rho_0 \left(\boldsymbol{u}_0 \cdot \boldsymbol{u}_1 \times \boldsymbol{\omega}_0 + \boldsymbol{u}_1 \cdot \boldsymbol{u}_0 \times \boldsymbol{\omega}_0 \right) = 0 \quad (48)$$

3.5.3 – Second Order Expansion Process

The previous orders were presented to show that the energy equation could indeed be thought of as an identity for a flow satisfied by the set of the conservation of mass, momentum, and entropy equations. Their manipulation confirms the validity that energy within the system can be represented by characterization of the system flow with the other governing equations.

Upon rearrangement of the second-order equations, the terms do not cancel as in the expressions for the mean and first order. Also referred to as $O(\varepsilon^2)$, or order of epsilon squared, manipulation of the equations of this order yield valuable results. It is this step

in the analysis where all of the classical combustion instability results make their presence known. With a greater detail than the previous orders, it is shown that the system energy can be represented in the above form of the unsteady energy corollary balance.

The second-order expansion of the energy equation is shown as follows. To show the energy balance for this order requires a bit more math than the previous orders due to increasing complexity [19, 40].

$$\frac{\partial}{\partial t}\left[\left(\left(\rho e\right)_2+\left(\frac{1}{2}\rho \boldsymbol{u}\cdot\boldsymbol{u}\right)_2\right)\right]$$
$$+\nabla\cdot\begin{bmatrix}\boldsymbol{m}_0\left(h_2+\left(\frac{1}{2}\boldsymbol{u}\cdot\boldsymbol{u}\right)_2\right)+\boldsymbol{m}_1\left(h_1+\left(\frac{1}{2}\boldsymbol{u}\cdot\boldsymbol{u}\right)_1\right)\\ +\boldsymbol{m}_2\left(h_0+\frac{1}{2}\boldsymbol{u}_0^2\right)\end{bmatrix}=\begin{pmatrix}\boldsymbol{m}_0\cdot\psi_2\\ +\boldsymbol{m}_1\cdot\psi_1\\ +\boldsymbol{m}_2\cdot\psi_0\end{pmatrix}+\begin{pmatrix}T_0Q_1\\ +T_1Q_1\\ +T_2Q_0\end{pmatrix} \quad (49)$$

Its expansion requires use of all three ordered sets of the conservation of mass, momentum, and entropy equations, shown below (equation 50). Also, there are more terms within the equations that have expansion of their own as shown (equation 51), increasing the complexity. Though shown in great detail, this is a much-streamlined process. Greater detail into some of the mathematics may be gleamed from the dissertation effort by Jacob [19, 40].

$$\nabla \cdot \boldsymbol{m}_2 = -\frac{\partial \rho_2}{\partial t}, \quad \nabla \cdot \boldsymbol{m}_1 = -\frac{\partial \rho_1}{\partial t} \quad \nabla \cdot \boldsymbol{m}_0 = 0$$

$$\begin{cases} \dfrac{\partial \boldsymbol{u}_2}{\partial t} + \nabla\left(h_2 + \dfrac{1}{2}\left(\boldsymbol{u}_1 \cdot \boldsymbol{u}_1\right) + \boldsymbol{u}_0 \cdot \boldsymbol{u}_2 \right) - \begin{pmatrix} T_0 \nabla s_2 \\ -T_1 \nabla s_1 - T_2 \nabla s_0 \end{pmatrix} \\ = \begin{pmatrix} \boldsymbol{u}_0 \times \boldsymbol{\omega}_2 \\ +\boldsymbol{u}_1 \times \boldsymbol{\omega}_1 + \boldsymbol{u}_2 \times \boldsymbol{\omega}_0 \end{pmatrix} + \boldsymbol{\psi}_2 \\ \dfrac{\partial \boldsymbol{u}_1}{\partial t} + \nabla\left(h_1 + \boldsymbol{u}_0 \cdot \boldsymbol{u}_1\right) - \left(T_0 \nabla s_1 - T_1 \nabla s_0\right) = \left(\boldsymbol{u}_0 \times \boldsymbol{\omega}_1 + \boldsymbol{u}_1 \times \boldsymbol{\omega}_0\right) + \boldsymbol{\psi}_1 \\ \dfrac{\partial \boldsymbol{u}_0}{\partial t} + \nabla\left(h_0 + \dfrac{1}{2}\boldsymbol{u}_0^2 \right) - T_0 \nabla s_0 = \boldsymbol{u}_0 \times \boldsymbol{\omega}_0 + \boldsymbol{\psi}_0 \end{cases} \tag{50}$$

$$\begin{cases} \dfrac{\partial}{\partial t}\left(\rho_0 s_2 + \rho_1 s_1 + \rho_2 s_0\right) + \nabla \cdot \left(\boldsymbol{m}_0 s_2 + \boldsymbol{m}_1 s_1 + \boldsymbol{m}_2 s_0\right) = Q_2 \\ \dfrac{\partial}{\partial t}\left(\rho_0 s_1 + \rho_1 s_0\right) + \nabla \cdot \left(\boldsymbol{m}_0 s_1 + \boldsymbol{m}_1 s_0\right) = Q_1 \\ \boldsymbol{m}_0 \nabla \cdot \left(s_0\right) = Q_0 \end{cases}$$

$$\begin{cases} \boldsymbol{m}_2 = \rho_0 \boldsymbol{u}_2 + \rho_1 \boldsymbol{u}_1 + \rho_2 \boldsymbol{u}_0, \quad \boldsymbol{m}_1 = \rho_0 \boldsymbol{u}_1 + \rho_1 \boldsymbol{u}_0, \quad \boldsymbol{m}_0 = \rho_0 \boldsymbol{u}_0 \\ h_1 = \dfrac{a_0^2}{\rho_0}\rho_1 + \gamma T_0 s_1 \\ \left(\rho e\right)_2 = h_0 \rho_2 + \rho_0 T_0 s_2 + T_0 \rho_1 s_1 + \dfrac{\rho_0 T_0}{2C_P} s_1^2, \quad \left(\rho e\right)_1 = h_0 \rho_1 + \rho_0 T_0 s_1 \\ \left(\dfrac{1}{2}\boldsymbol{u} \cdot \boldsymbol{u}\right)_2 = \dfrac{1}{2}\left(\boldsymbol{u}_1 \cdot \boldsymbol{u}_1\right) + \boldsymbol{u}_0 \cdot \boldsymbol{u}_2, \quad \left(\dfrac{1}{2}\boldsymbol{u} \cdot \boldsymbol{u}\right)_1 = \boldsymbol{u}_0 \cdot \boldsymbol{u}_1 \\ \left(\dfrac{1}{2}\rho \boldsymbol{u} \cdot \boldsymbol{u}\right)_2 = \rho_0 \left[\dfrac{1}{2}\left(\boldsymbol{u}_1 \cdot \boldsymbol{u}_1\right) + \boldsymbol{u}_0 \cdot \boldsymbol{u}_2\right] + \rho_1\left(\boldsymbol{u}_0 \cdot \boldsymbol{u}_1\right) + \dfrac{1}{2}\rho_2 \boldsymbol{u}_0^2, \\ \left(\dfrac{1}{2}\boldsymbol{u} \cdot \boldsymbol{u}\right)_1 = \rho_0\left(\boldsymbol{u}_0 \cdot \boldsymbol{u}_1\right) + \dfrac{1}{2}\rho_1 \boldsymbol{u}_0^2 \end{cases} \tag{51}$$

Inserting these into the second order energy equation, the following expression results:

$$\frac{\partial}{\partial t}\left[\frac{p_1^2}{2\rho_0 a_0^2}+\rho_1\left(\boldsymbol{u}_0\cdot\boldsymbol{u}_1\right)+\frac{1}{2}\rho_0\left(\boldsymbol{u}_1\cdot\boldsymbol{u}_1\right)+\frac{\rho_0 T_0}{2C_P}s_1^2\right]$$
$$+\begin{bmatrix}\frac{\partial\rho_2}{\partial t}\left(h_0+\frac{1}{2}\boldsymbol{u}_0^2\right)+\boldsymbol{m}_0\cdot\frac{\partial\boldsymbol{u}_2}{\partial t}+\rho_0 T_0\frac{\partial s_2}{\partial t}+T_0\frac{\partial}{\partial t}\left(\rho_1 s_1\right)\\ +\nabla\left[\boldsymbol{m}_1\left(h_1+\boldsymbol{u}_0\cdot\boldsymbol{u}_1\right)\right]\\ +\boldsymbol{m}_0\cdot\nabla\left(h_2+\frac{1}{2}\left(\boldsymbol{u}_1\cdot\boldsymbol{u}_1\right)+\boldsymbol{u}_0\cdot\boldsymbol{u}_2\right)\\ +\boldsymbol{m}_2\cdot\nabla\left(h_0+\frac{1}{2}\boldsymbol{u}_0^2\right)+\left(h_0+\frac{1}{2}\boldsymbol{u}_0^2\right)\nabla\cdot\boldsymbol{m}_2\end{bmatrix}=\begin{pmatrix}\boldsymbol{m}_0\cdot\boldsymbol{\psi}_2\\ +\boldsymbol{m}_1\cdot\boldsymbol{\psi}_1\\ +\boldsymbol{m}_2\cdot\boldsymbol{\psi}_0\end{pmatrix}+\begin{pmatrix}T_0Q_1\\ +T_1Q_1\\ +T_2Q_0\end{pmatrix} \tag{52}$$

Simplifying yields the following:

$$\frac{\partial}{\partial t}\left[\frac{p_1^2}{2\rho_0 a_0^2}+\rho_1\left(\boldsymbol{u}_0\cdot\boldsymbol{u}_1\right)+\frac{1}{2}\rho_0\left(\boldsymbol{u}_1\cdot\boldsymbol{u}_1\right)+\frac{\rho_0 T_0}{2C_P}s_1^2\right]$$
$$+\begin{bmatrix}\nabla\left[\boldsymbol{m}_1\left(h_1+\boldsymbol{u}_0\cdot\boldsymbol{u}_1\right)\right]+\rho_0 T_0\frac{\partial s_2}{\partial t}+T_0\frac{\partial}{\partial t}\left(\rho_1 s_1\right)\\ +\boldsymbol{m}_0\cdot\left(T_0\nabla s_2+T_1\nabla s_2+T_2\nabla s_0\right)+\boldsymbol{m}_2\cdot T_0\nabla s_0\\ +\boldsymbol{m}_0\cdot\nabla\cdot\begin{pmatrix}\boldsymbol{u}_0\times\boldsymbol{\omega}_2+\boldsymbol{u}_1\times\boldsymbol{\omega}_1\\ +\boldsymbol{u}_2\times\boldsymbol{\omega}_0\end{pmatrix}+\boldsymbol{m}_2\left(\boldsymbol{u}_0\times\boldsymbol{\omega}_0\right)\end{bmatrix}=\begin{pmatrix}\boldsymbol{m}_1\cdot\boldsymbol{\psi}_1\\ +T_0Q_2\\ +T_1Q_1+T_2Q_0\end{pmatrix} \tag{53}$$

The terms in this above expression involving entropy, shown separately below, can be simplified through use of the three entropy equation expansions shown in equation 50.

$$\rho_0 T_0\frac{\partial s_2}{\partial t}+T_0\frac{\partial}{\partial t}\left(\rho_1 s_1\right)+\boldsymbol{m}_0\cdot\left(T_0\nabla s_2+T_1\nabla s_2+T_2\nabla s_0\right)+\boldsymbol{m}_2\cdot T_0\nabla s_0 \tag{54}$$

Beginning with the second-order entropy equation,

$$\frac{\partial}{\partial t}\left(\rho_0 s_2+\rho_1 s_1+\rho_2 s_0\right)+\nabla\cdot\left(\boldsymbol{m}_0 s_2+\boldsymbol{m}_1 s_1+\boldsymbol{m}_2 s_0\right)=Q_2 \tag{55}$$

simplifying, and plugging it into the simplified energy equation, yields the following.

$$\frac{\partial}{\partial t}\left[\frac{p_1^2}{2\rho_0 a_0^2}+\rho_1\left(\boldsymbol{u}_0\cdot\boldsymbol{u}_1\right)+\frac{1}{2}\rho_0\left(\boldsymbol{u}_1\cdot\boldsymbol{u}_1\right)+\frac{\rho_0 T_0}{2C_P}s_1^2\right]$$
$$+\begin{bmatrix}\nabla\left[\boldsymbol{m}_1\left(h_1+\boldsymbol{u}_0\cdot\boldsymbol{u}_1\right)\right]+\\ T_0Q_2+T_2Q_0-\nabla\cdot\left(\boldsymbol{m}_1T_0s_1\right)+\nabla\cdot\left(\boldsymbol{m}_0T_1s_1\right)+\\ \boldsymbol{m}_1s_1\cdot\nabla T_0-\boldsymbol{m}_0s_1\cdot\nabla T_1\\ +\boldsymbol{m}_0\cdot\begin{pmatrix}\boldsymbol{u}_0\times\omega_2+\boldsymbol{u}_1\times\omega_1\\ +\boldsymbol{u}_2\times\omega_0\end{pmatrix}+\boldsymbol{m}_2\left(u_0\times\omega_0\right)\end{bmatrix}=\begin{bmatrix}\boldsymbol{m}_1\cdot\psi_1\\ +T_0Q_2\\ +T_1Q_1\\ +T_2Q_0\end{bmatrix} \tag{56}$$

Equation 56 is now nearly in the form of unsteady system energy balance. However, focusing on linear behavior, second order terms are removed from the above expression. This results in the following equation,

$$\frac{\partial}{\partial t}\left[\frac{p_1^2}{2\rho_0 a_0^2}+\rho_1\left(\mathbf{u}_0\cdot\mathbf{u}_1\right)+\frac{1}{2}\rho_0\left(\mathbf{u}_1\cdot\mathbf{u}_1\right)+\frac{\rho_0 T_0}{2C_P}s_1^2\right]$$
$$+\begin{bmatrix}\nabla\cdot\left[\mathbf{m}_1\left(h_1+\mathbf{u}_0\cdot\mathbf{u}_1\right)-\mathbf{m}_1T_0s_1+\mathbf{m}_0T_1s_1\right]\\ +\mathbf{m}_1s_1\cdot\nabla T_0-\mathbf{m}_0s_1\cdot\nabla T_1\\ -\rho_0\mathbf{u}_0\cdot\left(\mathbf{u}_1\times\boldsymbol{\omega}_1\right)+\rho_1\mathbf{u}_1\cdot\left(\mathbf{u}_0\times\boldsymbol{\omega}_0\right)\end{bmatrix}=\mathbf{m}_1\cdot\boldsymbol{\psi}_1+T_1Q_1 \tag{57}$$

After cancellation of terms and some rearrangement, the following form results.

$$\frac{\partial}{\partial t}\left(\frac{p_1^2}{2\rho_0 a_0^2}+\rho_1\left(\boldsymbol{u}_0\cdot\boldsymbol{u}_1\right)+\frac{1}{2}\rho_0\left(\boldsymbol{u}_1\cdot\boldsymbol{u}_1\right)+\frac{\rho_0 T_0}{2C_P}s_1^2\right)=$$
$$\nabla\cdot\begin{pmatrix}\boldsymbol{m}_1\left(h_1+\boldsymbol{u}_0\cdot\boldsymbol{u}_1\right)\\ -\boldsymbol{m}_1T_0s_1+\boldsymbol{m}_0T_1s_1\end{pmatrix}+\begin{pmatrix}\boldsymbol{m}_1\boldsymbol{\psi}_1+T_1Q_1\\ -\boldsymbol{m}_1s_1\cdot\nabla T_0+\boldsymbol{m}_0s_1\cdot\nabla T_1\\ \rho_0\boldsymbol{u}_0\cdot\left(\boldsymbol{u}_1\times\boldsymbol{\omega}_1\right)-\rho_1\boldsymbol{u}_1\cdot\left(\boldsymbol{u}_0\times\boldsymbol{\omega}_0\right)\end{pmatrix} \tag{58}$$

This is the linear system energy balance. It can be seen that all of the familiar effects that lead to the combustion instability mechanisms are present. This includes effects due to change in entropy, rotational flow effects, vortex shedding, viscous and body forces, as well as additions due to heat. Section 3.8 discusses how this expression can be rearranged to develop the growth rate and nonlinear corrections.

3.6 – Incorporation of Heat Release Terms

It can be seen in the above equation that there is a placeholder for the heat expression, Q_1. As discussed previously in Section 3.2, the full expression for the heat is as follows.

$$Q = \frac{\Phi - \nabla \cdot q + \mathscr{H}}{T} \tag{59}$$

Since this term is to be included as part of the linear analysis, its contribution can easily be added back in at anytime. It is thus acceptable to forego expanding it in the above expansion to avoid carrying the text through the manipulation process and so that it may be presented here for clarity purposes.

In the end, the overall heat term is typically considered to have negligible effects and eliminated from further analysis [40]. This term, however, encompasses the focus of this research, because it includes the heat release term due to combustion. Thus, when reinserted into the analysis, it is assumed that viscous energy dissipation and heat transfer can be neglected. These could easily be reincorporated into the equation, but since the focus of this research is to determine the effects of the heat release on the stability of the system, they are not included for clarification of heat release effects. Therefore, the only term remaining in the Q equation is a term involving the heat release due to the combustion process, as shown.

$$Q = \frac{\mathscr{H}}{T} \tag{60}$$

Through a perturbation expansion, the fully expanded form of this equation can be seen as follows.

$$Q = Q_0 + \varepsilon Q_1 + \varepsilon^2 Q_2 = \frac{\mathscr{H}_0}{T_0} + \varepsilon\left(\frac{\mathscr{H}_1}{T_0} - \frac{\mathscr{H}_0 T_1}{T_0^2}\right) + \varepsilon^2\left(\frac{\mathscr{H}_2}{T_0} - \frac{\mathscr{H}_1 T_1}{T_0^2} + \left(\left(\frac{T_1}{T_0}\right)^2 - \frac{T_2}{T_0}\right)\frac{\mathscr{H}_0}{T_0}\right) + \ldots \tag{61}$$

The terms T_0 and T_1 represent the steady and unsteady temperature distributions. Likewise, the terms $\mathscr{H}_0$ and $\mathscr{H}_1$ represent the steady and unsteady heat release distributions.

Since focus is only placed upon first order components in this analysis, only the first-order component of the heat equation,

$$Q_1 = \frac{\mathscr{H}_1}{T_0} - \frac{\mathscr{H}_0 T_1}{T_0^2} \tag{62}$$

is used in the linear balance. This expression can then be summed with the other terms in the linear energy balance as shown in the following section.

3.7 – Integral Formulation

It can be seen that equation 58 is in the form of the energy corollary, shown again.

$$\frac{\partial \mathscr{E}}{\partial t} + \nabla \cdot \boldsymbol{W} = \mathscr{D} \tag{63}$$

It is of interest to note that the second-order energy density is of the following form.

$$\mathscr{E} = \frac{p_1^2}{2\rho_0 a_0^2} + \rho_1\left(\boldsymbol{u}_0 \cdot \boldsymbol{u}_1\right) + \frac{1}{2}\rho_0\left(\boldsymbol{u}_1 \cdot \boldsymbol{u}_1\right) + \frac{\rho_0 T_0}{2C_P} s_1^2 \tag{64}$$

The first two terms may be recognized by some as the classical Kirchhoff energy density [1] consisting of the elastic potential energy and kinetic energy per unit volume. However, this energy density term includes two others energy terms. The third term

represents the unsteady kinetic energy contribution carried by the mean flow. This term grows to great importance in high-speed flow problems. The fourth term is a result of not assuming isentropic flow. The importance of this term will be greatly affected by the results of the combustion heat release analysis. Depending upon the size of the heat release, it could encourage the unsteady entropy result. [1]

Integration of equation 63 over the chamber volume yields the second-order unsteady energy balance, as discussed in the beginning of the chapter [1]. Integrating over the combustion chamber control volume determines the rate of change of the system energy, E [1]. This integration, upon further rearrangement from equation 58 yields an expression containing all the familiar combustion instability results, seen in equation 68 [1].

$$\begin{aligned}
&\frac{\partial}{\partial t}\iiint_V\left(\frac{p_1^2}{2\rho_0 a_0^2}+\rho_1\left(\boldsymbol{u}_0\cdot\boldsymbol{u}_1\right)+\frac{1}{2}\rho_0\left(\boldsymbol{u}_1\cdot\boldsymbol{u}_1\right)+\frac{\rho_0 T_0}{2C_P}s_1^2\right)dV= \\
&-\iint_S \boldsymbol{n}\cdot\begin{pmatrix} a_0^2\rho_1\boldsymbol{u}_1+\dfrac{a_0^2}{\rho_0}\rho_1^2\boldsymbol{u}_0+\rho_0\boldsymbol{u}_1\left(\boldsymbol{u}_0\cdot\boldsymbol{u}_1\right) \\ +\rho_1\boldsymbol{u}_0\left(\boldsymbol{u}_0\cdot\boldsymbol{u}_1\right)+(\gamma-1)T_0\left(\rho_0\boldsymbol{u}_1+\rho_1\boldsymbol{u}_0\right)s_1 \\ +\rho_0\boldsymbol{u}_0\left(T_1 s_1\right) \end{pmatrix}dS \\
&+\iiint_V\begin{pmatrix} \\ -\rho_0\boldsymbol{u}_0\cdot\left(\boldsymbol{u}_1\times\boldsymbol{\omega}_1\right)-\rho_1\boldsymbol{u}_1\cdot\left(\boldsymbol{u}_0\times\boldsymbol{\omega}_0\right)+ \\ \left[\rho_0\boldsymbol{u}_0\cdot\nabla T_1-\left(\rho_0\boldsymbol{u}_1+\rho_1\boldsymbol{u}_0\right)\cdot\nabla T_0\right]s_1 \\ +T_1\left(\dfrac{\mathscr{H}_1}{T_0^2}-\dfrac{\mathscr{H}_0 T_1}{T_0^2}\right) \end{pmatrix}
\end{aligned} \tag{65}$$

This above integral formulation now includes the term representing the combustion energy release, the focus of this research. Other effects, such as those due to viscous forces, dissipation, heat transfer, and two-phase flow are not shown but can be

included. The next section will show how this expression can be rearranged and expanded to develop the full expression for the change in oscillation amplitude, which includes the linear growth rate and nonlinear corrections.

3.8 – Overview of Nonlinear Analysis

It is now possible to develop an expression to aid in understanding the occurrence of oscillations within a combustion system. Equation 65 can be arranged to provide a formula to determine how the oscillatory mode amplitudes evolve in time in response to the linear and nonlinear effects. It is convenient to move the nonlinear term in the energy density to the right side of the equation where it will be handled as an additional source term.

To evaluate equation 65, it is useful to employ the Galerkin technique used in classical acoustic theory [1]. In this way, the unsteady flow field properties are represented through a superpositioning process, employing acoustic modes. This technique builds off the concept that a net response for a given place and time makes use of the response of a system due to the sum of responses from two or more stimuli. In this case, the technique employs linear superposition in which a set of linear solutions is added together to obtain a system solution.

It is necessary to represent the fluctuating velocity in terms of acoustic irrotational velocity fluctuations, $\hat{\mathbf{u}}_1$, and vortical rotational fluctuations, $\tilde{\mathbf{u}}_1$. The summation of these two gives the total system velocity vector, as shown.

$$\boldsymbol{u}_1(\boldsymbol{r},t) = \hat{\boldsymbol{u}}_1(\boldsymbol{r},t) + \tilde{\boldsymbol{u}}_1(\boldsymbol{r},t) \tag{66}$$

The term $\boldsymbol{\omega}_1$ represents the unsteady part of the vorticity.

$$\boldsymbol{\omega}_1(\boldsymbol{r},t) = \nabla \times \boldsymbol{u}_1 = \nabla \times \tilde{\boldsymbol{u}}_1 \tag{67}$$

The use of this technique results in the following representations for key variables, in which the term $\mathbf{S}_m$ is the vector potential [19, 40].

$$\begin{aligned} p_1(\boldsymbol{r},t) &= P_0(t)\sum_{m=1}^{\infty}\eta_m(t)\psi_m(\boldsymbol{r}) \\ \hat{\boldsymbol{u}}_1(\boldsymbol{r},t) &= \sum_{m=1}^{\infty}\frac{\eta_m(t)}{\gamma k_m^2}\nabla\psi_m(\boldsymbol{r}) \\ \tilde{\boldsymbol{u}}_1(\boldsymbol{r},t) &= \sum_{m=1}^{\infty}\dot{\eta}_m(t)\nabla\times\boldsymbol{S}_m(\boldsymbol{r}) \\ \boldsymbol{\omega}_1(\boldsymbol{r},t) &= \sum_{m=1}^{\infty}\dot{\eta}_m(t)\nabla\times\nabla\times\boldsymbol{S}_m(\boldsymbol{r}) \end{aligned} \tag{68}$$

$\psi_m(r)$ represents the mode shape form for the mth modal component and η represents a periodic function of time.

$$\eta_m(t) = R_m(t)\sin\left(\omega_m t + \Phi_m(t)\right) \tag{69}$$

where ω_m and Φ_m are the corresponding angular frequencies and phase angles, and R_m represents the oscillatory amplitude for each mode.

Utilizing the orthogonality properties of the normal modes allows each mode to be analyzed independently. Next an admittance boundary is introduced to represent interactions of the waves at injection surface [2, 19, 40]. These allow the problem to be reduced to a formula for the mode amplitudes. Products seen in equation 65 can be expressed as follows.

$$\begin{aligned} \left(p_1\right)^2 &= P_0^2\sum_{m=1}^{\infty}\eta_m(t)\psi_m(\boldsymbol{r})\sum_{n=1}^{\infty}\eta_n(t)\psi_n(\boldsymbol{r}) \\ &= P_0^2\sum_{m=1}^{\infty}\sum_{n=1}^{\infty}R_m R_n\, sin\left(\omega_m t+\Phi_m\right) sin\left(\omega_n t+\Phi_n\right)\psi_m\psi_n \end{aligned} \tag{70}$$

$$\hat{\boldsymbol{u}}_1 \cdot \hat{\boldsymbol{u}}_1 = \left[\sum_{m=1}^{\infty} \frac{\dot{\eta}_m(t)}{\gamma k_m^2} \nabla \psi_m(\boldsymbol{r})\right]\left[\sum_{n=1}^{\infty} \frac{\dot{\eta}_n(t)}{\gamma k_n^2} \nabla \psi_n(\boldsymbol{r})\right]$$
$$= \sum_{m=1}^{\infty}\sum_{n=1}^{\infty} \frac{a_0^2}{\gamma^2 k_m k_n} R_m R_n cos\mathbf{s}\left(\omega_m t + \Phi_m\right) cos\left(\omega_n t + \Phi_n\right) \nabla \psi_m \cdot \nabla \psi_n \tag{71}$$

$$\tilde{\boldsymbol{u}}_1 \cdot \tilde{\boldsymbol{u}}_1 = \left[\sum_{m=1}^{\infty} \dot{\eta}_m(t) \nabla \times \boldsymbol{S}_m\right]\left[\sum_{n=1}^{\infty} \dot{\eta}_n(t) \nabla \times \boldsymbol{S}_n\right]$$
$$= \sum_{m=1}^{\infty}\sum_{n=1}^{\infty} a_0^2 k_m k_n R_m R_n cos\left(\omega_m t + \Phi_m\right) cos\left(\omega_n t + \Phi_n\right) \nabla \times \boldsymbol{S}_m \cdot \nabla \times \boldsymbol{S}_n \tag{72}$$

The integral expression for the energy in equation 65, upon manipulation, can be placed in the following form. The time rate of change for the system mode amplitudes can be determined through extensive manipulation and implementation of boundary conditions [19, 40].

$$\frac{d}{dt}\iiint_V \left(\frac{p_1^2}{2\gamma P_0} + + \frac{1}{2}\rho_0 \boldsymbol{u}_1^2\right) dV = \left\{\begin{array}{l} \iint_{S_b} p_1 \boldsymbol{n} \cdot \boldsymbol{u}_1 \, dS + \iint_{S_N} p_1 \boldsymbol{n} \cdot \boldsymbol{u}_1 \, ddS + \iint_{S_{b\|}} p_1 \boldsymbol{n} \cdot \boldsymbol{u}_1 \, dS \\ + \frac{\boldsymbol{n} \cdot \boldsymbol{u}_0}{\gamma P_0} \iint_{S_b} \left(p_1\right)^2 dS + \frac{\boldsymbol{n} \cdot \boldsymbol{u}_0}{\gamma P_0} \iint_{S_N} \left(p_1\right)^2 dS \\ + \iiint_V \left(\rho_0 \boldsymbol{u}_0 \cdot \boldsymbol{u}_1 \times \boldsymbol{\omega}_1 + \rho_1 \boldsymbol{u}_1 \cdot \boldsymbol{u}_0 \times \boldsymbol{\omega}_0\right) dV \\ - \iiint_V \frac{1}{2} \frac{\partial \rho_1}{\partial t} \left(\boldsymbol{u}_1 \cdot \boldsymbol{u}_1\right) dV \end{array}\right\} \tag{73}$$

Since it is not the focus of this research to analyze the nonlinear effects on stability, involved mathematical detail is not included here. Through application of the above summations in equations 70-72, the individual pieces of equation 73 can be expanded as follows [19, 40].

$$\frac{d}{dt}\iiint_V \left(\frac{p_1^2}{2\gamma P_0} + + \frac{1}{2}\rho_0 \boldsymbol{u}_1^2\right) dV = \sum_{m=1}^{\infty} \frac{E_m^2}{2\gamma} \frac{d\left(P_0 R_m^2\right)}{dt} \tag{74}$$

$$-2\gamma\left\{\iint_{S_b} p_1\boldsymbol{n}\cdot\boldsymbol{u}_1\,dS+\iint_{S_N} p_1\boldsymbol{n}\cdot\boldsymbol{u}_1\,dS+\iint_{S_{b\|}} p_1\boldsymbol{n}\cdot\boldsymbol{u}_1\,dS\right\}$$

$$=2a_0P_0\sum_{m=1}^{\infty}\sum_{n=1}^{\infty}\left\{\begin{aligned}&\iint_{S_b} M_bA_b\psi_m\psi_n\,dS\\&-\iint_{S_N} M_NA_N\psi_m\psi_n\,dS\\&+\iint_{S_{b\|}} M_bB_b\psi_m\psi_n\,dS\end{aligned}\right\}R_mR_n\sin\left(\omega_mt+\Phi_m\right)\sin\left(\omega_nt+\Phi_n\right)\psi_m\psi_n \tag{75}$$

$$-2\gamma\left\{\frac{1}{\gamma P_0}\iint_{S_b}\boldsymbol{n}\cdot\boldsymbol{u}_0\left(p_1\right)^2dS+\frac{1}{\gamma P_0}\iint_{S_N}\boldsymbol{n}\cdot\boldsymbol{u}_0\left(p_1\right)^2dS\right\}$$

$$=2a_0P_0\sum_{m=1}^{\infty}\sum_{n=1}^{\infty}\left\{\begin{aligned}&\iint_{S_b} M_bA_b\psi_m\psi_n\,dS\\&-\iint_{S_N} M_NA_N\psi_m\psi_n\,dS\end{aligned}\right\}R_mR_n\sin\left(\omega_mt+\Phi_m\right)\sin\left(\omega_nt+\Phi_n\right)\psi_m\psi_n \tag{76}$$

$$-2\gamma\left\{\iiint_V\left(\rho_0\boldsymbol{u}_0\cdot\boldsymbol{u}_1\times\boldsymbol{\omega}_1+\rho_1\boldsymbol{u}_1\cdot\boldsymbol{u}_0\times\boldsymbol{\omega}_0\right)dV\right\}$$

$$=2\gamma P_0\sum_{m=1}^{\infty}\sum_{n=1}^{\infty}R_mR_n\cos\left(\omega_mt+\Phi_m\right)\cos\left(\omega_nt+\Phi_n\right)\iiint_V\frac{k_n}{k_m}\nabla\psi_m\cdot\left(\boldsymbol{u}_0\times\left(\nabla\times\nabla\times\boldsymbol{S}_j\right)\right)dV \tag{77}$$

$$2\gamma\iiint_V\frac{1}{2}\frac{\partial\rho_1}{\partial t}\left(\boldsymbol{u}_1\cdot\boldsymbol{u}_1\right)dV=\gamma\iiint_V\frac{\partial\rho_1}{\partial t}\left(\boldsymbol{u}_1\cdot\boldsymbol{u}_1\right)dV$$

$$=P_0\sum_{m=1}^{\infty}\sum_{i=1}^{\infty}\sum_{n=1}^{\infty}\left(\psi_m\nabla\psi_i\cdot\nabla\psi_n\right)\frac{\left(\omega_m+\dfrac{d\Phi_m}{dt}\right)}{k_ik_n}R_mR_iR_n\cos\left(\omega_mt+\Phi_m\right)\cos\left(\omega_it+\Phi_i\right)\cos\left(\omega_nt+\Phi_n\right) \tag{78}$$

Inserting these expressions into equation 73, after much manipulation, results in the following summation over acoustic modes [19, 40].

$$\sum_{m=1}^{\infty} R_m E_m^2 \frac{dR_m}{dt} =$$

$$\left\{ \begin{array}{l} a_0 \sum_{m=1}^{\infty}\sum_{n=1}^{\infty} \left\{ \begin{array}{l} \iint_{S_b} M_b A_b \psi_m \psi_n \, dS \\ -\iint_{S_N} M_N A_N \psi_m \psi_n \, dS \\ +\iint_{S_{b\|}} M_b B_b \psi_m \psi_n \, dS \end{array} \right\} R_m R_n \sin\left(\omega_m t + \Phi_m\right) \sin\left(\omega_n t + \Phi_n\right) \\ +a_0 \sum_{m=1}^{\infty}\sum_{n=1}^{\infty} \left\{ \begin{array}{l} \iint_{S_b} M_b A_b \psi_m \psi_n \, dS \\ -\iint_{S_N} M_N A_N \psi_m \psi_n \, dS \end{array} \right\} R_m R_n \sin\left(\omega_m t + \Phi_m\right) \sin\left(\omega_n t + \Phi_n\right) \\ +\sum_{m=1}^{\infty}\sum_{n=1}^{\infty} \left(\iiint_V \frac{1}{k_m k_n} \nabla \psi_m \cdot \left(\boldsymbol{u}_0 \times \zeta_n\right) dV \right) R_m R_n \cos\left(\omega_m t + \Phi_m\right) \cos\left(\omega_n t + \Phi_n\right) \\ +\sum_{m=1}^{\infty}\sum_{i=1}^{\infty}\sum_{n=1}^{\infty} A_{\min} \frac{\left(\omega_m + \frac{d\Phi_m}{dt}\right)}{k_i k_n} R_m R_i R_n \cos\left(\omega_m t + \Phi_m\right) \cos\left(\omega_i t + \Phi_i\right) \cos\left(\omega_n t + \Phi_n\right) \\ -\sum_{m=1}^{\infty} E_m^2 R_m^2 \frac{1}{2P_0} \frac{dP_0}{dt} \end{array} \right\} \tag{79}$$

Upon simplification of this equation, it can be seen that the growth rate results as shown.

$$\alpha_m = \frac{a_0}{2E_m^2} \left(\begin{array}{l} \iint_{S_b} M_b \left(A_b + 1\right) \psi_m^2 \, dS - \iint_{S_N} M_N \left(A_N + 1\right) \psi_m^2 \, dS \\ +\iint_{S_{b\|}} M_b B_b \psi_m^2 \, dS + \iiint_V \frac{1}{k_m k_n} \nabla \psi_m \cdot \left(\boldsymbol{u}_0 \times \zeta_n\right) dV \end{array} \right) \tag{80}$$

$$\sum_{m=1}^{\infty} R_m \frac{dR_m}{dt} = \left\{ \begin{array}{l} \sum_{m=1}^{\infty} \alpha_m R_m - \sum_{m=1}^{\infty} \frac{R_m^2}{2P_0} \frac{dP_0}{dt} \\ +\sum_{m=1}^{\infty} \frac{R_m}{4E_m^2} \left(\omega_m + \frac{d\Phi_m}{dt} \right) \sum_{i=1}^{\infty}\sum_{n=1}^{\infty} \frac{A_{\min}}{k_i k_n} R_i R_n \left[\begin{array}{l} \delta\left(m - i - n\right) \cos\left(-\Phi_m + \Phi_i + \Phi_n\right) \\ +\delta\left(m + i - n\right) \cos\left(\Phi_m + \Phi_i - \Phi_n\right) \\ +\delta\left(m - i - n\right) \cos\left(-\Phi_m + \Phi_i - \Phi_n\right) \end{array} \right] \end{array} \right\} \tag{81}$$

Applying the following Kronecker delta functions,

$$\delta_1 = \delta\left(m - i - n\right) \quad \delta_2 = \delta\left(m + i - n\right) \quad \delta_3 = \delta\left(m - i - n\right) \quad \textit{where} \quad \delta\left(\xi\right) = \begin{cases} 1 & \textit{if} \quad \xi = 0 \\ 0 & \textit{if} \quad \xi \neq 0 \end{cases} \tag{82}$$

for a single mode of oscillation, inserting a developed expression for the derivative of the phase angle, equation 81 can be expressed as shown below. This equation can then be used to determine the change in oscillation amplitude for each mode of oscillation, where A_{min} is a geometrical weighting function [1, 19, 40].

$$\frac{dR_m}{dt} = \alpha_m R_m - \frac{R_m}{2P_0}\frac{dP_0}{dt} + \left(\frac{\gamma+1}{4\gamma E_m^2}\right)\omega_m \sum_{i=1}^{\infty}\sum_{n=1}^{\infty} A_{\min} R_i R_n \begin{bmatrix} -\delta_1 \cos\left(-\Phi_m + \Phi_i + \Phi_n\right) \\ +\delta_2 \cos\left(\Phi_m + \Phi_i - \Phi_n\right) \\ +\delta_3 \cos\left(-\Phi_m + \Phi_i - \Phi_n\right) \end{bmatrix} \quad (83)$$

It can be seen that α_m, the linear growth rate for component m, comprises only a small part of the equation. The second term in the equation represents important changes in mean properties over time and is ignored in the classical problem. This is where the infamous DC shift comes into play. As noted earlier, in solid rockets, this effect is often seen as a drastic change in mean operating pressure; in liquid rockets, it usually appears as a change in the mean chamber temperature. The third set of terms show the nonlinear correction that help explain the cascading effect and transition to limit cycle, discussed in Chapter 2.

As a result of these last terms, the complete equation for the change of the system amplitude is clearly nonlinear. As equation 83 shows, it is actually comprised of a set of coupled first-order differential equations that must be solved numerically. This results from the summation series in the third term. This nonlinear effect results from the inclusion of the last term in the integral expression in equation 73.

From equation 83, it is clear that even though nonlinear effects are accounted for in the summation, this equation for the pressure disturbance amplitude also depends upon the linear growth rate. As previously discussed, this linear part of the system amplitude

equation has received the most attention by far. To accurately determine the nonlinear behavior of the system, the linear behavior of the system must also be accurately represented. Since the linear stability problem itself is imbedded within the nonlinear problem, an accurate calculation of amplitude oscillations depends critically on the correctness of the linear solution.

This leads back to the focus of this research, which is to concentrate on determining the contribution to the linear growth rate from the heat release due to the combustion process for inclusion into the overall system growth rate as shown again in equation 84. Calculation of this contribution to the overall system stability will greatly increase the fidelity of the nonlinear analysis for determination of the severity of expected oscillations in an unstable system [1].

$$\alpha_m = \left[\begin{array}{l} \underbrace{\frac{1}{2E_m^2}\iint_{S_{inj}} M_{inj}\left(A_{inj}^{(r)}+1\right)\psi_m^2 dS}_{\text{Pressure Coupling}} - \underbrace{\frac{1}{2E_m^2}\iint_{S_N} M_N\left(A_N^{(r)}+1\right)\psi_m^2 dS}_{\text{Nozzle Damping}} \\ \underbrace{+\frac{1}{2E_m^2}\iint_{S_{injll}} M_{inj}B_{inj}^{(r)}\psi_m^2 dS}_{\text{Acoustic Boundary Layer Pumping (ABL)}} - \underbrace{\frac{1}{2E_m^2}\iint_{S_{injll}}\left(\frac{\delta}{2\gamma M_{inj}}\right)^2\langle\nabla\psi_m\cdot\nabla\psi_m\rangle dS}_{\text{Viscous Damping at Injection Surfaces}} \\ \underbrace{-\frac{1}{2\gamma P_0 E_m^2}\iiint_V \rho_0\boldsymbol{u}_0\cdot\langle\boldsymbol{u}_1\times\boldsymbol{\omega}_1\rangle dV - \frac{1}{2\gamma P_0 E_m^2}\iiint_V \rho_1\boldsymbol{u}_1\cdot\langle\boldsymbol{u}_0\times\boldsymbol{\omega}_0\rangle dV}_{\text{Vortex Shedding Effects and Flow Turning Loss}} \\ \underbrace{+\frac{1}{2\gamma P_0 E_m^2}\iiint_V\left\langle\frac{\mathscr{H}_1 T_1}{T_0}-\frac{\mathscr{H}_0 T_1^2}{T_0^2}\right\rangle dV + other\ sources}_{\text{Distributed Combustion Heat Release}} \end{array} \right] \tag{84}$$

CHAPTER 4 – VOLUMETRIC COMBUSTION ANALYSIS

This chapter presents the combustion model and mathematics used in developing the unsteady combustion linear growth rate. Discussion of the combustion process within rocket systems is first presented, followed by discussion of the heat release growth rate to be determined. The combustion model and limiting assumptions are then explained, including background material needed in understanding the combustion model. This is followed by development of the equations used to solve for the variables needed for determination of the growth rate. Equations for both steady and unsteady combustion are developed. The mathematical steps performed by the author in development of these expressions are presented. These equation developed agree with those determined by Tien [75]. This chapter ends showing the process used in separating the unsteady equations into real and imaginary parts to solve for the oscillatory properties.

4.1 – Rocket Combustion

The combustion process in a rocket engine is inherently complex, with strong temporal and spatial gradients. Typical reactions involve numerous chemical species and dozens of reactions. Add to this the intricacies of propellant atomization, vaporization and mixing, and the system of equations becomes truly daunting. Even with modern numerical tools and simple reactants, a full detailed analysis of the combustion process can tax the most sophisticated supercomputers.

To simplify the analysis process, equilibrium chemistry techniques are commonly used. However, since equilibrium models are inherently steady state, they are generally only useful in performance calculations. While they are of little use in combustion stability calculations due to the need to model the dynamic oscillatory behavior, equilibrium models may play a role in the determination of the quasi-steady flow field characteristics. This is generally accomplished by invoking a thin flame assumption to provide an instantaneous transition from the unburned reactants to the equilibrium products. In a thin flame model, it is assumed that the chemical reactions are nearly instantaneous and that propellants are sufficiently premixed prior to the combustion zone. This greatly simplifies the combustion analysis by separating the chemistry from the flow field.

This approach is generally acceptable for the steady combustion analysis of solid and liquid rockets. In solid rockets, the premixed solid phase fuel and oxidizer promotes rapid combustion in a thin zone that sits just above the burning surface. Also, while premixed liquid rockets are rare, most well designed liquid rockets confine the propellant atomization, vaporization and mixing to a small zone near the injector face [76]. This rapid mixing and atomization process makes it reasonable to use a thin flame assumption to analyze the steady-state performance of most liquid rockets. This is shown graphically in Figure 20. For comparison, the combustion processes for both a liquid engine and a solid motor are shown on the top and bottom halves of the rocket diagram, respectively. This figure is not drawn to scale so that the combustion zone can be shown in greater detail. This figure shows the liquid combustion process occurring in a more distributed

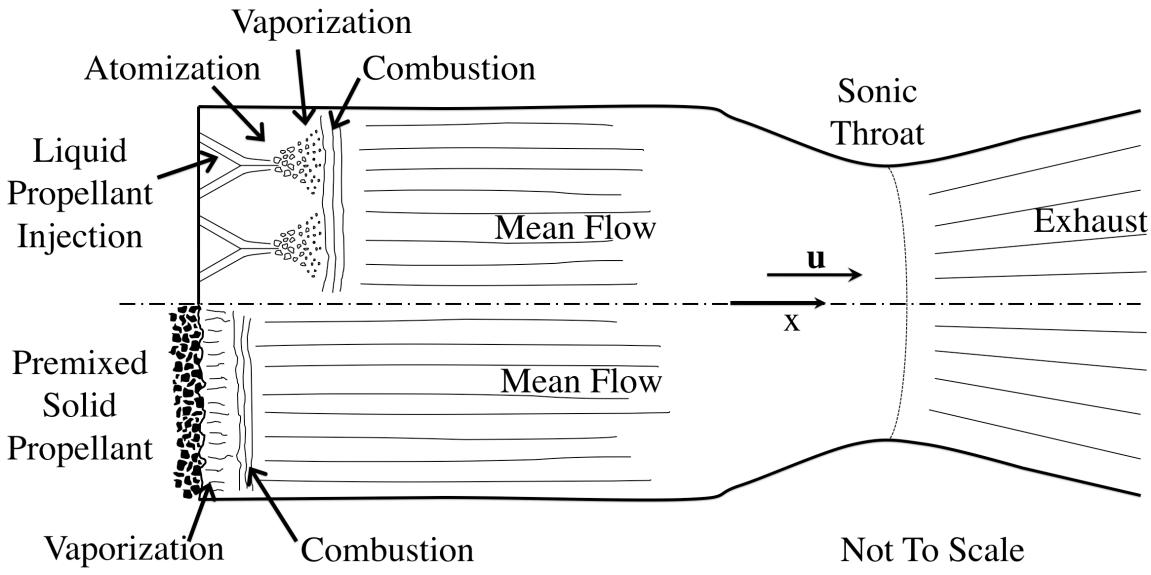

Figure 20. Diagrams Showing Combustion Of Liquid/Solid Rocket

zone than the solid combustion with the inclusion of atomization and vaporization shown prior to the combustion zone.

However, there are circumstances that inhibit the use of the thin flame assumption in both solid motors and liquid engines. In solid motors, the presence of aluminum particles or large propellant granules can distort the thin flame by extending the burning process into the interior of the motor. Since this process has an effect on the combustion stability it is necessary to capture the temporal behavior of the particle combustion in addition to the steady chemistry.

In liquid rocket engines, the presence of recirculation zones or coarse injection patterns can significantly thicken or distort the flame zone. Additionally, some liquid propellants, such as kerosene, are relatively slow burning, thickening the flame. In such cases, a portion of the propellant flow may be expelled from the engine without combusting. To capture these effects, it is necessary to account for the finite time that is

required for combustion, along with the time needed to atomize, vaporize and mix the liquid propellants.

Traditionally, instead of equilibrium chemistry, chemical kinetics theory is used to model the time varying combustion process. To do so introduces a significant increase in analysis, or simulation complexity, for a reaction process due to the need to compute the reaction rates and concentrations of numerous species for dozens of possible sub-reactions.

In the current analysis, the combustion process is modeled through the use of chemical kinetics theory. Focus is placed upon isolating the oscillatory effects of the combustion process itself on the self-excited gas dynamics (i.e. combustion instability) in the chamber. Since this study provides an initial understanding of the magnitude of the unsteady combustion growth rate, to limit the complexity of the current analysis, the combustion is modeled as a one-step forward chemical reaction.

To isolate the effects of the combustion process, the analysis first presented in Section 3.5 will be used. It is desired to determine unsteady combustion's relative importance to other instability mechanisms within a liquid system. Therefore, it is necessary to determine the higher order effects of the heat release on the system. The steady state heat release of the system can readily be determined. It is the effects of the oscillatory heat release that will lend understanding in the effect of an oscillatory disturbance upon the combustion zone. This is done through determination of the linear growth rate, α, for the distributed heat release in the system.

Second order nonlinear effects need to be determined at a later time. Calculation of these, however, is an entirely separate task from determination of first order effect and

leads to a greater mathematical endeavor. Before these second order corrections can be applied, evaluation of the first order effects is of primary focus.

The perturbation-expanded equation for the distributed heat release comes about as shown in Section 3.6. Expanding the heat term, Q, shown in equation 59, neglecting heat transfer and viscous dissipation, the first-order component of the heat release was determined as shown.

$$Q_1 = \frac{\mathscr{H}_1}{T_0^2} - \frac{\mathscr{H}_0 T_1}{T_0^2} \tag{85}$$

The terms T_0 and T_1 represent the steady and unsteady temperature distributions. Likewise, the terms $\mathscr{H}_1$ and $\mathscr{H}_0$ represent the steady and unsteady heat release distributions.

Using this expression for the first-order heat, the unsteady combustion linear growth rate is determined directly from insertion into the volumetric integral for the unsteady energy balance, shown in equation 65 in Section 3.7. As demonstrated in Section 3.8, through extensive manipulation, the expression for the overall system growth rate, including unsteady combustion, can be arranged into the form shown in equation 84. The last term in the expression is the unsteady combustion linear growth rate, shown again in the following equation [1, 77].

$$\alpha_{HR} = \left\{ \frac{1}{2\gamma P_0 E_m^2} \iiint_V \left\langle \frac{\mathscr{H}_1 T_1}{T_0} - \frac{\mathscr{H}_0 T_1^2}{T_0^2} \right\rangle dV \right\} \tag{86}$$

This expression for the growth rate is developed through inclusion of the heat release volume integral from equation 65 into the derivation process of Section 3.8. In equation 84, this term, and some of the others, have the γP_0 multiplier in them, not seen in the first

four terms of this equation. This is because in derivation of the other terms (from equations 75-78), the P_0 multiplier was eliminated through a Galerkin expansion, and the γ was canceled due to application of boundary conditions that resulted in the forms of equations 75-78. These mathematical manipulations are not required in the determination of the heat release growth rate, since the required steady and unsteady temperature, T, and heat release, $\mathscr{H}$, values needed must be determined numerically. Thus, the form shown in equation 86 results for determination of the growth rate. The angled brackets represent a time average, to be discussed in Chapter 5.

Once the linear growth rate for the heat release is determined in this analysis, it will then be compared to the growth rate contributions of the other mechanisms. The relative magnitudes can be determined. The heat release growth rate can then be included into a cumulative linear growth rate for the system. From this cumulative growth rate, the effect on pressure oscillations in the system can be determined. Before the effects from the distributed combustion heat release can be determined, a model must be developed to represent the combustion process within the rocket chamber.

4.2 – Combustion Model

The model used to represent combustion within a liquid rocket system follows along with the analysis presented by Tien [75] in his analysis of oscillatory burning of a solid propellant. While his analysis was focused on the calculation of an acoustic admittance response for a solid propellant surface, the ideas presented in Tien's study are useful for this initial modeling a simple premixed liquid rocket combustion system experiencing a small amplitude pressure disturbance.

In this analysis, the governing equations for the system are nondimensionalized and expanded in a perturbation analysis approach for small amplitude pressure oscillations as done by Tien. The equations are then separated into steady and unsteady problems; it is shown in the following sections how these equations can be arrived upon. They are then evaluated numerically to obtain solutions for the steady and unsteady temperature distributions, used in calculation of the unsteady combustion growth rate. The steady and unsteady heat release distributions can then be obtained, along with the combustion flame length. These computed values are then used in the unsteady combustion linear growth rate equation (equation 89).

It is important to note at this point that calculation of the heat release growth rate solely focuses upon the interaction of heat release due to the overall combustion process with that of an oncoming acoustic wave. The reaction-specific chemical kinetics required to reach the end state of combustion are not of relevance in this dissertation. In effect, calculation of the growth rate indicates whether the combustion heat release provides a feedback mechanism for amplification of acoustic waves on the stability within a liquid rocket system [77].

It must be emphasized that this model merely provides an initial insight into the effects of unsteady combustion and its distributed heat release on the stability within a liquid rocket system [77]. It is therefore acknowledged that a great deal of additional work will be needed to fully explore this effect. This research forms a foundation for understanding the importance of this mechanism in combustion instability modeling and will be extended to include greater detail in continuing research. This investigation is a first step and is intended to characterize the magnitude of a given heat release upon

system stability. As a result, this approach leads to several simplifying assumptions. It is anticipated that in future continuation of this work all assumptions will be one by one withdrawn.

The first assumption made in this initial model is that the combustion is assumed to occur in a premixed laminar flame. This approach assumes that the propellant being injected into the system has been premixed, that is that atomization and mixing has occurred prior to the planar combustion zone being investigated. This zone can either be thought of as an injector face at which a premixed propellant is being injected, or, as a point downstream of injection at which mixing and atomization has completed. Therefore, the propellant can be assumed to have reached a gaseous state. If it were desired to know the entire time history for combustion in the latter case, a model for the mixing and atomization would need to be included; this is intended in future work [77].

The laminar flame assumption assumes that the bulk convective motion occurs along distinct streamlines rather than having randomly fluctuating properties due to turbulent effects. In addition to greatly simplifying the model, this laminar flame approach allows the mixing processes to be separated from the combustion effects in the stability assessment [77].

In a further simplification, the flame is also assumed to be one-dimensional with combustion occurring in a one-step forward chemical reaction. Many quantities are taken to be constant in this analysis, including specific heat, specific gravity, and the coefficient of heat conduction. The Lewis number is taken to be equal to unity. The flow is assumed to be isobaric, meaning it is at constant mean pressure. Lastly, it is assumed that

the acoustic wave travels lengthwise down the chamber, which is consistent with the one-dimensional flame assumption [75, 77].

4.3 – Mathematical Technique

With the assumptions for the combustion model fully laid out, the following governing equations are used to represent the combustion flow [75, 77-78]. These equations are the conservation of mass, the energy equation, and the species concentration equation, as well as the ideal gas equation of state. These equations are shown in dimensional form; however, in order to isolate the effect of various parameters in the growth rate analysis, the following work is performed in dimensionless form. In the following equations, the * superscript is used to represent the dimensional forms rather than the dimensionless forms to simplify the bookkeeping.

$$\frac{\partial \rho^*}{\partial t^*} + \frac{\partial \rho^* u^*}{\partial x^*} = 0 \tag{87}$$

$$\rho^* C_P \frac{\partial T^*}{\partial t^*} + \rho^* u^* C_P \frac{\partial T^*}{\partial x^*} - \lambda \frac{\partial^2 T^*}{\partial x^{*2}} - \frac{\partial p^*}{\partial t^*} = -\sum_{i=1}^{N} h_i^0 w_i^* \tag{88}$$

$$\rho^* \frac{\partial Y_i}{\partial t^*} + \rho^* u^* \frac{\partial Y_i}{\partial x^*} - \frac{\lambda}{C_P} \frac{\partial^2 Y_i}{\partial x^{*2}} = w_i^* \tag{89}$$

$$p^* = \rho^* R T^* \tag{90}$$

The energy and species equations used are in Shvab-Zel'dovich form [78]. The Shvab-Zel'dovich formulation makes use of a quantity known as a conserved scalar. This approach is used to decouple the system energy and species equations from their dependence on the chemical reactions in the flow. The resulting conserved scalar parameter, or coupling function, is obtained through the use of a stoichiometrically

combined relationship between reactive species, which frees the quantities from dependence upon the reaction process. This is discussed in Section 4.3.

The conservation of momentum equation is not included in this set of governing equations, because it can be assumed that momentum is conserved during molecular collision leading to chemical reaction. As a result, chemical reaction terms do not explicitly appear in the momentum equation, so the equation is identical to that of chemically non-reacting flows. Therefore, it need not be included in this analysis [78].

The Shvab-Zel'dovich formulation is applicable to general chemical reactions but is most useful for a one-step chemical reaction used in this analysis [78]. The one-step reaction process can be represented in the following notation, where the subscripts f, o, and p refer to the fuel, oxidizer, and reaction products.

$$\nu_f'\left[f\right]+\nu_o'\left[O\right]\rightarrow\nu_P''\left[P\right] \tag{91}$$

It is a simple relation, showing that the addition of two reactive species, a fuel and an oxidizer, leads to the production of another product species. The terms ν_i' and ν_i'' represent the stoichiometric coefficients on the reactants and products side of the equation, respectively, for a species i.

Another way of expressing this is with the following summation relation where the symbol W_i represents the molecular weight for the ith species [78].

$$\sum_{i=1}^{N}\nu_i'W_i\rightarrow\sum_{i=1}^{N}\nu_i''W_i \tag{92}$$

This process makes use of a species-independent reaction rate, w, expressed through the following relationship with the each of the individual species reaction rates, w_i [78].

$$w = \frac{w_i}{W_i\left(v_i'' - v_i'\right)} \tag{93}$$

This reaction rate, w, is assumed to obey the Arrhenius Law, a well known empirical relationship that shows reaction rate dependence upon temperature variation, as shown (in dimensional notation) [75, 77-78].

$$w^* = B^* T^{*\delta} \left(\frac{p^*}{RT^*}\right)^n \prod_{j=1}^{N} \left(\frac{Y_j}{W_j}\right)^{n_j} e^{-\left(E^*/RT^*\right)} \tag{94}$$

The right side of the energy equation can be expressed through use of the species-independent reaction rate as shown in the following form,

$$-\sum_{i=1}^{N} h_i^0 w_i^* = w^* q^* \tag{95}$$

where q^*, the heat of combustion per unit mass of fuel consumed, can be expressed as shown [75, 78].

$$q^* = \sum_{j=1}^{N} h_i^o \frac{W_i\left(v_i' - v_i''\right)}{W_f\left(v_f'\right)} \tag{96}$$

Upon rearrangement of the energy equation to include the species independent reaction rate and heat of combustion, the equations can now be nondimensionalized. The use of nondimensionalization was selected as a means to reveal general trends, independent of a particular reaction scheme. However, the model could be implemented in dimensional form, if desired. It is anticipated that this will be done in future work. Thus, to place the governing equations (equations 87-89) into dimensionless form, the following scaling relationships were used [75, 77].

$$\rho^* \equiv \bar{\rho}_\infty \rho \quad T^* = \bar{T}_\infty T \quad u^* = \bar{u}_\infty u \quad p^* = \bar{p}_\infty p \quad x^* = \left(\frac{\bar{\lambda}_\infty}{\bar{\rho}_\infty C_P \bar{u}_\infty} \right) x$$

$$\mathrm{t}^* = \left(\frac{\bar{\lambda}_\infty}{\bar{\rho}_\infty C_P \bar{u}_\infty^2} \right) t \quad w^* = \left(\frac{\bar{\rho}_\infty^2 C_P \bar{u}_\infty^2}{\bar{\lambda}_\infty} \right) w \quad q^* = C_p \bar{T}_\infty q \tag{97}$$

These scaling parameters are of the typical form used in combustion problems. The expressions of density ($\bar{\rho}_\infty$), pressure ($\bar{P}_\infty$), temperature ($\bar{T}_\infty$), velocity ($\bar{u}_\infty$), and thermal conductivity ($\bar{\lambda}_\infty$) refer to those properties' conditions at infinity. The dimensional density (ρ^*), pressure (p^*), temperature (T^*), and velocity, (u^*) can simply be placed in dimensionless form by division of their respective infinity conditions. This infinity nomenclature is used to specify a downstream position at great distance on the length scale of the combustion region of nonuniformity. In engineering units, this is actually a finite length, which is small compared to the dimensions of the combustion chamber. The flame zone is a "region of nonuniformity", which is analogous to a boundary layer; the infinity symbol is used there to also represent the boundary layer thickness. The interpretation used here is that an axial position ($x \to \infty$) refers to a point at which the main variables (temperature, fuel species concentration, etc.) have reached local uniformity. This does not mean that some variables could not vary downstream due to other interactions.

To scale the dimensional values of the position, time, and reaction rate, a distance scaling parameter was needed. These parameters were nondimensionalized by the characteristic flame length (δ_f), a typical procedure when dealing with combustion dynamics, [78]. It is defined by the ratio of the thermal diffusivity ($\bar{\alpha}_\infty$) to the velocity,

or written in terms of thermal conductivity, density and specific heat ratio, as follows.

$$\delta_f = \frac{\bar{\alpha}_\infty}{\bar{u}_\infty} = \frac{\bar{\lambda}_\infty}{\bar{\rho}_\infty C_P \bar{u}_\infty} \tag{98}$$

This term is used to nondimensionalize the flame length, and, along with the velocity, it is used to place the time and reaction rate in dimensionless form. The heat of combustion is simply nondimensionalized by the product of the specific heat ratio, C_P, and the temperature at infinity.

Application of these nondimensionalizing parameters to equations 87 results in the following dimensionless forms of the conservation of mass, conservation of energy, and conservation of species equations, as well as the dimensionless equation of state [75].

$$\frac{\partial \rho}{\partial t} + \frac{\partial \rho u}{\partial x} = 0 \tag{99}$$

$$\rho \frac{\partial T}{\partial t} + \rho u \frac{\partial T}{\partial x} - \frac{\partial^2 T}{\partial x^2} - \frac{\gamma - 1}{\gamma} \frac{\partial p}{\partial t} = wq \tag{100}$$

$$\rho \frac{\partial Y_i}{\partial t} + \rho u \frac{\partial Y_i}{\partial x} - \frac{\partial^2 Y_i}{\partial x^2} = v_i w \tag{101}$$

$$p = \rho T \tag{102}$$

The gas constant R in the dimensionless equation of state is naturally removed when nondimensionalizing with the chamber conditions at infinity.

These three governing equations are actually a set of five equations, because the subscript, i, in the species equation can be represented as f, o, or p, representing fuel, oxidizer, and reaction product, respectively. Thus, the combustion system is governed by five equations; the conservation of mass equation, the conservation of energy equation,

and the conservation of fuel, oxidizer, and product species equations. This system of equations can be solved, with the help of the equation of state, for the velocity, temperature, and three species concentrations.

When the species equation is expressed in terms of the individual reaction species, such as the following fuel, oxidizer, or product species equations, it can be seen that they are of the same form. Since the species concentrations can be related through stoichiometry relations, discussed in the following section, it is thus only necessary to solve one of the species equations. The other two concentrations can then be obtained through the use of stoichiometry. In this case, the equation for fuel species was solved [75, 77].

$$\begin{aligned}
\rho\frac{\partial Y_f}{\partial t}+\rho u\frac{\partial Y_f}{\partial x}-\frac{\partial^2 Y_f}{\partial x^2}&=v_f w\\
\rho\frac{\partial Y_o}{\partial t}+\rho u\frac{\partial Y_o}{\partial x}-\frac{\partial^2 Y_o}{\partial x^2}&=v_o w\\
\rho\frac{\partial Y_p}{\partial t}+\rho u\frac{\partial Y_p}{\partial x}-\frac{\partial^2 Y_p}{\partial x^2}&=v_p w
\end{aligned} \tag{103}$$

4.4 – Role of the Stoichiometrically Weighted Mass Fraction

The stoichiometric scaling technique must be used in order to obtain a full solution for the above dimensionless equations [78]. This methodology results in the conserved scalar parameter obtained through the use of a stoichiometrically combined relationship between reactive species. It will be shown in the following section the connection between temperature and species employed to aid in determining the fuel species profile. In order to determine the other species profiles, a stoichiometrically weighted mass fraction is employed to relate them to one another. This relationship is

shown in the following equation where the term, σ_i, can be thought of as a stoichiometrically weighted mass ratio of species, i, to an unspecified reference species, n. B represents an unspecified boundary location, i.e., the freestream [78].

$$\widetilde{Y}_i = \frac{1}{\sigma_{i,n}}\left(\frac{Y_i}{Y_{n,B}}\right) \tag{104}$$

$$\sigma_{i,n} = \frac{W_i\left(v_i'' - v_i'\right)}{W_n\left(v_n'' - v_n'\right)} \tag{105}$$

In the case of a stoichiometric reaction, this relationship can be explained quite simply. However, cases of off-stoichiometry require a greater amount of explanation. The case used in this initial investigation is that of a stoichiometric reaction.

The choice for reference species used in the weighting ratio is not set; it is typically governed by the species that is in the greatest percentage. For a stoichiometric reaction the reference species can be whichever the analyst chooses. Selecting the fuel as the reference species, results in the following expressions.

$$\sigma_{f,f} = 1 \qquad \sigma_{f,o} = \frac{W_i\left(v_i'\right)}{W_n\left(v_n'\right)} = OF\ Ratio \tag{106}$$

$$\widetilde{Y}_f = \frac{Y_f}{Y_{f,B}} \qquad \widetilde{Y}_o = \frac{Y_o}{\sigma_{f,o}Y_{f,B}} \tag{107}$$

The term $Y_{f,B}$ represents the freestream amount of fuel required for stoichiometric combustion, hence the name stoichiometric scaling. The value in the denominator of the scaled oxidizer species, $\sigma_{f,o}Y_{f,B}$, represents the stoichiometric amount of oxidizer required for complete stoichiometric reaction. As a result, each of these terms has a

value of unity. Thus, from the scaled oxidizer expression, the following relationship appears.

$$Y_o = \sigma_{f,o} Y_f \tag{108}$$

This process can also be performed for the product species concentration as well. Thus solution of the fuel species equation allows for easy determination the remaining reaction species. With an understanding of the scaling process, though a bit more involved, if it were desired to perform a study upon a system that is not in stoichiometry, this analysis could be extended for use in this case.

4.5 – Derivation of the Steady and Unsteady Governing Equations

To solve the dimensionless governing equations (equations set 96-98), a perturbation expansion process was performed to separate the equations into sets of time independent steady equations and time dependent unsteady equation. Each of the resulting sets of steady and unsteady conservation of mass, energy, and species equations can then be solved individually for the steady and unsteady velocity, temperature and species profiles.

To achieve this, the following first order perturbation expansions for a small magnitude pressure disturbance, ε, were inserted into the equations [75, 77].

$$\begin{aligned} p(t) &= 1 + \varepsilon e^{i\omega t} \\ T(x,t) &= \overline{T}(x) + \varepsilon \tau(x) e^{i\omega t} \\ u(x,t) &= \overline{u}(x) + \varepsilon v(x) e^{i\omega t} \\ Y_f(x,t) &= \overline{Y}_f(x) + \varepsilon Y(x) e^{i\omega t} \end{aligned} \tag{109}$$

The first terms in each of the above equations represent the time independent steady state parameters. The mean pressure, $\bar{P}(x)$, is taken to be unity to simplify the analysis, which is acceptable since the pressure gradient is assumed to be negligible at the scale of the flame thickness. Additionally, since the pressure wavelength in the combustor is always much larger than the flame thickness, the oscillatory pressure is assumed to be just a function of time in the region of the flame. Thus, this assumption implies that the steady pressure is not only time independent but also position independent and is effectively constant across the flame. However, the assumption would break down if the flame length became large due to the introduction of mixing or diffusion, or if the flame thickness were to become a significant percentage of the imposed pressure oscillation wavelength, i.e., at very high frequencies. To avoid this limit, only premixed flames were considered and the oscillatory frequencies were constrained to lower values, i.e., less than a nondimensional frequency of ten.

The symbols $\nu, \tau,$ and Y in the second term represent the position dependent oscillatory components of the velocity, temperature, and fuel species, respectively. The exponential multiplier represents that each position dependent function is also a time oscillatory parameter with frequency, ω. Each of the position dependent parameters can also be broken down into its exponential form, as discussed in Chapter 5.

4.5.1 – Steady Equations

The steady state equations can be developed by application of the above perturbation expansions to the dimensionless governing equations (equations 96-98). Removing the time dependent terms, the following expansions result. Since it is assumed

that the flame is one-dimensional, the equations are expressed as ordinary differential equations rather than in partial differential form as shown in equations 96-98.

$$\begin{aligned}
&\frac{d\left[\rho\left(\bar{u}(x)+\varepsilon v(x)e^{i\omega t}\right)\right]}{dx}=0\\
&\frac{d\left(\bar{T}(x)+\varepsilon\tau(x)e^{i\omega t}\right)}{dx}-\frac{d^2\left(\bar{T}(x)+\varepsilon\tau(x)e^{i\omega t}\right)}{dx^2}=\bar{w}q\\
&\frac{d\left(\bar{Y}_f(x)+\varepsilon Y(x)e^{i\omega t}\right)}{dx}-\frac{d^2\left(\bar{Y}_f(x)+\varepsilon Y(x)e^{i\omega t}\right)}{dx^2}=\bar{w}
\end{aligned} \tag{110}$$

Only focusing upon the time independent steady terms, the following equations result for the steady conservation of mass, energy, and species equations [75, 77].

$$\frac{d(\rho u)}{dx}=0 \tag{111}$$

$$\frac{d\bar{T}}{dx}-\frac{d^2\bar{T}}{dx^2}=\bar{w}q \tag{112}$$

$$\frac{d\bar{Y}_f}{dx}-\frac{d^2\bar{Y}_f}{dx^2}=\bar{w} \tag{113}$$

4.5.1.1 – Conservation of Mass Equation

Useful results for the velocity can readily be obtained from the conservation of mass equation. Through a straightforward manipulation of the equation, it can be shown that the steady state dimensionless velocity is equivalent to the steady state dimensionless temperature.

Noting that the density, ρ, in equation 111 is expanded as follows,

$$\rho=\frac{1+\varepsilon e^{i\omega t}}{\bar{T}(x)+\varepsilon\tau(x)e^{i\omega t}} \tag{114}$$

with a mean dimensionless pressure of unity, the steady state density can be seen to be the reciprocal of the mean temperature.

$$\bar{\rho} = \frac{1}{\bar{T}} \tag{115}$$

This can also be seen from rearranging the dimensionless equation of state.

Through integration of the conservation of mass equation it can be seen that the mass flow rate has a constant value due to the earlier assumption of constant chamber pressure and is unity due to the dimensionless form. The mean velocity is seen to be equivalent to the mean temperature as shown below.

$$\bar{\rho}\bar{u} = \bar{m} = 1 \quad \Rightarrow \quad \bar{u} = \frac{1}{\bar{\rho}} = \frac{1}{\left(1/\bar{T}\right)} = \bar{T} \tag{116}$$

Thus, the numerical solution to the steady state problem has been simplified such that the solution to the velocity profile can be obtained through determination of the temperature profile.

4.5.1.2 – Conservation of Energy and Species Equations

To obtain the solutions to the temperature and species profiles the conservation of mass and species equations, shown again below, can be solved.

$$\begin{aligned} \frac{d\bar{T}}{dx} - \frac{d^2\bar{T}}{dx^2} &= \bar{w}q \\ \frac{d\bar{Y}_f}{dx} - \frac{d^2\bar{Y}_f}{dx^2} &= -\bar{w} \end{aligned} \tag{117}$$

As second order differential equations, their solution is not as direct as the conservation of mass equation and requires the use of a numerical technique. However, it can be seen

that they have a very similar form to one another. Through an expression of equivalency, the species equation can be adapted into the same form as the temperature equation, making it only necessary to solve for the temperature profile to obtain a solution for both parameters.

Using the principle of conservation of energy across the laminar flame, the temperature and species equations can be related. From the discussion in Section 4.4 of complete reaction of species, assuming no heat loss and constant specific heat, the following expression relation results [78]:

$$C_p\left(T_\infty - T_o\right) = q_c Y_f \tag{118}$$

This is simply a statement that all of the heat released during the reaction process is used to increase the temperature of incoming gasses from their initial freestream value to a final temperature upon complete consumption of the stoichiometric fuel species.

Through use of the nondimensionalizing scaling parameters (equation 97) for heat and temperature, upon rearrangement, the following expression of equivalency results.

$$\bar{Y}_f = \frac{1-\bar{T}}{q} \tag{119}$$

Through application of this relationship it can be seen that in just a couple of manipulations the species fraction equation can be made into the temperature equation, the second and first equations in equation set 117, respectively.

$$\frac{d\left(\frac{\left(1-\bar{T}\right)}{q}\right)}{dx} - \frac{d^2\left(\frac{\left(1-\bar{T}\right)}{q}\right)}{dx^2} = -\bar{w} \tag{120}$$

$$-\frac{1}{q}\frac{d\overline{T}}{dx}+\frac{1}{q}\frac{d^2\overline{T}}{dx^2}=-\overline{w} \tag{121}$$

$$\frac{d\overline{T}}{dx}-\frac{d^2\overline{T}}{dx^2}=\overline{w}q \tag{122}$$

Upon some rearrangement and simplification, the reaction rate can be expressed in the following form, where E is known as the activation temperature.

$$w=BjT^{\partial}\left(\frac{p}{T}\right)^{n}Y_f^2e^{-\left(E/T\right)} \tag{123}$$

$$E=\frac{E^*}{RT_{\infty}}\ where\ \frac{E^*}{R}=T_{activation} \tag{124}$$

The dimensionless activation energy represents the amount of energy required to initiate the chemical reaction. It is developed by the ratio of the activation temperature to the temperature at the flame edge. The activation energy is an experimentally derived parameter that is used in the Arrhenius equation.

Replacing Y_f with equation 119 and inserting the reaction rate, w, from equation 123 into equation 122, the following single equation results to be solved for the steady state temperature profile.

$$\frac{d^2\overline{T}}{dx^2}=\frac{d\overline{T}}{dx}-\left(\frac{B}{q}j\right)\left(\frac{1-\overline{T}}{\overline{T}}\right)^2e^{-\left(E/T\right)} \tag{125}$$

Using the boundary conditions, discussed in Section 5.1, this equation can then be used to determine the steady velocity and fuel species fraction profiles. The resulting numerical solution will be discussed in Chapter 5.

4.5.2 – Unsteady Equations

The derivation of the unsteady equations is not nearly as simple as it was for steady state equations. Before the equations can be fully expanded, remembering the above expressions representing the oscillatory properties,

$$\begin{aligned} p(t) &= 1 + \varepsilon e^{i\omega t} \\ T(x,t) &= \overline{T}(x) + \varepsilon\tau(x)e^{i\omega t} \\ u(x,t) &= \overline{u}(x) + \varepsilon v(x)e^{i\omega t} \\ Y_f(x,t) &= \overline{Y_f}(x) + \varepsilon Y(x)e^{i\omega t} \end{aligned} \tag{126}$$

other key variables such as the density, ρ, velocity, u, and mass flow rate, m, can be expanded as follows.

$$\begin{aligned} \rho(t) &= \frac{p(t)}{T(x,t)} = \frac{1+\varepsilon e^{i\omega t}}{\overline{T}(x)+\varepsilon\tau e^{i\omega t}} = \frac{1}{\overline{T}}\left(1+\varepsilon e^{i\omega t}\right)\left(1+\varepsilon\frac{\tau}{\overline{T}}e^{i\omega t}\right)^{-1} \\ &= \frac{1}{\overline{T}}\left(1+\varepsilon e^{i\omega t}\right)\left(1+\varepsilon\frac{\tau}{\overline{T}}e^{i\omega t}+O\left(\varepsilon^2\right)\right) \\ &= \frac{1}{\overline{T}}\left(1+\varepsilon\left(1-\frac{\tau}{\overline{T}}\right)e^{i\omega t}+O\left(\varepsilon^2\right)\right) = \frac{1}{\overline{T}}+\varepsilon\frac{1}{\overline{T}}\left(1-\frac{\tau}{\overline{T}}\right)e^{i\omega t}+O\left(\varepsilon^2\right) \end{aligned} \tag{127}$$

$$u(x,t) = \overline{u}(x) + \varepsilon v e^{i\omega t} = \overline{T}(x) + \varepsilon v e^{i\omega t} \tag{128}$$

$$\begin{aligned} m = \rho u &= \left(\frac{1}{\overline{T}}+\varepsilon\frac{1}{\overline{T}}\left(1-\frac{\tau}{\overline{T}}\right)e^{i\omega t}\right)\left(\overline{T}+\varepsilon v e^{i\omega t}\right) \\ &= \left(1+\varepsilon\left(1-\frac{\tau}{\overline{T}}\right)e^{i\omega t}\right)\left(1+\varepsilon\frac{v}{\overline{T}}e^{i\omega t}\right) \\ &= 1+\varepsilon\left(1-\frac{\tau}{\overline{T}}+\frac{v}{\overline{T}}\right)e^{i\omega t}+O\left(\varepsilon^2\right) \end{aligned} \tag{129}$$

4.5.2.1 – Derivation of the Unsteady Conservation of Mass Equation

Applying the results obtained in equations 127 to 129, the continuity equation

$$\frac{d\rho}{dt} + \frac{d\rho u}{dx} = 0 \tag{130}$$

can be expanded as shown in the following steps. The first and second derivative terms are developed as follows.

$$\begin{aligned} \frac{d\rho}{dt} &= \frac{d}{dt}\left(\frac{1}{\overline{\overline{T}}} + \varepsilon \frac{1}{\overline{\overline{T}}}\left(1 - \frac{\tau}{\overline{\overline{T}}} \right) e^{i\omega t} \right) = i\omega \frac{1}{\overline{\overline{T}}}\left(1 - \frac{\tau}{\overline{\overline{T}}} \right) e^{i\omega t} \\ \frac{d\rho u}{dx} &= \frac{d}{dx}\left(1 + \varepsilon\left(1 - \frac{\tau}{\overline{\overline{T}}} + \frac{\nu}{\overline{\overline{T}}} \right) e^{i\omega t} \right) = \frac{d}{dx}\left(\frac{-\tau + \nu}{\overline{T}} \right) e^{i\omega t} \end{aligned} \tag{131}$$

Substituting these expressions into the conservation of mass equation, dividing out the exponential multiplier, and carrying through the second derivative leads to the following steps.

$$\begin{aligned} & i\omega \frac{1}{\overline{\overline{T}}}\left(1 - \frac{\tau}{\overline{\overline{T}}} \right) + \frac{1}{\overline{\overline{T}}}\left(-\frac{d\tau}{dx} + \frac{d\nu}{dx} \right) - \frac{\left(-\tau + \nu \right)}{\overline{T}^2} \frac{d\overline{T}}{dx} = 0 \\ & = i\omega\left(1 - \frac{\tau}{\overline{\overline{T}}} \right) + \left(\frac{d\nu}{dx} - \frac{d\tau}{dx} \right) - \frac{\left(\nu - \tau \right)}{\overline{T}} \frac{d\overline{T}}{dx} = 0 \end{aligned} \tag{132}$$

Direct rearrangement of the above expression results in the final form of the unsteady conservation of mass equation.

$$\frac{d\nu}{dx} - \frac{d\tau}{dx} + \frac{1}{\overline{T}} \frac{d\overline{T}}{dx} \tau - \frac{1}{\overline{\overline{T}}} \frac{d\overline{T}}{dx} \nu + i\omega - i\omega \frac{\tau}{\overline{\overline{T}}} = 0 \tag{133}$$

4.5.2.2 – Derivation of the Unsteady Conservation of Energy Equation

The next equation to be expanded is the energy equation, shown again below. It requires a greater amount of algebraic manipulation than the conservation of mass equation.

$$\rho\frac{dT}{dt}+\rho u\frac{dT}{dx}-\frac{d^2T}{dx^2}-\frac{\gamma-1}{\gamma}\frac{dp}{dt}=wq \tag{134}$$

Each of the four derivative terms can be expanded as follows.

$$\begin{aligned}
&\frac{dT}{dx}=\frac{d}{dx}\left(\overline{T}+\varepsilon\tau e^{i\omega t}\right)=\frac{d\overline{T}}{dx}+\varepsilon\frac{d\tau}{dx}e^{i\omega t}\\
&\Rightarrow \rho u\frac{dT}{dx}=\left(1+\varepsilon\left(1+\frac{\tau}{\overline{T}}+\frac{\nu}{\overline{T}}\right)e^{i\omega t}\right)\left(\frac{d\overline{T}}{dx}+\varepsilon\frac{d\tau}{dx}e^{i\omega t}\right)\\
&\Rightarrow \rho u\frac{dT}{dx}=\frac{d\overline{T}}{dx}+\varepsilon\frac{d\overline{T}}{dx}\left(1-\frac{\tau}{\overline{T}}+\frac{\nu}{\overline{T}}\right)e^{i\omega t}+\varepsilon\frac{d\tau}{dx}e^{i\omega t}+O\left(\varepsilon^2\right)
\end{aligned} \tag{135}$$

$$\begin{aligned}
&\frac{dT}{dt}=\frac{d}{dt}\left(\overline{T}+\varepsilon\tau e^{i\omega t}\right)=i\omega\left(\varepsilon\frac{d\tau}{dx}e^{i\omega t}\right)\\
&\Rightarrow \rho\frac{dT}{dt}=i\omega\left(\frac{1}{\overline{T}}+\varepsilon\frac{1}{\overline{T}}\left(1-\frac{\tau}{\overline{T}}\right)e^{i\omega t}\right)\left(\varepsilon\frac{d\tau}{dx}e^{i\omega t}\right)=\varepsilon\frac{1}{\overline{T}}i\omega\frac{d\tau}{dx}e^{i\omega t}+O\left(\varepsilon^2\right)
\end{aligned} \tag{136}$$

$$\frac{d^2T}{dx^2}=\frac{d}{dx}\left(\frac{d\overline{T}}{dx}+\varepsilon\frac{d\tau}{dx}e^{i\omega t}\right)=\frac{d^2\overline{T}}{dx^2}+\varepsilon\frac{d^2\tau}{dx^2}e^{i\omega t}+O(\varepsilon^2) \tag{137}$$

$$\frac{\gamma-1}{\gamma}\frac{dp}{dt}=\frac{\gamma-1}{\gamma}\left(1+\varepsilon e^{i\omega t}\right) \tag{138}$$

The expansion for the product of the heat of combustion and the reaction rate

$$wq=qBjT^{\delta}\left(\frac{p}{T}\right)^n Y_f^2 e^{\left(-E/T\right)}=qBj\left(\overline{T}+\varepsilon\tau e^{i\omega t}\right)^{\delta-n}\left(1+\varepsilon e^{i\omega t}\right)^n\left(\overline{Y}_f(x)+\varepsilon Y e^{i\omega t}\right)^2 e^{\left(-E/T\right)} \tag{139}$$

requires several steps to reach its final form. Before simplifying further, the exponential term is expanded as follows.

$$e\left(-E/T\right)=e^{\left(-E/\bar{T}\left(1-\varepsilon\frac{\tau}{\bar{T}}e^{i\omega t}\right)\right)}=e^{-\frac{E}{\bar{T}}}\varepsilon^{\frac{E}{\bar{T}^2}\tau e^{i\omega t}}=\left(1+\varepsilon\frac{E}{\bar{T}^2}\tau e^{i\omega t}+O\left(\varepsilon^2\right)\right)e^{\frac{E}{\bar{T}}} \tag{140}$$

Plugging this into the above product results in the following manipulations.

$$\begin{aligned} &wq=qBjT^{\delta}\left(\frac{p}{T}\right)^n Y_f^2 e^{\left(-E/T\right)} \\ &\Rightarrow qBje^{\frac{E}{\bar{T}}}\left(\bar{T}+\varepsilon\tau e^{i\omega t}\right)^{\delta-n}\left(1+\varepsilon e^{i\omega t}\right)^n\left(\bar{Y}_f^2+\varepsilon 2\bar{Y}_f Y e^{i\omega t}+O\left(\varepsilon^2\right)\right)\left(1+\varepsilon\frac{E}{\bar{T}^2}\tau e^{i\omega t}\right) \end{aligned} \tag{141}$$

$$\begin{aligned} &=qBj\bar{Y}_f^2\bar{T}^{\delta-n}e^{\frac{E}{\bar{T}}}\left(1+\varepsilon(\delta-n)\frac{\tau}{\bar{T}}\right)(1+\varepsilon n)\left(1+\varepsilon\frac{E}{\bar{T}^2}\tau\right)\left(1+\varepsilon\left(2\frac{Y}{\bar{Y}_f}\right)\right) \\ &=\bar{qw}\left(1+\varepsilon(\delta-n)\frac{\tau}{\bar{T}}+\varepsilon n+\varepsilon\frac{E}{\bar{T}^2}\tau+\varepsilon\left(n\frac{Y}{\bar{Y}_f}\right)+O(\varepsilon^2)\right) \end{aligned} \tag{142}$$

Inserting all of the above expansions into the energy equation from 135-138 and 142

$$\begin{aligned} &\Rightarrow\frac{1}{\bar{T}}i\omega\tau+\frac{d\bar{T}}{dx}\left(1-\frac{\tau}{\bar{T}}+\frac{\nu}{\bar{T}}\right)+\frac{d\tau}{dx}-\frac{d^2\tau}{dx^2}-\frac{\gamma-1}{\gamma}i\omega \\ &=q\bar{w}\left((\delta-n)\frac{\tau}{\bar{T}}+n+\frac{E}{\bar{T}^2}\tau+\left(n\frac{Y}{\bar{Y}_f}\right)\right) \end{aligned} \tag{143}$$

results in the following form for the unsteady energy equation.

$$\begin{aligned} &\frac{d^2\tau}{dx^2}-\frac{d\tau}{dx}+\left[\frac{1}{\bar{T}}\frac{d\bar{T}}{dx}+\frac{q\bar{w}}{\bar{T}}\left(\delta-n+\frac{E}{\bar{T}}\right)\right]\tau \\ &-\frac{1}{\bar{T}}i\omega\tau+\left(nq\frac{\bar{w}}{\bar{Y}_f}\right)Y-\left(\frac{1}{\bar{T}}\frac{d\bar{T}}{dx}\right)\nu-q\bar{w}n-\frac{d\bar{T}}{dx}+\frac{\gamma-1}{\gamma}i\omega=0 \end{aligned} \tag{144}$$

4.5.2.3 – Derivation of the Unsteady Conservation of Species Equation

The species equation

$$\rho \frac{dY_f}{dt} + \rho u \frac{dY_f}{dx} - \frac{d^2 Y_f}{dx^2} = w \tag{145}$$

can be expanded as shown in the following steps. Each of the terms can be expanded as follows. The expression for the reaction rate in equation 149 results from division of equation 142 by q.

$$\begin{aligned}
\rho \frac{dY_f}{dt} &= \left(\frac{1}{\bar{T}} + \varepsilon \frac{1}{\bar{T}} \left(1 - \frac{\tau}{\bar{T}} \right) e^{i\omega t} \right) i\omega \varepsilon Y e^{i\omega t} \\
\rho u \frac{dY_f}{dx} &= \left(1 + \varepsilon \left(1 + \frac{\tau}{\bar{T}} + \frac{\nu}{\bar{T}} \right) e^{i\omega t} \right) \left(\frac{d\bar{Y}_f}{dx} + \varepsilon \frac{dY}{dx} e^{i\omega t} \right) \\
&= \frac{d\bar{Y}_f}{dx} + \varepsilon \frac{d\bar{Y}_f}{dx} \left(1 + \frac{\tau}{\bar{T}} + \frac{\nu}{\bar{T}} \right) + \varepsilon \frac{dY}{dx} e^{i\omega t} + O\left(\varepsilon^2\right)
\end{aligned} \tag{146}$$

$$\frac{d^2 Y_f}{dx^2} = \left(\frac{d\bar{Y}_f}{dx} + \varepsilon \frac{dY}{dx} e^{i\omega t} \right)^2 = \frac{d^2 \bar{Y}_f}{dx^2} + O\left(\varepsilon^2\right) \tag{147}$$

$$\frac{dT}{dx} = \frac{d}{dx}\left(\bar{T} + \varepsilon \tau e^{i\omega t} \right) = \frac{d\bar{T}}{dx} + \varepsilon \frac{d\tau}{dx} e^{i\omega t} \tag{148}$$

$$w = \bar{w} \left(1 + \varepsilon (\delta - n) \frac{\tau}{\bar{T}} + \varepsilon n + \varepsilon \frac{E}{\bar{T}^2} \tau + \varepsilon \left(n \frac{Y}{\bar{Y}_f} \right) \right) \tag{149}$$

Finally, inserting all of the above expansions into the species equation results in the following form for the unsteady species equation.

$$\frac{1}{\bar{T}} i\omega Y + \frac{d\bar{Y}_f}{dx} \left(1 + \frac{\tau}{\bar{T}} + \frac{\nu}{\bar{T}} \right) + \frac{dY}{dx} - \frac{d^2 \bar{Y}_f}{dx^2} = \bar{w} \left((\delta - n) \frac{\tau}{\bar{T}} + n + \frac{E}{\bar{T}^2} \tau + \left(n \frac{Y}{\bar{Y}_f} \right) \right) \tag{150}$$

Equation 133, 144, and 150 can be used to solve for the first order oscillatory components of the velocity, ν, temperature, τ, and fuel species Y, respectively.

Note that in equations 127-150, the appearance of the term $O(\varepsilon^2)$ represents higher order oscillatory terms generated during the expansion process but not retained in the final developed unsteady equations. A complete expansion of the initial equations into steady and unsteady parts would result in a combination of both first order as well as second order terms. However, since the focus of this effort is on the linear terms and not the nonlinear terms, the higher order terms were not included in the above expansion process. These terms can be included in future work if it is desired to extend this analysis to examine the effects of the second order oscillatory heat release effects.

4.5.2.4 – Expansion of the Unsteady Equations Into Real and Imaginary Form

The unsteady equations, shown again below, can now be used to determine the oscillatory components of the velocity, temperature, and fuel species concentration.

$$\frac{d\nu}{dx} - \frac{d\tau}{dx} + \frac{1}{\bar{T}}\frac{d\bar{T}}{dx}\tau - \frac{1}{\bar{T}}\frac{d\bar{T}}{dx}\nu + i\omega - i\omega\frac{\tau}{\bar{T}} = 0 \tag{151}$$

$$\begin{aligned}&\frac{d^2\tau}{dx^2} - \frac{d\tau}{dx} + \left[\frac{1}{\bar{T}}\frac{d\bar{T}}{dx} + \frac{q\bar{w}}{\bar{T}}\left(\delta - n + \frac{E}{\bar{T}}\right)\right]\tau \\ &-\frac{1}{\bar{T}}i\omega\tau + \left(nq\frac{\bar{w}}{\bar{Y}_f}\right)Y - \left(\frac{1}{\bar{T}}\frac{d\bar{T}}{dx}\right)\nu + \left[q\bar{w}n - \frac{d\bar{T}}{dx}\right] + \frac{\gamma-1}{\gamma}\omega = 0\end{aligned} \tag{152}$$

$$\frac{1}{\bar{T}}i\omega Y + \frac{d\bar{Y}_f}{dx}\left(1 + \frac{\tau}{\bar{T}} + \frac{\nu}{\bar{T}}\right) + \frac{dY}{dx} - \frac{d^2Y}{dx^2} = \bar{w}\left[(\delta - n)\frac{\tau}{\bar{T}} + n + \frac{E}{\bar{T}^2}\tau + \left(n\frac{Y}{\bar{Y}_f}\right)\right] \tag{153}$$

Using boundary conditions in Section 5.2, equations 151-153 are solved by expansion through use of the oscillatory properties of the unsteady velocity, temperature, and fuel species (ν, τ, and Y). As with all sinusoidally fluctuating functions, these unsteady variables can be expressed as follows in terms of their respective amplitudes and phase angles, ϕ.

$$\begin{aligned} \tau &= \tau_{amplitude}\left(\cos\phi_{\tau} + i\sin\phi_{\tau}\right) \\ \nu &= \nu_{amplitude}\left(\cos\phi_{\nu} + i\sin\phi_{\nu}\right) \\ Y &= Y_{amplitude}\left(\cos\phi_{Y} + i\sin\phi_{Y}\right) \end{aligned} \tag{154}$$

However, rather than using these trigonometric forms, it is convenient to represent the quantities in terms of real and imaginary components when working with oscillatory properties.

This is a common practice in solving oscillatory engineering problems; for example, oscillatory properties are often expressed in terms of real and imaginary components when working with electrical circuits and vibrations problems. This practice is used because it greatly simplifies the required mathematics used in the expansion process. If computations are performed employing such functions as sine and cosine, this often requires extensive mathematical manipulation through use of trigonometric identities to arrive at a solution. It is also necessary to make certain that no quadrant issues arise when performing operations between oscillatory variables. However, when performing the same manipulations using of real and imaginary components, the mathematics is simplified since there are no trigonometric functions. Thus, the oscillatory properties can be expressed in terms of real and imaginary components as follows.

$$\tau = \tau^{(r)} + i\tau^{(i)}$$
$$v = v^{(r)} + iv^{(i)} \tag{155}$$
$$Y = Y^{(r)} + iY^{(i)}$$

These expressions can be inserted into equations 151-153. Upon direct separation of each of the resulting equations into real and imaginary equations, the following sets of real and imaginary unsteady mass, energy, and fuel species equations are developed. These can be solved to obtain the real and imaginary components of the unsteady temperature, velocity, and fuel species solutions.

$$\frac{dv^{(r)}}{dx} = \frac{d\tau^{(r)}}{dx} - \frac{1}{\bar{T}}\frac{d\bar{T}}{dx}\tau^{(r)} + \frac{1}{\bar{T}}\frac{d\bar{T}}{dx}v^{(r)} - i\omega\frac{\tau^{(r)}}{\bar{T}}$$
$$\frac{dv^{(i)}}{dx} = \frac{d\tau^{(i)}}{dx} - \frac{1}{\bar{T}}\frac{d\bar{T}}{dx}\tau^{(i)} + \frac{1}{\bar{T}}\frac{d\bar{T}}{dx}v^{(i)} - i\omega - i\omega\frac{\tau^{(i)}}{\bar{T}} \tag{156}$$

$$\frac{d^2\tau^{(r)}}{dx^2} = \frac{d\tau^{(r)}}{dx} - \left[\frac{1}{\bar{T}}\frac{d\bar{T}}{dx} + \frac{q\bar{w}}{\bar{T}}\left(\delta - n + \frac{E}{\bar{T}}\right)\right]\tau^{(r)} - \frac{1}{\bar{T}}i\omega\tau^{(r)} - \left(nq\frac{\bar{w}}{\bar{Y}_f}\right)Y^{(r)} + \left(\frac{1}{\bar{T}}\frac{d\bar{T}}{dx}\right)v^{(r)} - \left[q\bar{w}n - \frac{d\bar{T}}{dx}\right] \tag{157}$$
$$\frac{d^2\tau^{(i)}}{dx^2} = \frac{d\tau^{(i)}}{dx} - \left[\frac{1}{\bar{T}}\frac{d\bar{T}}{dx} + \frac{q\bar{w}}{\bar{T}}\left(\delta - n + \frac{E}{\bar{T}}\right)\right]\tau^{(i)} - \frac{1}{\bar{T}}i\omega\tau^{(i)} - \left(nq\frac{\bar{w}}{\bar{Y}_f}\right)Y^{(i)} + \left(\frac{1}{\bar{T}}\frac{d\bar{T}}{dx}\right)v^{(i)} - \frac{\gamma-1}{\gamma}i\omega$$

$$\frac{d^2Y^{(r)}}{dx^2} = \frac{dY^{(r)}}{dx} + n\bar{w}\frac{Y^{(r)}}{\bar{Y}_f} + \frac{1}{\bar{T}}i\omega Y^{(r)} - \left[\frac{1}{\bar{T}}\frac{d\bar{Y}_f}{dx} - \frac{\bar{w}}{\bar{T}}\left(\frac{E}{\bar{T}} - (\delta - n)\right)\right]\tau^{(r)} + \frac{d\bar{Y}_f}{dx} + \frac{v^{(r)}}{\bar{T}}\frac{d\bar{Y}_f}{dx} + n\bar{w}$$
$$\frac{d^2Y^{(i)}}{dx^2} = \frac{dY^{(i)}}{dx} + n\bar{w}\frac{Y^{(i)}}{\bar{Y}_f} + \frac{1}{\bar{T}}i\omega Y - \left[\frac{1}{\bar{T}}\frac{d\bar{Y}_f}{dx} - \frac{\bar{w}}{\bar{T}}\left(\frac{E}{\bar{T}} - (\delta - n)\right)\right]\tau^{(i)} + \frac{v^{(i)}}{\bar{T}}\frac{d\bar{Y}_f}{dx} \tag{158}$$

From these components, an oscillatory amplitude and phase angle can be determined for each of the oscillating velocity, temperature, and fuel species

distributions. As seen in the following generic equations, the oscillatory amplitude can be calculated simply by taking the square root of the sum of the squares of the real and imaginary components for each parameter. The phase angle is calculated by taking the inverse tangent of the ratio of the imaginary and real components.

$$A_{amplitude} = \sqrt{A_{real}^2 + A_{imaginary}^2} \tag{159}$$

$$\Phi_A = \tan^{-1}\left(\frac{A_{imaginary}}{A_{real}}\right) \tag{160}$$

CHAPTER 5 – NUMERICAL TECHNIQUE

This chapter presents the methodology performed to solve for the unsteady combustion heat release linear growth rate. Following on the development of the steady and unsteady governing equations in the previous chapter, the numerical techniques developed in solving these nonlinear sets of ordinary differential equations are presented. It is explained how the equations for both orders must be separated into first order ODE's. It is first shown that since the solution is performed for a dimensionless system, the steady state solution must first be solved for determination of the combustion kinetics and to determine the combustion flame length. This steady state solution is then solved again in conjunction with the unsteady equations at each step in the combustion zone. A detailed discussion of the numerical technique for solving the system of equations is presented. The source code developed in Matlab is included in Appendix A. It is then shown how an expression for determination of the unsteady heat release is developed by the author in an expansion process similar to that shown in Chapter 4, followed by a discussion of the time-averaging performed for evaluation of the growth rate integral. The chapter concludes with discussion of a developed expression for dimensionalizing the heat release for determination of dimensional results.

The dimensionless steady and unsteady equations presented in Chapter 4 are solved through the use of two separate numerical routines. The steady state equations are first solved independently to determine the dimensionless reaction rate profile, the flame length, and steady solutions. These steady equations are again solved in conjunction with the unsteady equations to obtain the dimensionless unsteady property solutions. These

quantities are then used in determination of the dimensionless steady and unsteady heat release in the system. Then the dimensionless linear growth rate due to unsteady combustion heat release can be determined through evaluation of the integral in equation 86. These solutions can be put back into dimensional form upon completion of the dimensionless analysis.

Upon completion of this work, it is anticipated that these models will be incorporated into the general energy method for determination of the stability characteristics for a given system. This is shown in Figure 21, which lays out a generalized flowchart for the overall energy method. This shows the individual solutions to the flow fields leading to the linear stability model. These stability solutions then lead to the nonlinear stability model, from which results can be combined with those of the flow field analyses to give a detailed dynamic flow solution for a given system.

The unsteady combustion heat release growth rate model will be used as one of many linear stability models that combine to determine the total system growth rate for a given system. Figure 22 shows the overall flow of the numerical procedure for determination of the heat release growth rate, as discussed above. A discussion of the steady and unsteady models will be presented in the following sections. Figure 23 shows the flow of the unsteady numerical analysis that was performed.

5.1 – Steady Solution

The equation for calculation of the steady temperature profile (equation 125) is a second order ordinary differential equation. It can be solved by reduction to the following set of two first-order equations.

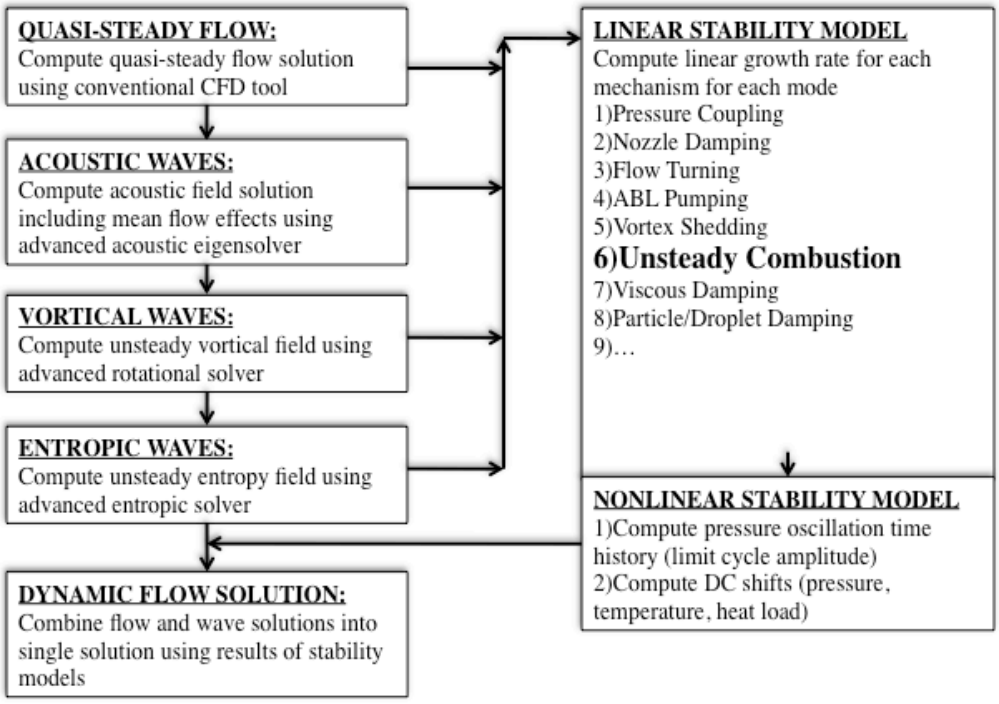

Figure 21. Flowchart For Overall Energy Method

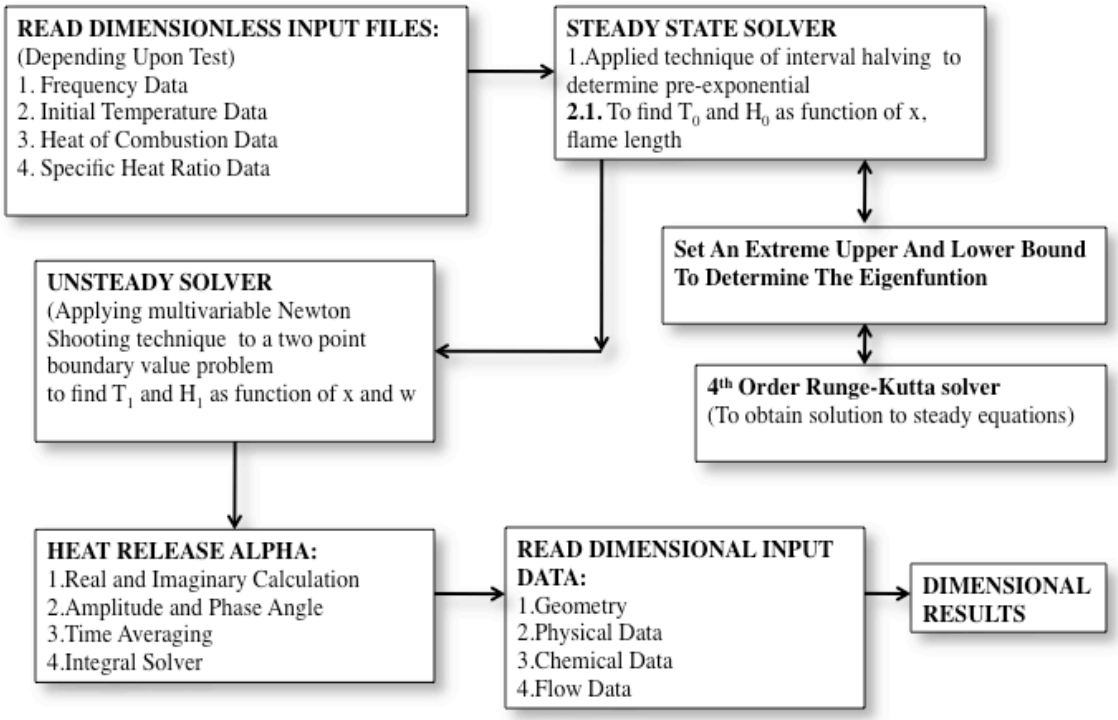

Figure 22. Program Flow Chart For Calculation of Heat Release Growth Rate

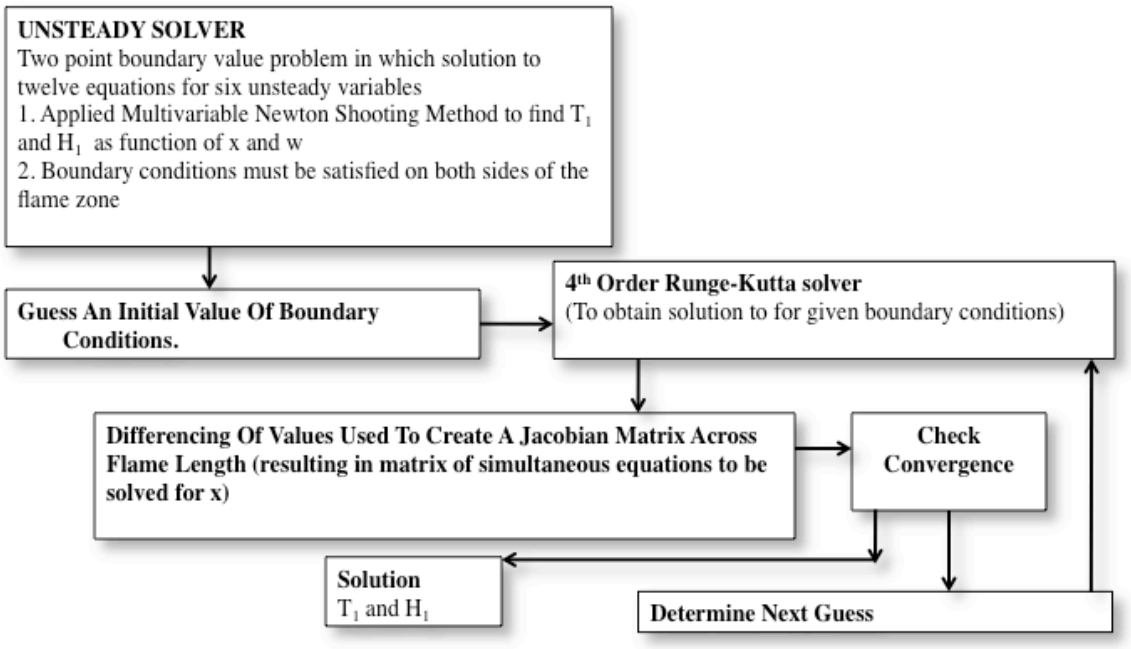

Figure 23. Flow Chart For Unsteady Program

$$\frac{d\bar{T}}{dx} = F$$
$$\frac{dF}{dx} = F - \left(\frac{B}{q}j\right)\left(\frac{1-\bar{T}}{\bar{T}}\right)^2 e^{-\left(E/\bar{T}\right)} \tag{161}$$

To obtain a solution to these equations, a fourth order Runge-Kutta solver is employed. The Runge-Kutta method is a commonly used numerical method for obtaining approximate solutions to first-order equations given some initial value of the dependent variable [79]. The procedure uses an approximation to a Taylor polynomial of degree four to add incremental changes to the value of the variable for each time step.

Since this is an initial-value problem solver, before further developing the numerical solution, initial boundary conditions must be defined. Since premixed gas combustion is being modeled, it has been assumed that the combustion begins at some

point downstream of the injector face, after the mixing and vaporization has occurred. Assuming an invisible hard wall boundary at this point, for convenience, the initial temperature can be assumed to be that of the incoming propellant mixture. Furthermore, since mixing and vaporization has occurred, it can be assumed that there is no temperature gradient at the interface, i.e., no upstream heat transfer. This results in the following initial boundary conditions to be used in the Runge-Kutta solver.

In addition to these initial conditions, the temperature and temperature gradient are also known at the edge of the flame (i.e. at infinity). To solve this problem in dimensionless form, the initial temperature was divided by the final flame temperature at infinity. Therefore, in terms of dimensionless variables, the temperature at the edge of the flame must be unity. Also, since the combustion is complete at the edge of the flame, the temperature gradient must be zero at infinity.

$$\begin{aligned} &T = T_{premixed\_initial} \quad @\ \mathrm{x} = 0 \qquad T = T_{premixed\_final} = 1 \quad @\ \mathrm{x} = \infty \\ &\frac{dT}{dx} = 0 \quad @\ \mathrm{x} = 0 \qquad \frac{dT}{dx} = 0 \quad @\ \mathrm{x} = \infty \end{aligned} \tag{162}$$

Both the initial value conditions and those at infinity had to be utilized to obtain the steady solution. In addition to employing the Runge-Kutta method to obtain a steady state solution, knowledge of these flame edge conditions had to be employed in a solving routine to determine the value of the coefficient from the second half of equation 161. This unknown value, **B,** is referred to as an eigenvalue.

$$\mathbf{B} = \left(\frac{B}{q} j \right) \tag{163}$$

This eigenvalue represents the need to determine the Arrhenius reaction rate pre-exponential factor. Since this analysis is performed in dimensionless form, this results in

a generic set of initial conditions that are not specific to any particular reaction. While the Arrhenius pre-exponential factor is determined experimentally for specific real reactions, in this case it is not specified for the generic dimensionless reaction. This unknown eigenvalue is the Arrhenius pre-exponential needed for the specific reaction to produce the specified temperature change. Since the flame edge boundary conditions were known, they were used to obtain the specific Arrhenius pre-exponential value needed to generate the steady solution.

To solve for this eigenvalue the numerical technique known as the Regula Falsi Method was employed [79]. In this case, extreme high and low bounding values for the desired parameter were assumed. An iterative process then occurred in which the Runge-Kutta solver was employed to obtain a solution for the calculated eigenvalue. If the solution did not meet within a specified tolerance of the flame edge conditions, a new eigenvalue was determined based on the difference of the two bounds until a desired tolerance was reached. Upon convergence to a solution, the Runge-Kutta solver is then employed one last time to obtain the final steady state temperature solution.

Through use of this technique, the flame length for the combustion zone was also determined. For each iteration loop, the higher bounding value used for determination of the pre-exponential was assumed at a position one step down from the last. In this case, a step size of 0.1 was used. Upon reaching convergence to the final steady state solution within a tolerance of 0.01, the flame length was determined in this way. The use of a step size of 0.01 was also attempted; however, this only increased the accuracy of the solution by a factor of 10^{-4}, and greatly increased the convergence time. Since this was less than the specified tolerance, it of course also yielded the same flame length value for the case

tested. Thus, to efficiently run a number of cases, the step size of 0.1 was used.

Using this approach and the associated code, the steady temperature, T_0, required in the heat release growth rate integral in equation 86, is then determined at each position within the combustion zone along with the fuel species profiles using equation 119. The results of the steady analysis aid in determination of the steady heat release rate, $\mathscr{H}_0$, as shown in Section 5.3.

5.2 – Unsteady Solution

To determine the profiles of the unsteady properties, the six equations (equations 156-158) in Section 4.5.2 were solved to obtain the real and imaginary components of the oscillatory temperature, τ, velocity, ν, and species, Y_i. This system of equations, assuming n=2 and δ=0 (i.e. second order reaction with a temperature exponent of zero), contains two first-order ODE's for the conservation of mass equation and four second-order ODE's for the conservation of energy and species equations.

Since the unsteady conservation of mass equations, shown again below, are first order ODEs, they can readily be solved for the real and imaginary components of the oscillatory velocity through the implementation of a first order numerical solving routine.

$$\begin{aligned}\frac{d\nu^{(r)}}{dx} &= \frac{d\tau^{(r)}}{dx} - \frac{1}{\bar{\bar{T}}}\frac{d\bar{\bar{T}}}{dx}\tau^{(r)} + \frac{1}{\bar{\bar{T}}}\frac{d\bar{T}}{dx}\nu^{(r)} - i\omega\frac{\tau^{(r)}}{\bar{\bar{T}}} \\ \frac{d\nu^{(i)}}{dx} &= \frac{d\tau^{(i)}}{dx} - \frac{1}{\bar{\bar{T}}}\frac{d\bar{T}}{dx}\tau^{(i)} + \frac{1}{\bar{\bar{T}}}\frac{d\bar{T}}{dx}\nu^{(i)} - i\omega - i\omega\frac{\tau^{(i)}}{\bar{\bar{T}}}\end{aligned} \tag{164}$$

As in the case of the steady state analysis, the method employed was that of a fourth-order Runge-Kutta solver. However, in order to solve for the velocity components, the full system of unsteady equations must be solved concurrently. Thus, it is first

necessary to break the second-order differential equations for energy and species into two first-order equations.

The real and imaginary energy equations,

$$\frac{d^2\tau^{(r)}}{dx^2} = \frac{d\tau^{(r)}}{dx} - \left[\frac{1}{\bar{T}}\frac{d\bar{T}}{dx} + \frac{q\bar{w}}{\bar{T}}\left(\frac{E}{\bar{T}} - 2\right)\right]\tau^{(r)} - \frac{1}{\bar{T}}i\omega\tau^{(r)} - \left(2q\frac{\bar{w}}{\bar{Y}_f}\right)Y^{(r)} + \left(\frac{1}{\bar{T}}\frac{d\bar{T}}{dx}\right)v^{(r)} - \left[2q\bar{w} - \frac{d\bar{T}}{dx}\right] \quad (165)$$
$$\frac{d^2\tau^{(i)}}{dx^2} = \frac{d\tau^{(i)}}{dx} - \left[\frac{1}{\bar{T}}\frac{d\bar{T}}{dx} + \frac{q\bar{w}}{\bar{T}}\left(\frac{E}{\bar{T}} - 2\right)\right]\tau^{(i)} - \frac{1}{\bar{T}}i\omega\tau^{(i)} - \left(2q\frac{\bar{w}}{\bar{Y}_f}\right)Y^{(i)} + \left(\frac{1}{\bar{T}}\frac{d\bar{T}}{dx}\right)v^{(i)} - \frac{\gamma-1}{\gamma}\omega$$

were separated into first order equations as follows. Their solution aids in solving for the oscillatory temperature, τ. First, the derivative of the oscillatory temperature was represented as a function G.

$$\frac{d}{dx}\tau^{(r)} = G^{(r)}$$
$$\frac{d}{dx}\tau^{(i)} = G^{(i)} \quad (166)$$

Then equation 165 was then expressed as the following first order differential equations.

$$\frac{dG^{(r)}}{dx} = G^{(r)} - \left[\frac{1}{\bar{T}}\frac{d\bar{T}}{dx} + \frac{q\bar{w}}{\bar{T}}\left(\frac{E}{\bar{T}} - 2\right)\right]\tau^{(r)} - \frac{1}{\bar{T}}i\omega\tau^{(r)} - \left(2q\frac{\bar{w}}{\bar{Y}_f}\right)Y^{(r)} + \left(\frac{1}{\bar{T}}\frac{d\bar{T}}{dx}\right)v^{(r)} - \left[2q\bar{w} - \frac{d\bar{T}}{dx}\right] \quad (167)$$
$$\frac{dG^{(i)}}{dx} = G^{(i)} - \left[\frac{1}{\bar{T}}\frac{d\bar{T}}{dx} + \frac{q\bar{w}}{\bar{T}}\left(\frac{E}{\bar{T}} - 2\right)\right]\tau^{(i)} - \frac{1}{\bar{T}}i\omega\tau^{(i)} - \left(2q\frac{\bar{w}}{\bar{Y}_f}\right)Y^{(i)} + \left(\frac{1}{\bar{T}}\frac{d\bar{T}}{dx}\right)v^{(i)} - \frac{\gamma-1}{\gamma}\omega$$

These four equations are now in the form to solved for the real and imaginary components of the oscillatory temperature as well as the rate of the change of the oscillatory temperature.

Similarly, the real and imaginary forms of the species equations,

$$\frac{d^2Y^{(r)}}{dx^2} = \frac{dY^{(r)}}{dx} + 2\bar{w}\frac{Y^{(r)}}{\bar{Y}_f} + \frac{1}{\bar{T}}i\omega Y^{(r)} - \left[\frac{1}{\bar{T}}\frac{d\bar{Y}_f}{dx} - \frac{\bar{w}}{\bar{T}}\left(\frac{E}{\bar{T}} - 2\right)\right]\tau^{(r)} + \frac{d\bar{Y}_f}{dx} + \frac{v^{(r)}}{\bar{T}}\frac{d\bar{Y}_f}{dx} + 2\bar{w} \quad (168)$$
$$\frac{d^2Y^{(i)}}{dx^2} = \frac{dY^{(i)}}{dx} + 2\bar{w}\frac{Y^{(i)}}{\bar{Y}_f} + \frac{1}{\bar{T}}i\omega Y - \left[\frac{1}{\bar{T}}\frac{d\bar{Y}_f}{dx} - \frac{\bar{w}}{\bar{T}}\left(\frac{E}{\bar{T}} - 2\right)\right]\tau^{(i)} + \frac{v^{(i)}}{\bar{T}}\frac{d\bar{Y}_f}{dx}$$

were rearranged as follows to determine the oscillatory species. Assuming that the derivative of the oscillatory species concentration could be represented by a function H,

$$\begin{aligned} \frac{d}{dx}Y^{(r)} &= H^{(r)} \\ \frac{d}{dx}Y^{(i)} &= H^{(i)} \end{aligned} \tag{169}$$

equation 160 was expressed as the following first order differential equation.

$$\begin{aligned} \frac{dH^{(r)}}{dx} &= H^{(r)} + 2\bar{w}\frac{Y^{(r)}}{\bar{Y}_f} + \frac{1}{\bar{T}}i\omega Y^{(r)} - \left[\frac{1}{\bar{T}}\frac{d\bar{Y}_f}{dx} - \frac{\bar{w}}{\bar{T}}\left(\frac{E}{\bar{T}} - 2\right)\right]\tau^{(r)} + \frac{d\bar{Y}_f}{dx} + \frac{v^{(r)}}{\bar{T}}\frac{d\bar{Y}_f}{dx} + 2\bar{w} \\ \frac{dH^{(i)}}{dx} &= H^{(i)} + 2\bar{w}\frac{Y^{(i)}}{\bar{Y}_f} + \frac{1}{\bar{T}}i\omega Y^{(i)} - \left[\frac{1}{\bar{T}}\frac{d\bar{Y}_f}{dx} - \frac{\bar{w}}{\bar{T}}\left(\frac{E}{\bar{T}} - 2\right)\right]\tau^{(i)} + \frac{v^{(i)}}{\bar{T}}\frac{d\bar{Y}_f}{dx} \end{aligned} \tag{170}$$

These four equations, along with the other six equations (equations 164, 166-167) yield ten equations to be solved for the real and imaginary components of the oscillatory velocity, temperature, and species, as well as the unsteady temperature and species derivatives. Along with these ten equations, the two steady equations (equations 161) were incorporated into the unsteady numerical routine. They were again included here because the above unsteady equations require the steady results at each step in the calculation along the flame length. The separate routine for the steady state was first performed not only to determine the necessary reaction rate coefficient, but also to obtain the flame length over which the combustion was occurring.

To aid in understanding the relationship between the variables (considering that twelve equations were solved), a matrix relating variables used in these equations is provided in the format: [a] = [b][x] + [c]. The [x] values are the parameters for which a solution is being calculated while the [a] values are their changes across each step in the flame.

Looking at the equations in matrix form, it can be seen more clearly how the solutions to each of the unsteady variables are interdependent upon the solution of the other variables. This presentation also shows dependence upon the steady state temperature and its derivative; not only do they occur as some of the [x] variables, but they are also multipliers to several terms in the [b] matrix.

When the Runge-Kutta technique is employed to obtain the solutions for the twelve system variables, it is this matrix that is used to hold the calculated values. During each calculation iteration this matrix is updated until a final matrix relationship between all of the variables is obtained. Since this [a] matrix represents the changes in each of the desired properties, the final values obtained must be added to last values obtained for each of the parameters of interest in [x].

$$
\begin{bmatrix}
\frac{d\overline{T}}{dx} \\
\frac{dF}{dx} \\
\frac{dG^{(r)}}{dx} \\
\frac{dG^{(i)}}{dx} \\
\frac{d\tau^{(r)}}{dx} \\
\frac{d\tau^{(i)}}{dx} \\
\frac{dH^{(r)}}{dx} \\
\frac{dH^{(i)}}{dx} \\
\frac{dY^{(r)}}{dx} \\
\frac{dY^{(i)}}{dt} \\
\frac{dv^{(r)}}{dx} \\
\frac{dv^{(i)}}{dx}
\end{bmatrix}
=
\begin{bmatrix}
1 & 0 & 0 & 0 & 0 & 0 & 0 & 0 & 0 & 0 & 0 & 0 \\
0 & 1-q\overline{w} & 0 & 0 & 0 & 0 & 0 & 0 & 0 & 0 & 0 & 0 \\
0 & 0 & 1 & 0 & -\left(\frac{1}{\overline{T}}\frac{d\overline{T}}{dx}+\frac{q\overline{w}}{\overline{T}}\left(\frac{E}{\overline{T}}-2\right)\right) & -\frac{\omega}{\overline{T}} & 0 & 0 & -2q\frac{\overline{w}}{Y_f} & 0 & \frac{1}{\overline{T}}\frac{d\overline{T}}{dx} & 0 \\
0 & 0 & 0 & 1 & -\frac{\omega}{\overline{T}} & -\left(\frac{1}{\overline{T}}\frac{d\overline{T}}{dx}+\frac{q\overline{w}}{\overline{T}}\left(\frac{E}{\overline{T}}-2\right)\right) & 0 & 0 & -2q\frac{\overline{w}}{Y_f} & 0 & \frac{1}{\overline{T}}\frac{d\overline{T}}{dx} \\
0 & 0 & 1 & 0 & 0 & 0 & 0 & 0 & 0 & 0 & 0 & 0 \\
0 & 0 & 0 & 1 & 0 & 0 & 0 & 0 & 0 & 0 & 0 & 0 \\
0 & 0 & 0 & 0 & -\left(\frac{1}{\overline{T}}\frac{dY_f}{dx}-\frac{\overline{w}}{\overline{T}}\left(\frac{E}{\overline{T}}-2\right)\right) & 0 & 1 & 0 & 0 & \frac{2w}{Y_f}+\frac{\omega}{\overline{T}} & \frac{1}{\overline{T}}\frac{dY_f}{dx} & 0 \\
0 & 0 & 0 & 0 & 0 & -\left(\frac{1}{\overline{T}}\frac{dY_f}{dx}-\frac{\overline{w}}{\overline{T}}\left(\frac{E}{\overline{T}}-2\right)\right) & 0 & 1 & \frac{2w}{Y_f}+\frac{\omega}{\overline{T}} & 0 & 0 & \frac{1}{\overline{T}}\frac{dY_f}{dx} \\
0 & 0 & 0 & 0 & 0 & 0 & 1 & 0 & 0 & 0 & 0 & 0 \\
0 & 0 & 0 & 0 & 0 & 0 & 0 & 1 & 0 & 0 & 0 & 0 \\
0 & 0 & 1 & 0 & -\frac{1}{\overline{T}}\frac{d\overline{T}}{dx} & -\frac{\omega}{\overline{T}} & 0 & 0 & 0 & 0 & \frac{1}{\overline{T}}\frac{d\overline{T}}{dx} & 0 \\
0 & 0 & 0 & 1 & \frac{\omega}{\overline{T}} & -\frac{1}{\overline{T}}\frac{d\overline{T}}{dx} & 0 & 0 & 0 & 0 & 0 & \frac{1}{\overline{T}}\frac{d\overline{T}}{dx}
\end{bmatrix}
\begin{bmatrix}
F \\
\overline{T} \\
G^{(r)} \\
G^{(i)} \\
\tau^{(r)} \\
\tau^{(i)} \\
H^{(r)} \\
H^{(i)} \\
Y^{(r)} \\
Y^{(i)} \\
v^{(r)} \\
v^{(i)}
\end{bmatrix}
+
\begin{bmatrix}
0 \\
0 \\
-2q\overline{w}+\frac{d\overline{T}}{dx} \\
\frac{\gamma-1}{\gamma}\omega \\
0 \\
0 \\
\frac{dY_f}{dx}+2w \\
0 \\
0 \\
0 \\
0 \\
-\omega
\end{bmatrix}
$$

(Equation 171)

Since the Runge-Kutta method is an initial value problem solver, it requires that a boundary condition be specified at the initial boundary for each property being determined. The initial conditions are straightforward for this case of a premixed liquid rocket combustion system. Since the initial position in the flow at which combustion occurs is assumed to be an arbitrary point after the occurrence of mixing and vaporization, the boundary conditions are greatly simplified. It is assumed that no oscillations are occurring at the beginning of the flame. Thus, for the initial position in the chamber, it was assumed that temperature, velocity, and fuel species fluctuations are all zero. In future work, when mixing and vaporization models are included, the boundary conditions at this location will need to be adjusted.

However, he initial conditions for the temperature slope and species concentration slope are not readily known. Therefore, it is necessary to determine them in order to obtain a solution to the unsteady equations. Thus, the initial conditions at the interface can be written as follows.

$$\tau = 0; \quad \upsilon = 0; \quad Y = 0; \quad \frac{d\tau}{dx} = x_1; \quad \frac{dY}{dx} = x_2 \quad @x = 0 \tag{172}$$

Since there are ten unsteady equations in terms of real and imaginary components, these initial conditions must actually be expressed as initial conditions for the real and imaginary componets of the oscillating porperties, as shown.

$$\begin{aligned} &\tau^{(r)} = 0; \quad \upsilon^{(r)} = 0; \quad Y^{(r)} = 0; \quad \frac{d\tau^{(r)}}{dx} = x_1; \quad \frac{d\tau^{(i)}}{dx} = x_2 \quad @x = 0 \\ &\tau^{(i)} = 0; \quad \upsilon^{(i)} = 0; \quad Y^{(i)} = 0; \quad \frac{dY^{(r)}}{dx} = x_3; \quad \frac{dY^{(i)}}{dx} = x_4 \quad @x = 0 \end{aligned} \tag{173}$$

Though their initial values are not immediately known, the values for the rate of change of the oscillatory temperature and species can be expected to become zero at the end of the flame (i.e. at infinity), because all of the fuel has been consumed. At this point, the chemical reaction process has ceased, and the temperature will have reached a constant value. These boundary conditions at infinity can be expressed as follows.

$$\frac{d\tau}{dx}=0;\quad \frac{dY}{dx}=0\quad @x=\infty \qquad \text{or} \qquad \frac{d\tau^{(r)}}{dx}=0;\quad \frac{dY^{(r)}}{dx}=0\quad @x=\infty$$
$$\frac{d\tau^{(i)}}{dx}=0;\quad \frac{dY^{(i)}}{dx}=0\quad @x=\infty \tag{174}$$

This designation of boundary conditions at both zero and infinity results in a two-point boundary value problem to be solved, which means conditions are specified at both ends of the flame zone.

It is important to note that these boundary conditions differ from those used by Tien [75] in several important ways. First, Tien defined all of the initial gas boundary conditions through the inclusion of a heat transfer routine to model the heat flux from the gas into the solid propellant. This type of model is unnecessary in the current effort, since the propellant mass addition to the liquid rocket chamber is defined by flow pressure drop, not by the propellant burning rate, as in a solid rocket. Additionally, since Tien focused on the thin flame near the propellant surface, his model required the use of a complex downstream temperature boundary condition that incorporated downstream heat transfer effects. However, the current effort can make use of far field conditions designated by equation 174 at which point these effects are negligible, because focus is being placed on the effects of the combustion kinetics upon the overall chamber dynamics.

Returning to the numerical analysis, in order to obtain the unknown initial conditions for the two slope properties to solve this two-point boundary value problem, it is necessary to use a numerical technique known as the shooting method [79]. This is a method typically utilized for solving a boundary value problem by reducing it to the solution of an initial value problem.

The solution is obtained through an iterative process by first taking a guess at the value of the initial boundary condition. A solution is then calculated for this guess using the Runge-Kutta solver. A difference is then taken between the solution obtained for this initial condition and the value specified at the end boundary, until a desired convergence is reached.

To obtain the next initial values to be used, a root finding technique is typically employed. Root finding techniques are used to find the value of the independent variable that yields a solution of zero in the dependent variable [79]. Thus the use of a root finding technique is a useful aid in obtaining an initial boundary value. In this analysis, the secant method is employed, a well-known root finding technique. Therefore, this problem makes use of a multivariable secant shooting method, since it is being used to solve all twelve of the unknown variables in conjunction with one another.

To use this method, initial values of zero were assumed for the four real and imaginary unknown variables, $G^{(r)}$, $G^{(i)}$, $H^{(r)}$, and $H^{(i)}$, in equations 173. A solution for the twelve variables was then calculated through use of the Runge-Kutta method based on their initial conditions. A solution was then calculated at a position downstream of the initial guess by an amount Δx equal to 1e-7. The program then uses the difference of the two different solutions in the construction of a Jacobian matrix.

The Jacobian matrix is a tool used in multivariable system problems in which the matrix is composed of all first order partial derivatives of the system variables with respect to another variable [79]. This matrix can be constructed by first placing the x position values of the initial 'guesses' of the unknown oscillatory properties being sought after in an [X] matrix consisting of the four initial boundary condition positions, as shown in equation 175, below. Also, the solutions obtained for these initial conditions can be placed into a [Z] matrix, as also shown in equation 175. The following equation can then be developed that shows the general expression of the Jacobian matrix in terms of the partial derivatives of these z terms, with respect to the differences of their x values, which in the first iteration their differences are equivalent.

$$X = \begin{bmatrix} x[1] \\ x[2] \\ x[3] \\ x[4] \end{bmatrix} = \textit{initial positions used in determination of the unknown variables} \quad \textit{and} \quad Z = \begin{bmatrix} \dfrac{d\tau^{(r)}}{dx} \\ \dfrac{d\tau^{(i)}}{dx} \\ \dfrac{dY^{(r)}}{dx} \\ \dfrac{dY^{(i)}}{dx} \end{bmatrix} = \begin{bmatrix} z[1] \\ z[2] \\ z[3] \\ z[4] \end{bmatrix}$$

$$J = \begin{bmatrix} \dfrac{\partial z[1]}{\partial x[1]} & \dfrac{\partial z[1]}{\partial x[2]} & \dfrac{\partial z[1]}{\partial x[3]} & \dfrac{\partial z[1]}{\partial x[4]} \\ \dfrac{\partial z[2]}{\partial x[1]} & \dfrac{\partial z[2]}{\partial x[2]} & \dfrac{\partial z[2]}{\partial x[3]} & \dfrac{\partial z[2]}{\partial x[4]} \\ \dfrac{\partial z[3]}{\partial x[1]} & \dfrac{\partial z[3]}{\partial x[2]} & \dfrac{\partial z[3]}{\partial x[3]} & \dfrac{\partial z[3]}{\partial x[4]} \\ \dfrac{\partial z[4]}{\partial x[1]} & \dfrac{\partial z[4]}{\partial x[2]} & \dfrac{\partial z[4]}{\partial x[3]} & \dfrac{\partial z[4]}{\partial x[4]} \end{bmatrix} \tag{175}$$

In lieu of actual partial derivative values, in this routine the Jacobian matrix was created through implementation of the secant method using a finite difference

approximation between the two solutions rather than taking the actual derivative of each function. For example, the derivative for the real oscillatory temperature with respect to the difference between its initial boundary conditions 'guess' and the next x[i] in the iteration was determined as shown.

$$\frac{\partial z[1]}{\partial x[1]} = \frac{z[1]_n - z[1]_{(n-1)}}{x[1]_n - x[1]_{(n-1)}} \tag{176}$$

Expressing all the partial derivatives of equation 175 in the above finite-difference form (equation 176), the following Jacobian matrix in terms of finite difference approximations is created, as shown in equation 177 below.

$$J = \begin{bmatrix} \frac{\partial z[1]}{\partial x[1]} = \frac{z[1]_n - z[1]_{(n-1)}}{x[1]_n - x[1]_{(n-1)}} & \frac{\partial z[1]}{\partial x[2]} = \frac{z[1]_n - z[1]_{(n-1)}}{x[2]_n - x[2]_{(n-1)}} & \frac{\partial z[1]}{\partial x[3]} = \frac{z[1]_n - z[1]_{(n-1)}}{x[3]_n - x[3]_{(n-1)}} & \frac{\partial z[1]}{\partial x[4]} = \frac{z[1]_n - z[1]_{(n-1)}}{x[4]_n - x[4]_{(n-1)}} \\ \frac{\partial z[2]}{\partial x[1]} = \frac{z[2]_n - z[2]_{(n-1)}}{x[1]_n - x[1]_{(n-1)}} & \frac{\partial z[2]}{\partial x[2]} = \frac{z[2]_n - z[2]_{(n-1)}}{x[2]_n - x[2]_{(n-1)}} & \frac{\partial z[2]}{\partial x[3]} = \frac{z[2]_n - z[2]_{(n-1)}}{x[3]_n - x[3]_{(n-1)}} & \frac{\partial z[2]}{\partial x[4]} = \frac{z[2]_n - z[2]_{(n-1)}}{x[4]_n - x[4]_{(n-1)}} \\ \frac{\partial z[3]}{\partial x[1]} = \frac{z[3]_n - z[3]_{(n-1)}}{x[1]_n - x[1]_{(n-1)}} & \frac{\partial z[3]}{\partial x[2]} = \frac{z[3]_n - z[3]_{(n-1)}}{x[2]_n - x[2]_{(n-1)}} & \frac{\partial z[3]}{\partial x[3]} = \frac{z[3]_n - z[3]_{(n-1)}}{x[3]_n - x[3]_{(n-1)}} & \frac{\partial z[1]}{\partial x[4]} = \frac{z[3]_n - z[3]_{(n-1)}}{x[4]_n - x[4]_{(n-1)}} \\ \frac{\partial z[4]}{\partial x[1]} = \frac{z[4]_n - z[4]_{(n-1)}}{x[1]_n - x[1]_{(n-1)}} & \frac{\partial z[4]}{\partial x[2]} = \frac{z[4]_n - z[4]_{(n-1)}}{x[2]_n - x[2]_{(n-1)}} & \frac{\partial z[4]}{\partial x[3]} = \frac{z[4]_n - z[4]_{(n-1)}}{x[3]_n - x[3]_{(n-1)}} & \frac{\partial z[4]}{\partial x[4]} = \frac{z[4]_n - z[4]_{(n-1)}}{x[4]_n - x[4]_{(n-1)}} \end{bmatrix} \tag{177}$$

These Jacobian matrix values were then used to determine the new initial values of [X] to be used in the next iteration; this method is known as the multivariable Newton-Raphson root finding technique for nonlinear systems [79]. In this technique, the expression $[J][\Delta X] = [Z]$ is solved to determine the incremental values of $[\Delta X]$ to be added to the matrix [X] of initial conditions. To calculate a new matrix [X] containing each of the x[i] 'guess' values (in this attempt to bring the final [Z] solutions to the infinite boundary condition values of zero), a [ΔX] matrix was created. To obtain each Δx[i] value, the [Z] matrix values must be multiplied by the inverse matrix using the expression $[\Delta X]=[J]^{-1}[Z]$. However, rather than explicitly calculating the inverse

Jacobian, the four simultaneous equations represented in (178) are solved simultaneously for the change to the boundary condition vector, $[\Delta X]$. Using the computed [ΔX] matrix, a new [X] matrix for the four initial boundary values was determined through its addition to the old [X] matrix values, as shown below. A more thorough explanation of this routine and the multivariable Newton-Raphson technique for nonlinear systems is given in Appendix C.

$$[J][\Delta x]=[Z] \quad \textit{yields} \quad \begin{bmatrix} \frac{\partial z[1]}{\partial x[1]} & \frac{\partial z[1]}{\partial x[2]} & \frac{\partial z[1]}{\partial x[3]} & \frac{\partial z[1]}{\partial x[4]} \\ \frac{\partial z[2]}{\partial x[1]} & \frac{\partial z[2]}{\partial x[2]} & \frac{\partial z[2]}{\partial x[3]} & \frac{\partial z[2]}{\partial x[4]} \\ \frac{\partial z[3]}{\partial x[1]} & \frac{\partial z[3]}{\partial x[2]} & \frac{\partial z[3]}{\partial x[3]} & \frac{\partial z[3]}{\partial x[4]} \\ \frac{\partial z[4]}{\partial x[1]} & \frac{\partial z[4]}{\partial x[2]} & \frac{\partial z[4]}{\partial x[3]} & \frac{\partial z[4]}{\partial x[4]} \end{bmatrix} \begin{bmatrix} \Delta x_1 \\ \Delta x_2 \\ \Delta x_3 \\ \Delta x_4 \end{bmatrix} = \begin{bmatrix} z[1] \\ z[2] \\ z[3] \\ z[4] \end{bmatrix} \tag{178}$$

$$\Rightarrow \quad \begin{bmatrix} x[1] \\ x[2] \\ x[3] \\ x[4] \end{bmatrix}_{(i+1)} = \begin{bmatrix} x[1] \\ x[2] \\ x[3] \\ x[4] \end{bmatrix}_{(i)} + \begin{bmatrix} \Delta x_1 \\ \Delta x_2 \\ \Delta x_3 \\ \Delta x_4 \end{bmatrix}$$

Thus, the four new values for the initial 'guess' are obtained from summing the old values of the initial guess and with the Δx values obtained. Unlike in the case of the first run, in the following iterations, the ∂x values in the Jacobian may not necessarily be the same since the Δx step sizes computed will be based upon all of the different values obtained in the Jacobian matrix.

Until a suitable convergence is met, then, through application of the secant method for determination of the Jacobian matrix, the next 'root' or guess is determined

for the new value of the slope quantities at zero. This technique is then repeated until the Runge-Kutta method is able to obtain a solution to the above matrix set of equations (equation 163) that matches the values for the known boundary conditions at infinity. In this case, a convergence value of 1e-7 was used.

Using this approach and the associated code, the unsteady temperature, T_1, required in the heat release integral in equation 86, was determined at each position within the combustion zone, as well as the unsteady velocity and species profiles. These terms were then used in determination of the unsteady heat release rate, $\mathscr{H}_1$, as shown in the following section.

5.3 – Heat Release Calculation

The above sections allowed the steady and unsteady temperature distributions in the flame zone to be determined. Similarly the steady and unsteady heat release falls directly out of the above analysis. These results are then used calculate the linear heat release growth rate

The steady and unsteady heat release, $\mathscr{H}_0$ and $\mathscr{H}_1$, can be determined at each point in the flow field through an expansion process similar to that used to obtain unsteady equations above. The heat release of a system is noted to be the product of the heat of combustion with the reaction rate, as shown.

$$\mathscr{H} = qw_i = qBjT^{\delta}\left(\frac{p}{T}\right)^{n} Y_f^2 e^{-(E/T)} \tag{179}$$

As shown in equation 142 in Section 4.5.2, the terms in this expression can be expanded into steady and unsteady components, as follows.

$$\Rightarrow \mathscr{H} = qBj\bar{T}^{\delta-n}\bar{Y}_f^{\,2}e^{-\frac{E}{\bar{T}}}\left(1+\varepsilon(\delta-n)\frac{\tau}{\bar{T}}e^{i\omega t}\right)\left(1+\varepsilon\frac{E}{\bar{T}^2}\tau e^{i\omega t}\right)\left(1+\varepsilon ne^{i\omega t}\right)\left(1+\varepsilon\left(2\frac{Y}{\bar{Y}_f}\right)e^{i\omega t}\right)$$

$$= q\bar{w}\left(1+\varepsilon\left[(\delta-n)\frac{\tau}{\bar{T}}+\frac{E}{\bar{T}^2}\tau\right]e^{i\omega t}\right)\left(1+\varepsilon\left[n+2\frac{Y}{\bar{Y}_f}\right]e^{i\omega t}\right) \tag{180}$$

$$= q\bar{w}\left(1+\varepsilon\left[(\delta-n)\frac{\tau}{\bar{T}}+\frac{E}{\bar{T}^2}\tau+n+n\frac{Y}{\bar{Y}_f}\right]e^{i\omega t}\right)$$

$$\mathscr{H} = \mathscr{H}_0 + \varepsilon\mathscr{H}_1 = q\bar{w} + q\bar{w}\left(\varepsilon\left[(\delta-n)\frac{\tau}{\bar{T}}+\frac{E}{\bar{T}^2}\tau+n+n\frac{Y}{\bar{Y}_f}\right]\right)e^{i\omega t} \tag{181}$$

It can be seen that the steady heat release, $\mathscr{H}_0$, falls out of the above expansion. The steady heat release rate simply comes from the multiplication of the heat of formation with the reaction rate, as shown.

$$\mathscr{H}_0 = q\bar{w} \tag{182}$$

This release rate can be determined at each point in the flow field. The spatial distribution of this parameter is then used in determination of the linear growth rate.

The terms of order ε represent the contribution due to the unsteady heat release.

$$\mathscr{H}_1 = \mathscr{H}_0\left[(\delta-n)\frac{\tau}{\bar{T}}+\frac{E}{\bar{T}^2}\tau+n+n\frac{Y}{\bar{Y}_f}\right]e^{i\omega t} \tag{183}$$

For the particular case of interest, (n=2 and δ=0), the following expression for the unsteady heat release results.

$$\Rightarrow \mathscr{H}_1 = \mathscr{H}_0\left[\left(\frac{E}{\bar{T}}-2\right)\frac{\tau}{\bar{T}}+2\frac{Y}{\bar{Y}_f}+2\right]e^{i\omega t} \tag{184}$$

Since it is an oscillatory quantity, the unsteady heat release can be expressed in terms of its real and imaginary components. Thus, representing the oscillatory

temperature and species in terms of real and imaginary components, as shown in equation 152 in Section 4.5.2, the following expressions for the real and imaginary heat release components can be developed.

$$\mathscr{H}_1^{(r)} = \mathscr{H}_0\left[\left(\frac{E}{\bar{T}} - 2\right)\frac{\tau^{(r)}}{\bar{T}} + 2\frac{Y^{(r)}}{\bar{Y}_f} + 2\right] \tag{185}$$

$$\mathscr{H}_1^{(i)} = \mathscr{H}_0\left[\left(\frac{E}{\bar{T}} - 2\right)\frac{\tau^{(i)}}{\bar{T}} + 2\frac{Y^{(i)}}{\bar{Y}_f}\right] \tag{186}$$

The magnitude and phase angle of the heat release can be determined as done previously for the other oscillatory components through use of equations 159-160. The spatial distributions of this parameter are then used in determination of the linear growth rate along with the steady heat release.

5.4 – Heat Release Linear Growth Rate

Once the steady and unsteady temperature and heat release profiles have been determined, the heat release growth rate can be calculated. The integral, shown previously in equation 86, is shown again below for ease of reference.

$$\alpha_{HR} = \left\{\frac{1}{2\gamma P_0 E_m^2}\iiint_V \left\langle \frac{\mathscr{H}_1 T_1}{T_0} - \frac{\mathscr{H}_0 T_1^2}{T_0^2}\right\rangle dV\right\} \tag{187}$$

In order to evaluate the integral, the time average shown in the angled brackets must be computed. As previously mentioned, these brackets signify what is called a time

average. This technique was employed, though not presented, in Section 3.7. The time average of a given function is defined as the integral of that function across the period of oscillation, τ, divided by the period

$$\langle f(t) \rangle = \frac{1}{\tau} \int_0^{\tau} f(t) dt \tag{188}$$

where the period is defined as:

$$\tau = \frac{2\pi}{\omega} \tag{189}$$

Note that this symbology is used because it is typically representative of time. This is not to be confused with the oscillatory temperature, τ, shown in equations 190.

Before this time-average can be performed, the two terms in the brackets in equation 187 contain products of the oscillatory components that must first be expanded. These are the products of the oscillatory heat release and the oscillatory temperature in the first term and the square of the oscillatory temperature in the second term. Remember that the full oscillatory solutions for the system parameters are expanded as follows.

$$\begin{aligned} p(t) &= 1 + \varepsilon e^{i\omega t} \\ T(x,t) &= \bar{T}(x) + \varepsilon \tau e^{i\omega t} \\ u(x,t) &= \bar{u}(x) + \varepsilon v e^{i\omega t} \\ Y_f(x,t) &= \bar{Y}_f(x) + \varepsilon Y e^{i\omega t} \end{aligned} \tag{190}$$

where

$$\bar{T}(x) = T_0 \tag{191}$$

as determined in the steady state analysis.

The oscillatory temperature term can first be written as follows, where τ is the unsteady temperature component that was solved for in the unsteay analysis.

$$T_1 = \tau e^{i\omega t} = \tau\left(\cos\omega t + i\sin\omega t\right) \tag{192}$$

From its real and imaginary components, τ can be expressed in terms of its amplitude and phase angle, ϕ, determined from equations 159 and 160 as shown.

$$\tau = \tau_{amplitude}\left(\cos\phi_\tau + i\sin\phi_\tau\right) \tag{193}$$

Placing this expression into equation 184, the full expression of the oscillatory temperature can be written as:

$$\Rightarrow T_1 = \tau_{amplitude}\left(\cos\phi_\tau + i\sin\phi_\tau\right)\left(\cos\omega t + i\sin\omega t\right) \tag{194}$$

resulting in its fully expanded form in terms of real and imaginary components.

$$T_1 = \tau_{amplitude}\left[\left(\cos\phi_\tau\cos\omega t - \sin\phi_\tau\sin\omega t\right) + i\left(\cos\phi_\tau\sin\omega t + \sin\phi_\tau\cos\omega t\right)\right] \tag{195}$$

The oscillatory heat release can be written in the same form as the other oscillatory properties in equations 190 as shown,

$$H\left(x,t\right) = \bar{H}(x) + \varepsilon\mathscr{H}_1 e^{i\omega t} \tag{196}$$

where

$$\bar{H}(x) = \mathscr{H}_0 \tag{197}$$

The full expression for the oscillatory heat release can be developed as done for the temperature, as shown below.

$$\begin{aligned} H_1 &= \mathscr{H}_1 e^{i\omega t} = \mathscr{H}_1\left(\cos\omega t + i\sin\omega t\right) \\ \mathscr{H}_1 &= \mathscr{H}_{1amplitude}\left(\cos\phi_{\mathscr{H}_1} + i\sin\phi_{\mathscr{H}_1}\right) \\ \Rightarrow H_1 &= \mathscr{H}_{1amplitude}\left(\cos\phi_{\mathscr{H}_1} + i\sin\phi_{\mathscr{H}_1}\right)\left(\cos\omega t + i\sin\omega t\right) \end{aligned} \tag{198}$$

resulting in its fully expanded from in terms of real and imaginary components.

$$H_1 = \mathscr{H}_{1amplitude}\left[\left(\cos\phi_{\mathscr{H}_1}\cos\omega t - \sin\phi_{\mathscr{H}_1}\sin\omega t\right) + i\left(\cos\phi_{\mathscr{H}_1}\sin\omega t + \sin\phi_{\mathscr{H}_1}\cos\omega t\right)\right] \tag{199}$$

After the required multiplication and expansion, the following real components result.

$$T_1^2 = \tau_{amplitude}^2 \left(\cos^2\phi_\tau \cos^2\omega t - 2\sin\phi_\tau \sin\omega t \cos\phi_\tau \cos\omega t + \sin^2\phi_\tau \sin^2\omega t\right)$$
$$H_1\ T_1 = \mathscr{H}_{1amplitude}\tau_{amplitude}\begin{pmatrix}\cos\phi_{\mathscr{H}_1}\cos\phi_\tau\cos^2\omega t - \sin\phi_{\mathscr{H}_1}\sin\omega t\cos\phi_\tau\cos\omega t - .... \\ \cos\phi_{\mathscr{H}_1}\cos\omega t\sin\phi_\tau\sin\omega t + \sin\phi_{\mathscr{H}_1}\sin\phi_\tau\sin^2\omega t\end{pmatrix} \quad (200)$$

The time averaging process is used to eliminate the time dependent trigonometric functions. The time average of the sine function is shown below, as an example.

$$\left\langle \sin^2(\omega t)\right\rangle = \frac{\omega}{2\pi}\int_0^{\frac{2\pi}{\omega}} \sin^2(\omega t)dt = \left[\frac{t}{2} - \frac{\sin(\omega t)}{4\omega}\right]_0^{\frac{2\pi}{\omega}} \quad (201)$$

$$= \frac{\omega}{2\pi}\left[\frac{\pi}{\omega} - \frac{\left(\sin(2\pi) - \sin(0)\right)}{4\omega}\right] = \frac{1}{2} \quad (202)$$

The time averaging results of the other required trigonometric expressions are shown as follows.

$$\left\langle \cos^2(\omega t)\right\rangle = \frac{1}{2}$$
$$\left\langle \sin(\omega t)\cos(\omega t)\right\rangle = 0 \quad (203)$$

Application of these results to equations 200, result in the following functions of the amplitude and phase only.

$$T_1^2 = \tau_{amplitude}^2\left(\frac{\cos^2\phi_\tau}{2} + \frac{\sin^2\phi_\tau}{2}\right)$$
$$H_1\ T_1 = \mathscr{H}_{1amplitude}\tau_{amplitude}\left(\frac{\cos\phi_{\mathscr{H}_1}\cos\phi_\tau}{2} + \frac{\sin\phi_{\mathscr{H}_1}\sin\phi_\tau}{2}\right) \quad (204)$$

Upon calculation of these terms, the growth rate is then able to be determined. Calculation of the growth rate is carried through following completion of the unsteady analysis in the program.

The units of the growth rate are in inverse seconds. Since the heat release is a volumetric heat release, the units in the metric system are watts per meter cubed. To calculate the growth rate in dimensional units, the following multiplier was applied to the dimensionless values of the heat release.

$$\mathscr{H}^* = \left(\frac{C_P^2 \bar{T}_\infty \bar{\rho}_\infty \bar{u}_\infty^2}{\bar{\lambda}_\infty} \right) \mathscr{H} \tag{205}$$

This value was developed through noting that the expression used to nondimensionalize time could be employed. And, through a simple multiplication of another specific heat, C_p, and the temperature at infinity, $\bar{T}_\infty$, the property units could be obtained.

A simple unit balance shows these to be the correct units for the heat release so that the growth rate results in units of inverse seconds. Using metric units, the pressure can be expressed in Pascals. The modal energy E_m^2 for a cylindrical chamber can be expressed as

$$E_m^2 = \frac{\pi R^2 L}{2} \tag{206}$$

and thus has units of length cubed. Thus balancing of the units into the expression for growth rate, equation 187, results in the following unit analysis.

$$\left\{\frac{1}{\left(N/m^2\right)\left(m^3\right)}\left(\mathscr{H}\right)\left(m^3\right)\right\}=\frac{1}{s}$$
$$\left\{\frac{1}{\frac{kg}{ms^2}}\left(\mathscr{H}\right)\right\}=\frac{1}{s}\Rightarrow\mathscr{H}=\frac{kg}{ms^3}=\frac{W}{m^3} \quad (207)$$

With the inclusion of the term in equation 207 into the calculation, a dimensional value for the heat release growth rate can then be determined.

CHAPTER 6 – ANALYSIS OF PROGRAM RESULTS

6.1 – Discussion of Setup

The objective of this investigation was to enhance the understanding of unsteady combustion and to quantify its effects on the stability of a rocket system. To do this, it must first be determined whether the unsteady combustion mechanism acts as a driving or damping feature in the system. This is done by calculating the linear growth rate, a commonly used parameter for determination of the effects of system disturbances on rocket stability. A positive growth rate result means that the heat release due to unsteady combustion acts as a driving mechanism, therefore encouraging instability, while a negative value means that it behaves as a damping mechanism, therefore discouraging instability. Through determination of the steady and unsteady temperature and heat release distributions, this growth rate can be calculated as presented in Chapters 4 and 5.

The second objective of the effort is to determine the relative importance of the unsteady combustion mechanism. This is accomplished by comparing the calculated unsteady combustion growth rate to the magnitudes of the growth rate for other mechanisms.

The next objective was to examine the sensitivity of the growth rate and system behavior due to different parameters. In addition to expanding the understanding of unsteady combustion behavior, the sensitivity results may reveal opportunities to improve the stability of rocket systems.

In order to develop the most useful results for understanding the effects of unsteady combustion, the analysis was performed using dimensionless variables. This

was done as a means to easily note the direct effects of altering individual system parameters. Performing the analysis in dimensionless form resulted in a very small set of initial input parameters in the numerical program. This set of parameters included the initial dimensionless temperature, the specific heat ratio, the dimensionless activation energy, the dimensionless heat of combustion, and the dimensionless chamber frequency. The expressions used in nondimensionalizing these parameters are shown in the following set of equations.

$$T = T_i = \frac{T^*}{\bar{T}_\infty} \qquad E = \frac{E^*}{R\bar{T}_\infty} \; where \; \frac{E^*}{R} = T_{activation} \qquad q = \frac{q^*}{C_p \bar{T}_\infty} \tag{208}$$

The initial dimensionless temperature used is the ratio of the initial temperature of the propellant to the final chamber temperature at the flame edge. The specific heat ratio is a traditional dimensionless parameter associated with how the gas molecules handle the addition of thermal energy. The dimensionless activation energy represents the amount of energy required to initiate the chemical reaction. Its dimensionless value is developed by the ratio of the activation temperature to the temperature at the flame edge. The activation energy is an experimentally derived parameter that is used in the Arrhenius equation. The dimensionless heat of combustion represents the amount of energy released in a reaction and is directly proportional to the dimensionless temperature in this analysis. This was discussed in Chapter 4.

$$\omega = \omega^* \frac{\bar{\lambda}}{\bar{\rho}_\infty C_p \bar{u}_\infty^2} = \frac{\bar{\alpha}_\infty}{\bar{u}_\infty^2} \tag{209}$$

The dimensionless chamber frequency is an important parameter that is typically of interest in determining system growth rate values. This expression is the reciprocal of that used for determining the dimensional time; the α in this expression represents the thermal diffusivity. Though the expression in this equation can be used to determine the dimensionless frequency from a known dimensional value, it is not used to determine the dimensionless frequency in this parametric study. The values of dimensionless frequencies used were simply a logarithmic range from 0.001 to 10 to determine sensitivity. The reciprocal of this expression is employed later in the analysis when the frequency is taken back to dimensional form.

6.2 – Comparison to Tien's Results

Before the program was run for computation of the unsteady combustion growth rate, initial computations were performed to see how the oscillatory property results for Tien's solid modeling analysis compared to those for the premixed liquid system in this analysis. Though Tien's focus was upon determining the acoustic admittance of a burning solid propellant and had no interest in understanding the effects of the combustion process on stability dynamics, the oscillatory temperature, velocity, and species concentration should still follow similar trends. It is expected that they will differ to some degree, because all of the boundary conditions are different for the two cases. Also, Tien did not specify his ratio of specific heats, of which 1.17 was used in this comparison.

The program was run for the same values of the system variables for which Tien performed his solid analysis. These values included an initial temperature (T_i) of 0.35, activation energy (E) of 10, and a frequency (ω) of 1. The following two figures show the results for the real and imaginary components of some of the oscillatory properties obtained by Tien and obtained in this analysis. Figure 24 shows the steady and unsteady results from Tien's solid propellant analysis. Figures 25 and 26 show the steady and unsteady results of the current premixed liquid analysis.

Comparison of these figures shows that both models give the same dimensionless flame length, x, as discussed in Section 5.2. This is considered valid because the flame length is dictated by the steady analysis. Moreover, as seen in Figures 24 and 25, in both analyses, the steady state temperature profiles are the same. This is because they both have an initial temperature set to be 0.35, and the final temperature known to go to a dimensionless value of 1. Since both programs use the same steady state equations for analysis, their identical steady state temperature profiles have the same flame lengths.

Although the steady state results are the same for both cases, it can be see in Figures 24 and 26 that the unsteady profiles are different. The real and imaginary profiles of the temperature follow similar trends to those in Tien's analysis; however, the real component profiles of velocity and species concentration are flipped. It is expected that some of these results should be different. Specifically, the initial boundary conditions for the velocity and fuel species concentration were based on the heat transfer model that Tien used, whereas the initial conditions for these two properties in the present analysis were set to zero. It is noted, however, that the profiles for the imaginary

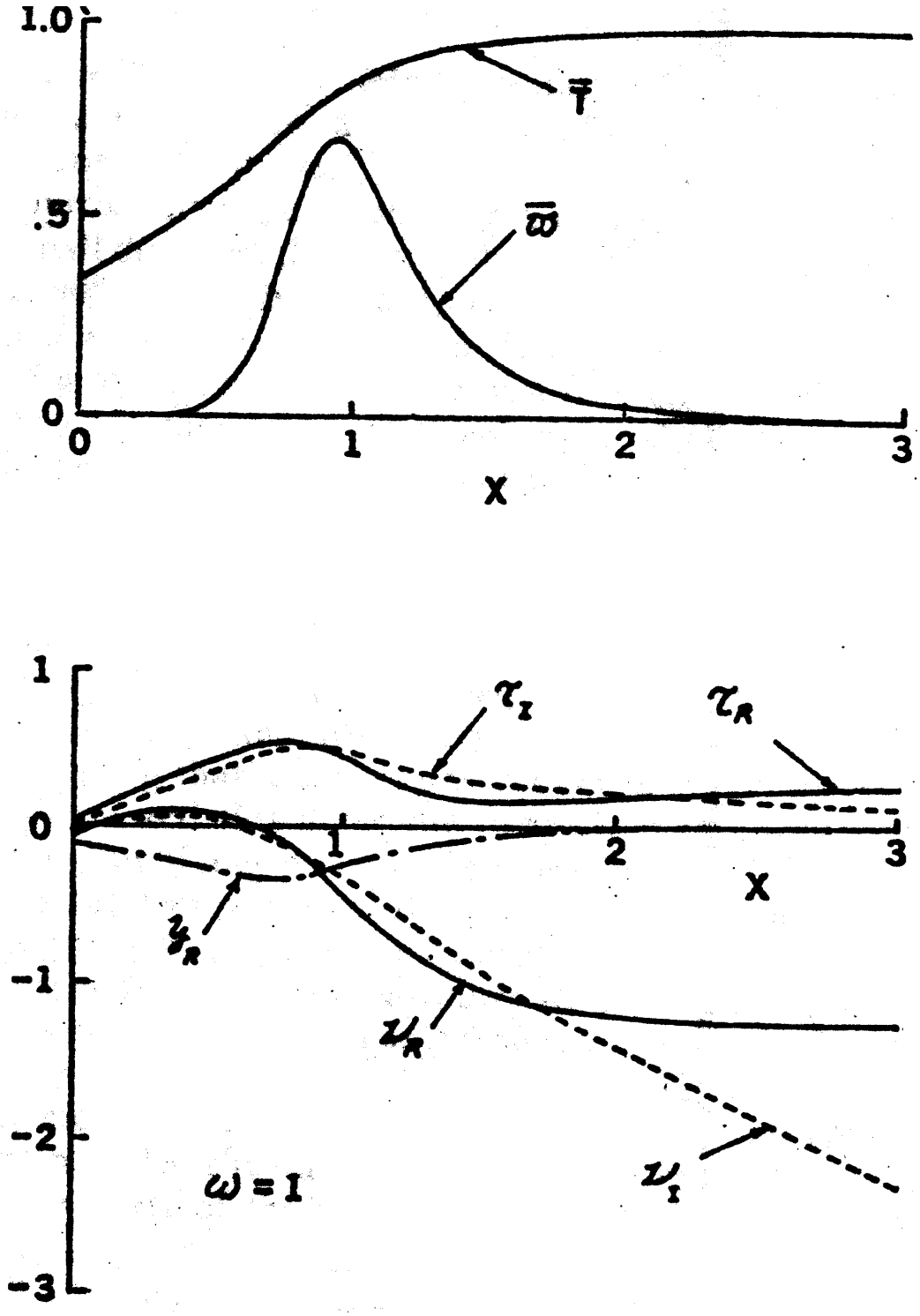

Figure 24. Tien's Oscillatory Results for Solid Rocket Motor [75]

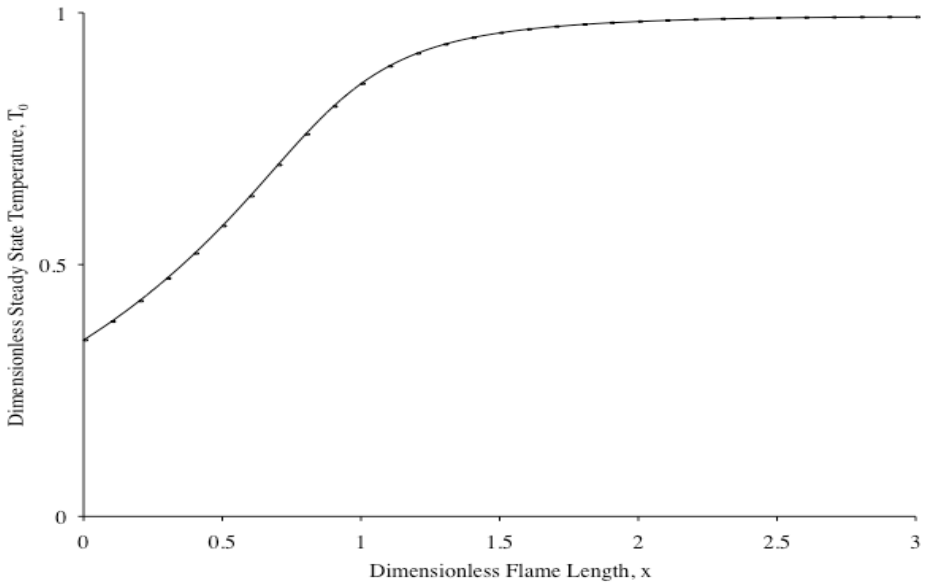

Figure 25. Results of Steady State Temperature For Liquid Rocket Engine

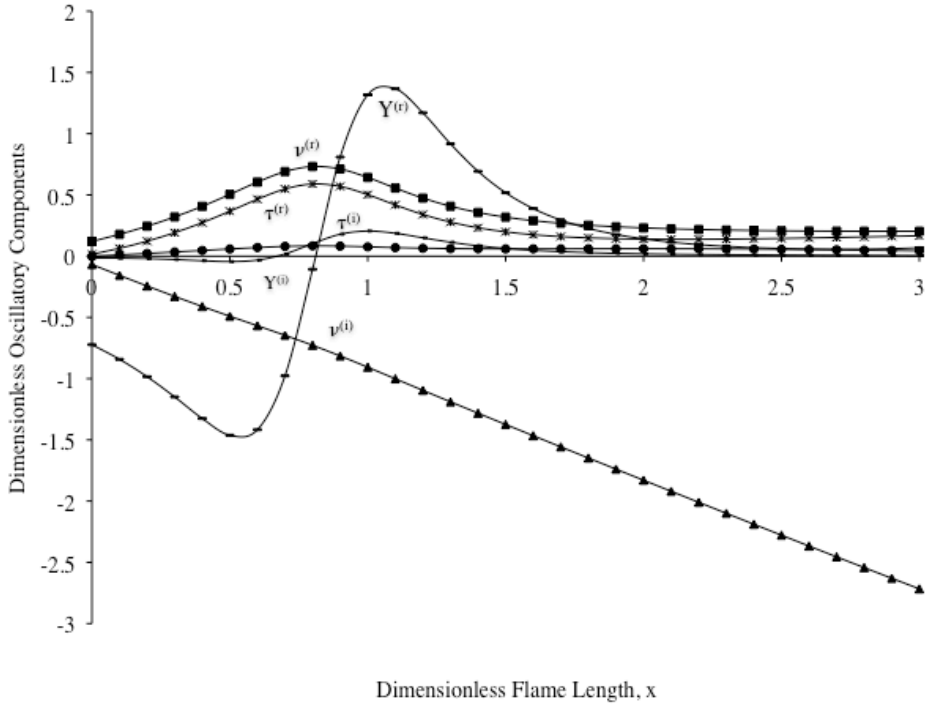

Figure 26. Results of Oscillatory Components For Liquid Rocket Engine

velocity components follow similar trends. Although many of these values are clearly different for the two cases, the comparison was worthwhile to show the difference as well as some of the similarities between the oscillatory results obtained in Tien's solid propellant analysis and this liquid the present analysis.

6.3 – Initial Baseline Liquid Rocket Results

An initial run of the steady state and unsteady programs was performed for a baseline set of input parameters to determine the magnitude of the growth rate. These values are shown in Table 2, along the ranges of the parameters that were used in the later sensitivity analysis.

These parameters were chosen since they represent a typical set of initial variables for a liquid rocket engine, such as LOX/RP-1 [76, 78]. The sensitivity ranges in this table were chosen to capture the values for most liquid rocket engines, including monopropellants and high-energy bipropellants, such as LOX/LH2.

Figures 27 and 28 show the resulting steady fuel species profile and the reaction rate profile, respectively, as they change as a function of the dimensionless position in the flame. As stated earlier, the steady state analysis determines the dimensionless flame

Table 2. Dimensionless Variable Values

Dimensionless Variable	Initial Values	Sensitivity Range
Temperature (initial), T_i	0.2	0.05-0.4
Specific Heat Ratio, γ	1.17	1.1-1.667
Heat of Combustion, q	0.8	0.6-0.95
Activation Energy, E	10	10
Angular Frequency, ω	1	0.001-10

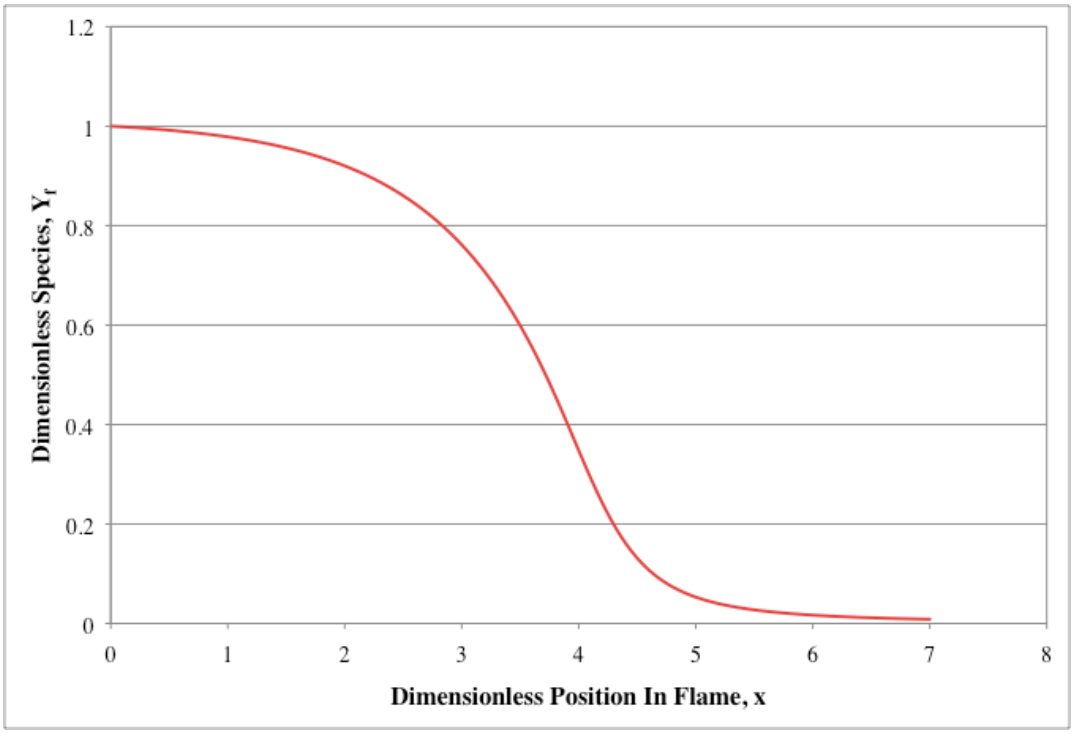

Figure 27. Fuel Species Profile (Y_f) for T_i=0.2, γ=1.17

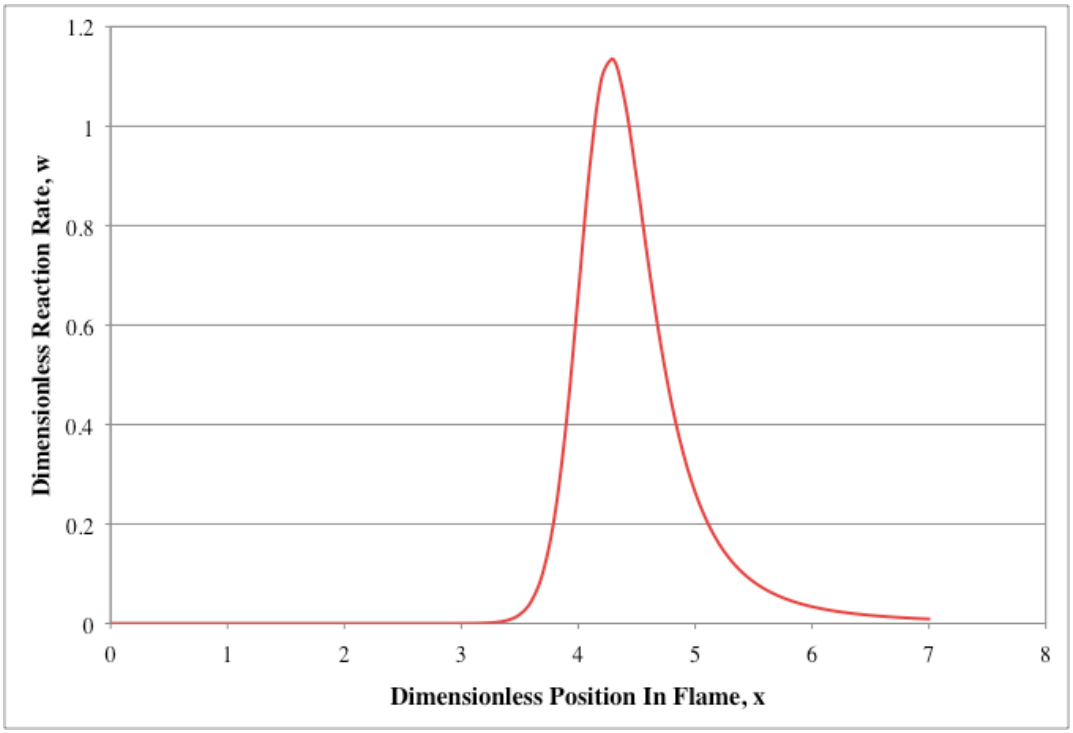

Figure 28. Reaction Rate Profile (w) for T_i=0.2, γ=1.17

length. The flame length for this case is seen in both figures to be at approximately 7. Since these results are dimensionless, the species can be seen to begin at one and then proceed to zero as the fuel is consumed, while the reaction rate results are proportional to the slope of the fuel species results. It is noted that the fuel species profile and reaction rate are similar to typical results for a laminar flame.

Figures 29 and 30 show the steady state heat release and temperature profiles. The steady heat release profile is seen to simply be a multiple of the reaction rate. In this case, it is 0.8 times the reaction rate. The overall heat release that occurs in the system is found by integrating the heat release curve, which yields the total change in non-dimensional temperature. The steady state temperature profile that results as in the case of the other profiles exhibits typical temperature profile behavior for a laminar flame. It begins at an initial input temperature of 0.2 and then levels off to a final chamber temperature specified as 1. These two figures yield the T_0 and $\mathscr{H}_0$ values to be used in the growth rate integral for determination of the unsteady combustion growth rate.

Figures 31 and 32 show the unsteady temperature and heat release profiles. The unsteady heat release profile shows a dip at the point of maximum steady state heat release that should bear further examination in future work. These two figures yield the T_0 and $\mathscr{H}_1$ values to be used in determination of the unsteady combustion growth rate.

Figures 33 and 34 show the peak change over frequency for both unsteady temperature and unsteady heat release. These can be seen to grow steadily as frequency decreases, with a slight rise at midrange frequencies and then again rising slightly as the

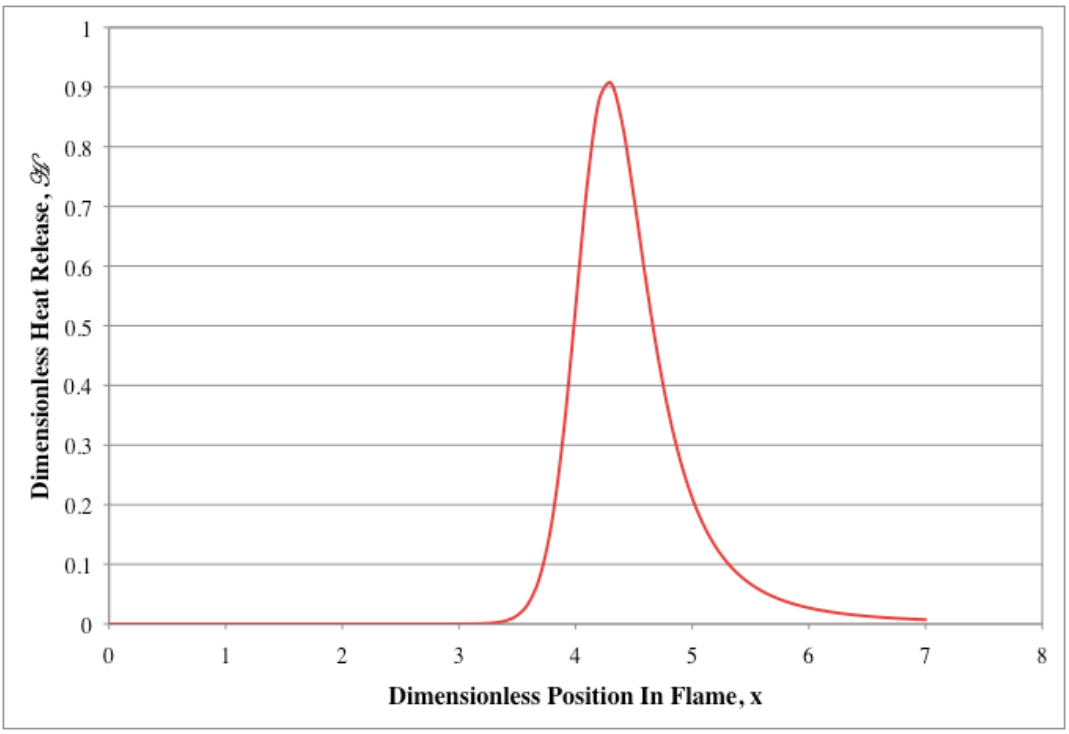

Figure 29. Steady State Heat Release Profile ($\mathscr{H}_0$) for T_i=0.2, γ=1.17

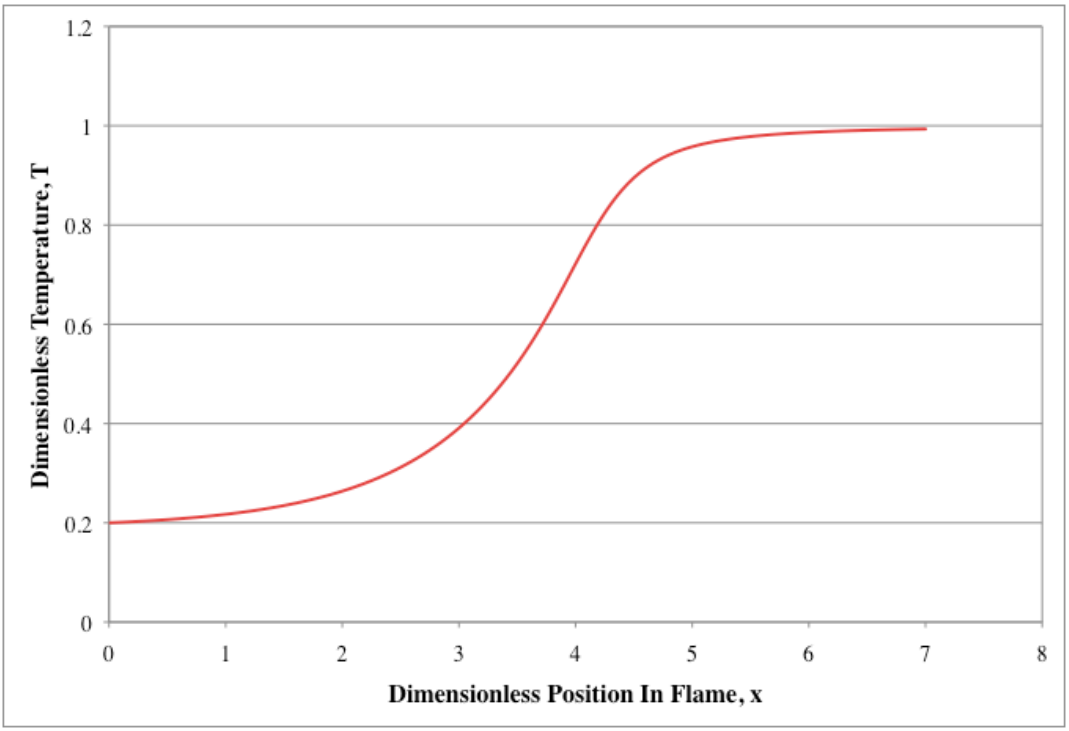

Figure 30. Steady State Temperature Profile (T_0) for T_i=0.2, γ=1.17

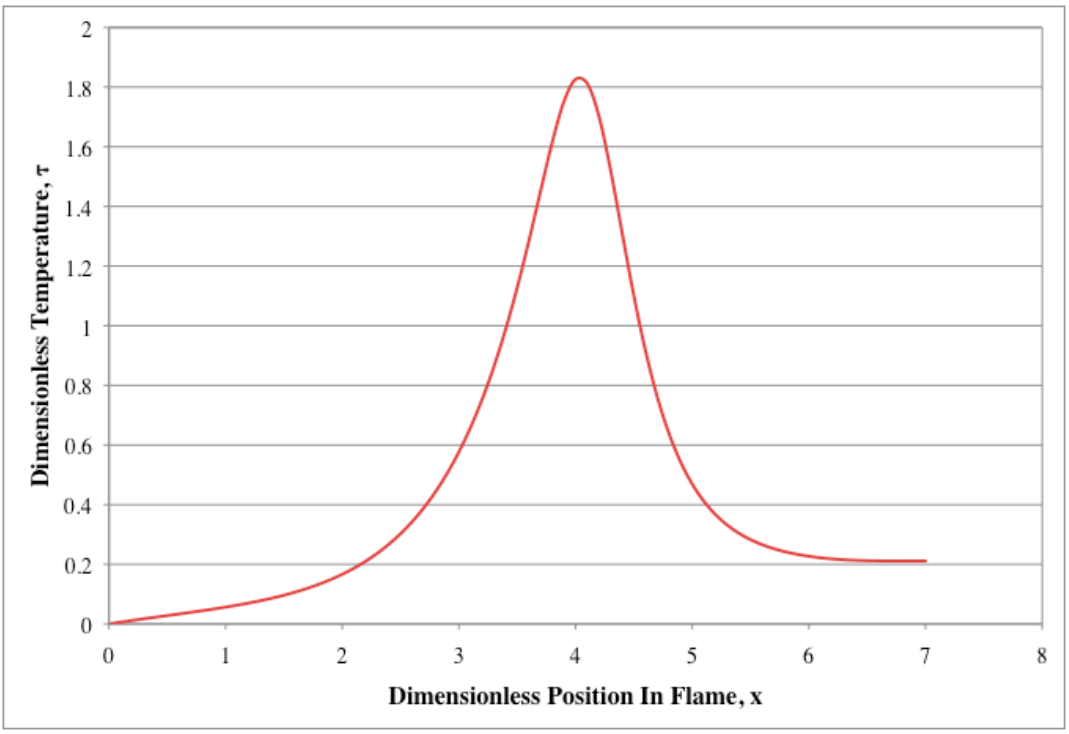

Figure 31. Unsteady Temperature Amplitude Profile (τ) for T_i=0.2, γ=1.17, ω=1

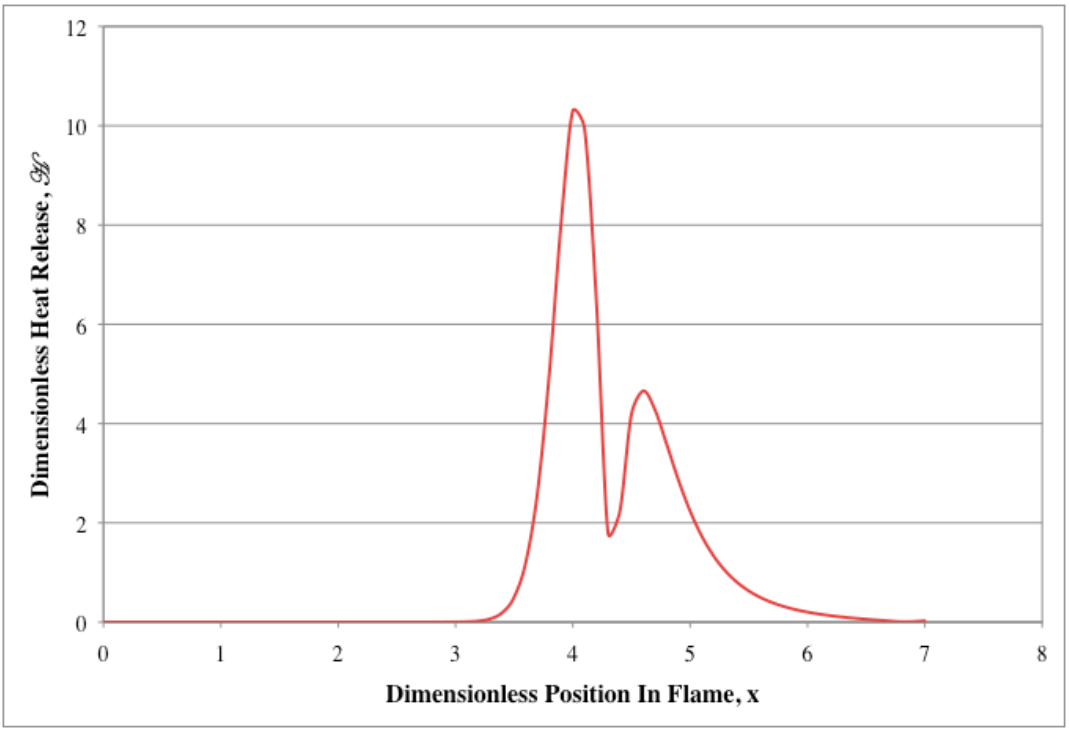

Figure 32. Unsteady Heat Release Amplitude Profile ($\mathscr{Q}_1$) for T_i=0.2, γ=1.17, ω=1

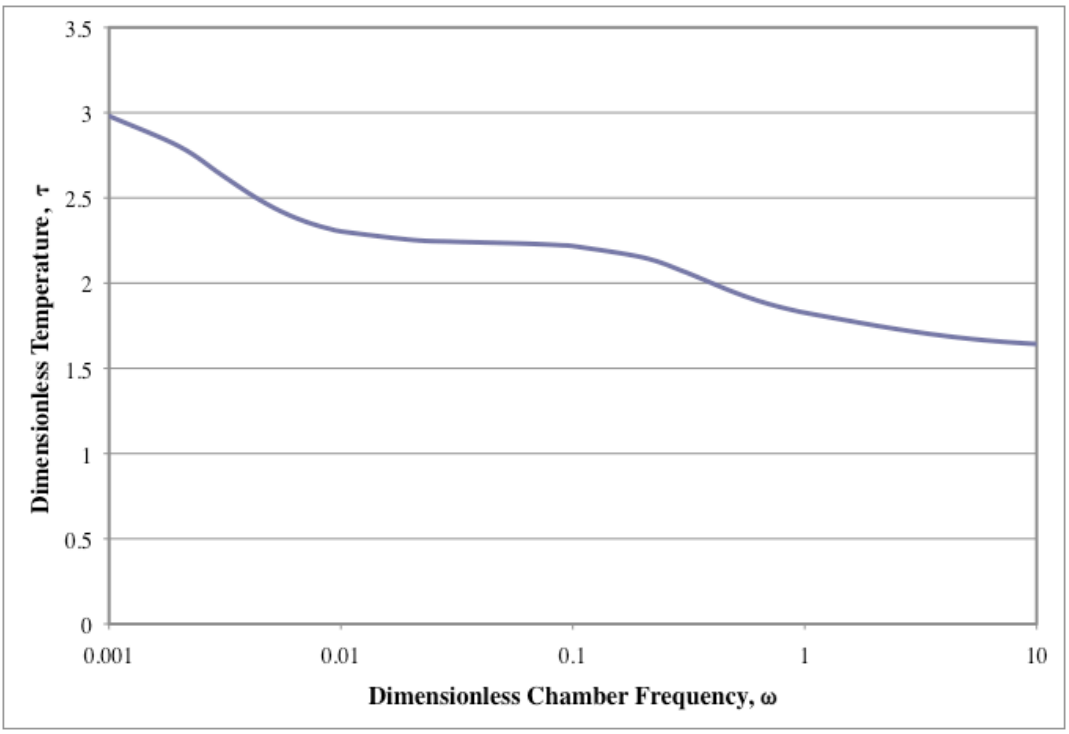

Figure 33. Unsteady Temperature (peak) Change with Frequency for T_i=0.2, γ=1.17

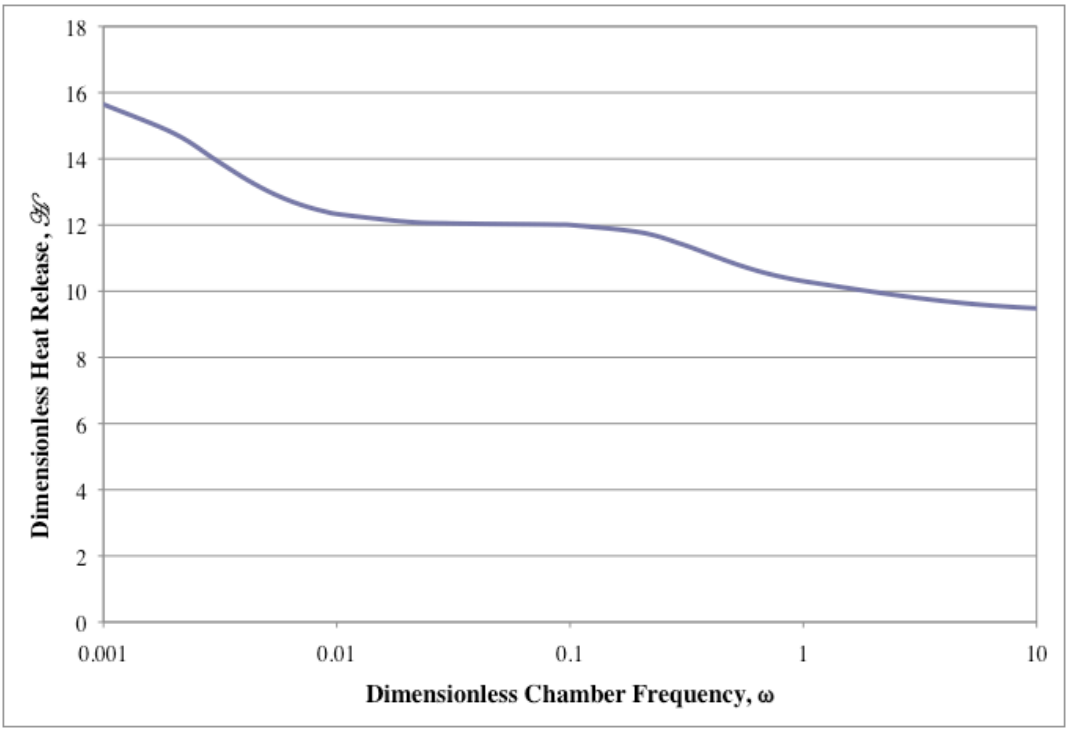

Figure 34. Unsteady Heat Release (peak) Change with Frequency for T_i=0.2, γ=1.17

frequency decreases. When these values along with the steady temperature and heat release values, that are independent of frequency, are inserted into equation 187, the growth rate due to unsteady combustion can be determined. This growth rate is shown in Figure 35. It can be seen to follow a similar trend to the two previous figures, increasing as frequency decreases. In addition to showing that the unsteady combustion growth rate is larger (i.e. destabilizing) for lower modes, it also shows that the unsteady combustion growth rate increases with combustion chamber size. Most importantly, this figure indicates that the growth rate contribution due to unsteady combustion is positive for a full range of reasonable frequencies; therefore, it acts as a driving term in a system and enhances instability.

6.4 – Sensitivity Analysis

Before going into a discussion of the magnitude of the growth rate when dimensionalized and comparing it to other mechanisms, it is useful to look at the dimensionless sensitivity analysis first. Remember that part of the motivation for performing this investigation in dimensionless form was to more easily identify the direct effects of altering individual system parameters. This investigation was performed by running the numerical program with variations of key parameters for a generic reaction. By the term generic reaction, it is meant that no specific reaction was in mind when varying inputs. Using the set of conditions shown in Table 2 as a baseline case, one dimensionless parameter at a time was altered while others remained constant to note the impact of the parameter change.

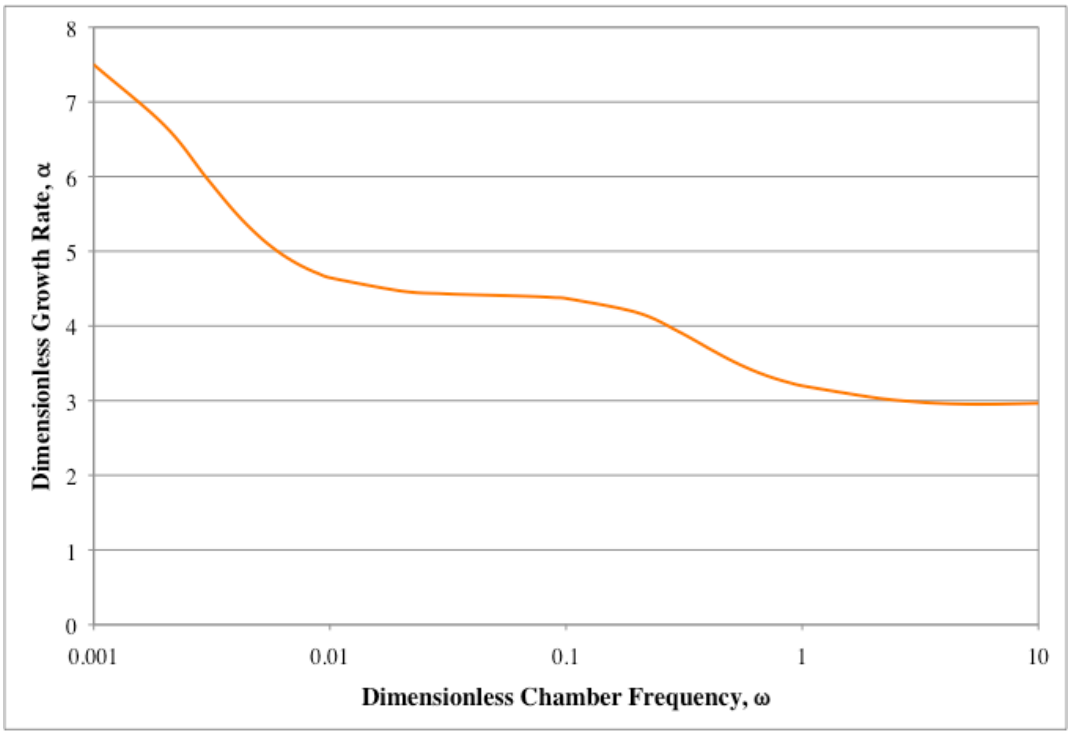

Figure 35. Dimensionless Growth Rate (α_{UC}) for T_i=0.2, γ=1.17

Though there are five input parameters that could be varied, the problem actually simplifies to investigating the dependence of system properties upon the specific heat ratio and the initial dimensionless temperature. While the dependence upon dimensionless activation energy was initially investigated, it turned out that only a very narrow range of numbers about the value of ten were realistic. This value was used throughout the computations to maintain a connection with physical devices. Due to the relationship between the heat of combustion and temperature shown in equation 119, the heat of combustion could technically be used instead of the initial temperature, if desired. Because the nondimensional fuel species concentration can be assumed to be one, as discussed in Section 4.5, the nondimensional heat of combustion is the difference of one minus the initial temperature. Therefore, since inputting the value of one automatically

calculates the other's value, the set of results for either approach are the same.

Since the frequency is a critical parameter of interest, its sensitivity is investigated in conjunction with each of the other parameters by running each sensitivity case for a range of frequencies, as can be noted in Figures 33 and 34. To determine this dependency, the program was run for whichever parameter of interest, e.g. initial temperature, over a range of forty dimensionless frequencies. It was of course expected that there would be a dependency upon the dimensionless chamber frequency, since stability has been seen to be a strong function of frequency.

Results for changes in system parameters are calculated across increments of the dimensionless flame length determined initially by running the steady state program. The following figures show the changes in major system properties over a range of initial temperatures for the specific heat ratio of 1.17. Figure 36 shows the reaction rate profile over a range of initial dimensionless temperature from 0.1-0.4. This dimensionless temperature represents the ratio of the initial dimensional temperature to the chamber temperature and directly correlates with the amount of energy in the propellant. It can be seen that for lower initial temperature, the reaction requires a greater amount of energy to reach the end state.

Figure 37 shows the change in heat release over flame length for this same range of initial temperatures. It can be seen, as noted in Section 5.3 equation 179, that the steady heat release is a multiple of the reaction rate. Figure 38 shows the steady temperature profile over flame length. Again, note that the initial temperature values can be seen to correspond to the propellant energy release. Low energy propellants have a

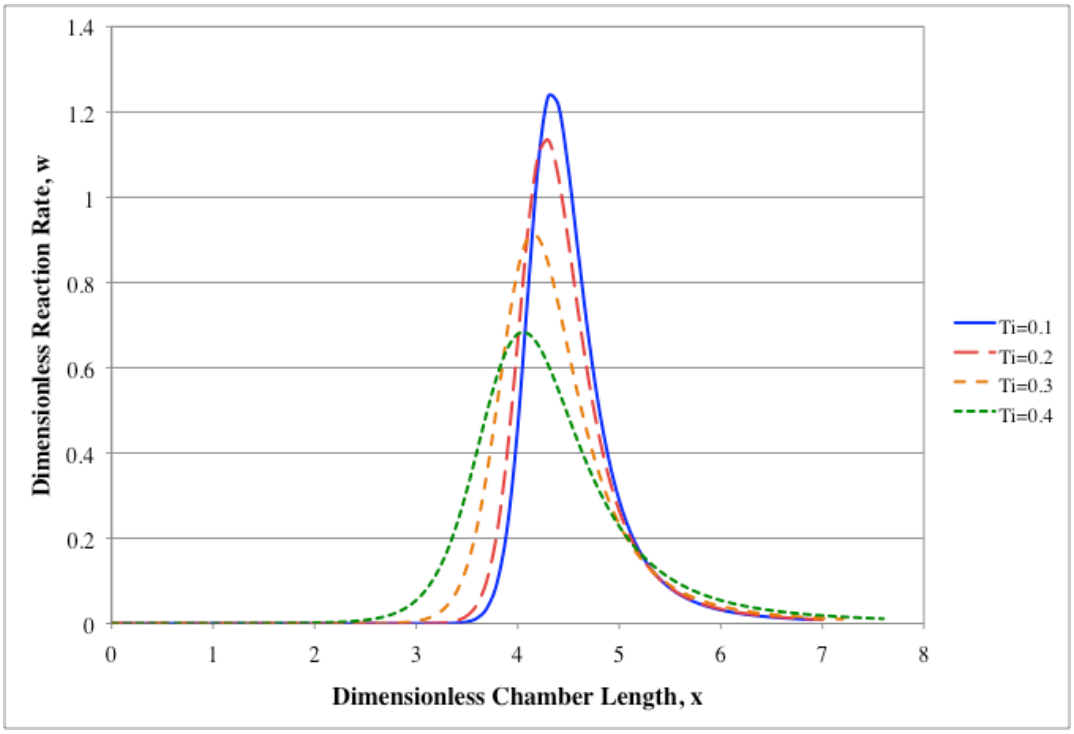

Figure 36. Reaction Rate Profile (w) Varying Initial Temperature (γ=1.17)

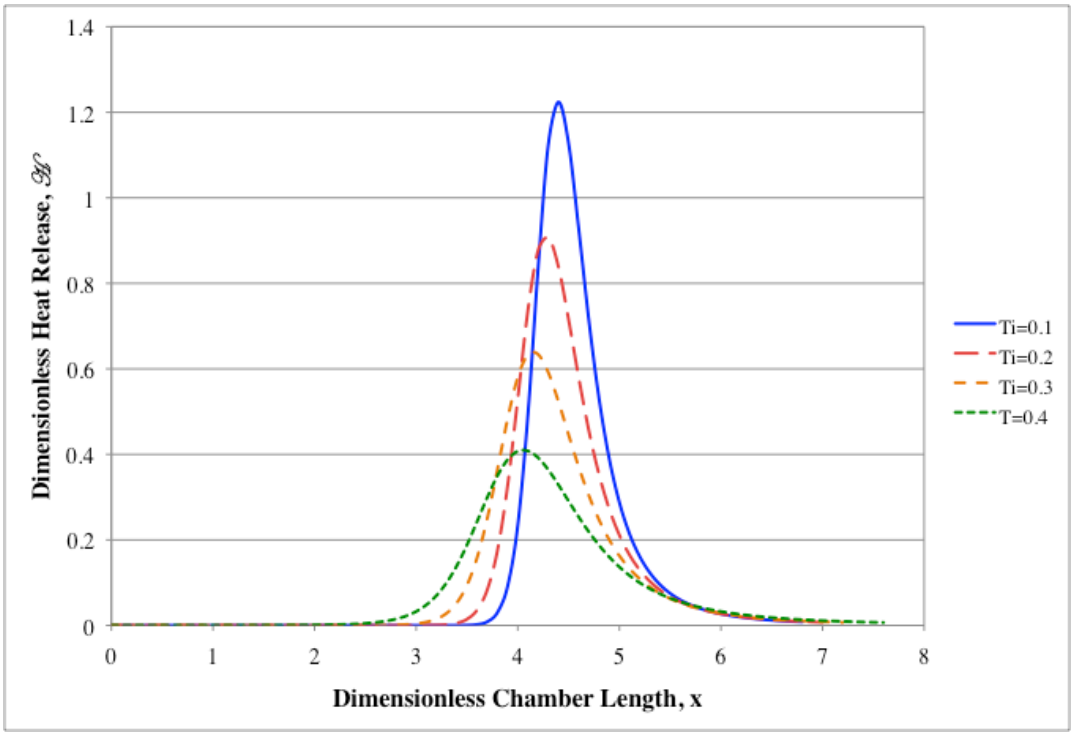

Figure 37. Steady Heat Release ($\mathscr{Q}_0$) Varying Initial Temperature (γ=1.17)

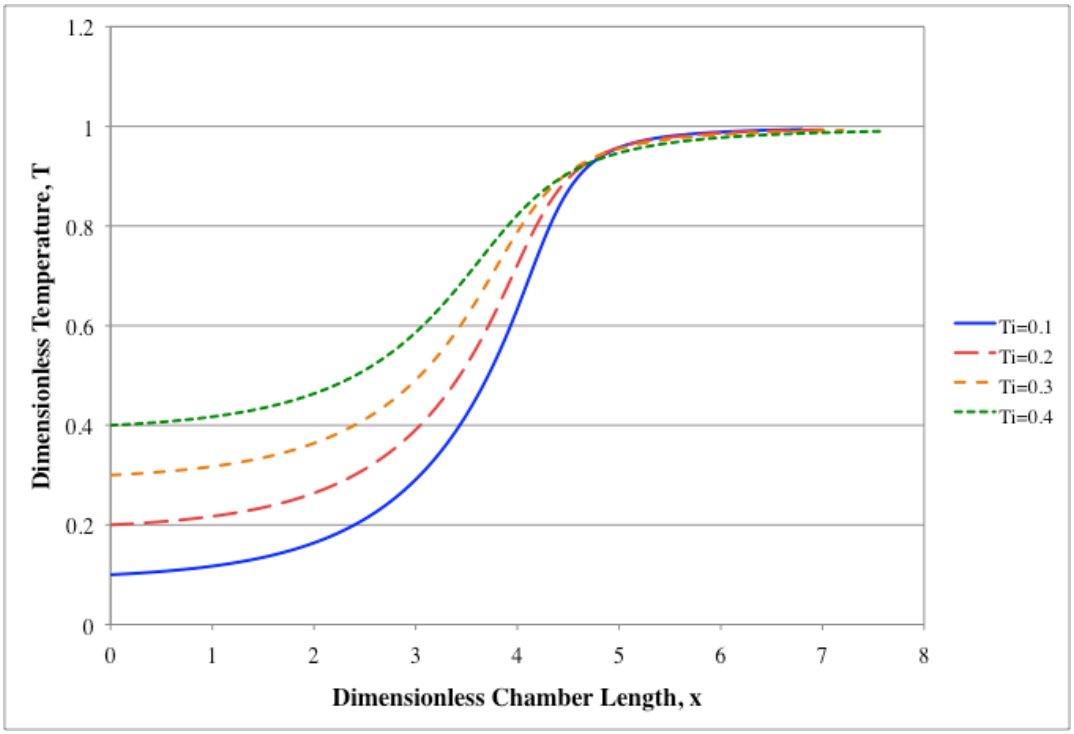

Figure 38. Steady Temperature Profile (T_0) Varying Initial Temperature (γ=1.17)

high T_i and high energy propellants have a low T_i. Since the combustion process is modeled as a simple one-step reaction, the reaction is assumed to proceed to completion with no quenching mechanism; it can be seen in the figure for steady heat release that the lower temperature reactions require a greater amount of heat in order to reach the final chamber temperature. The max heat release can be seen to correspond to the max temperature slope. These two graphs provide the T_0 and $\mathscr{H}_0$ values for inclusion in the growth rate calculation.

Figure 39 shows the change in fuel species over flame length for changing initial temperature. While other species profiles could be graphed based on the analysis from Section 4.5.1, these graphs are not presented since they would only be of significant interest if a more complex reaction were modeled.

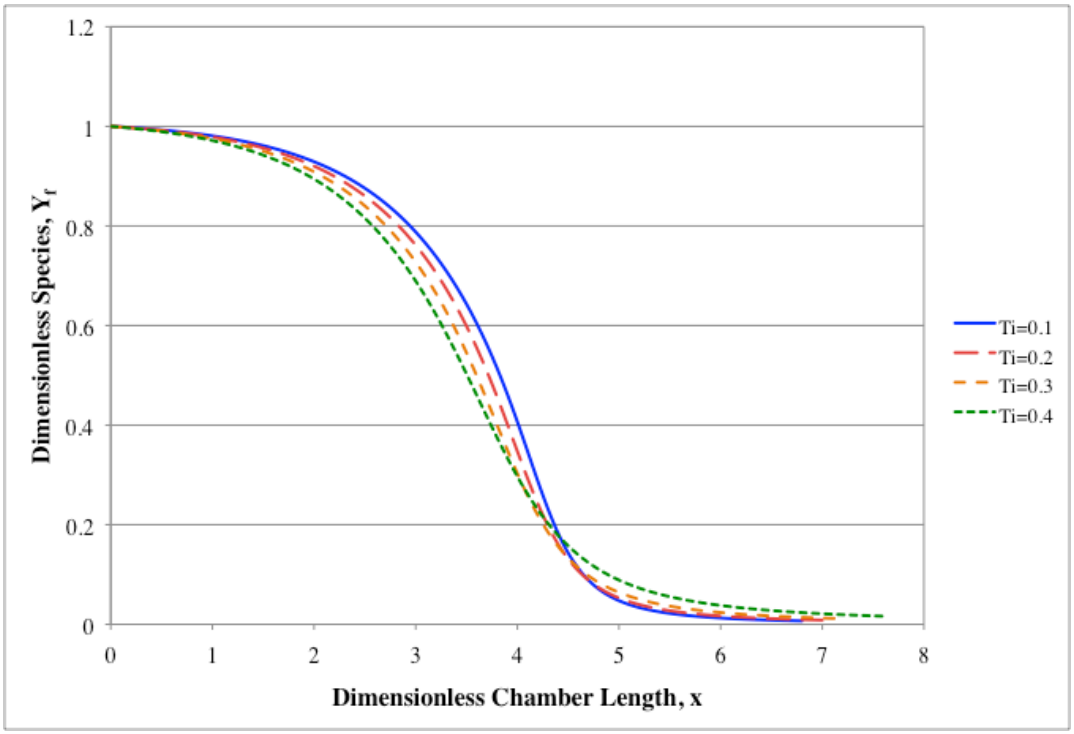

Figure 39. Steady Fuel Species Profile (Y_f) Varying Initial Temperature (γ=1.17)

The results of the unsteady combustion model are shown in the next seven figures; these figures correspond to a dimensionless chamber frequency of one. Figures 40 and 41 show the real and imaginary components of the unsteady temperature. As discussed in Section 5.2 these values can be combined to determine the dimensionless amplitudes of the unsteady temperature fluctuation, as shown in Figure 42. This figure provides the T_1 values for the alpha calculation. Figure 43 displays the oscillatory time dependent behavior of the temperature, computed using the perturbed equations set 109 used to expand the combustion equations based upon a sinusoidal pressure waveform. In these equations, the normalized amplitude of the pressure oscillation, ε, is used to scale the oscillatory parameter, e.g., τ. Given a certain value, such as 0.1 used in Figure 42,

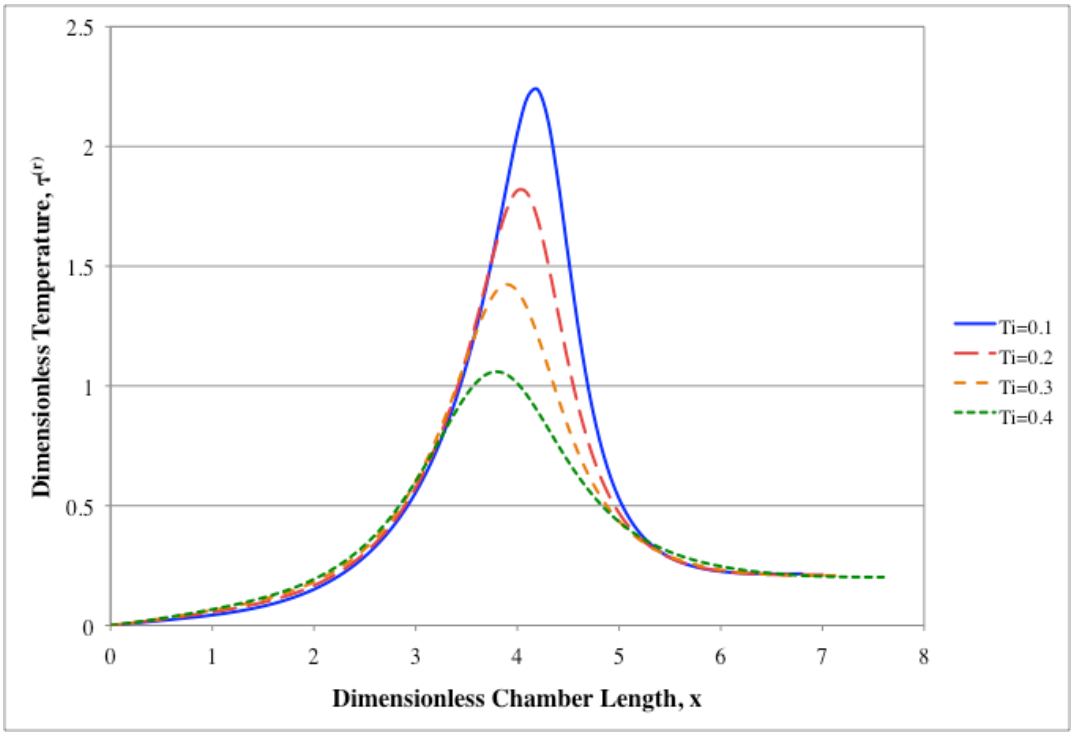

Figure 40. Real Unsteady Temperature Component ($\tau^{(r)}$) Varying Initial Temperature (γ=1.17, ω=1)

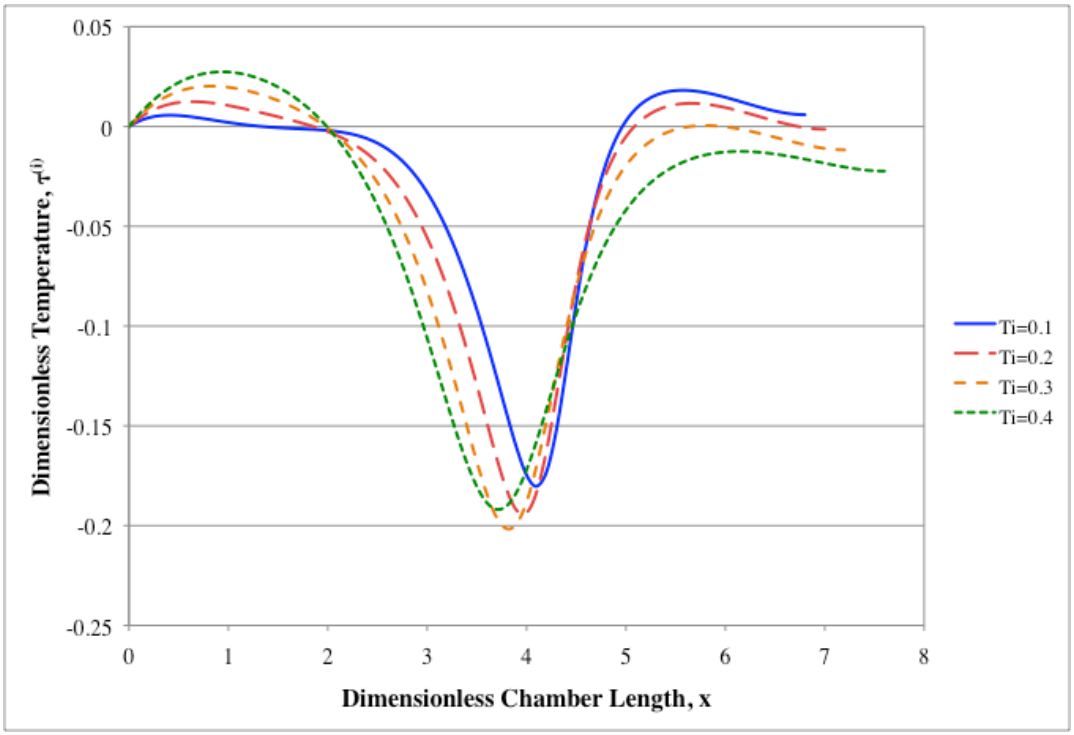

Figure 41. Imaginary Unsteady Temperature Component ($\tau^{(i)}$) Varying Initial Temperature (γ=1.17, ω=1)

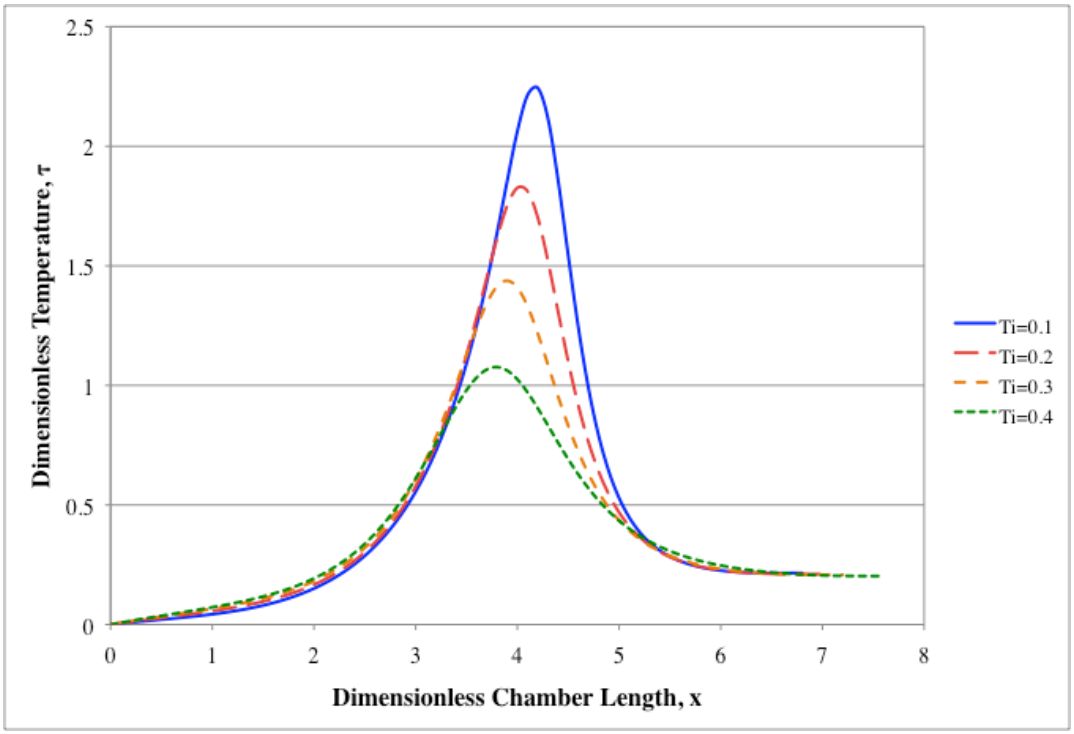

Figure 42. Unsteady Temperature Amplitude (τ) Varying Initial Temperature (γ=1.17, ω=1)

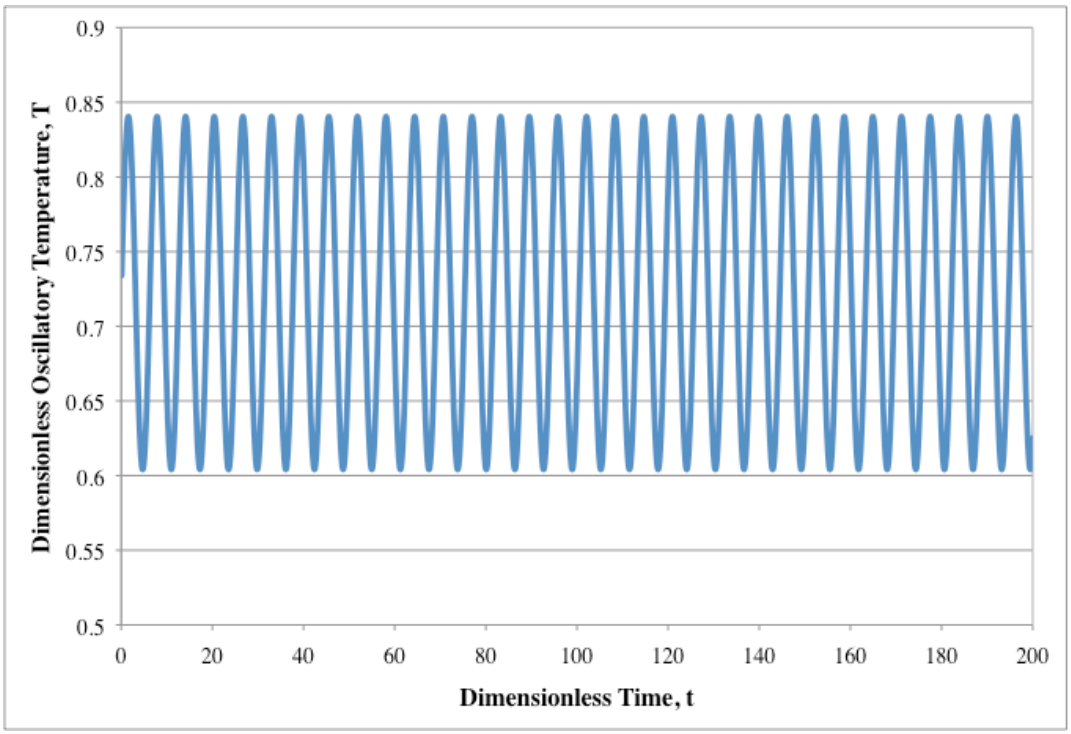

Figure 43. Plot of Oscillatory Time Dependant Temperature (ω=1)

when combined with the steady temperature value, the oscillatory temperature equation produces a time dependent result such as that shown.

Figures 44 and 45 show the real and imaginary components of the unsteady heat release profile. As with the temperature, these values can be combined to determine the dimensionless amplitudes of the unsteady heat release fluctuations, as shown in Figure 46. This figure provides the $\mathscr{H}_1$ values for the alpha calculation. The dip can again be seen to occur in the unsteady heat release between four and five on the length axis. While it is speculated that this results from a finite rate chemistry effect, this aspect was not investigated. Not pertinent to determination of the growth rate, graphs of the oscillatory species concentration and velocity are included in Appendix B.

Having determined all of the steady and unsteady temperature and heat release distributions required, the heat release growth rate can then be computed to investigate the contribution of the unsteady combustion to the system instability. When the results from Figures 37, 38, 42, and 46 are integrated using the heat release growth rate equation, equation 187, for a range of frequencies, the value of the dimensionless linear growth rate is generated. Figure 47 shows the change in dimensionless growth rate over dimensionless chamber frequency for various initial temperatures, given a specific heat ratio of 1.17. This figure clearly indicates that energetic propellants (i.e. low T_i) are destabilizing, as displayed by the increase in the alpha as initial temperature decreases. These results also show some frequency sensitivity that needs to be investigated further in future work.

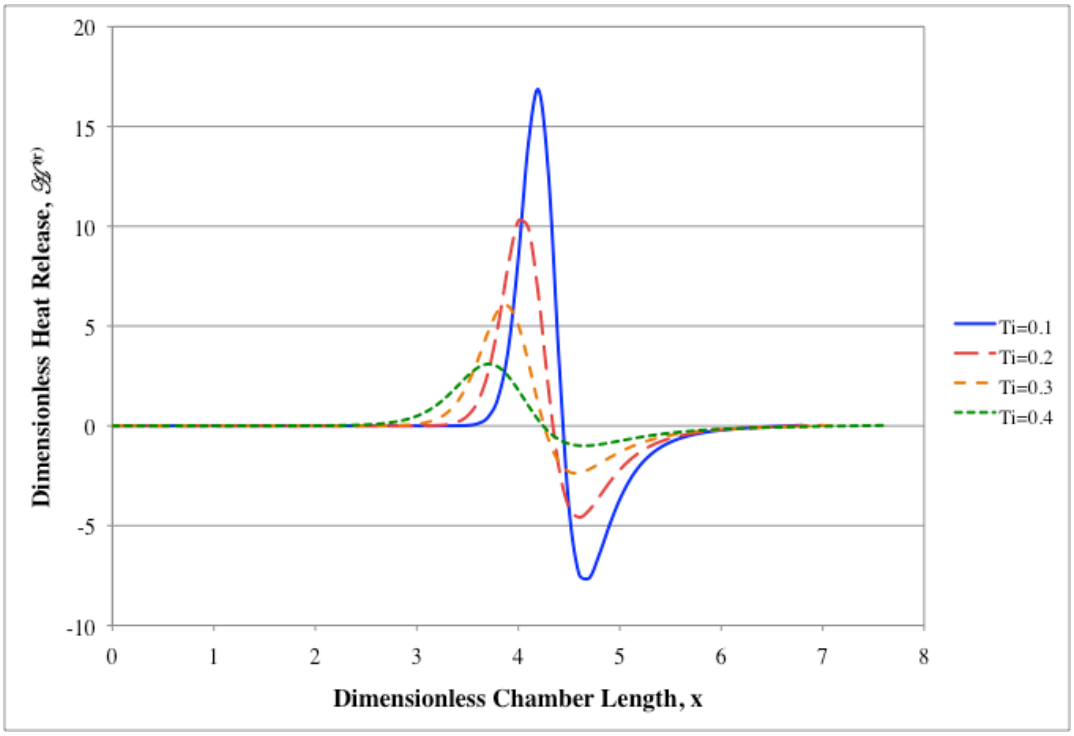

Figure 44. Real Unsteady Heat Release Component ($\mathscr{Y}^{(r)}$) for Varying Initial Temperature (γ=1.17, ω=1)

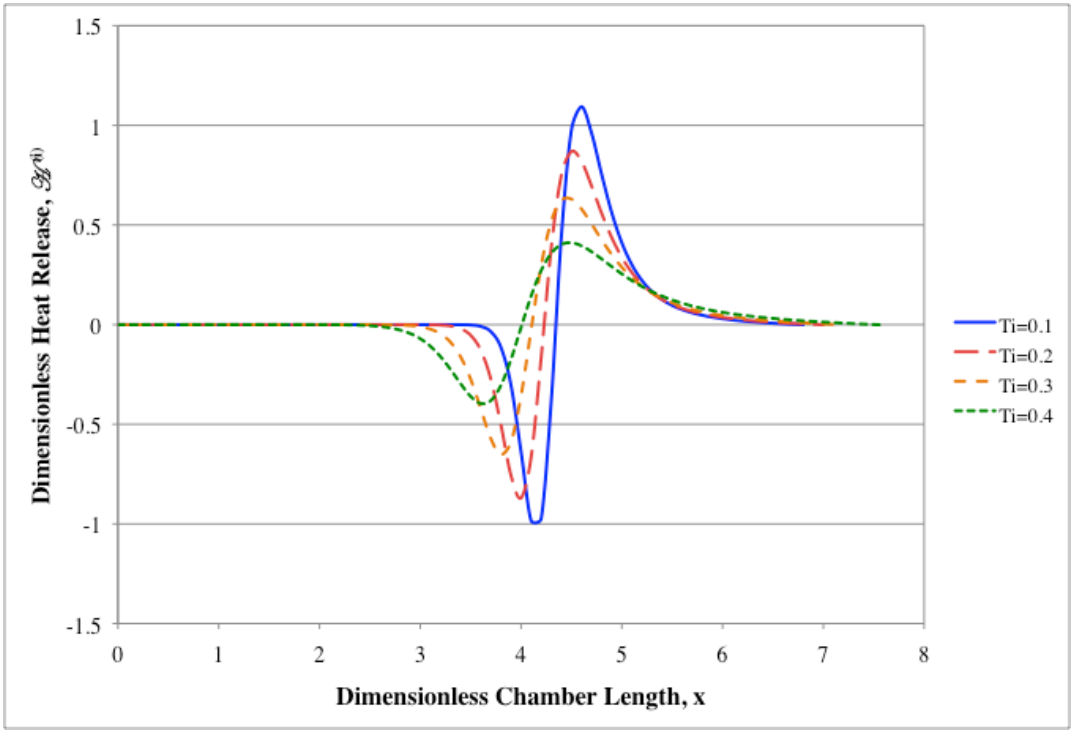

Figure 45. Imaginary Unsteady Heat Release Component ($\mathscr{Y}^{(i)}$) Varying Initial Temperature (γ=1.17, ω=1)

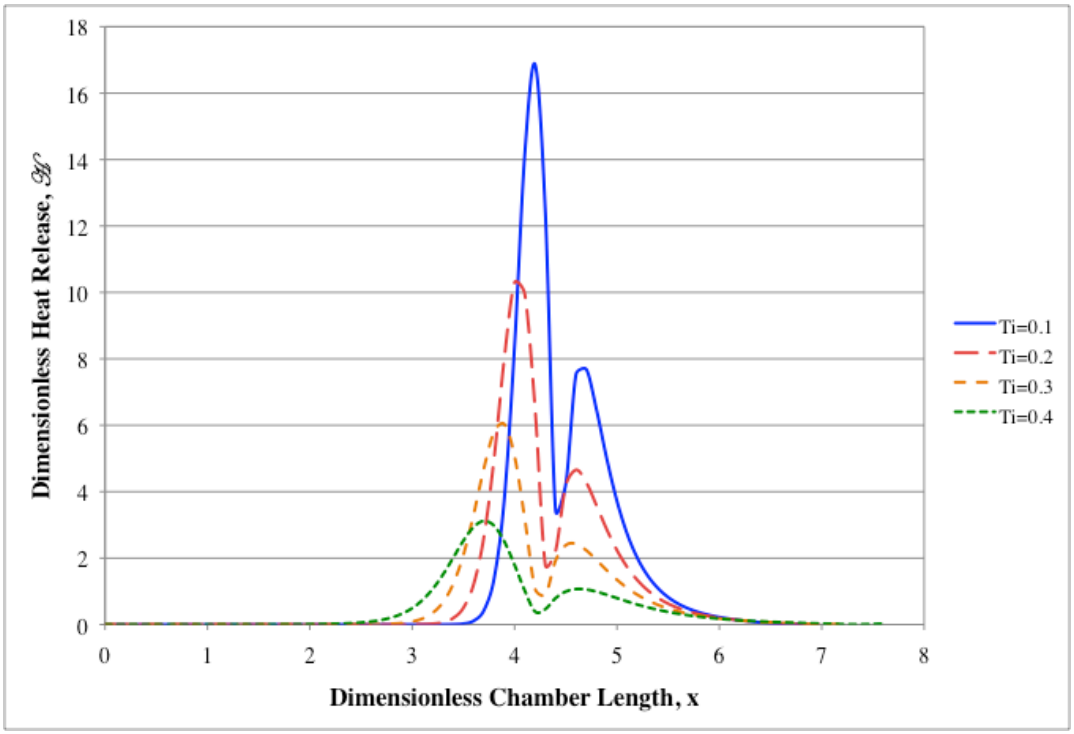

Figure 46. Unsteady Heat Release Amplitude ($\mathscr{H}_1$) Varying Initial Temperature (γ=1.17, ω=1)

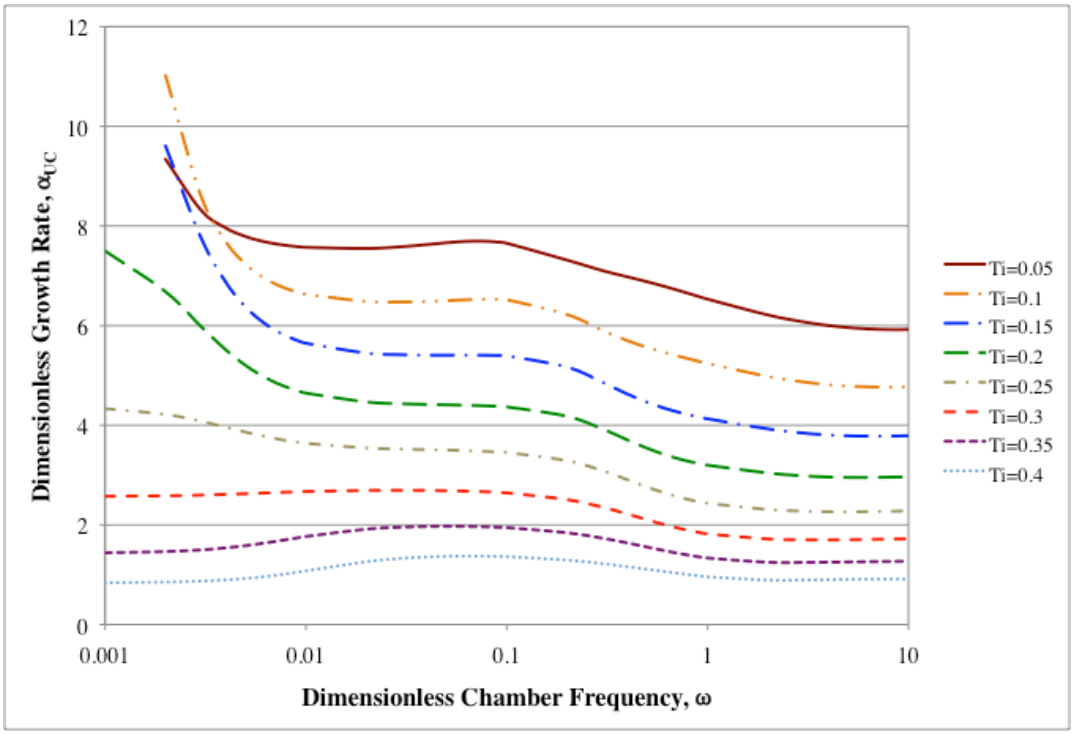

Figure 47. Dimensionless Growth Rate (α_{UC}) Varying Initial Temperature (γ=1.17)

To compare growth rate sensitivity to gamma versus sensitivity to initial temperature, Figure 48 shows the variation in dimensionless growth rate for a range of specific heat ratios for an initial dimensionless temperature of 0.35. This case is highlighted here due to its unusual sensitivity to specific heat ratio. The graph shows a greater amount of frequency sensitivity than the graph for varying initial temperature. The data reveals that the sensitivity decreases with reduced specific heat ratio. This figure indicates that propellants with high specific heat ratios are destabilizing. While the large destabilizing effect at mid-range frequencies with increasing ratio is interesting and should be investigated further in future work, when dimensionalized the sensitivity to specific heat ratio is actually small compared to other effects and may not be significant.

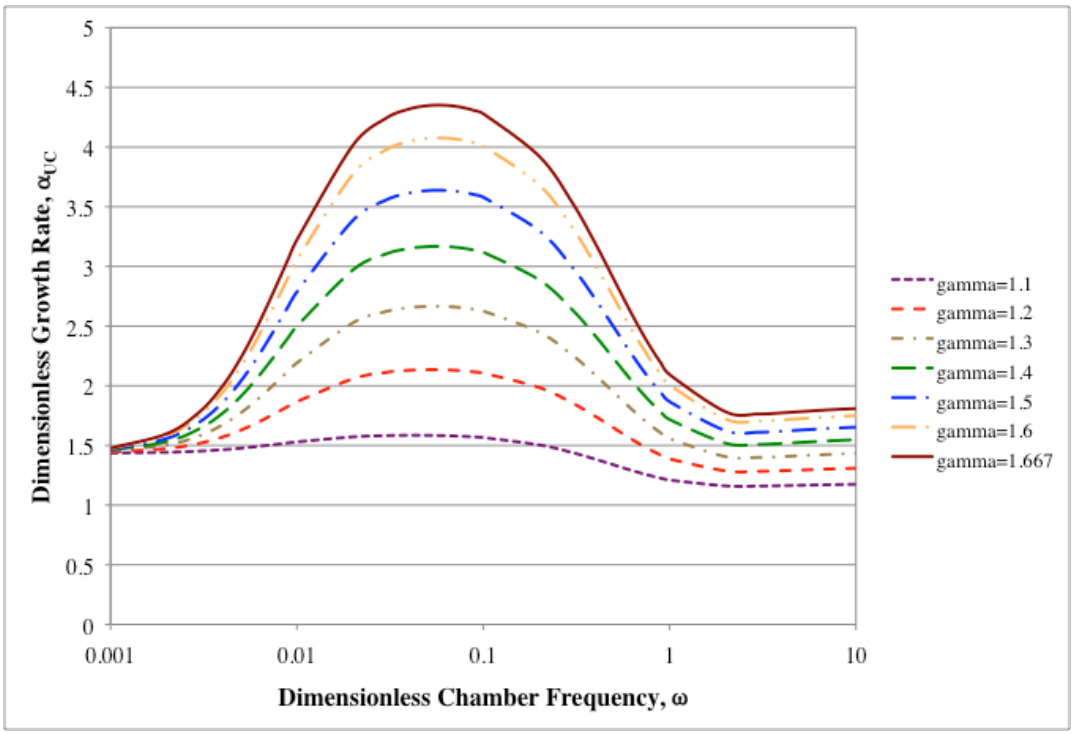

Figure 48. Dimensionless Growth Rate (α_{UC}) for Varying Gamma (T_i=0.35)

Since graphs for steady and oscillatory features were shown and discussed for the case of altering initial temperature, the graphs for the oscillatory properties for the case of varying specific heat ratio are shown in Appendix B.

Another way to display the sensitivity of the growth rate to initial temperature is through the following series of graphs. Figures 49-56 show the change in growth rate for varying gamma over the range of T_i=0.5-4.0. Noted by the growing contrast between the successive graphs, again, higher energy propellants (i.e. low T_i) are seen to have a destabilizing effect on the growth rate; this is easily seen by the decreasing values in the growth rate at the lowest frequency as initial temperature increases. However, it is interesting to note that the case for an initial temperature of 0.05 has a higher growth rate than that of 0.1. It can also be seen that as initial temperature increases, the sensitivity to chamber frequency increase and moves to lower frequency values. These results also show some frequency sensitivity that needs to be investigated further in future work.

This sensitivity to both specific heat ratio and initial temperature is displayed in Figure 57. While not identified in this effort, it appears that some combination of initial temperature and specific heat ratio may be a characteristic parameter.

It was determined that a comparison of propellant combinations could be made through dimensionless analysis based upon the two quantities of specific heat ratio and dimensionless initial temperature. The initial dimensionless temperature used was based upon the ratio of the initial propellant injection temperature to the typical chamber operating temperature for the propellant combination. Typical operating specific heat ratios were used.

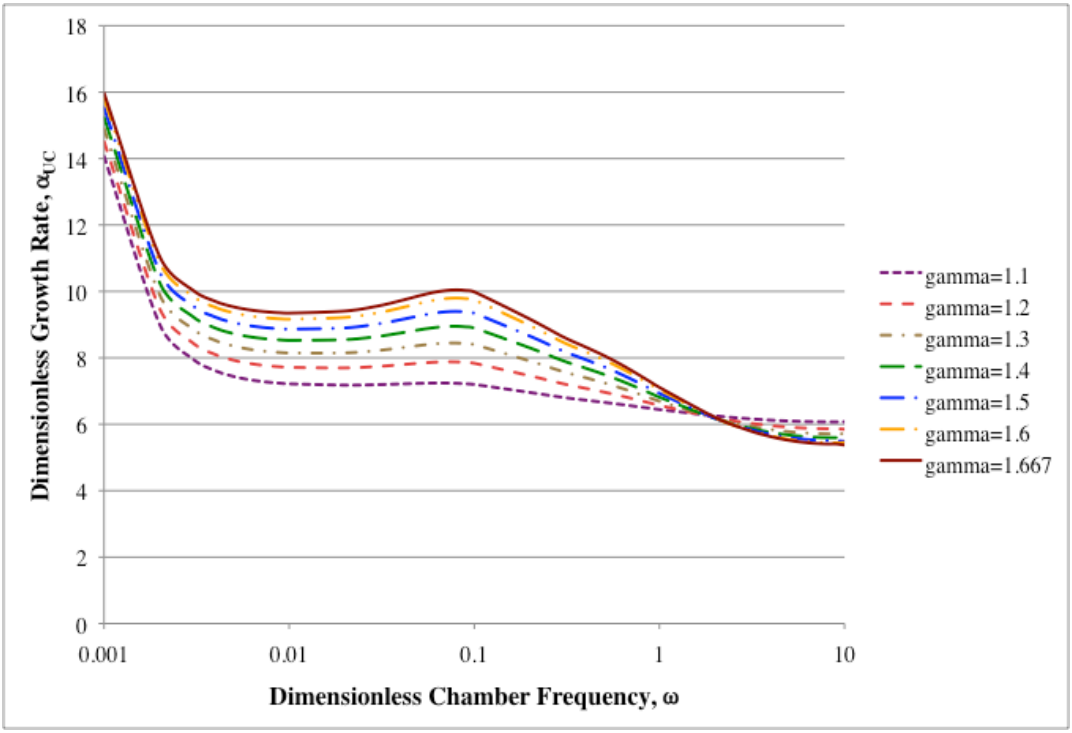

Figure 49. Dimensionless Growth Rate (α_{UC}) Varying Gamma (T_i=0.05)

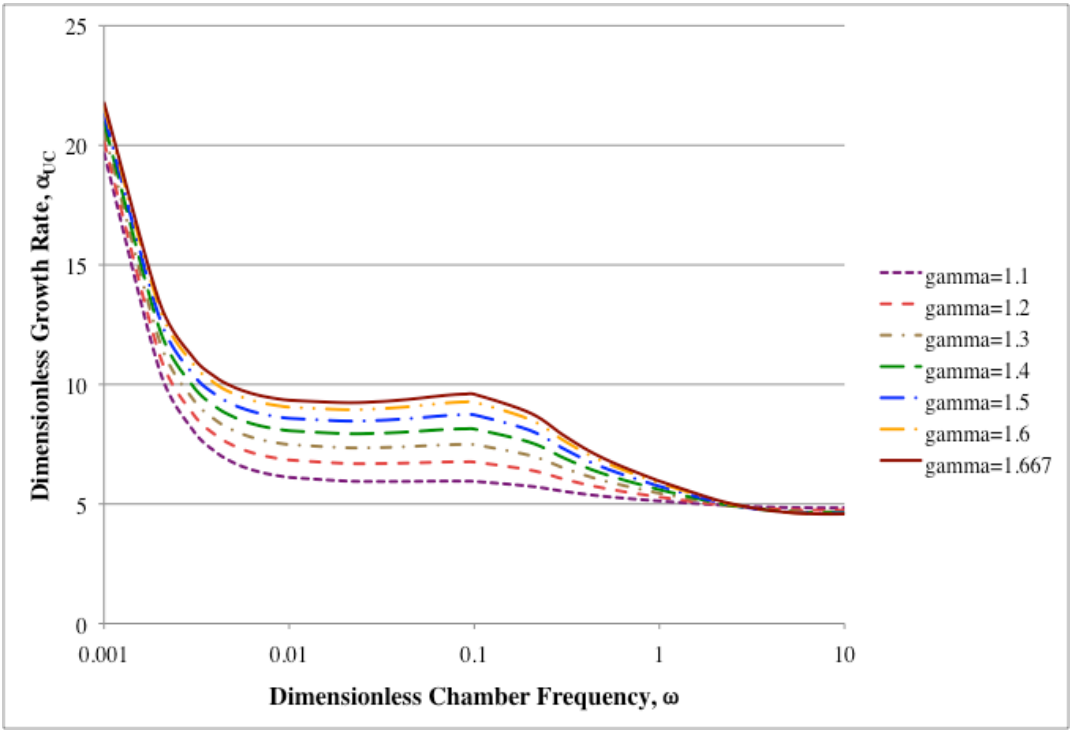

Figure 50. Dimensionless Growth Rate (α_{UC}) Varying Gamma (T_i=0.1)

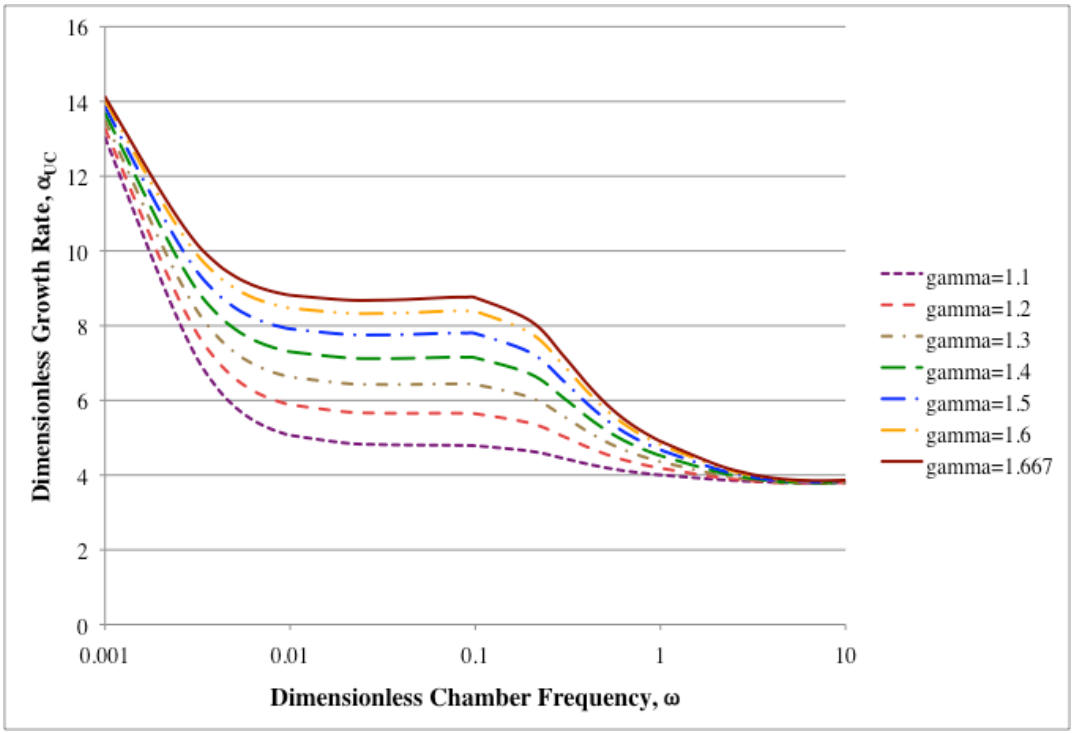

Figure 51. Dimensionless Growth Rate (α_{UC}) Varying Gamma (T_i=0.15)

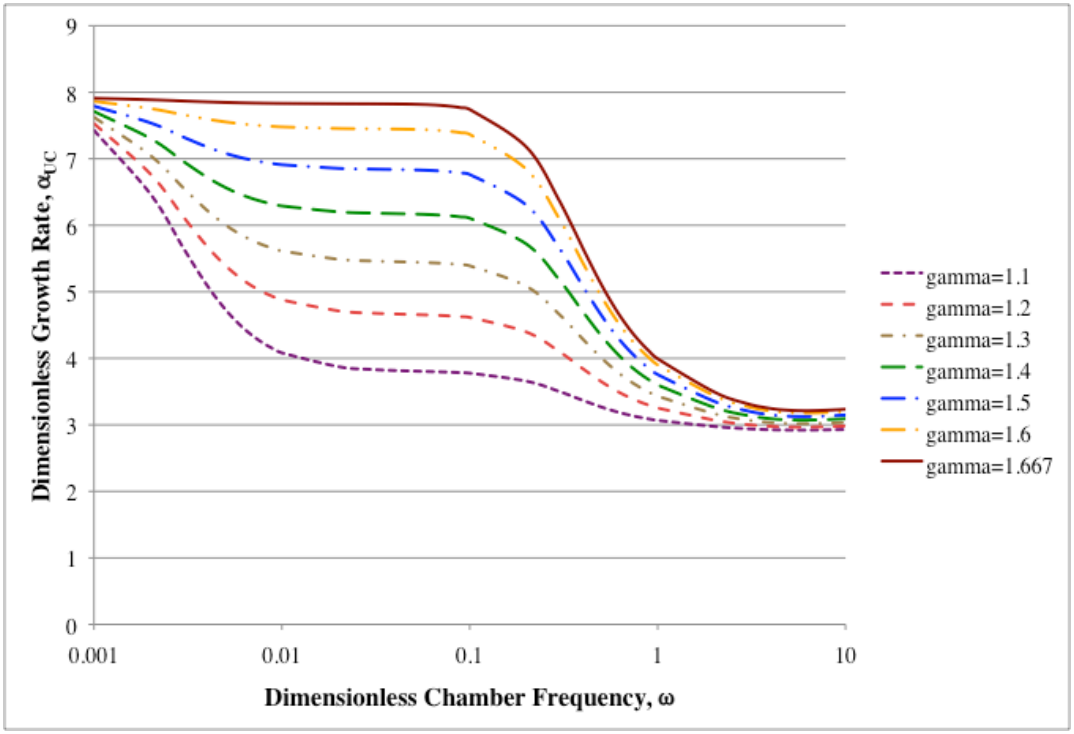

Figure 52. Dimensionless Growth Rate (α_{UC}) Varying Gamma (T_i=0.2)

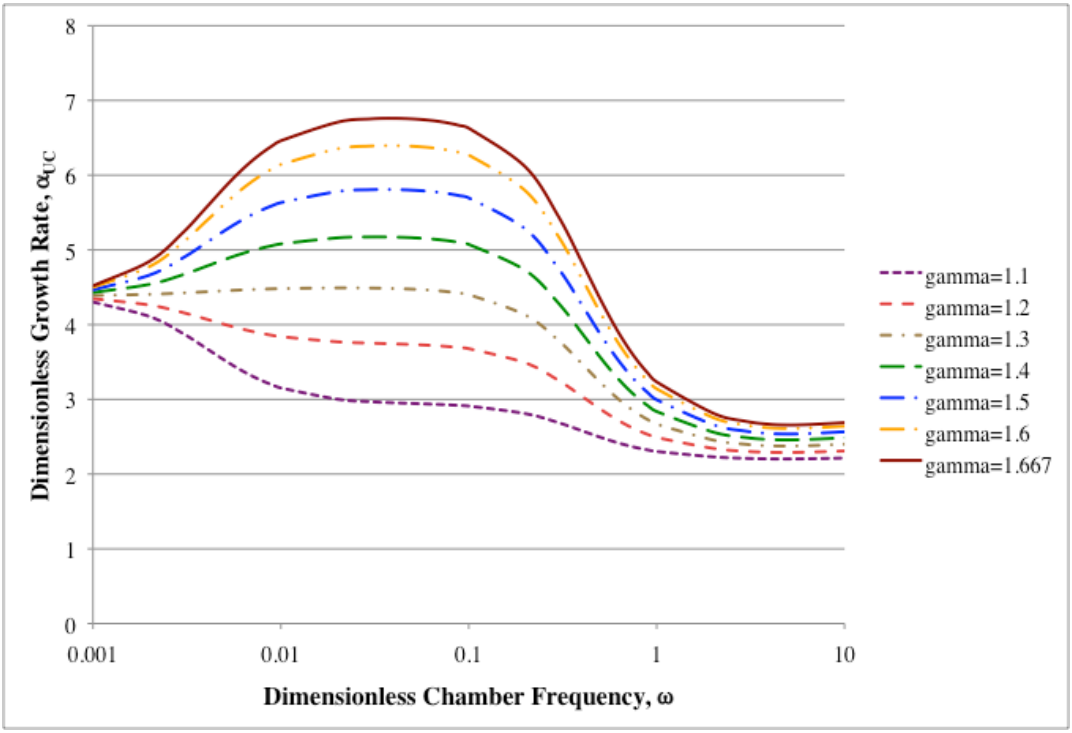

Figure 53. Dimensionless Growth Rate (α_{UC}) Varying Gamma (T_i=0.25)

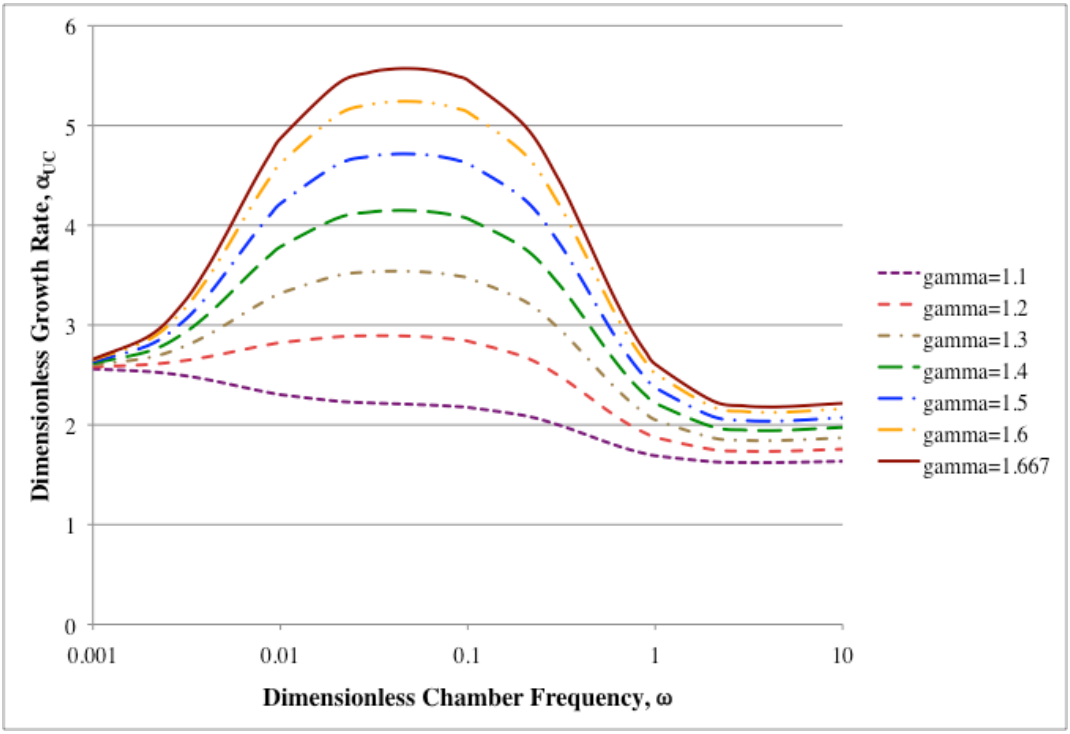

Figure 54. Dimensionless Growth Rate (α_{UC}) Varying Gamma (T_i=0.3)

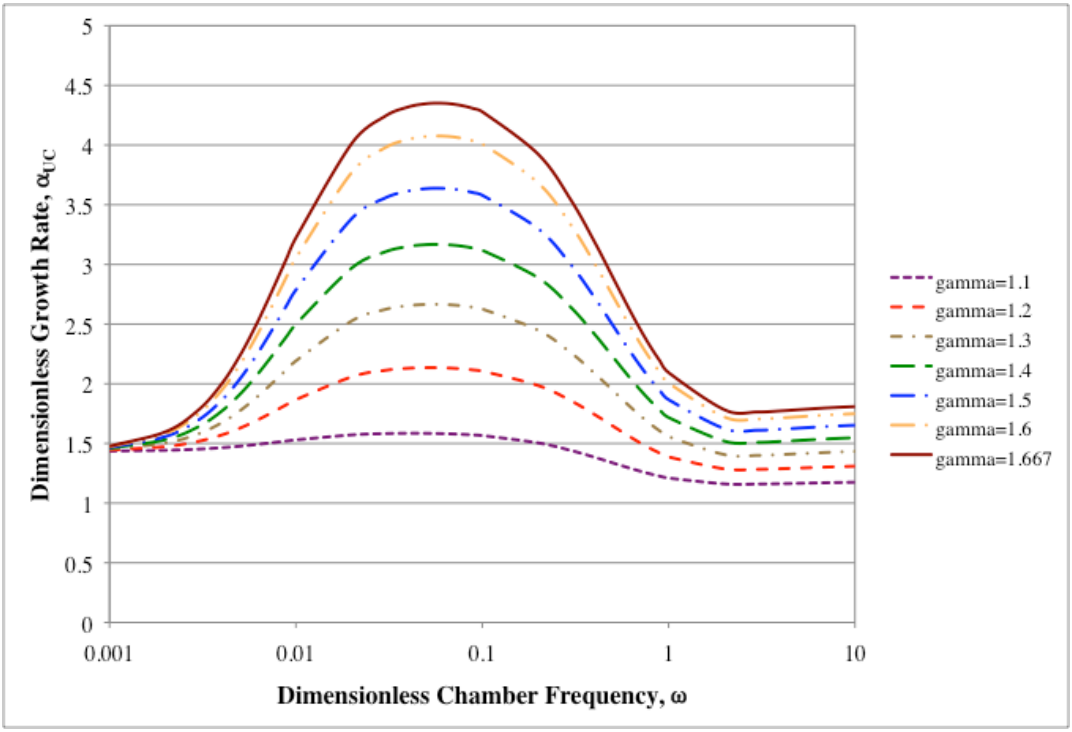

Figure 55. Dimensionless Growth Rate (α_{UC}) Varying Gamma (T_i=0.35)

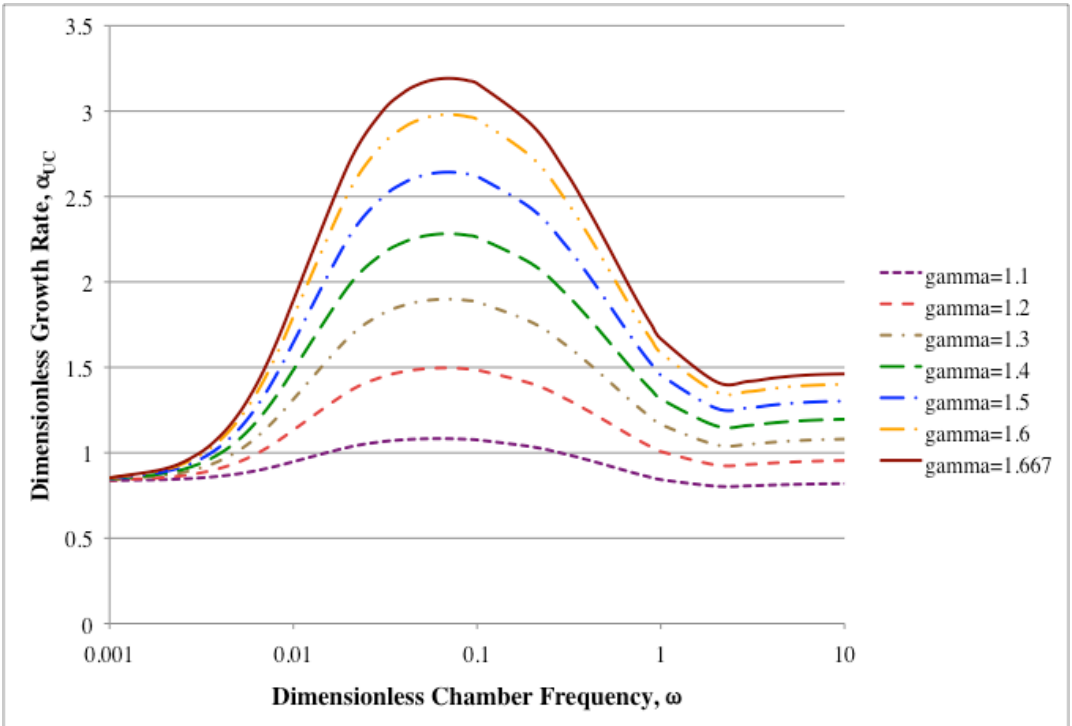

Figure 56. Dimensionless Growth Rate (α_{UC}) Varying Gamma (T_i=0.4)

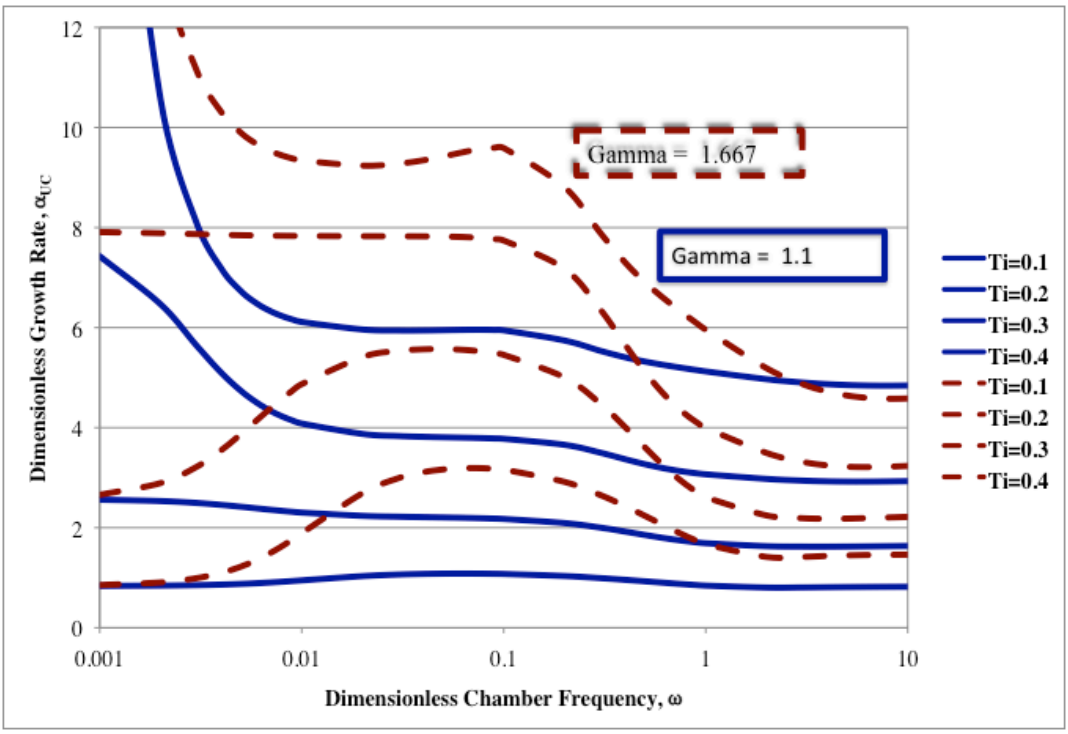

Figure 57. Change in Dimensionless Growth Rate (α_{UC}) over Varying Temperature for γ=1.1 and γ=1.667

Figure 58 shows the calculated growth rate for the monopropellant nitrous oxide for different nitrous oxide decomposition percentages [80]. Figure 59 shows the calculated growth rate for different mixture ratios for a typical liquid oxygen and methane propellant combination [80]. Figure 60 shows the calculated growth rate for different mixture ratios for a typical liquid oxygen and kerosene propellant combination; the values used specifically apply the PA-E liquid rocket engine [81]. Some of these, as well as other propellant combinations are combined together in Figure 61 [76, 80-81]. Note that the 90% hydrogen peroxide monopropellant has a very low growth rate value. This results because it has such a high initial temperature, as is the case in many monoprops.

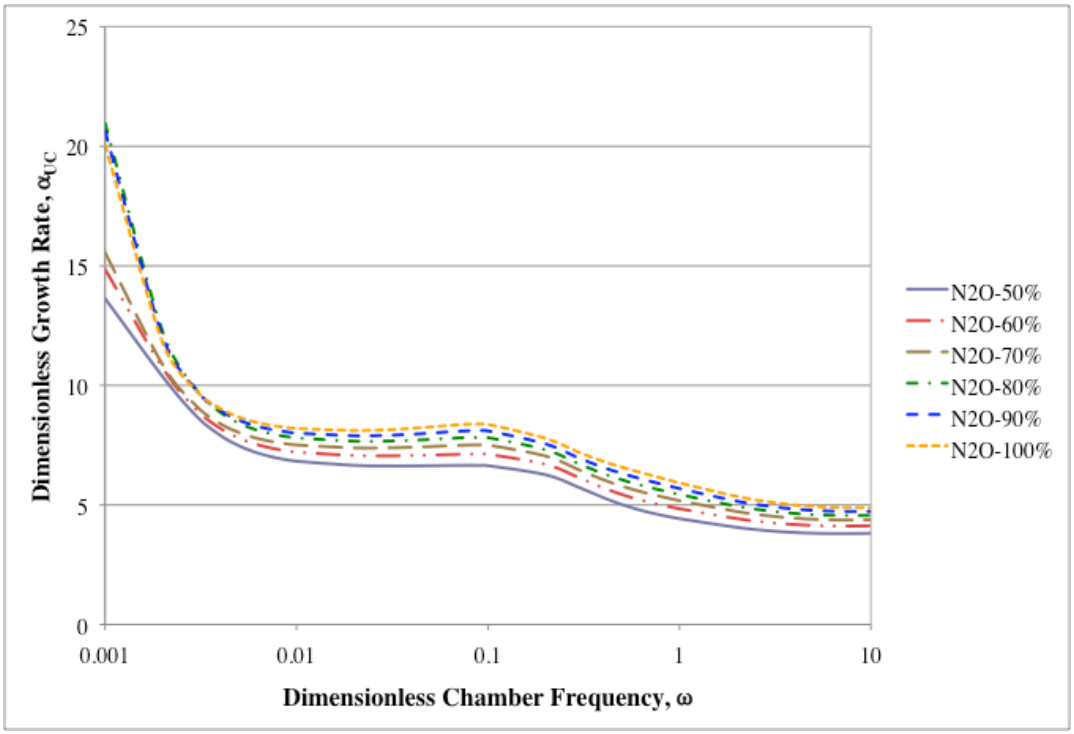

Figure 58. Dimensionless Growth Rate (α_{UC}) for Nitrous Oxide Decomposition

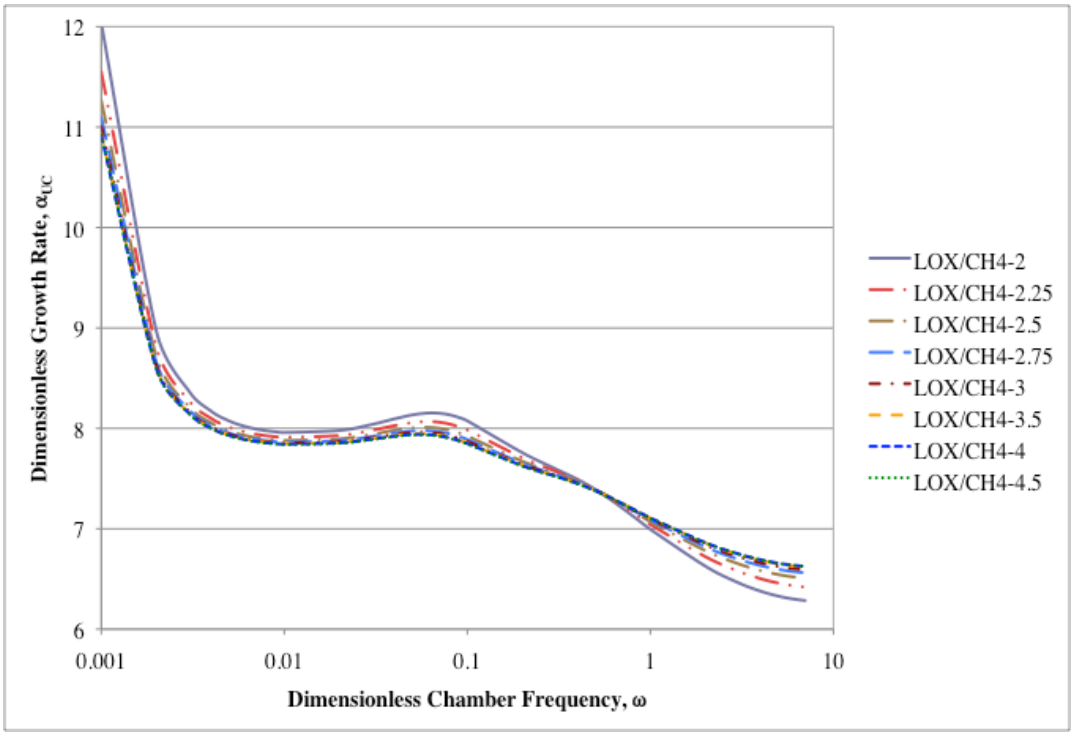

Figure 59. Dimensionless Growth Rate (α_{UC}) for LOX/CH_4

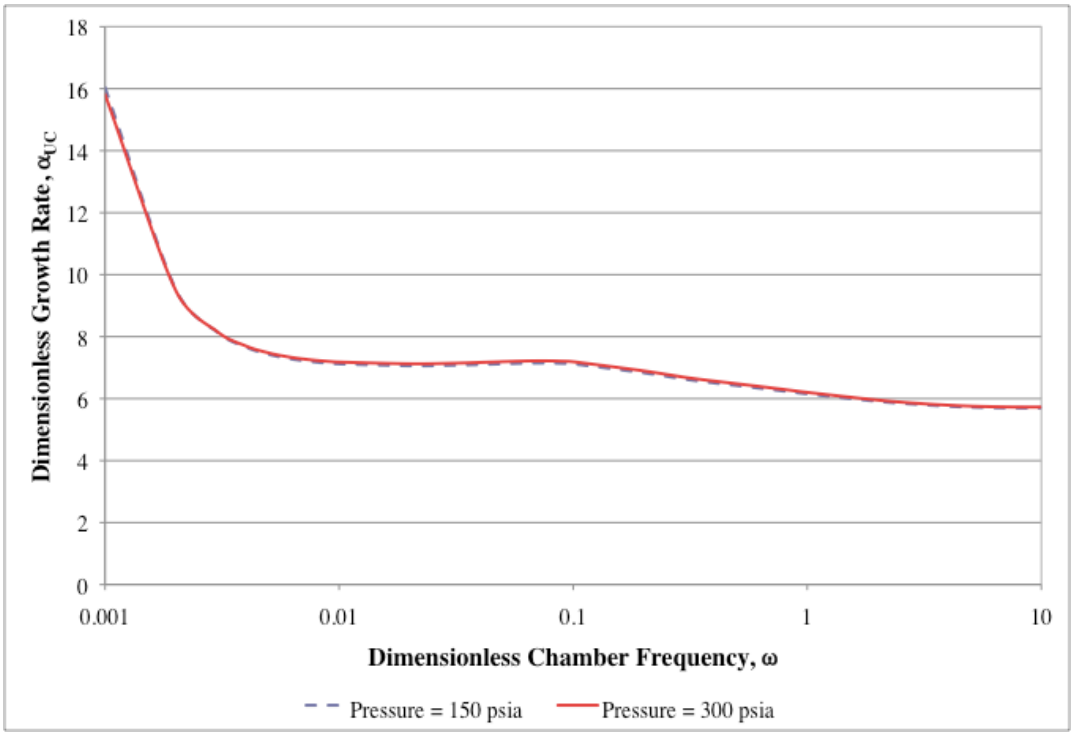

Figure 60. Dimensionless Growth Rate (α_{UC}) for LOX/RP-

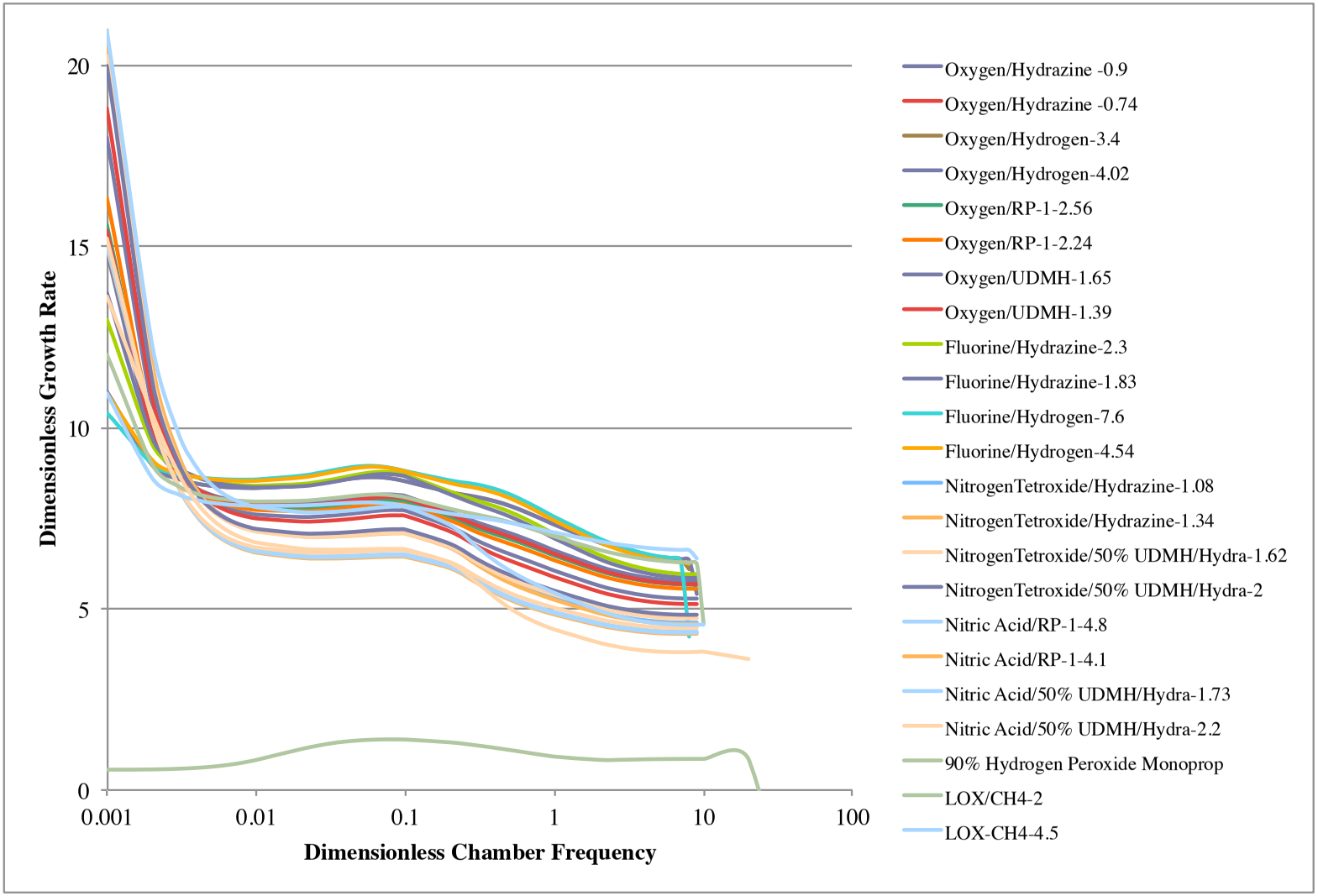

Figure 61. Comparison of Dimensionless Growth Rate (α_{UC}) for Different Propellant Combinations

Table 3 shows some of the data used in Figure 61. The mixture ratio value was used in determination of the initial temperature to be used for the particular mixture combination based off of the two propellants' initial temperatures. Then, based upon specified operating temperatures for a given propellant combination, as tabulated in Sutton [76] for typical liquid rocket engines, the dimensionless initial temperature could be determined for use in the program along with the specific heat ratio.

The following figures were produced as a different way to examine how growth rate based upon the three dimensionless variables, T_i, γ, and ω, altered as these variables changed in relation to one another. Figure 62 shows a comparison of how the growth rate changes for different specific heat ratios while varying initial temperature. This case was run for a dimensionless frequency of 0.001. Four other figures are included in Appendix B for logarithmic multiples of frequency. These figures seem to show a generally linear relationship for the change initial temperature versus specific heat ratio.

Figure 63 shows a comparison of how the growth rate changes for different chamber frequencies while varying initial temperature. This particular case was run for a specific heat ratio of 1.1. Six other figures are included in Appendix B for previously shown values for γ. These figures all show seemingly upward increases in growth rate as initial temperature decreases. All the frequency curves seem to follow similar near linear trends; however, the frequency of 0.001 has a markedly larger value than the others in all of the graphs. This is an interesting feature that may result because this dimensionless frequency range corresponds to the dimensional frequencies seen in following graphs for dimensional growth rates.

Table 3. Propellant Combination Data

Oxidizer	Fuel	Initial Oxidizer Temp (K)	Initial Fuel Temp (K)	Initial Mixture Temp (K)	Mix Ratio by mass	g	Chamber Temp (K)	T_0
Oxygen	Hydrazine	90	386.66	260.49	0.74	1.25	3285	0.08
		90	386.66	246.14	0.9	1.25	3404	0.07
	Hydrogen	90	20.4	74.18	3.4	1.26	2959	0.03
		90	20.4	76.14	4.02	1.26	2999	0.03
	RP-1	90	500	216.54	2.24	1.24	3571	0.06
		90	500	205.17	2.56	1.24	3677	0.06
	UDMH	90	336	192.93	1.39	1.25	3542	0.05
		90	336	182.83	1.65	1.25	3594	0.05
	Hydrazine	85.02	386.66	191.61	1.83	1.33	4553	0.04
		85.02	386.66	176.43	2.3	1.33	4713	0.04
Fluorine	Hydrogen	85.02	20.4	73.36	4.54	1.33	3080	0.02
		85.02	20.4	77.51	7.6	1.33	3900	0.02
	Hydrazine	294.3	386.66	338.70	1.08	1.26	3258	0.10
		294.3	386.66	333.77	1.34	1.26	3152	0.11
Nitrogen Tetroxide	50% UDMH and Hydrazine	294.3	361.33	319.88	1.62	1.24	3242	0.10
		294.3	361.33	316.64	2	1.24	3372	0.09
	RP-1	355.7	500	383.99	4.1	1.22	3175	0.12
		355.7	500	380.58	4.8	1.22	3230	0.12
Nitric Acid	50% UDMH and Hydrazine	355.7	361.33	357.76	1.73	1.22	2997	0.12
		355.7	361.33	357.46	2.2	1.22	3172	0.11

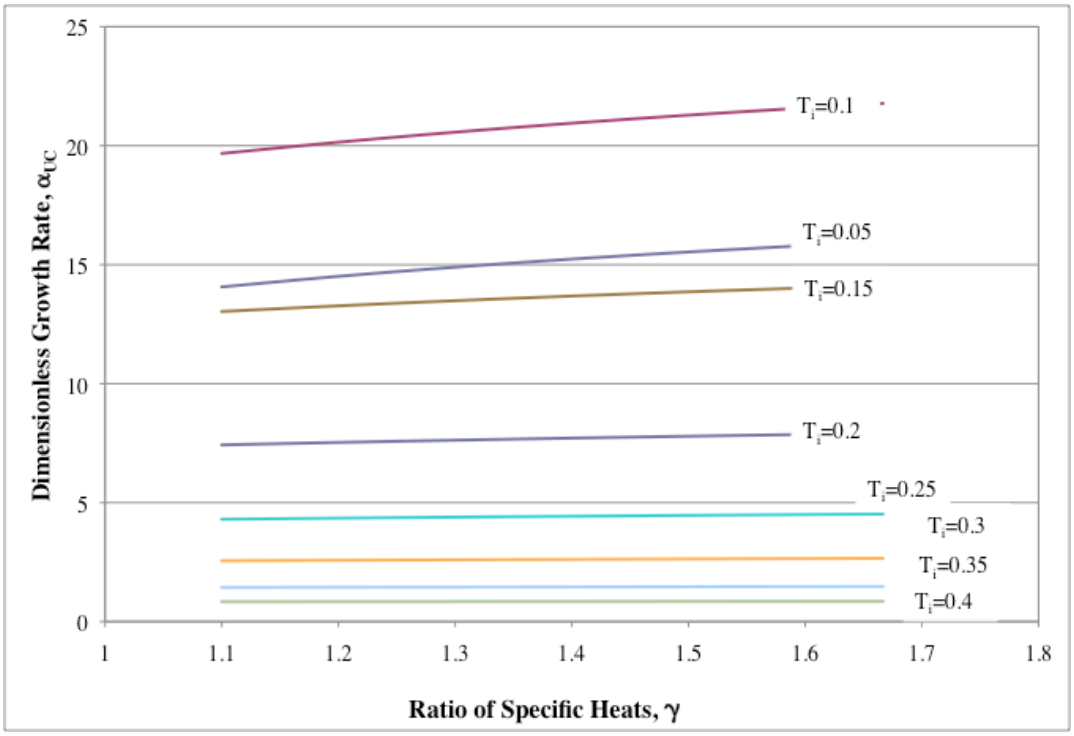

Figure 62. Comparison of Dimensionless Growth Rate (α_{UC}) for Different Gamma Over Varying Initial Temperature (ω=0.001)

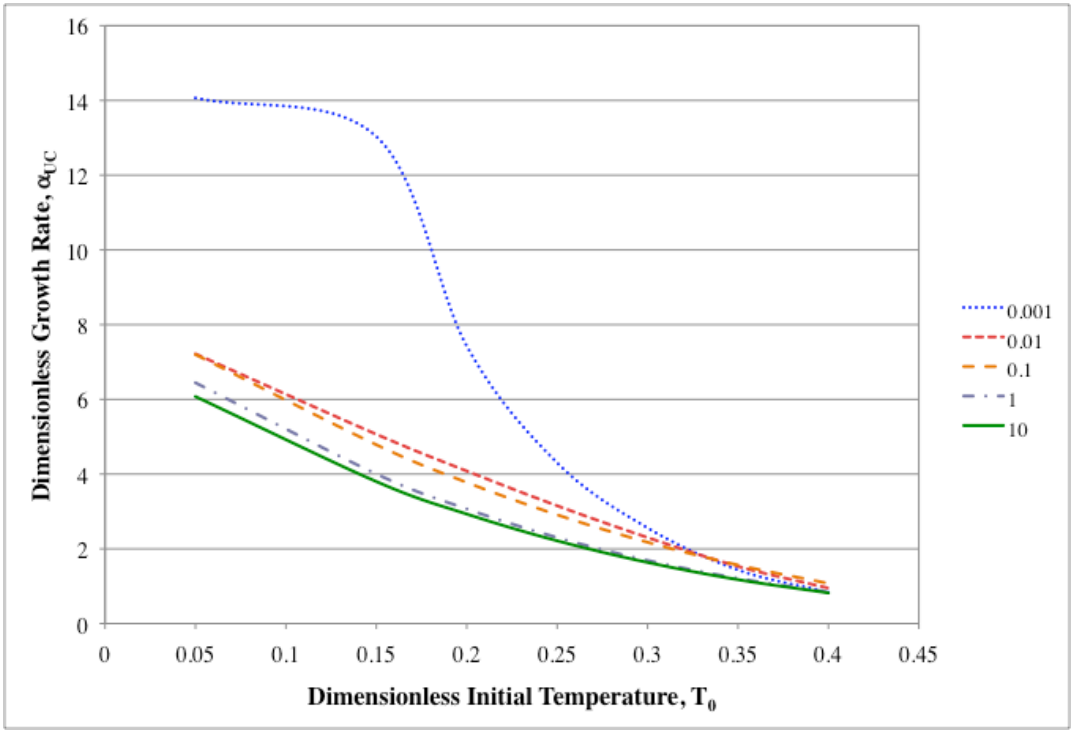

Figure 63. Comparison of Dimensionless Growth Rate (α_{UC}) for Different Chamber Frequency Over Initial Temperature (γ=1.1)

Figures 64-66 show comparison of the oscillatory temperature, velocity, and heat release with the oscillatory pressure wave computed as explained for Figure 40 using the expressions for the perturbation expansions in the unsteady analysis. It can be seen that these properties are all in phase. Figure 67 shows the comparison of the oscillatory temperature and heat release. Since these show the temperature and heat release to be in phase, this supports the driving of oscillations in the system.

6.5 – Analysis of Dimensional Results

To obtain the unsteady combustion growth rate in dimensional form, dimensionalizing parameters were simply applied to the dimensionless results. Then dimensional input parameters for system behavior were applied to obtain the dimensional growth rate result. The values used to return the system to dimensional form are shown in Table 4. These values were obtained through email exchanges of simulation data computed by French [82]; they refer to typical operating conditions in an Oxygen-Methane liquid rocket engine for an operating pressure of 750 psia [80].

Figures 68 and 69 show the dimensional growth rate for a specific heat ratio of 1.2 for a chamber length of 0.5 meters and 3 meters, respectively. The initial chamber length and specific heat ratio were selected based on typical liquid rocket systems. The longer length is shown for contrast, though not a typical liquid rocket length. The first six oscillatory modes are shown in the figure. This growth rate result is not dependent upon the chamber radius since only longitudinal modes are considered in this one-dimensionally constrained model. It can be seen in the expression for the heat release growth rate (equation 187) that the radius contribution cancels mathematically.

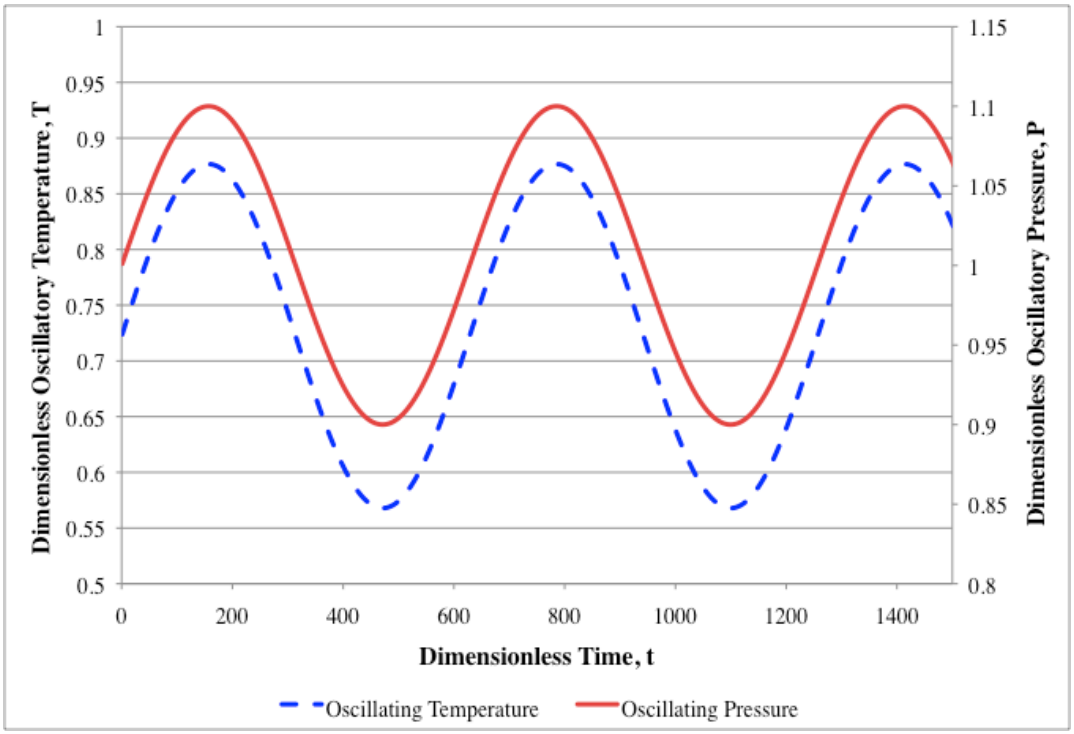

Figure 64. Phase Comparison of Oscillatory Temperature (T) and Pressure (P) (ω=0.01)

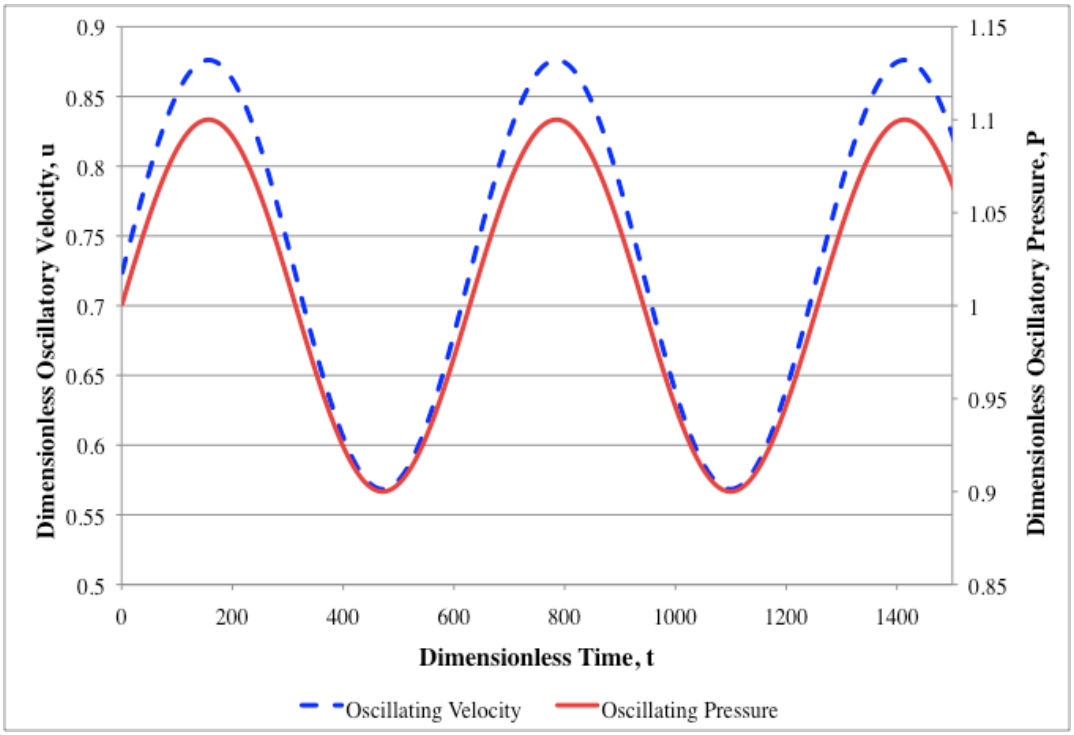

Figure 65. Phase Comparison of Dimensionless Oscillatory Velocity (u) and Pressure (P) (ω=0.01)

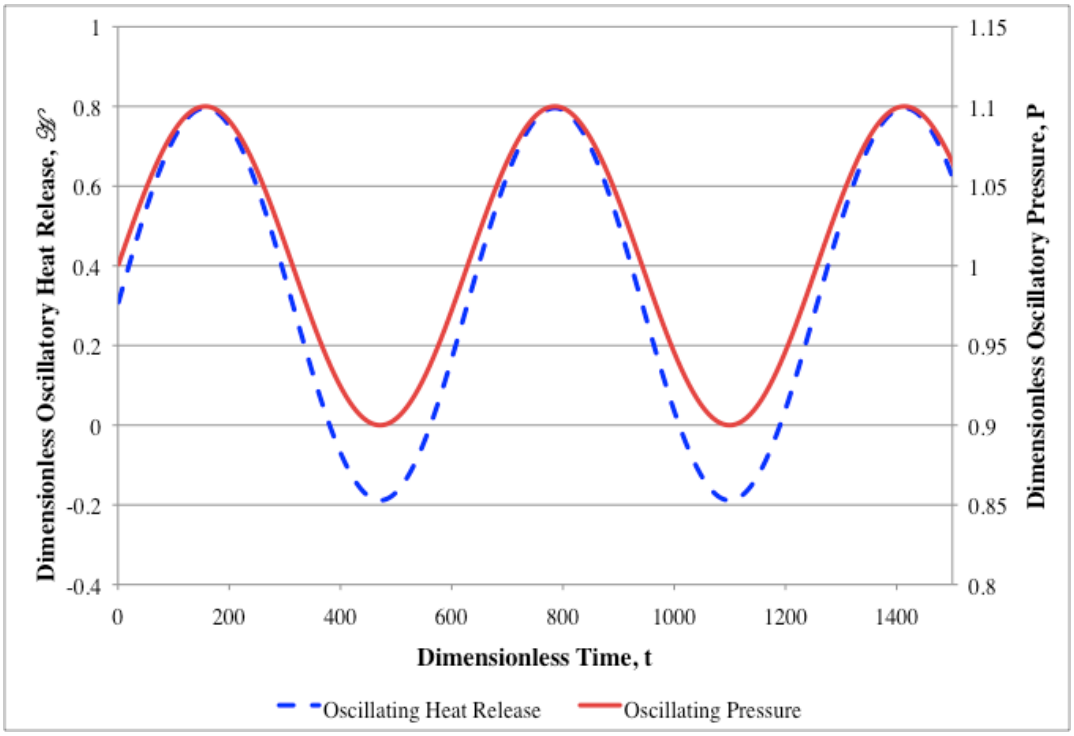

Figure 66. Phase Comparison of Dimensionless Oscillatory Heat Release (𝒢) and Pressure (P) (ω=0.01)

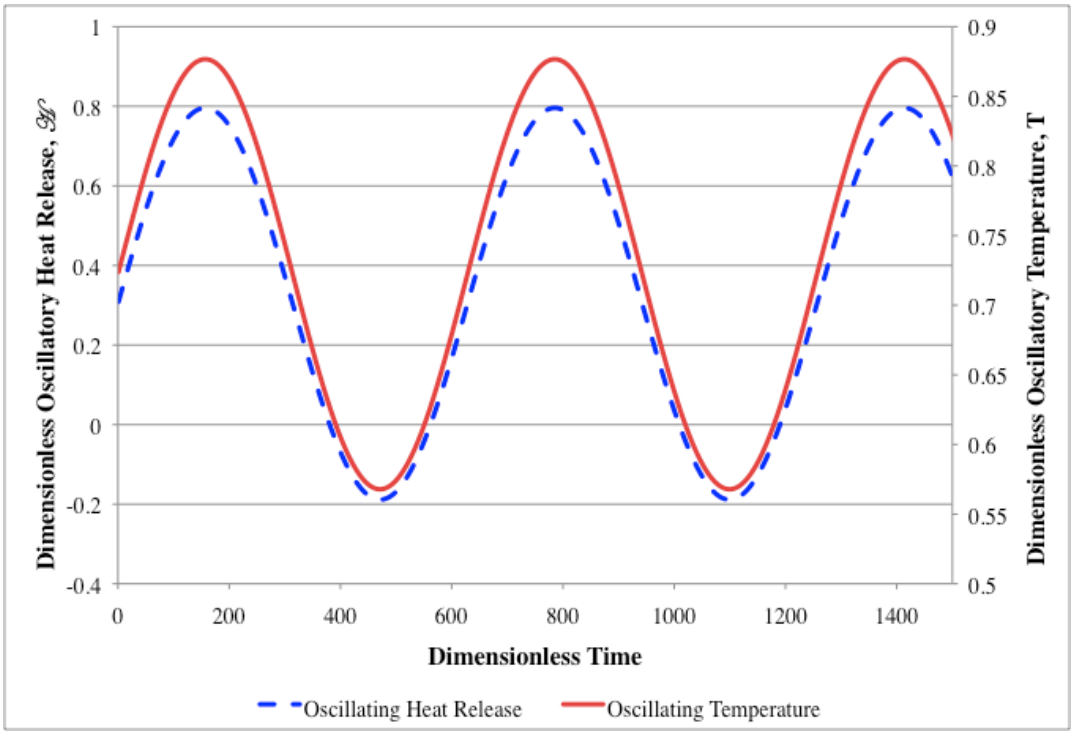

Figure 67. Phase Comparison of Dimensionless Oscillatory Heat Release (𝒢) and Temperature (T) (ω=0.01)

Table 4. Dimensionalizing Variable Values

Dimensional Variables	Value
Chamber Temperature (K)	3518.67
Chamber Velocity (m/s)	5
Specific Heat (J/kg-K)	2209.2
Thermal Conductivity (W/m-K)	0.36658
Chamber Pressure (Pa)	3.45e6 – 1.03e7 (500 -1500 psi)

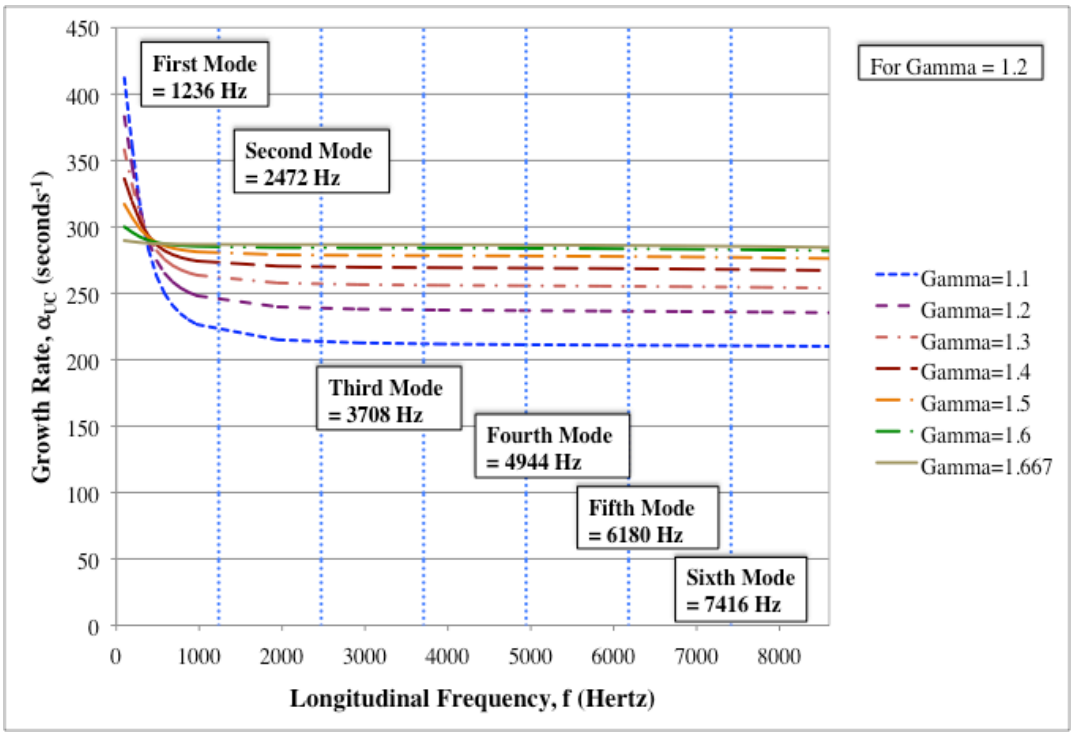

Figure 68. Dimensional Growth Rate (α_{UC}) over Longitudinal Frequency for L=0.5 meters (Noting Modes for a System with γ=1.2)

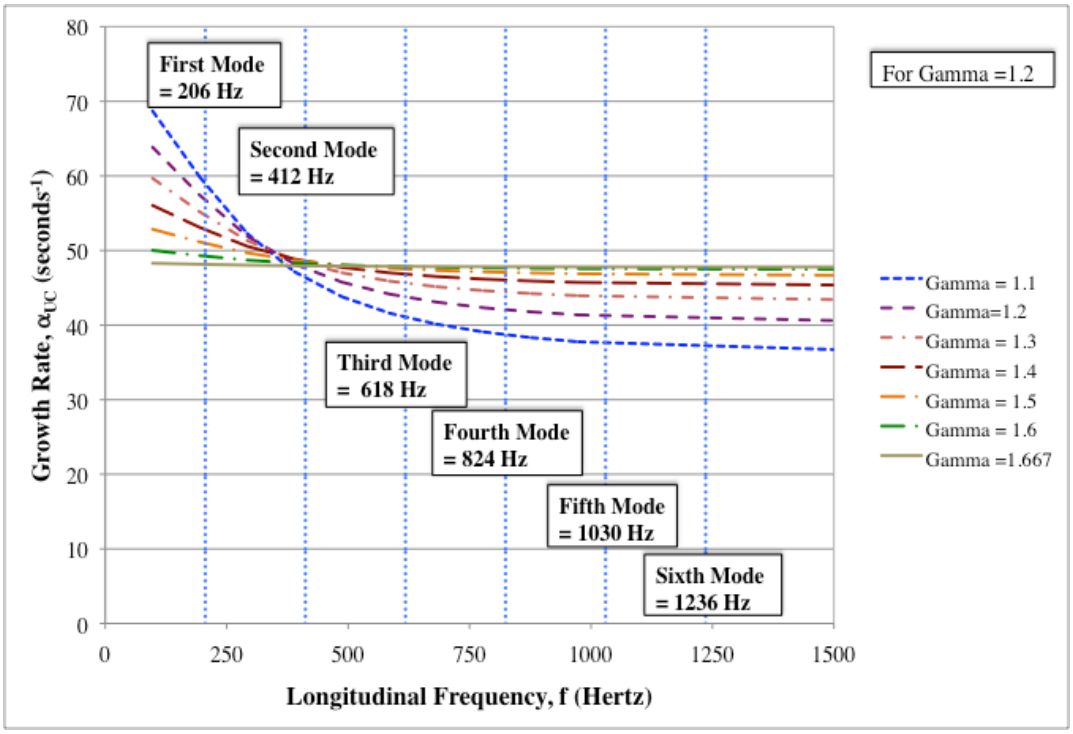

Figure 69. Dimensional Growth Rate (α_{UC}) over Longitudinal Frequency for L=3.0 meters (Noting Modes for a System with γ=1.2)

six oscillatory modes are shown in the figure. This growth rate result is not dependent upon the chamber radius since only longitudinal modes are considered in this one-dimensionally constrained model. It can be seen in the expression for the heat release growth rate (equation 187) that the radius contribution cancels mathematically.

For a typical liquid rocket chamber length of 0.5 meters, the growth rate has a value between 200 and 300 s^{-1}. Looking at the growth rate values obtained for the chamber length of 3.0 meters, it can be seen that longer chambers reduce destabilizing effects and shift frequencies of interest. These growth rate values range from 40 to 70 s^{-1}. While the dimensional results still show some sensitivity to specific heat ratio (γ), there is little frequency sensitivity except at very low frequencies in long chambers.

The magnitude of the growth rate values in these figures is consistent with those of other growth rates for other stability mechanisms in similar sized chambers. Figure 70 shows the change in nozzle damping growth rate over frequency, as computed by French [82]. Note that the nozzle damping results are insensitive to chamber pressure. It can be seen that for a similarly sized chamber, the growth rates are of a comparable size, though negative, representing a damping feature. Since nozzle damping is traditionally one of the largest growth rate mechanisms, it can be concluded that calculating the unsteady combustion effects is important since it is similar in magnitude.

As with all of the mechanisms, a small growth rate has a much larger effect on oscillation amplitude in a large chamber than it does in a small chamber. Therefore, a large growth rate is needed to drive a significant oscillation in a small chamber, while the same oscillation amplitudes can be achieved with a much lower growth rate in a larger chamber. This is a key factor that promotes instability when scaling a small engine to a larger size [2, 40].

Additionally, increasing the chamber length while maintaining a constant propellant flow decreases the growth rate by averaging the unsteady energy released over a larger volume. This can be seen in the difference in magnitude in Figures 68 and 69 with increased chamber length. However, it is important to note that the natural frequencies of these chambers also vary with length.

Figure 71 shows how the unsteady combustion growth rate for a chamber length of three meters changes over chamber pressure. In contrast to the pressure independent nozzle damping growth rate in Figure 69, it has a linear dependence upon pressure.

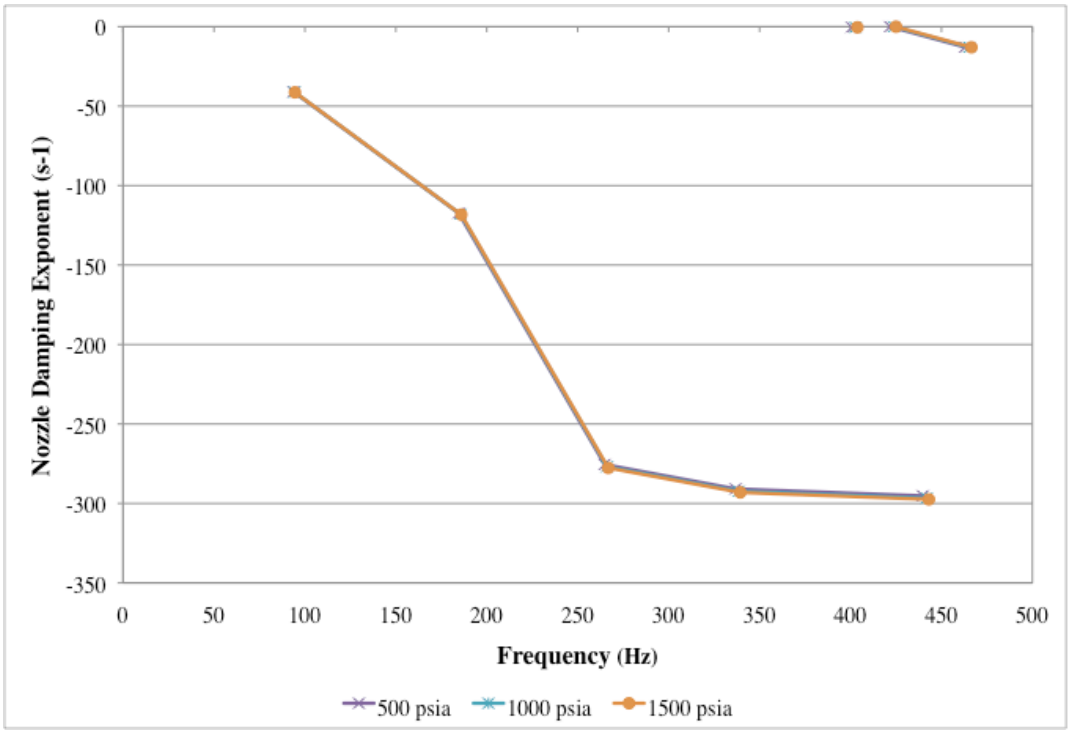

Figure 70. Nozzle Damping Growth Rate (α_{ND}) Over Changing Chamber Pressure

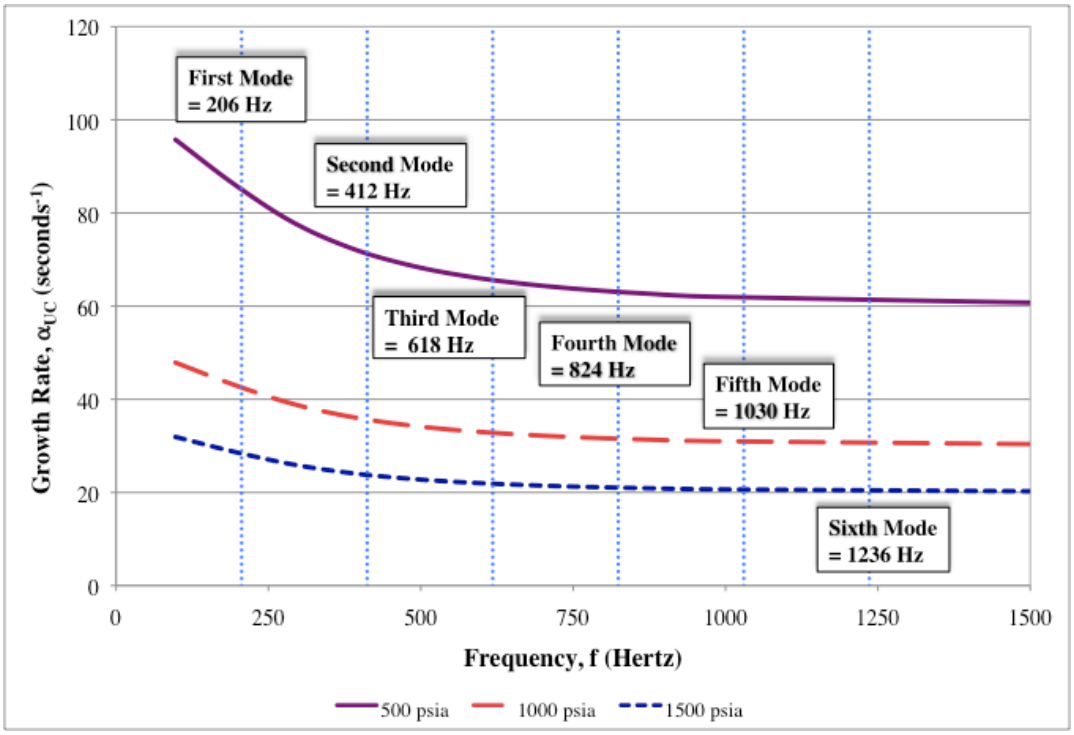

Figure 71. Dimensional Growth Rate (α_{UC}) for L=3.0 meters Over Changing Chamber Pressure

CHAPTER 7 – RECOMMENDATIONS AND FUTURE WORK

The research conducted in this dissertation was done with the intent of increasing the ability to predict the stability of combustion systems, specifically liquid rocket systems. This analysis provides initial insight into the magnitude and effect of unsteady combustion and the resulting volumetric heat release on the stability within a liquid rocket system. It forms a foundation for an ongoing effort to fully simulate the detailed behavior of the combustion process and its influence upon the system stability. As a result, there are several adjustments, from the assumptions discussed in Chapter 4, that must be made to the model.

Upon completion of this work, the first task to be performed is to carry out the above analysis in dimensional form. This must be done because the model into which it will be incorporated determines all of the other stability characteristics dimensionally. Remember, the only reason this analysis was done in dimensionless form was because it was desired to determine which system features had a direct effect upon the stability. The above calculations can be easily done in dimensional form by performing the initial perturbation expansion and separation process in dimensional form.

Additionally, the basic assumptions will need to be removed one by one as each adds restrictions and inaccuracies into the model. The first assumption to be removed will most likely be that of one a one dimensional laminar flame. Instead, the flame will be remodeled in two or three dimensions. While this should be relatively easy to implement, a full three-dimensional simulation is expected to be computationally intensive. Therefore, the next step may be to implement the model in two dimensions.

The assumption of a one-dimensional flame was essentially looking at the problem as a streamtube. Incorporation of two-dimensionality would allow for the representation of the chamber volume as a matrix of streamtubes. Then the effects each of the streamtube contributions across the chamber can be combined together to represent the entire three-dimensional stability contribution. This is acceptable, since experience has shown that there is little mixing between stream tubes in rockets [40, 80].

Also, this current stability analysis only concentrated upon the effects due to longitudinal waves in a system. With the extension to three dimensions, the effects due to transverse waves in the system can be examined. Analysis of transverse waves stability, not presented here, is quite a bit more involved in terms of understanding the interaction of the acoustic modes with the combustion processes. It is necessary to extend the analysis to transverse waves since those are typically of the most interest in liquid rocket stability analysis.

The assumption of a premixed propellant would likely be the next assumption to be removed. The process of mixing and vaporization is quite involved process that will increase the complexity of the analysis a great deal. This will require two- or three-dimensional modeling of the flow field including two-phase effects. As part of this effort, the combustion model would be expanded to include turbulent flame effects.

The movement towards inclusion of multiple step reactions both forwards and backwards in a reaction process will be one of the last inclusions into the modeling. Increasing the steps in a process greatly increases the amount of species concentrations of which to keep track. Computation time drastically increases. Simulation of even the simplest reaction to form water involves over thirty forward and backward reactions

between compounds forming and breaking apart before actual water is produced.

Also, quantities such as specific heat, specific gravity, and the coefficient of heat conduction will be represented more realistically. Additionally, the isobaric assumption will need to be removed, allowing the steady and unsteady pressure to vary across the chamber volume. The constant coefficient and pressure assumptions used in this effort were merely to simplify the model.

CHAPTER 8 – CONCLUSIONS

This dissertation presents an approach to evaluate the effect of unsteady combustion heat release on the overall combustion instability of a liquid rocket engine or other propulsion device. In other words, this approach allows the stability effects of unsteady chemical kinetics to be isolated from other processes (e.g. mixing), providing the means for sensitivity to key parameters to be explored. Clarification of these effects will aid in understanding overall combustion instability phenomena.

This work includes an overview of the formulation for the heat release linear growth rate equation explaining how it fits within the overall Energy Corollary Method. This equation is then implemented using a simplified model for a generic reaction. Using this model, initial insight into the variation of the linear growth rate for a range of frequencies was gained.

This investigation was performed with the intent of determining whether the unsteady combustion process was indeed a driving terms as has often been suspected. It can be seen in both dimensionless as well as dimensional form that the calculated growth rate shows that the heat release due to unsteady combustion in a system behaves as a driving mechanism. The study also showed that the growth rate due to volumetric heat release has a magnitude comparable to those growth rates of other stability mechanisms in similar sized engines, most notably that of nozzle damping.

A sensitivity analysis was performed to determine the effect of various system parameters upon the heat release growth rate. The dimensionless results showed

interesting growth rate sensitivity to both the initial temperature and the specific heat ratio. It was seen that for a lower value temperature, there was a greater value for the heat release growth rate, since a greater amount of energy was required to reach the end state condition. There was also sensitivity to the specific heat ratio at mid frequency ranges that moved to lower frequency as initial temperature increased. The results reveal a dependency upon frequency that will need to be examined in more detail in future efforts. This and other factors will be explored during the ongoing research and development effort.

Since focus was placed upon longitudinal waves within the chamber, resulting in investigation of a one-dimension flame, there was no radius effect when dimensionalized. A point of interest to those in the field is that unlike features such as nozzle damping, it was discovered that the volumetric heat release does have a linear dependence upon the value of the chamber pressure.

With the establishment of the heat release growth to indeed be a driving force, it is desirable to increase the fidelity of the unsteady combustion model to examine how different combustion features affect the value of this growth rate. Recommendations for future work, discussed in the previous chapter, include the incorporation of combustion features such as mixing, as well as the complex multi-step chemical kinetics to take the place of the current one-step generic reaction model.

The results of this analysis have established that the effects of unsteady combustion upon the stability of a system is an important mechanism that warrants further investigation. This study establishes a firm foundation upon which to extend the

analysis of this important mechanism to fully understand all of its effects within a rocket system. Since the representation of the unsteady combustion within a system is an ongoing effort, it will take a great deal of time and effort to tackle this problem. However, upon completion of the suggested work, this analysis will lend a powerful contribution to the combustion stability framework.

REFERENCES

1. Flandro, G. A., "Oscillatory Behavior of Liquid Propellant Rockets, Scramjets, and Thrust Augmenters," Invited Plenary Lecture, *Seventh International Symposium on Special Topics in Chemical Propulsion* (7-ISICP), Kyoto, Japan, 2007, Published by Kenneth Kuo, Pennsylvania State University.

2. Price, E. W. and Flandro, G. A., "Combustion Instability in Solid Rockets," AFOSR TR-87-0459, Air Force Rocket Propulsion Laboratory, 23 February 1987.

3. Culick, F. E. C., "High Frequency Oscillations in Liquid Rockets", AIAA *Journal*, Vol. 1, No. No. 5, 1963, pp. 1097-1104.

4. Culick, F. E. C., "Non-Linear Growth and Limiting Amplitude of Acoustic Oscillations in Combustion Chambers," *Combustion Science and Technology*, Vol. 3, No. 1, 1971, pp. 1-16.

5. Culick, F. E. C., "Interactions Between the Flow Field, Combustion, and Wave Motions in Rocket Motors", NWC TP-5349, Naval Weapons Center, China Lake, CA, 1972, pp. 41-46.

6. Culick, F. E. C., *Nonlinear Behavior of Acoustic Waves in Combustion Chambers*, California Institute of Technology, Pasadena, CA, 1975

7. Nickerson, G. R., Culick, F. E. C., and Dang, L. G., "Standardized Stability Prediction Method for Solid Rocket Motors Axial Mode Computer Program," Software and Engineering Associates, Inc., AFRPL TR-83-017, Sept. 1983.

8. Culick, F. E. C., and Yang, V., "Prediction of the Stability of Unsteady Motions in Solid Propellant Rocket Motors," *Nonsteady Burning and Combustion Stability of Solid Propellants*, Vol. 143, AIAA, 1992, pp. 719-779.

9. Culick, F. E. C., and Yang, V., "Overview of Combustion Instabilities in Liquid Propellant Rocket Engines", *Liquid Rocket Engine Combustion Instability*, Vol. 169, AIAA Progress in Astronautics and Aeronautics, 1995, pp. 1-37.

10. Culick, F. E. C., "Combustion Instabilities in Propulsion Systems", *Unsteady Combustion*, Kluwer Academic Publishers, 1996, pp. 173-241.

11. Culick, F. E. C., *Unsteady Motions in Combustion Chambers*, Cambridge University Press, 2007, pp. 6.38 – 6.40.

12. Oefelein, J. C, and Yang, V., "Comprehensive Review of Liquid-Propellant Combustion Instabilities in F-1 Engines," Journal of Propulsion and Power, Vol. 9, No. 5, 1993, pp. 657-677.

13. Cantrell, R. H., and Hart, R. W., "Interaction between Sound and Flow in Acoustic Cavities: Mass, Momentum, and Energy Considerations," *J. Acoustical Society of America*, Vol. 36, No. 4, 1964, pp. 697-706.

14. Hart, R. W., and McClure, F. T., "Combustion Instability: Acoustic Interaction with a Burning Propellant Surface," *The Journal of Chemical Physics*, Vol. 10, No. 6, 1959, pp. 1501-1514.

15. Hart, R. W., and McClure, F. T., "Theory of Acoustic Instability in Solid Propellant Rocket Combustion," *Tenth Symposium (International) on Combustion*, 1964, pp. 1047-1066.

16. Larson, C., Gloyer, P., Flandro, G., et al., "Ares I Solid Rocket Booster Thrust Oscillation," NASA Engineering and Safety Center (NESC) Technical Report, RP-08-60, June 2008. Preprint Copy 2008

17. Gloyer, P.W., Rice. T. M., et al., "Ares I Thrust Oscillation Mitigation Via Motor Modifications", *56th JANNAF Propulsion Meeting* April 2009

18. Jacob Eric J., and Flandro, G.A. "Nonlinear Liquid Rocket Combustion Instability Behavior using UCDS™ Process", *46th Joint Propulsion Conference,* AIAA-2010-6800, Nashville, TN, July 2010

19. Jacob, Eric J., "Nonlinear Combustion Instability Generalized Framework," PhD Dissertation, Department of Aerospace Engineering, The University of Tennessee Knoxville, TN, 2009

20. Flandro, G. A., "Rotating Flows in Acoustically Unstable Rocket Motors," Ph.D. Dissertation, Department of Aerospace Engineering, California Institute of Technology, 1967.

21. Flandro, G. A., "Solid Propellant Acoustic Admittance Corrections," *Journal of Sound and Vibration*, Vol. 36, No. 3,1974, pp. 297-312.

22. Flandro, G.A., "Effects of Vorticity Transport on Axial Acoustic Waves in a Solid Propellant Rocket Chamber," *Proceedings of the 1989 ASME Annual Meeting*, San Francisco, CA, December 1989.

23. Flandro, G. A., "Vortex Driving Mechanisms in Oscillatory Rocket Flows," *Journal of Propulsion and Power*, Vol. 2, No. 3, 1986, pp. 206-214.

24. Flandro, G.A., "On Flow Turning," *31st AIAA Joint Propulsion Conference*, AIAA 95-2730, San Diego, CA, July 1995.

25. Flandro, G. A. and Fischbach, S. R., "Effects of Parallel Wave Incidence on Combustion Instability Driving Mechanisms," AIAA Paper 2007-5807. 43rd AIAA/ASME/ SAE/ASEE Joint Propulsion Conference and Exhibit, Cincinnati, OH,

July 2007.

26. Flandro, G. A. and Jacob, E., "Finite Amplitude Waves in Liquid Rocket Combustion Chambers," *46th AIAA Aerospace Sciences Meeting*, AIAA-2008-1003, 2008.

27. Saenger, R. A., "Periodic Shock Waves in Resonating Gas Columns," Ph. D. Dissertation, New York University, New York, NY, December 1958.

28. Saenger, R. A. and Hudson, G. E., "Periodic Shock Waves in Resonating Gas Columns," *The Journal of the Acoustical Society of America*, Vol. 32, No. 8, August 1960, pp. 961-970.

29. Jacob, E. J., Flandro, G. A., Banuti, D, "Forced Resonant Shock Waves and Mean Pressure Shift in a Closed Tube," *AIAA Joint Propulsion Conference*, AIAA-2007-5806, 2007

30. Flandro, G. A., Fischbach, S. R., Majdalani, J., and French, J. C., "Nonlinear Rocket Motor Stability Prediction: Limit Amplitude, Triggering, and Mean Pressure Shift," AIAA Paper 2004-4054, July 2004.

31. Brownlee, W. G., "Nonlinear Axial Mode Combustion Instability in Solid Propellant Motors," *AIAA Journal*, Vol. 2, pp. 275-284, Feb. 1964.

32. Flandro, G. A., "Approximate Analysis of Nonlinear Instability with Shock Waves", AIAA Paper 82-1220, July 1982.

33. Levine, J. N., and Baum, J. D., "A Numerical Study of Nonlinear Phenomena in Solid Rocket Motors," *AIAA Journal*, Vol. 21, No. 4, 1983, pp. 557-564.

34. Flandro, G. A., "Energy Balance Analysis of Nonlinear Combustion Instability," *Journal of Propulsion and Power*, Vol. 1, No. 3, (1985), pp. 210-221.

35. Flandro, G. A., Sims, J. D. and Majdalani, J, "On Nonlinear Combustion Instability in Liquid Propellant Rocket Engines," AIAA Paper 2004-3516, July 2004.

36. Flandro, G. A., French, J., and Majdalani, J, "Incorporation of Nonlinear Capabilities in the Standard Stability Prediction Program," 40th *AIAA Joint Propulsion Conference Paper* AIAA 2004-4182, 2004.

37. Flandro, G. A., Perry, E. H., and French, J. C., Nonlinear Rocket Motor Stability Computations: Understanding the Brownlee-Marble Observations, AIAA Paper No. 2006-539, *44th Aerospace Sciences Meeting*, January 2006.

38. Devarokonda, Nagini, "Nonlinear Behavior of Longitudinal Waves in the Oscillations of Rijke Tube," Master's Thesis, Department of Aerospace Engineering, University of Tennessee Space Institute, Knoxville, TN, 2007

39. Flandro, G. A., "Irregular Burning: On the Origin of the DC Shift," AIAA Paper No. 2007-5809, *43rd AIAA Joint Propulsion Conference*, July 2007.

40. Private communications - Gary Flandro

41. Bloomshield, F. S., "Stability Testing and Pulsing of Full Scale Tactical Engines, Parts I and II," Naval Air Warfare Center, 1996.

42. Bloomshield, F. S., C. J. Bicker, et al., "High Pressure Pulsed Firing Combustion Instability Investigations," *Proceedings of the 1996 JANNAF 33rd Combustion Meeting*, Naval Postgraduate School, Montery, CA, 1996.

43. Bloomshield, F. S., J. E. Crump, et al., "Stability Testing of Full-Scale Tactical Engines," *Journal of Propulsion and Power*, Vol. 13, No. 3, 1997, pp.349-355.

44. Flandro, G. A., "Nonlinear Combustion Instability Prediction for Liquid rocket Engines", NASA Grant NNM04AA53G, George C. Marshall Space Flight Center

MSFC-TD61, Combustion Devices, Nov. 2005

45. Brownlee, W. G., "An Experimental Investigation of Unstable Combustion in Solid Propellant Rocket Motors," Ph.D. Dissertation, California Institute of Technology, 1959.

46. Brownlee, W. G., and Marble, F. E., "An Experimental Investigation of Unstable Combustion in Solid Propellant Rocket Motors", *Progress in Astronautics and Rocketry, Vol. I: Solid Propellant Rocket Research*, (1960), pp. 455-494.

47. Brownlee, W. G., "Nonlinear Axial Mode Combustion Instability in Solid Propellant Motors," *AIAA Journal*, Vol. 2, pp. 275-284, Feb. 1964.

48. Dawson, M.C. Flandro G.A. et. al., "Elimination of Flow of Induced Instabilities in Solid Rocket Motors by The Aerodynamic contouring of Internal Grain Geometries," AFRPL TR-82-058 Air Force Rocket Propulsion Laboratory, Edwards, CA, Jan. 1983

49. Clayton, R. M., "Experimental Measurements on Rotating Detonation-Like Combustion," JPL, Technical Rept. 32- 788, Pasadena, CA, Aug. 1965.

50. Clayton, R. M., Rogero, R. S., and Sotter, J. G., "An Experimental Description of Destructive Liquid Rocket Resonant Combustion," *AIAA Journal*, Vol. 6, No. 7, 1968, pp. 1252-1259.

51. Sotter, J. G.,and Flandro, G. A. "Unstable Combustion in Rockets," *Scientific American*, (1968).

52. Culick, Fred, *Unsteady Motions in Combustion Chambers for Propulsion Systems*, Propulsion and Energetics Panel (PEP) of NATO's Advisory Group for Aerospace Research and Development (AGARD), December 2006

53. French, Jonathan C. and Flandro, Gary A., "UCDS Nozzle Acoustic Dynamics

and Stability Modeling", *46th Joint Propulsion Conference,* AIAA-2010-6994, Nashville, TN, July 2010

54. Crocco, L., and Cheng, S. I., *Theory of Combustion Instability in Liquid Propellant Rocket Motors*, *Agard*, Vol. 8, Butterworths Science Publishers Ltd, London, UK, 1956

55. Sirignano, W. A., and Crocco, L., "A Shock Wave Model of Unstable Rocket Combustors," *AIAA Journal*, Vol. 2, No. 7, pp. 1285-1296 , July 1964.

56. Mitchell, C. E., Crocco, L., and Sirignano, W. A., "Nonlinear Longitudinal Instability in Rocket Motors with Concentrated Combustion," *Combustion Science and Technology*, Vol. 1, pp. 35-63 ,1969.

57. Zinn, B. T. and Powell, E. A., "Application of the Galerkin Method in the Solution of Combustion Instability Problems," *Proceedings of the 19th International Astronautical Congress*, Vol. 3, 1970, pp. 59-73.

58. Zinn, B. T., "A Theoretical Study of Nonlinear Combustion Instability in Liquid Propellant Engines," *AIAA Journal*, Vol. 6, No. 10, 1968, pp. 1966-1972.

59. Mitchell, C. E., "Analytical Models for Combustion Instability, Liquid Rocket Engine Combustion Instability", Vol. 169, *AIAA Progress in Astronautics and Aeronautics*, 1995, pp. 403-430.

60. Chu, B.T., and Kovasznay, L.S.G., "Nonlinear Interactions in a Viscous Heat-Conducting Compressible Gas," *Journal of Fluid Mechanics*, Vol. 3, 1958, pp. 494-514.

61. Morfey, C. L. and Temkin, S., "Unstable Combustion of Advanced Solid Propellants," BBN Report No. 1547, Bolt, Beranek and Newman, Inc. Cambridge, MA, Sept. 1967, pp. 1-38.

62. Morfey, C. L., "Acoustic Energy in Non-uniform Flows," *Journal of Sound and Vibrations*, Vol. 14, 1971, pp. 159-169.

63. Sandham, N. D., Morfey, C. L. and Hu, Z. W., "Nonlinear Mechanisms of Sound Generation in a Perturbed Parallel Jet Flow," *Journal of Fluid Mechanics,* Vol. 565, 2006, pp. 1-23.

64. Myers, M. K., "An Exact Energy Corollary for Homentropic Flow," *Journal of Sound and Vibrations*, Vol. 109, 1986, pp. 277-284.

65. Myers, M. K., "Generalization and Extension of the Law of Acoustic Energy Conservation in a Nonuniform Flow," *AIAA 24th Aerospace Sciences Meeting*, AIAA Paper No. 86-0471, 1986.

66. Myers, M. K., "Transport of Energy by Disturbances in Arbitrary Steady Flows," *Journal of Fluid Mechanics*, Vol. 226, 1991, pp. 383-400.

67. Pierce, A. D., "Aeroacoustic Fluid Dynamic Equations and Their Acoustic Energy Corollary with O_2 and N_2 Vibrational Relaxation Effects Included," *Journal of Sound and Vibration*, 1978, 58 (2), pp. 189-200.

68. Pierce, A. D., *Acoustics: An Introduction to its Physical Principles and Applications*, McGraw Hill, New York, 1981.

69. S.W. Rienstra and A. Hirschberg, "An Introduction to Acoustics", Instituut Wiskundige Dienstverlening Eindhoven (IDWE) Report 92-06, 2004, revised version March 2010 (EindhovenUniversity of Technology, www.win.tue.nl/~sjoerdr/papers/boek.pdf, Nov- 17, 2010, pp. 36-42

70. Gustav Robert Kirchhoff, *Vorlesungen über Mathematische Physik, Mechanik, Zweite Auflage*, (B.G. Teubner Verlag, Leipzig 1877) pp. 309-347.

71. Rayleigh, J. W. S., *Theory of Sound*, Macmillan and Co., London, England, pp. 97-148, 1877.

72. Enflo, B. O. and Hedberg, C. M., *Theory of Nonlinear Acoustics in Fluids*, Kluwer Academic Publishers, 2002.

73. L. D. Landau, E. M. Lifshitz, *Fluid Mechanics*, Butterworth-Heinemann, 1987.

74. Liepmann, H. W., and Roshko, A. *Elements of Gasdynamics*, Dover Publications, 1957.

75. Tien, James S, "Oscillatory Burning of Solid Propellant including Gas Phase Time Lag Combustion," *Science and Technology*, Vol. 5, Gordon and Breach, Science Publishers Limited, UK, 1972. pp. 47-54

76. Sutton, George P., *Rocket Propulsion Elements An Introduction to the Engineering of Rockets*, Sixth Edition, John Wiley and Sons, Inc., 1992.

77. Rice, Tina M., Flandro, Gary A., French, Jonathan, Gloyer, Paul, and Jacob, Eric., "Effects of Unsteady Heat Release on Liquid Rocket Combustion Instability", *46th Joint Propulsion Conference,* AIAA-2010-7153, Nashville, TN, July 2010

78. Law, Chung K., "Combustion Physics," First Edition, Cambridge University Press, 2006.

79. Chapra, Steven C., and Canale, Raymond P., *Numerical Methods For Engineers*, Second-Edition, McGraw–Hill, Inc., 1988.

80. Private Communication - Paul Gloyer

81. Gloyer, P., Repas, G., and, Pedlikin J., "Very Low Cost Orbital Vehicle Engine", Phase II Final Report, AFRL Contract Number F04611-96-C-0024, Dec. 1998

82. Private Communication - Jonathan French

APPENDICES

APPENDIX A

%LRE INSTABILITY_11: PREDICTION OF COMBUSTION-DRIVEN ACOUSTIC WAVE GROWTH IN A LIQUID PROPELLANT ROCKET CHAMBER, Tina M. Rice, September 2010%

```
%*************************************************************%
%            Equations for Use in the Runge-Kutta Solver for Steady State        %
%*************************************************************%

function dw = new_eqtn(w,B,E)
e1 = (1.0-w(1))/w(1);
q_w0 = B*(e1^2)*exp(-E/w(1));
% z(i) = q_w0(i);
% wdot = zeros(2,1);
dw(1) = w(2);
dw(2) = w(2) - q_w0;
if dw(1) < 0.0
    w(2) = 0.0;
 end;


%*************************************************************%
%       Equations for Use in the Runge-Kutta Solver for Unsteady Solution    %
%*************************************************************%

function dw = Full_equations(w,B,E,om,q,g2,x,p,steps,H1r,H1i)
w(1);
w(2);
E;
e1 = (1.0-w(1))/w(1);
q_w0 = B*(e1^2)*exp(-E/w(1));
w_0   = q_w0/q;
% wdot = zeros(12,1);
dw(1) = w(2);
dw(2) = w(2) - q_w0;
Yf   = (1.0 - w(1))/q;
dYf  = - w(2)/q;
%{---------Oscillatory,O(e)---------}
e2  = w(2)/w(1);
e3  = q_w0*(E/w(1) - 2.0)/w(1);
e4  = -(e2 + e3);
e5  = om/w(1);
e6  = -2.0*q_w0/Yf;
e7  = (2.0*q_w0 - w(2));
e8  = 2.0*w_0/(Yf);
e9  = dYf/w(1);
```

```
42      e10 = e9 - e3/q;
43      dw(3) = w(3) + e4*w(5) - e5*w(6) + e6*w(9) + e2*w(11) - e7;
44      dw(4) = w(4) + e4*w(6) + e5*w(5) + e6*w(10) + e2*w(12) - g2*om;
45      dw(5) = w(3);
46      dw(6) = w(4);
47      dw(7) = w(7) + e8*w(9) - e5*w(10) - e10*w(5) + e9*w(11) + dYf + 2.0*w_0;
48      dw(8) = w(8) + e8*w(10) + e5*w(9) - e10*w(6) + e9*w(12);
49      dw(9) =  w(7);
50      dw(10) = w(8);
51      dw(11) = w(3) - e2*w(5) + e2*w(11) - e5*w(6);
52      dw(12) = w(4) - e2*w(6) + e2*w(12) + e5*w(5) - om;
53
54
55      %*************************************************************%
56      %   Complete Program with Combined Steady and Unsteady Equation Solvers  %
57      %*************************************************************%
58
59      % clear all
60      % format long
61      % clear
62      function [T_0] = new_liquid_unsteady();
63      % Ts = input('\n\nWhat is the initial propellant temperature?(dimensionless)\n\n');
64      % Tinf = input('What is the final chamber temperature?');
65      load omegas.dat
66      % load upper_omegas.dat
67      % load InitialTemperature2.dat
68      % load HeatOfCombustion.dat
69      load SpecificGravity.dat
70      % load sub_omegas.dat
71      fid=fopen('testing_fixed_H_For_excel_stuff.dat','w');
72      Ts = 0.2                        %% Dimensionless Initial Temperature
73      for r = 1:40
74              om = omegas(r,1)
75              % load propellants.dat
76              % load nitrous_oxide.dat
77              %  g = SpecificHeatRatio(k,1)
78              % q = HeatOfCombustion(k,1)
79              %     q = Q_formation*1000 / (Cp_h2O*Tinf)
80              %      E = ActivationEnergy(k,1)
81              E = 10.0          %% Gas Phase Activation Energy
82              % q = 0.65;
83              d1 = 1.0;
84              d2 = 1.0;
85              g = 1.1                         %% Ratio of Specific Heats
86              g2 = (g-1.0)/g;
```

```
        global yfinal

%*************************************************************%
%       Solving for the steady temperature and heat release distributions      %
%*************************************************************%
        FLAG = 1;
        B_high = 1.5E+11;
        % B_low = 1.5E+2;
        B_low = 0.1;
        B = (B_high+B_low)/2;
        h =0.1;
        w = zeros(1,2)
        while  B_high-B_low >= 0.00000005;   %% Bdif >= 0.5
                if FLAG == 1 %% then begin
                        B = (B_high + B_low)/2.0;
                        %    Initial Yf is set to 1 using conseved scalar formulation
                        Yf(1) = 1;
                        w(1,1) = Ts;
                        %      w(1,1) = (1 - (Yf(1) * q))
                        w(1,2) = 0.01;
                        n = 1;
                        y_max = 0.2;
                        FLAG = 2;
                end
                if w(n,1) > 1.00000000 %% then begin
                        B_low = B;
                        FLAG = 1;
                end;
                if w(n,2) < 0.0 %% then begin
                        B_high = B;
                        FLAG = 1;
                        end;
                        if FLAG == 2 %% then begin
                        y = 0:h:y_max;
                        y_array = 0:h:y_max;
                        steps = length(y);
                        y = y_array(1);
                        h2 = h/2;
                        w;
                        q = (1 - w(1,1)) / Yf(1);
                        for p=1:(steps-1)
                                p;
                                f1 = new_eqtn(w(p,:),B,E);
                                w1 = w(p,:) + h2*f1;
                                y = y + h2;
```

```
131                                 f2 = new_eqtn(w1,B,E);
132                                 w1 = w(p,:) + h2*f2;
133                                 f3 = new_eqtn(w1,B,E);
134                                 w1 = w(p,:) + h*f3;
135                                 y = y + h2;
136                                 f4 = new_eqtn(w1,B,E);
137                                 w((p+1),:) = w(p,:) + (h/6)*(f1+2*(f2+f3)+f4);
138                                 Yf(p)    = (1.0 - w(p,1))/q;
139                         end
140                                 n = steps;
141                                 y_max = y_max + h;
142                                 Bdif = (B_high-B_low);
143                 end
144         end
145         y_final = y_max;
146         n = 1;
147         y_max = 0.02;
148         while w(n,2) >= 0.004
149                         y = 0:h:y_max;
150                         y_array = 0:h:y_max;
151                         steps = length(y);
152                         y = y_array(1);
153                         h2 = h/2;
154                 for p=1:(steps-1)
155                         p;
156                         f1 = new_eqtn(w(p,:),B,E);
157                         w1 = w(p,:) + h2*f1;
158                         y = y + h2;
159                         f2 = new_eqtn(w1,B,E);
160                         w1 = w(p,:) + h2*f2;
161                         f3 = new_eqtn(w1,B,E);
162                         w1 = w(p,:) + h*f3;
163                         y = y + h2;
164                         f4 = new_eqtn(w1,B,E);
165                         w((p+1),:) = w(p,:) + (h/6)*(f1+2*(f2+f3)+f4);
166                         Yf(p)    = (1.0 - w(p,1))/q;
167                 end
168                 w(steps,2);
169                 n = steps;
170                 y_max = y_max + h;
171         end
172         yfinal = y_max-h
173         w               %%%% Printing values to screen
174         B
175
```

```
%*****************************************************************%
% Solving for the steady and unsteady temperature & heat release distributions %
%*****************************************************************%

        h = 0.1
        x(1)=0;
        x(2)=0;
        x(3)=0;
        x(4)=0;

        global ndim
        global delx
        ndim = 4;
        delx = 1e-7;
%*****************************************************************%
        errlast  = inf;
        leave = 0;
        jacob = zeros(ndim,ndim);
        kk = 1;
        kk;
        while kk < 25
                kk;
                h2 = h/2;
                y = 0:h:yfinal;
                y_array = 0:h:yfinal;
                steps = length(y);
                % w = zeros(steps,N);
                w = zeros(steps,12);
                w;
                w(1,1) = Ts;            %  Initial Temperature
                %  w(1,1) = (1 - (Yf(1) * q));
                w(1,2) = 0.01;          %  Surface Temperature Slope
                w(1,3) = x(1);
                w(1,4) = x(2);
                w(1,5) = 0;
                w(1,6) = 0;
                w(1,7) = x(3);
                w(1,8) = x(4);
                w(1,11) = 0;
                w(1,12) = 0;
                w(1,9) =  0;
                w(1,10) = 0
                y = y_array(1);
                for p=1:(steps-1)
                        f1 = Full_equations(w(p,:),B,E,om,q,g2,x,p,steps);
```

```
                    w;
                    w1 = w(p,:) + h2*f1;
                    y = y + h2;
                    f2 = Full_equations(w1,B,E,om,q,g2,x,p,steps);
                    w1 = w(p,:) + h2*f2;
                    f3 = Full_equations(w1,B,E,om,q,g2,x,p,steps);
                    w1 = w(p,:) + h*f3;
                    y = y + h2;
                    f4 = Full_equations(w1,B,E,om,q,g2,x,p,steps);
                    w((p+1),:) = w(p,:) + (h/6)*(f1+2*(f2+f3)+f4);
                    end
                    w ;
%*************************************************************%
            % z = zeros(1,4)
            z(1) = w(steps,3);
            z(2) = w(steps,4);
            z(3) = w(steps,9);
            z(4) = w(steps,10);
            w;
            z;
            ybase = z;
            err = 0;
            for i =1:ndim
                err = err + (ybase(i)^2);
            end
            err = sqrt(err) ;
            if err < 10
                if kk > 3
                    if err >= errlast
                        leave = 1
                        kk = kk + 157
                    end
                end
            end
            if leave == 0
                errlast = err;
                %    Calculate Jacobian    %
                for j = 1:ndim
                    x(j) = x(j) + delx;
                    % h = 0.1;
                    h2 = h/2;
                    y = 0:h:yfinal;
                    y_array = 0:h:yfinal;
                    n_points = length(y);
                    steps = length(y);
```

```
266                             % w(1,1) = (1 - (Yf(1) * q));
267                             w(1,1) = Ts;
268                             w(1,2) = 0.01;   % {Surface Temperature Slope}
269                             w(1,3) = x(1);
270                             w(1,4) = x(2);
271                             w(1,5) = 0;
272                             w(1,6) = 0;
273                             w(1,7) = x(3);
274                             w(1,8) = x(4);
275                             w(1,11) = 0;
276                             w(1,12) = 0;
277                             w(1,9) =  0 ;
278                             w(1,10) = 0;
279                             y = y_array(1);
280                             for p=1:(steps-1)
281                              f1 = Full_equations(w(p,:),B,E,om,q,g2,x,p,steps);
282                              w1 = w(p,:) + h2*f1;
283                              y = y + h2;
284                              f2 = Full_equations(w1,B,E,om,q,g2,x,p,steps);
285                              w1 = w(p,:) + h2*f2;
286                              f3 = Full_equations(w1,B,E,om,q,g2,x,p,steps);
287                              w1 = w(p,:) + h*f3;
288                              y = y + h2;
289                              f4 = Full_equations(w1,B,E,om,q,g2,x,p,steps);
290                              w((p+1),:) = w(p,:) + (h/6)*(f1+2*(f2+f3)+f4);
291                             end
292                             w;
293     %*************************************************************%
294                             % z = zeros(1,4)
295                             z(1) = w(steps,3);
296                             z(2) = w(steps,4);
297                             z(3) = w(steps,9);
298                             z(4) = w(steps,10);
299                             w ;
300                             y_i = z;
301
302                             for i = 1:ndim
303                             jacob(i,j) = (y_i(i) - ybase(i)) / delx;
304                             end
305
306                             x(j) = x(j) - delx;
307                     end
308                     %       Solve for correction vector and correct x       %
309                     % ndim = 4;
310                     % delx = 1e-7;
```

```
311                         det = 1.0;
312                         for m = 1 : (ndim-1)
313                                 det = det*jacob(m,m);
314
315                                 for i = (m+1) : ndim
316
317                                         k = jacob(i,m)/jacob(m,m);
318
319                                         for j = (m+1):ndim
320                                                 jacob(i,j)=jacob(i,j)-k*jacob(m,j);
321                                         end
322
323                                         ybase(i) = ybase(i) - k*ybase(m);
324                                 end
325                         end
326                         det = det*jacob(ndim,ndim);
327                         m = 4;
328                         while m >= 1
329                                 m;
330                                 x1(m) = ybase(m)/jacob(m,m);
331                                 for i = 1: (m-1)
332                                         ybase(i)= ybase(i)-x1(m)*jacob(i,m);
333                                 end
334                                 m=m-1;
335                         end
336
337 %***************************************************************%
338                         for i=1:ndim
339                                 x(i) = x(i) - x1(i);
340                         end
341                 end
342                 kk = kk + 1;
343         end
344
345 %***************************************************************%
346         h2 = h/2;
347         y = 0:h:yfinal;
348         y_array = 0:h:yfinal;
349         n_points = length(y);
350         steps = length(y);
351         %       w = zeros(steps,N);
352         w(1,1) = Ts;  %%{Initial Temperature}
353         %       w(1,1) = (1 - (Yf(1) * q));
354         w(1,2) = 0.01;   %%{Surface Temperature Slope}
355         w(1,3) = x(1);
```

```
356             w(1,4) = x(2);
357             w(1,5) = 0;
358             w(1,6) = 0;
359             w(1,7) = x(3);
360             w(1,8) = x(4);
361             w(1,11) = 0;
362             w(1,12) = 0;
363             w(1,9) =  0;
364             w(1,10) = 0;
365             y = y_array(1);
366             for p=1:(steps-1)
367                     f1 = Full_equations(w(p,:),B,E,om,q,g2,x,p,steps);
368                     w1 = w(p,:) + h2*f1;
369                     y = y + h2;
370                     f2 = Full_equations(w1,B,E,om,q,g2,x,p,steps);
371                     w1 = w(p,:) + h2*f2;
372                     f3 = Full_equations(w1,B,E,om,q,g2,x,p,steps);
373                     w1 = w(p,:) + h*f3;
374                     y = y + h2;
375                     f4 = Full_equations(w1,B,E,om,q,g2,x,p,steps);
376                     w((p+1),:) = w(p,:) + (h/6)*(f1+2*(f2+f3)+f4);
377             end
378             w
379             hr=2
380     %*****************************************************************%
381             alpha_HR_no_constant = 0
382
383             for i =1:steps
384                     w1(i) = w(i,1);
385                     w2(i) = w(i,2);
386                     w3(i) = w(i,3);
387                     w4(i) = w(i,4);
388                     w5(i) = w(i,5);
389                     w6(i) = w(i,6);
390                     w7(i) = w(i,7);
391                     w8(i) = w(i,8);
392                     w9(i) = w(i,9);
393                     w10(i) = w(i,10);
394                     w11(i) = w(i,11);
395                     w12(i) = w(i,12);
396
397                     e1 = (1.0-w(i,1))/w(i,1);
398                     q_w0 = B*(e1^2)*exp(-E/w(i,1));
399                     w__0(i) = q_w0/q;
400                     %     w(i,1);
```

```
401                 Yf = (1.0 - w(i,1))/q;
402                 Species(i) = Yf;
403                 H__0(i) = q_w0;  %% Checked: same as qw_0
404                 % w_0(i)= w_0
405                 y_array = 0:h:(y_max-0.1);
406           end
407
408           w__0 = transpose(w__0);
409           H__0 = transpose(H__0);
410
411           for i = 1:steps
412                 e1 = (1.0-w(i,1))/w(i,1);
413                 q_w0 = B*(e1^2)*exp(-E/w(i,1));
414                 w_0    = q_w0/q;
415                 w(i,1);
416                 Yf    = (1.0 - w(i,1))/q;
417                 w(i,5);
418                 w(i,6);
419                 w(i,9);
420                 w(i,10);
421                 H_0 = q*w_0  %% Checked: same as qw_0
422                 e3  = q_w0*(E/w(i,1) - 2.0)/w(i,1);
423                 H1r = e3 * w(i,5) + 2.0 * q_w0 * (1.0 + w(i,9) / Yf)
424                 H1i = e3 * w(i,6) + 2.0 * q_w0 * (w(i,10) / Yf)
425                 Imag_Heat(i) = H1i;
426                 Real_Heat(i) = H1r;
427                 amplitude_H_1 = sqrt( (H1r)^2 + (H1i)^2 );
428                 phase_H_1 = atan2 (H1i,H1r);
429                 amplitude_T_1 = sqrt( (w(i,5))^2 + (w(i,6))^2 );
430                 phase_T_1 = atan2 (w(i,6),w(i,5));
431
432                 %     f = {(H_1*T_1) / T_0) - ((H_0*(T_1)^2)/((T_0)^2)} %%%%
433                 {} - Time Average
434
435                 first_term = (amplitude_H_1 * amplitude_T_1 *
436                 ((((cos(phase_H_1)) *          (cos(phase_T_1))) / 2 ) +
437                 (((sin(phase_H_1)) * (sin(phase_T_1)))/ 2 ))/ w(i,1))
438                 term_1(i) = first_term;
439
440                 second_term = (H_0*((amplitude_T_1)^2) *
441                 ((((cos(phase_T_1))^2) / 2) + (((sin(phase_T_1))^2) / 2))
442                 )/((w(i,1))^2)
443                 term_2(i) = second_term;
444
445                 difference = first_term - second_term;
```

```
446                     integrand(i) = difference;
447                     % integral = f(b) - f(a)
448                     % dV = r dr dq dz
449                     delta_x = h;
450                     %%% Some of numbers in next line were a run testing with real
451                     numbers for a certain case here-checking dimensionalization done
452                     in excel %%%
453                     integral = (difference*delta_x*(18649.86174^2)*3.14);
454                     int = integral;
455                     alpha_HR_no_constant = alpha_HR_no_constant + int
456                     i;
457             end
458
459             for i = 1:(steps-1)
460                     fprintf(fid,'%10.15f %10.15f %10.15f %10.15f %10.15f %10.15f
461                     %10.15f %10.15f %10.15f %10.15f %10.15f %10.15f %10.15f
462                     %10.15f %10.15f %10.15f %10.15f %10.15f %10.15f %10.15f
463                     %10.15f %10.15f %10.15f %10.15f %10.15f %10.15f %10.15f
464                     %10.15f %10.15f\t\n',om,g, w(1), E, y_array(i), w__0(i), H__0(i),
465                     Species(i), w1(i), w2(i), w3(i), w4(i),w5(i), w6(i),w7(i),
466                     w8(i),w9(i), w10(i),w11(i), w12(i), Real_Heat(i), Imag_Heat(i),
467                     term_1(i), term_2(i), integrand(i), alpha_HR_no_constant, B,
468                     yfinal,second_term) ;
469             end
470
471             for i = steps
472                     fprintf(fid,'%10.15f %10.15f %10.15f %10.15f %10.15f %10.15f
473                     %10.15f %10.15f %10.15f %10.15f %10.15f %10.15f %10.15f
474                     %10.15f %10.15f %10.15f %10.15f %10.15f %10.15f %10.15f
475                     %10.15f %10.15f %10.15f %10.15f %10.15f %10.15f %10.15f
476                     %10.15f %10.15f\t\n\r\r',om, g,w(1), E, y_array(i), w__0(i),
477                     H__0(i), Species(i), w1(i), w2(i), w3(i), w4(i),w5(i), w6(i),w7(i),
478                     w8(i),w9(i), w10(i),w11(i), w12(i), Real_Heat(i), Imag_Heat(i),
479                     term_1(i), term_2(i), integrand(i), alpha_HR_no_constant, B,
480                     yfinal,second_term) ;
481             end
482
483             om
484             E
485             w(1)
486     end
487     fclose(fid);
```

APPENDIX B

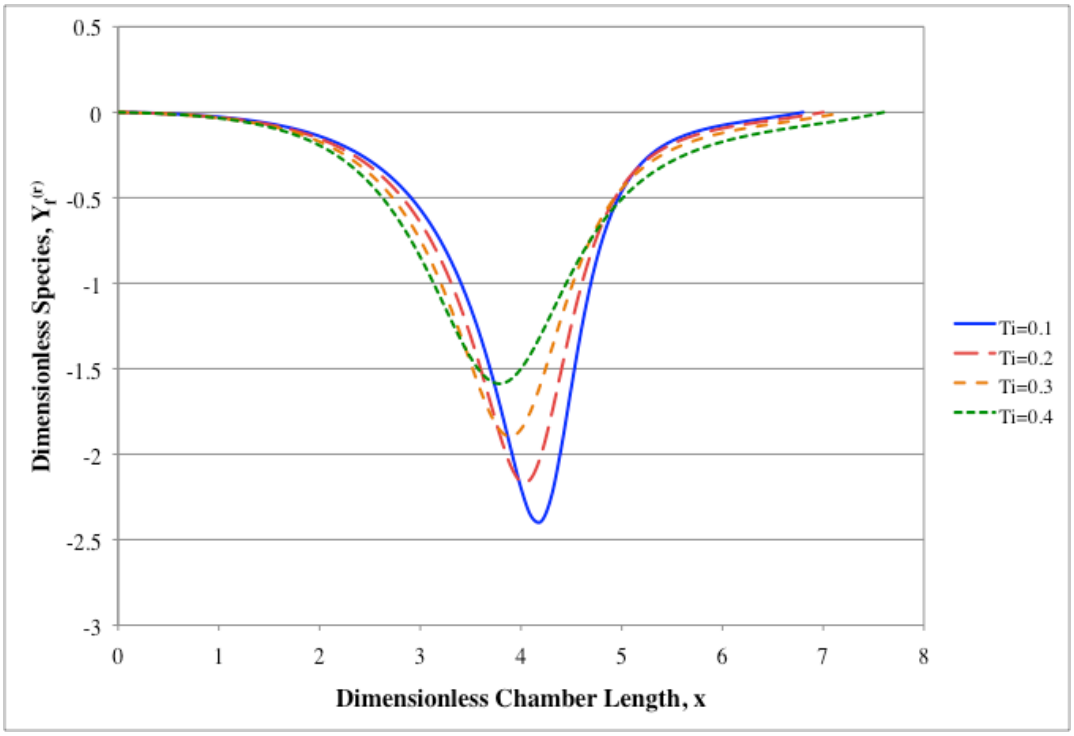

Figure A-1. Real Unsteady Species Component ($Y^{(r)}$) Varying Initial Temperature (γ=1.17, ω=1)

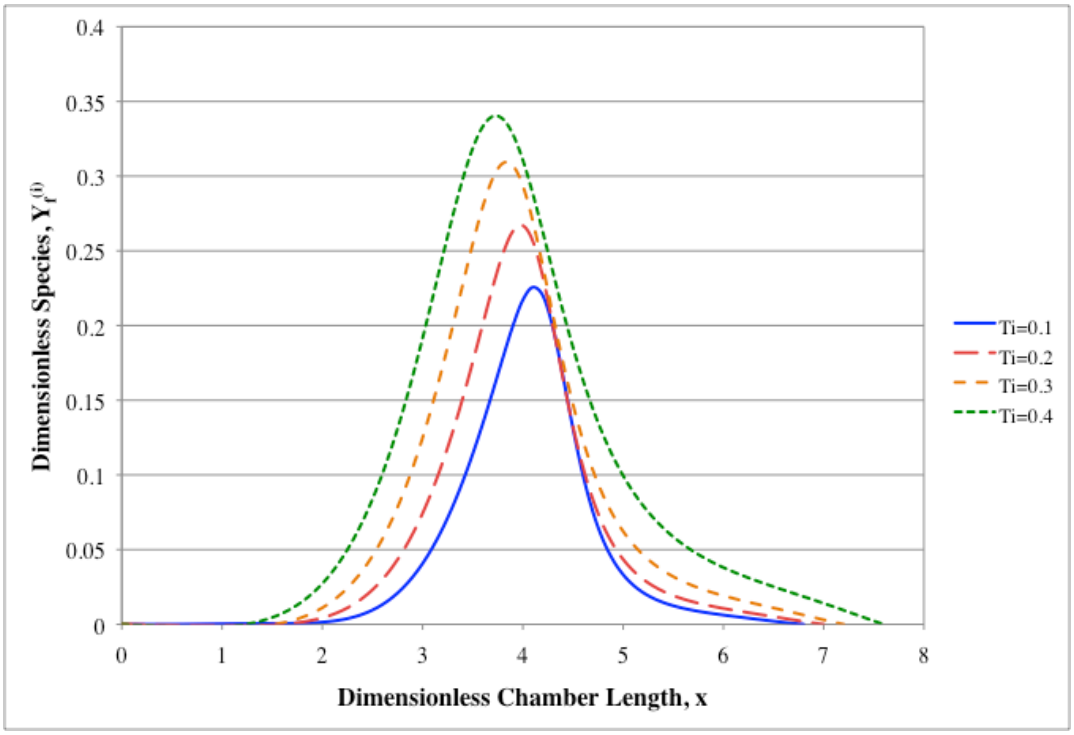

Figure A-2. Imaginary Unsteady Species Component $Y^{(i)}$ Varying Initial Temperature (γ=1.17, ω=1)

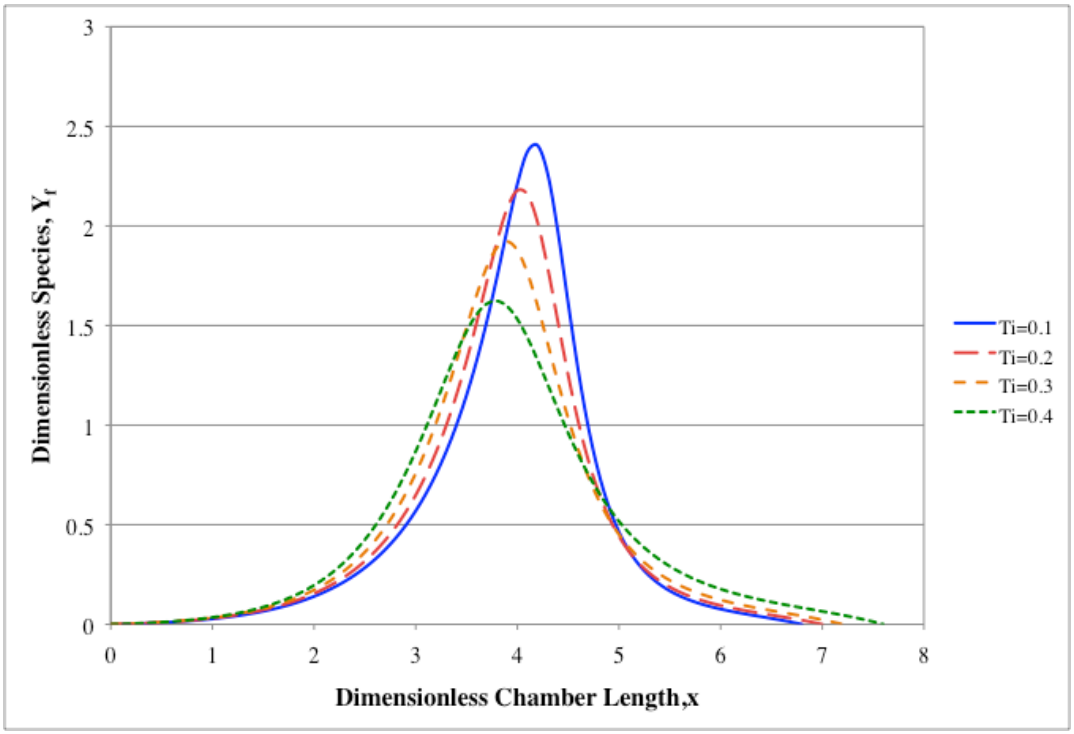

Figure A-3. Unsteady Species Amplitude Y for Varying Initial Temperature (γ=1.17, ω=1)

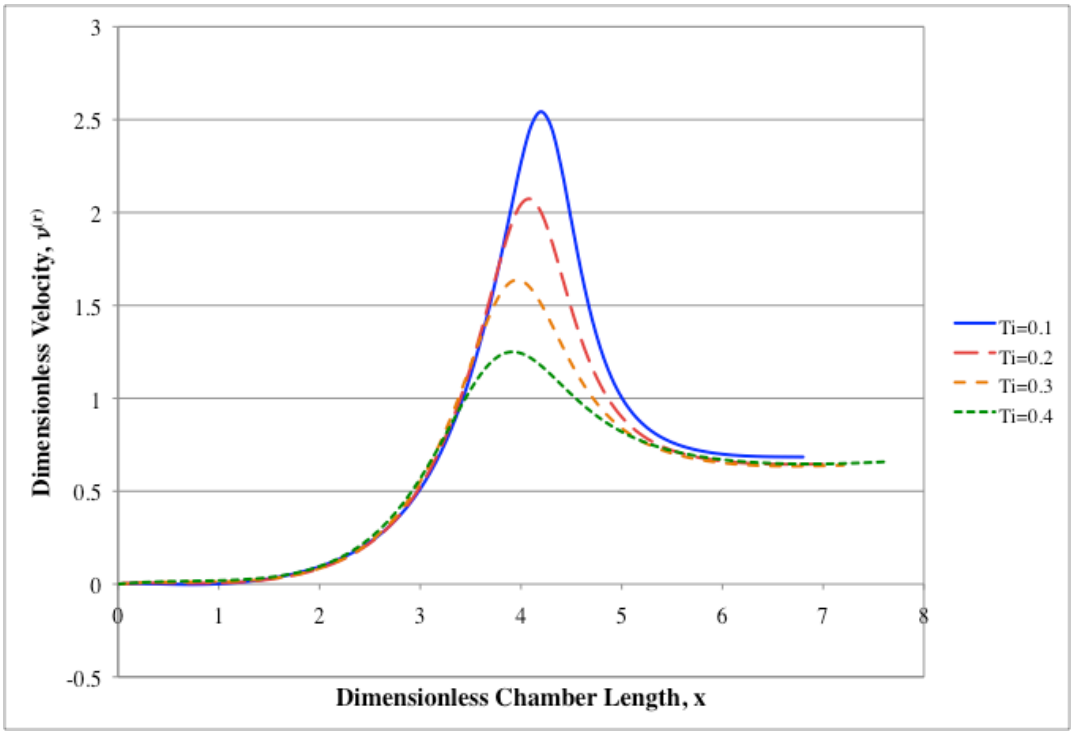

Figure A-4. Real Unsteady Velocity Component $v^{(r)}$ for Varying Initial Temperature (γ=1.17, ω=1)

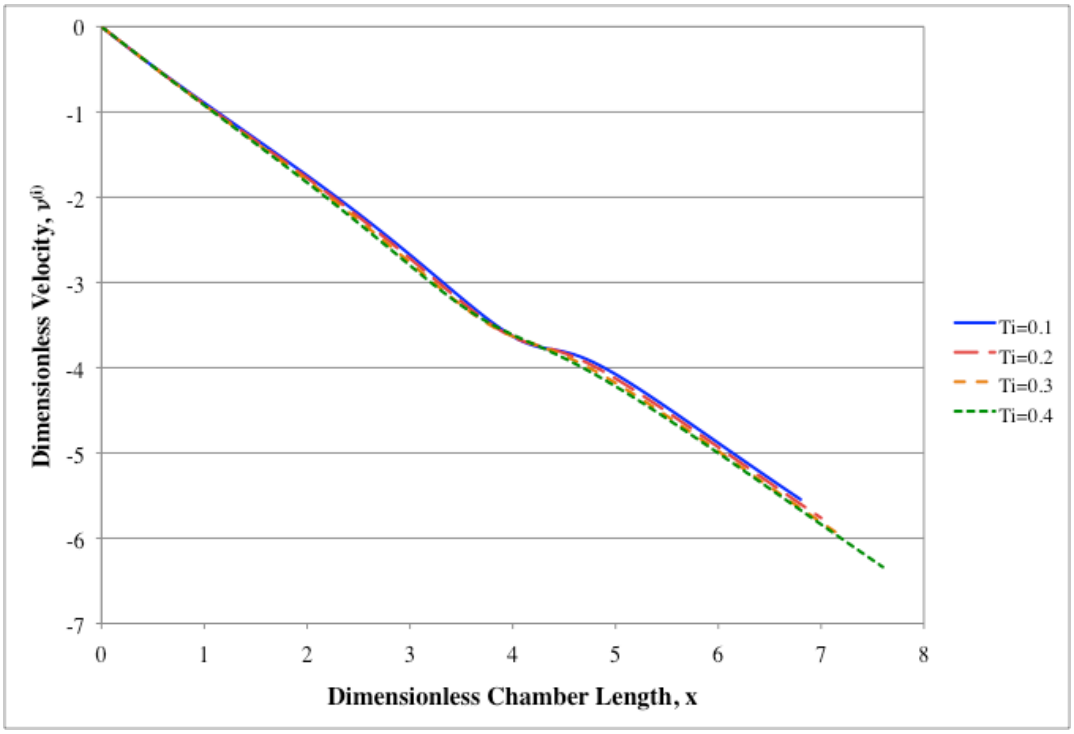

Figure A-5. Imaginary Unsteady Velocity Component $v^{(i)}$ for Varying Initial Temperature (γ=1.17, ω=1)



Figure A-6. Unsteady Velocity Amplitude v for Varying Initial Temperature (γ=1.17, ω=1)

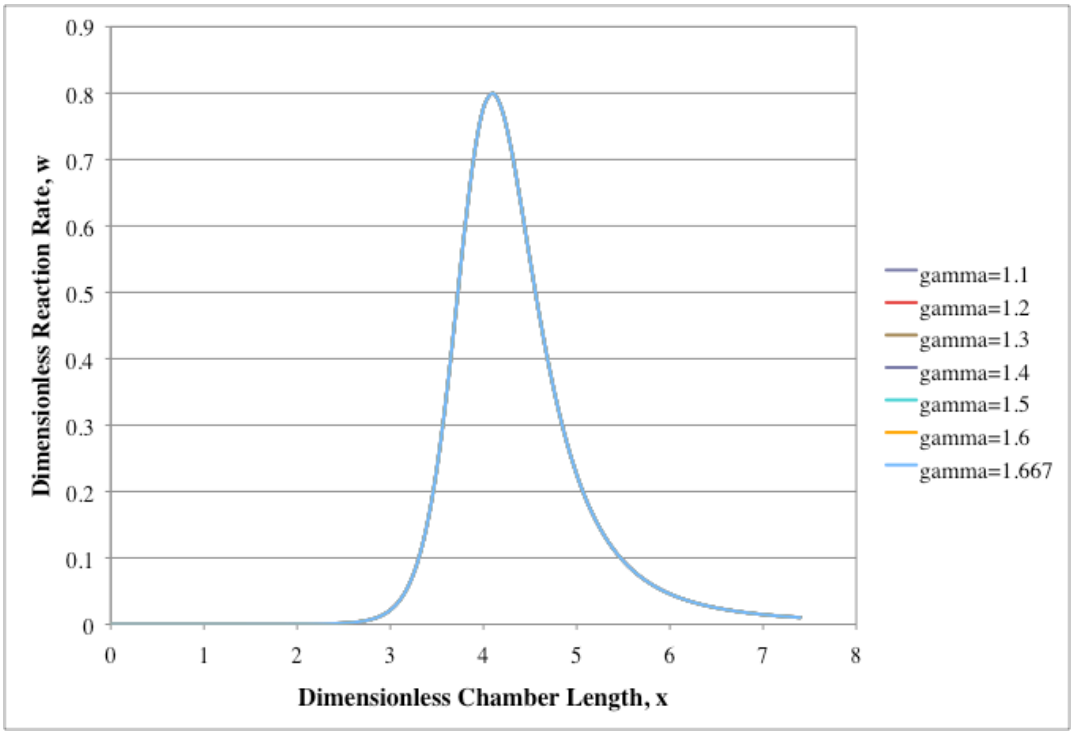

Figure A-7. Reaction Rate Profile (w) for Varying Gamma (T_i=0.35)

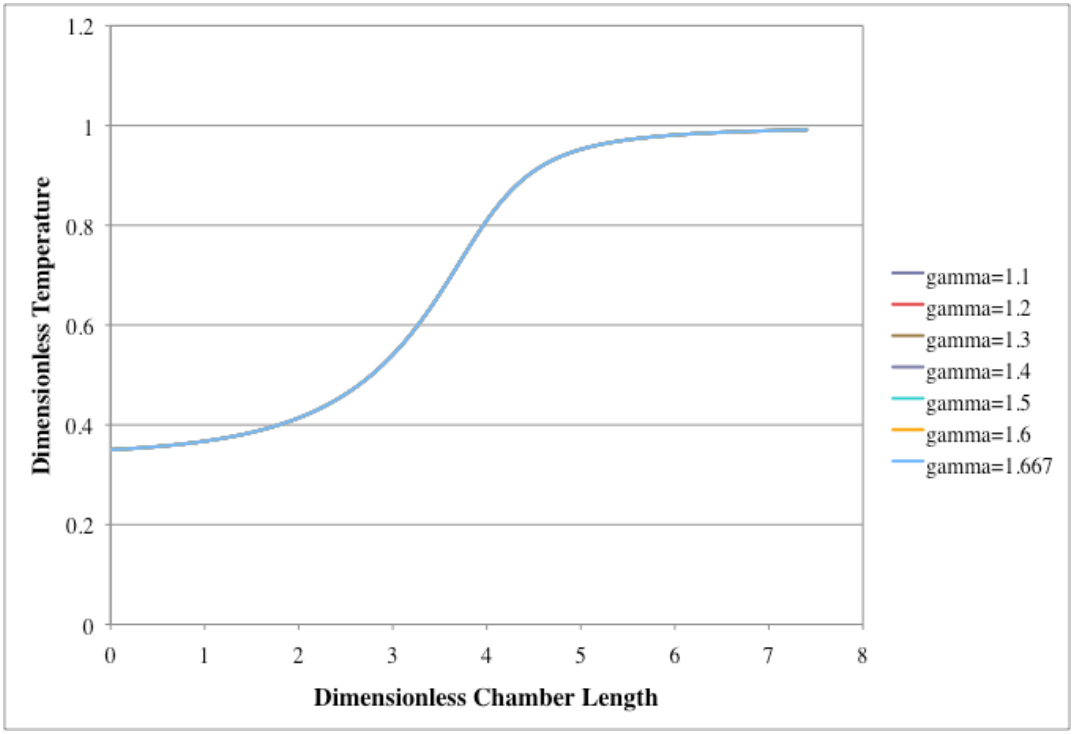

Figure A-8. Steady Temperature Profile (T_0) for Varying Gamma (T_i=0.35)

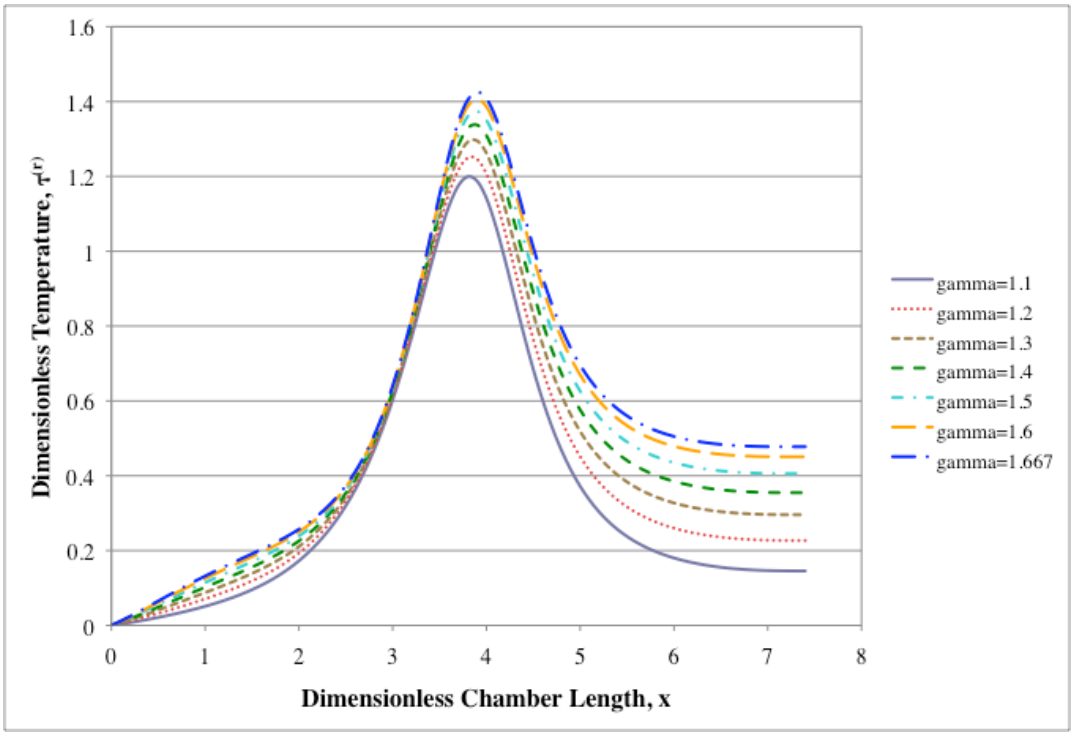

Figure A-9. Real Unsteady Temperature Component ($\tau^{(r)}$) Varying Gamma (T_i=0.35, ω=1)

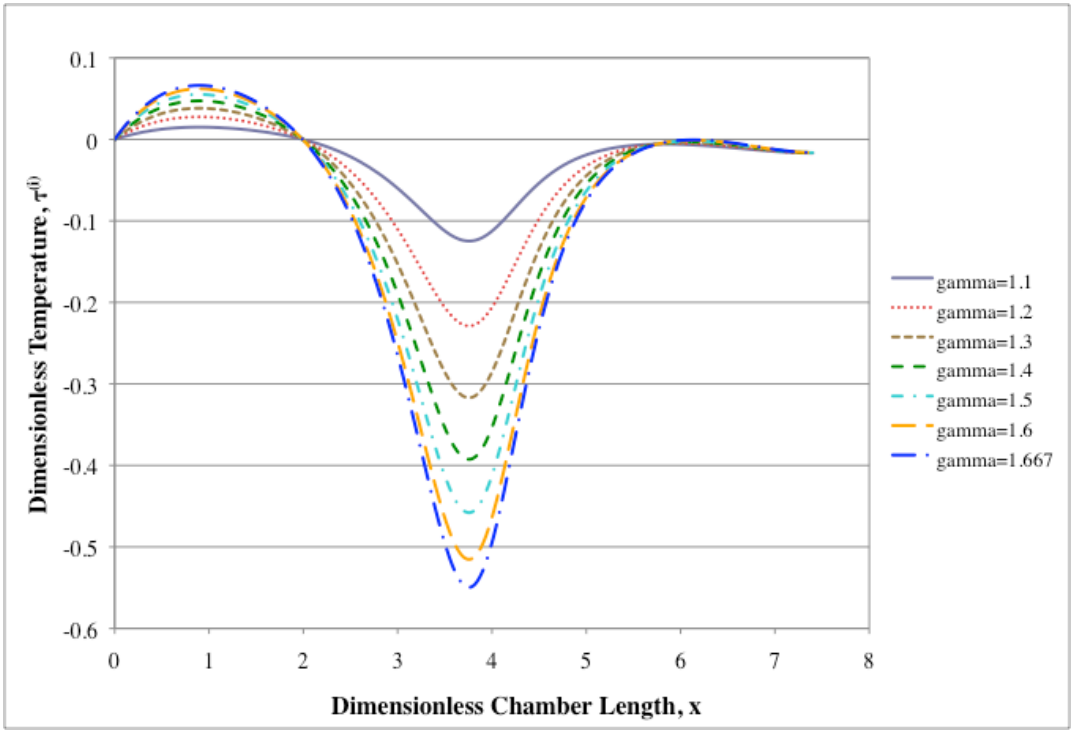

Figure A-10. Imaginary Unsteady Temperature Component ($\tau^{(i)}$) for Varying Gamma (T_i=0.35, ω=1)

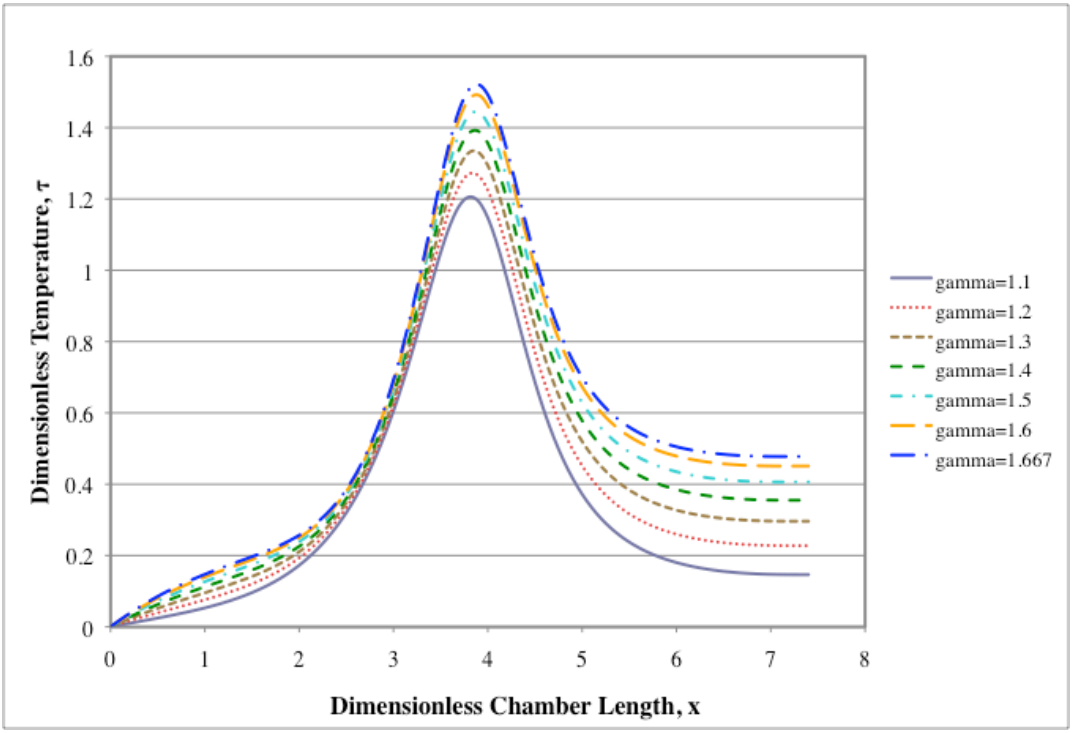

Figure A-11. Unsteady Temperature Component (τ) Varying Gamma (T_i=0.35, ω=1)

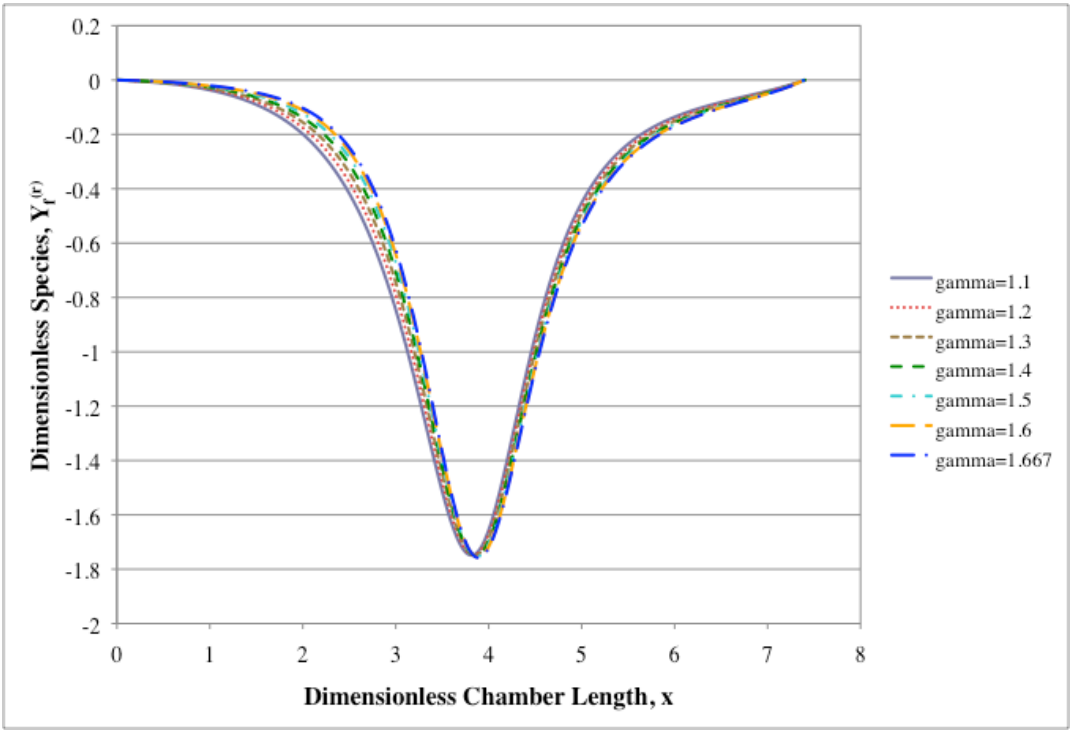

Figure A-12. Real Unsteady Species Component ($Y^{(r)}$) Varying Gamma (T_i=0.35, ω=1)

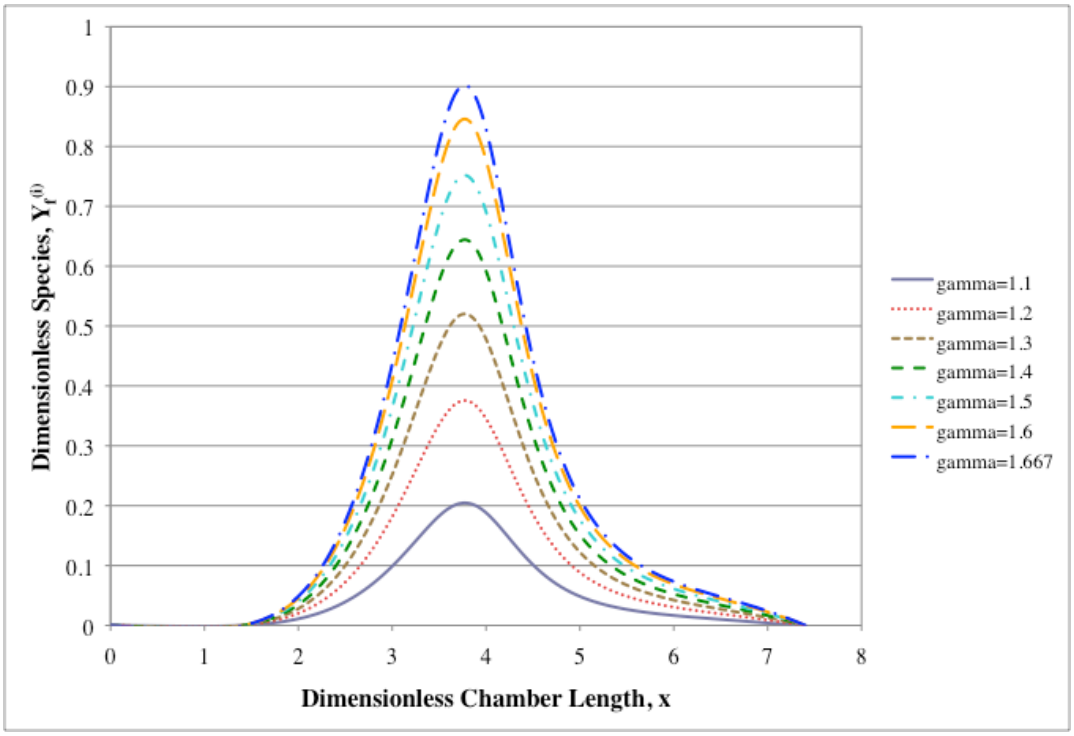

Figure A-13. Imaginary Unsteady Species Component ($Y^{(i)}$) Varying Gamma (T_i=0.35, ω=1)

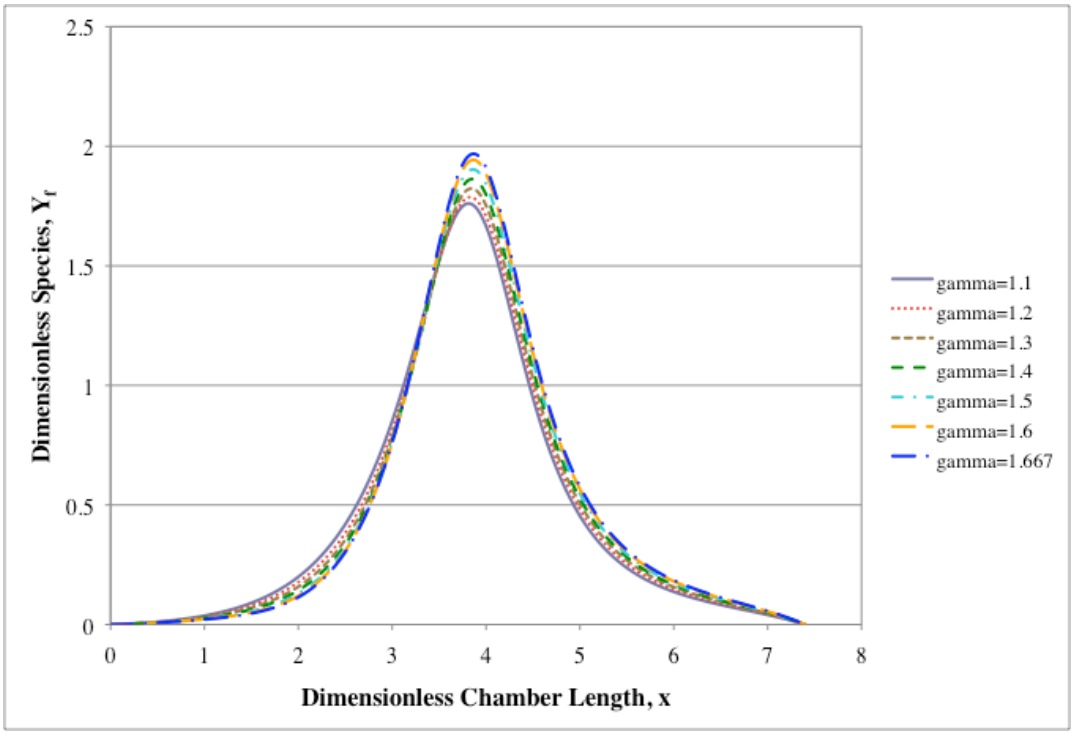

Figure A-14. Unsteady Species Amplitude (Y) Varying Gamma (T_i=0.35, ω=1)

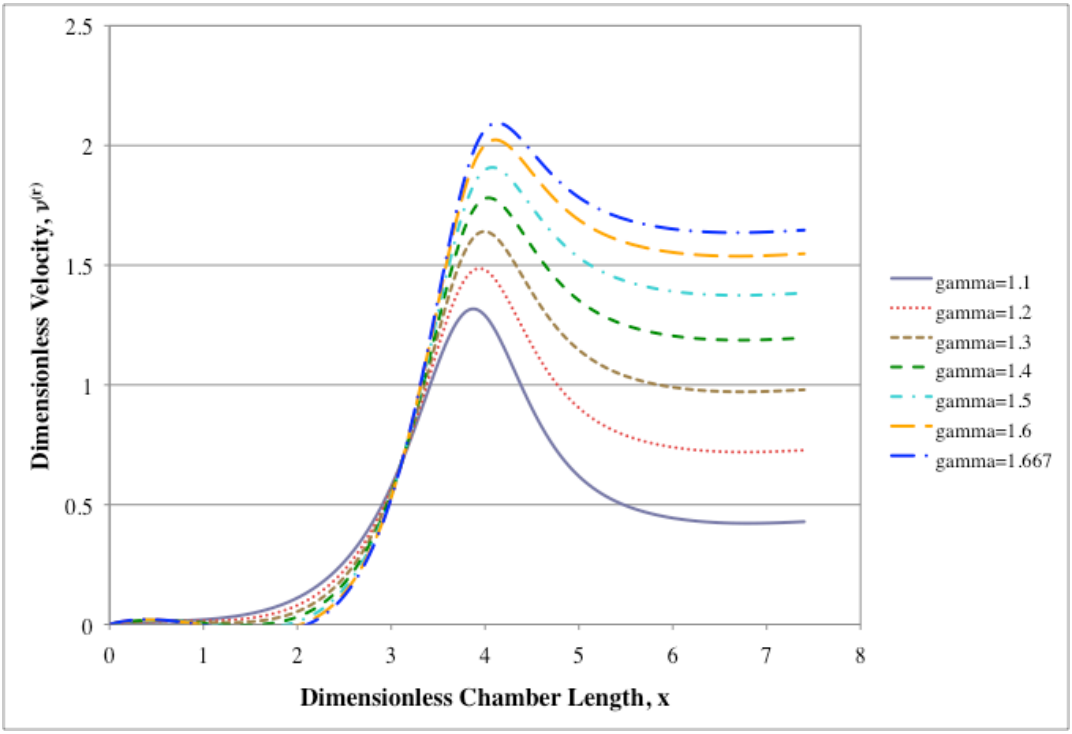

Figure A-15. Real Unsteady Velocity Component ($v^{(r)}$) Varying Gamma (T_i=0.35, ω=1)

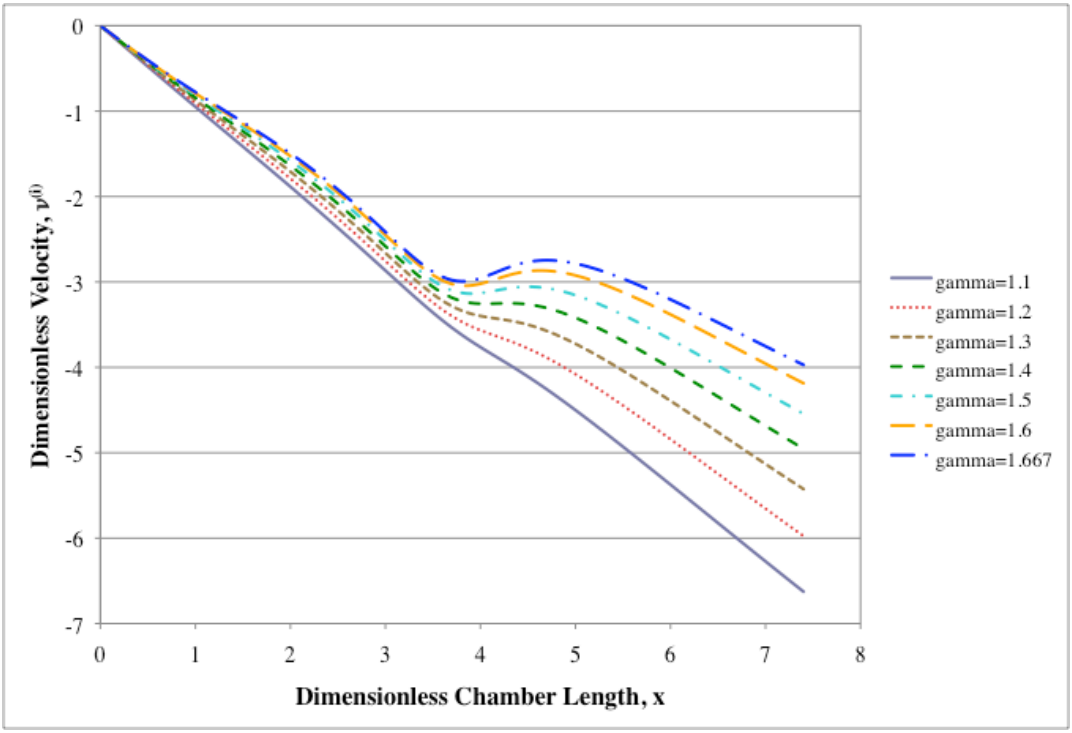

Figure A-16 Imaginary Unsteady Velocity Component ($v^{(i)}$) Varying Gamma (T_i=0.35, ω=1)

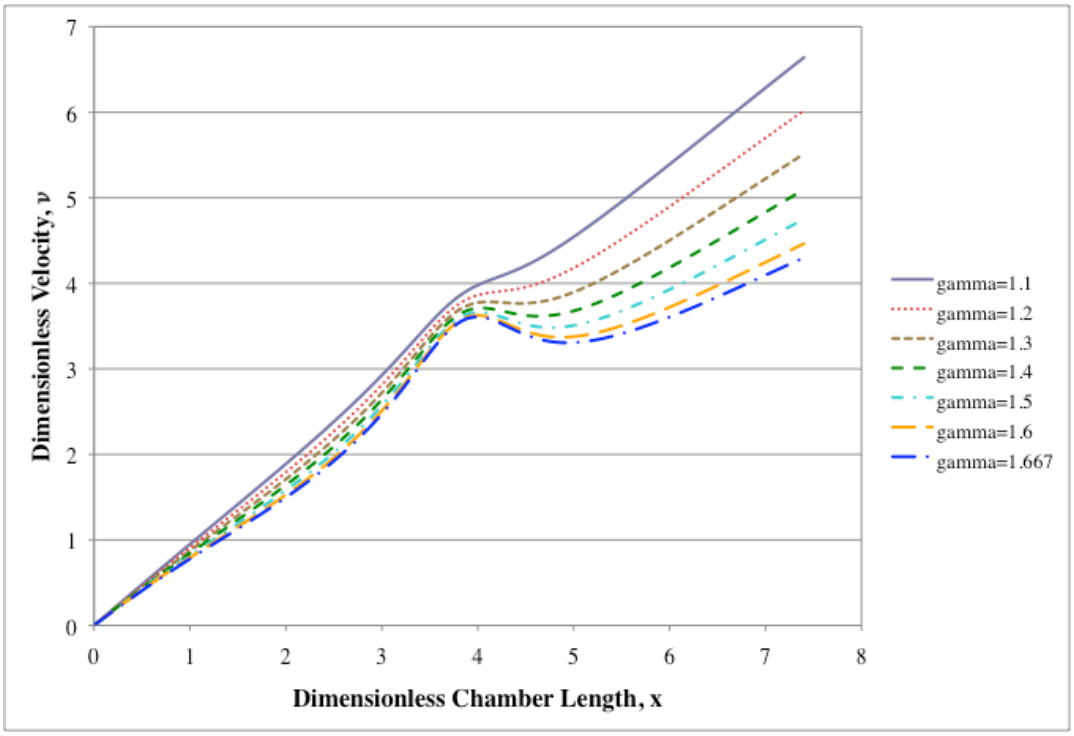

Figure A-17. Unsteady Velocity Component (ν) Varying Gamma (T_i=0.35, ω=1)

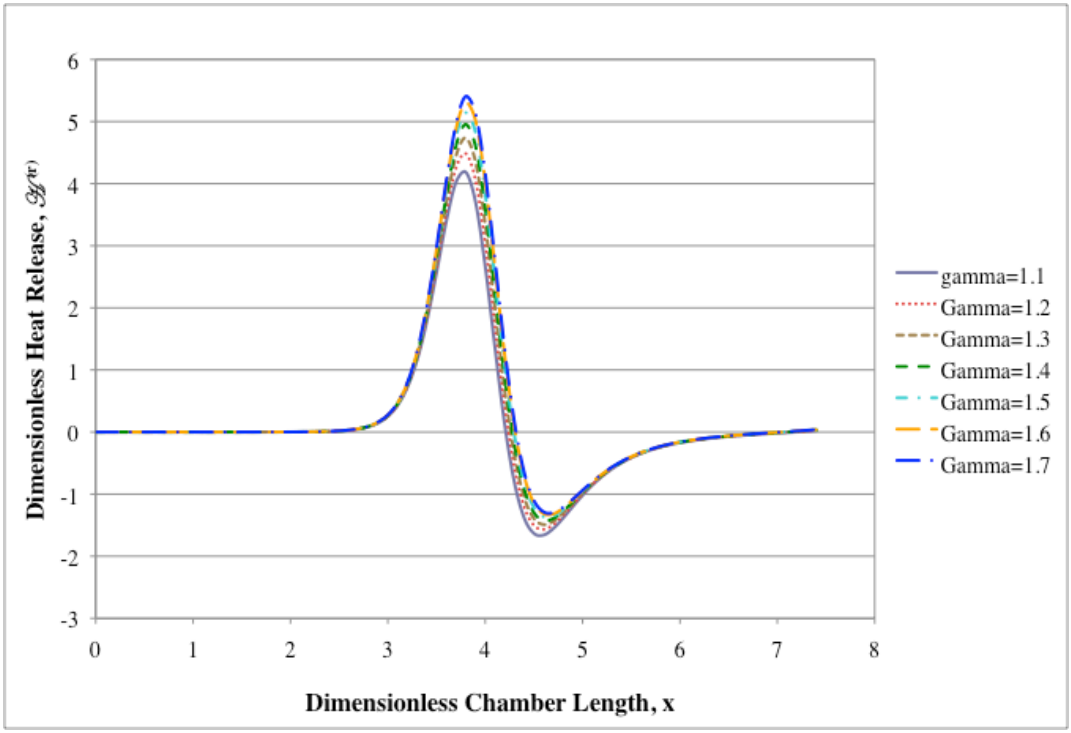

Figure A-18. Real Unsteady Heat Release Component ($\mathscr{Y}^{(r)}$) Varying Gamma (T_i=0.35, ω=1)

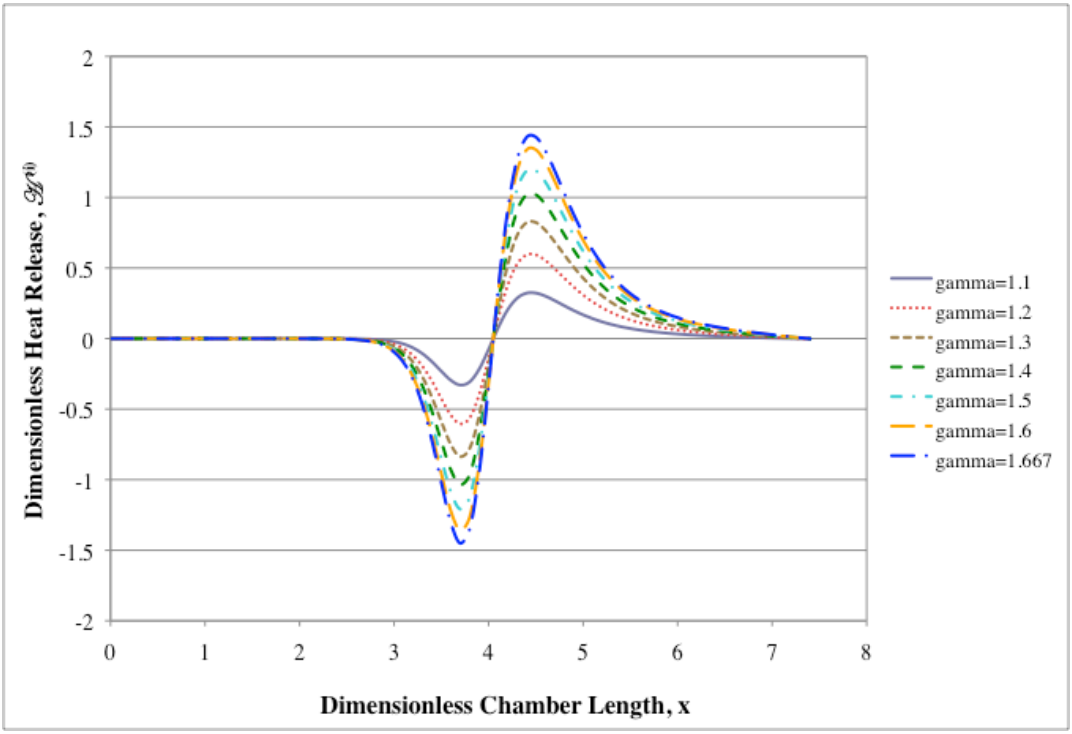

Figure A-19. Imaginary Unsteady Heat Release Component ($\mathscr{H}^{(i)}$) Varying Gamma (T_i=0.35, ω=1)

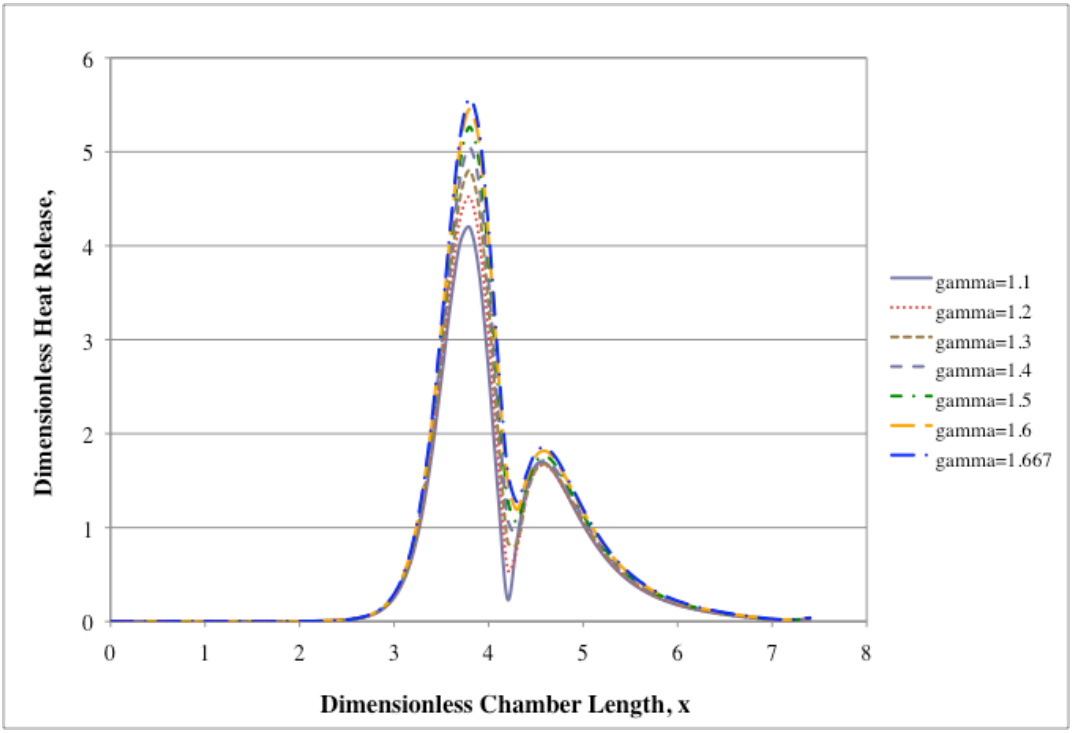

Figure A-20. Unsteady Heat Release Component ($\mathscr{H}_1$) Varying Gamma (T_i=0.35, ω=1)

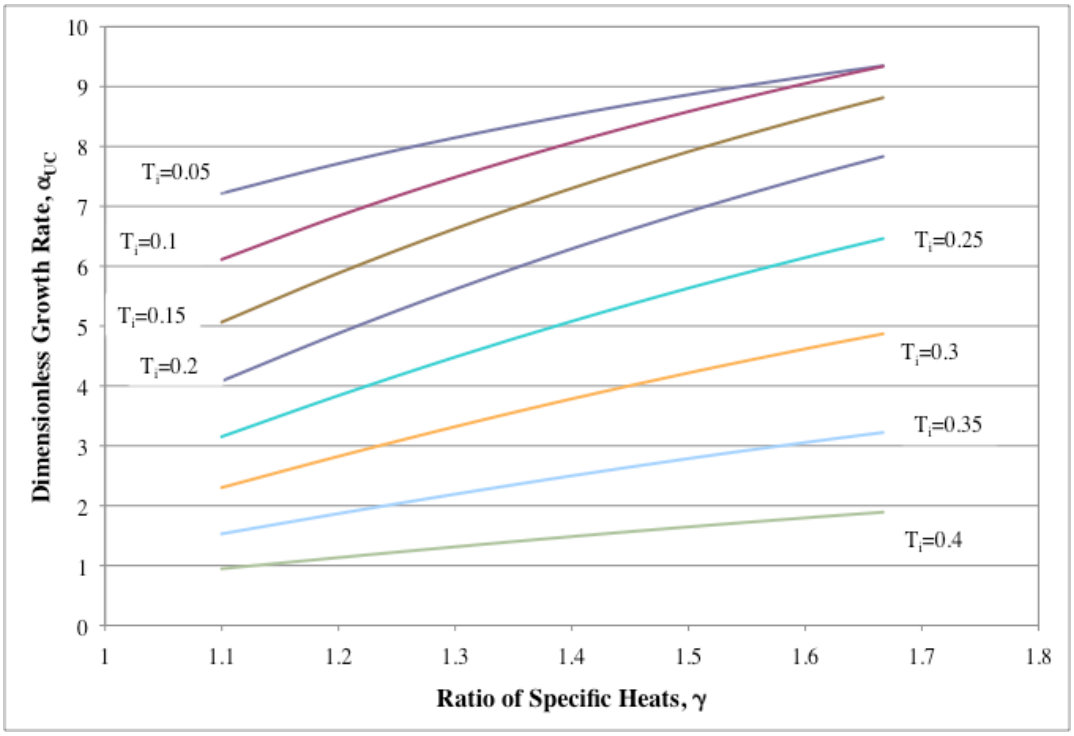

Figure A-21. Comparison of Dimensionless Growth Rate for Different Gamma Over Varying Initial Temperature (ω=0.01)

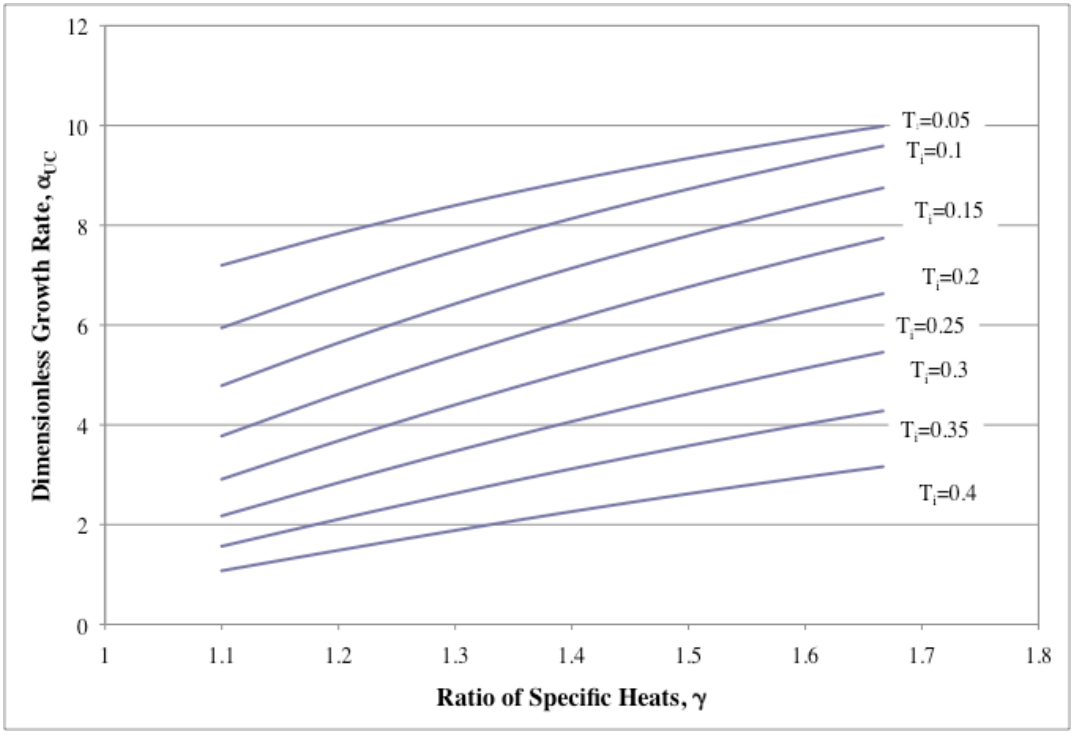

Figure A-22. Comparison of Dimensionless Growth Rate for Different Gamma Over Varying Initial Temperature (ω=0.1)

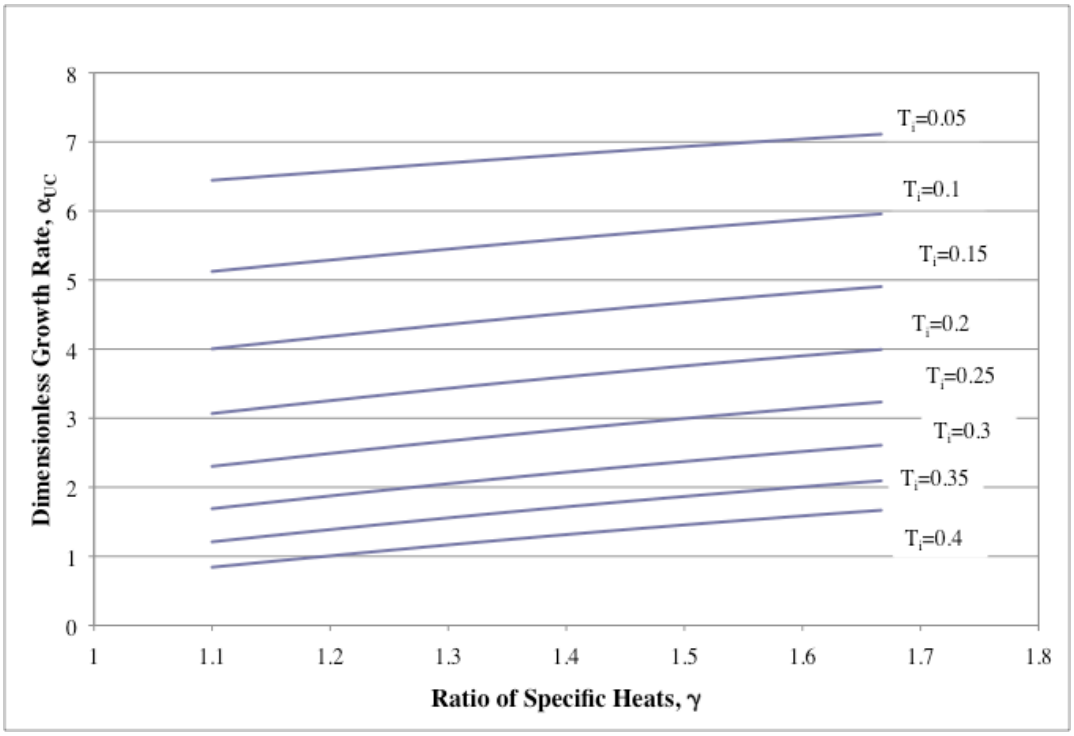

Figure A-23. Comparison of Dimensionless Growth Rate for Different Gamma Over Varying Initial Temperature (ω=1)

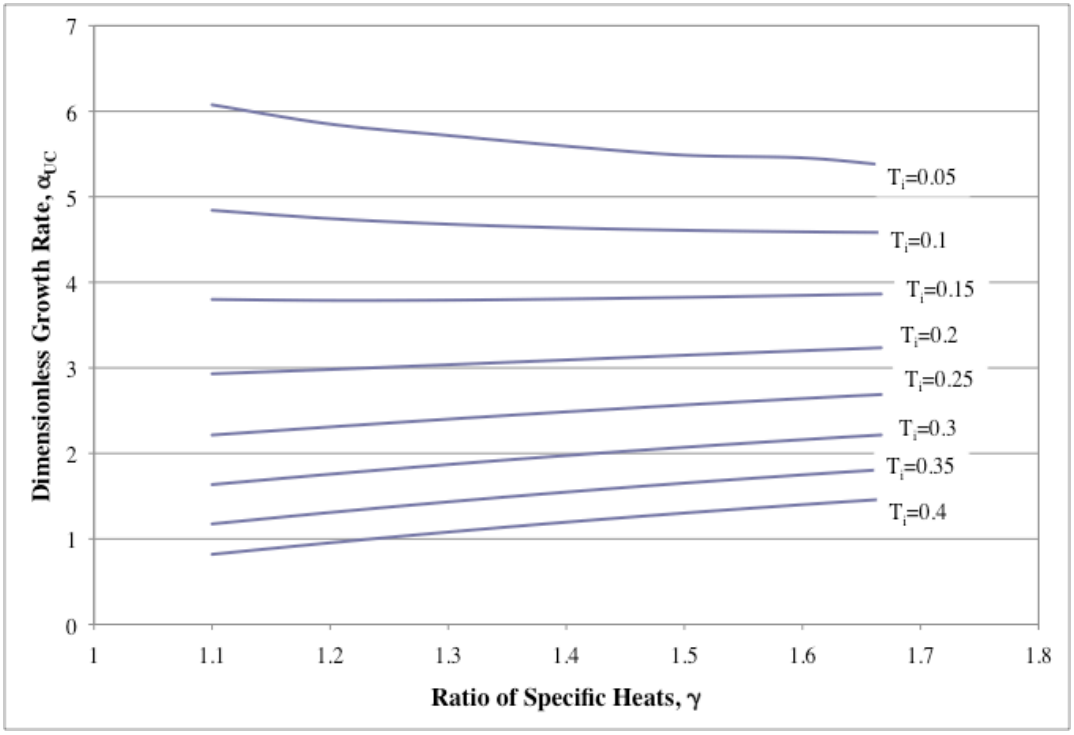

Figure A-24. Comparison of Dimensionless Growth Rate for Different Gamma Over Varying Initial Temperature (ω=10)

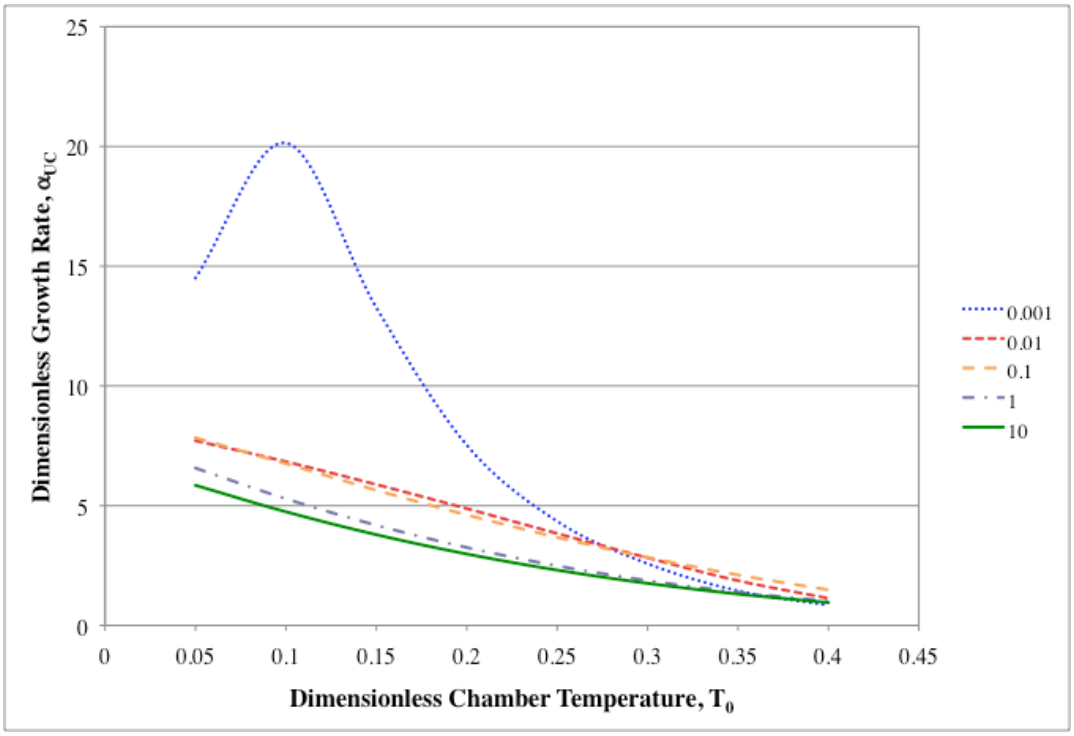

Figure A-25. Comparison of Dimensionless Growth Rate for Different Chamber Frequency Over Initial Temperature (γ=1.2)

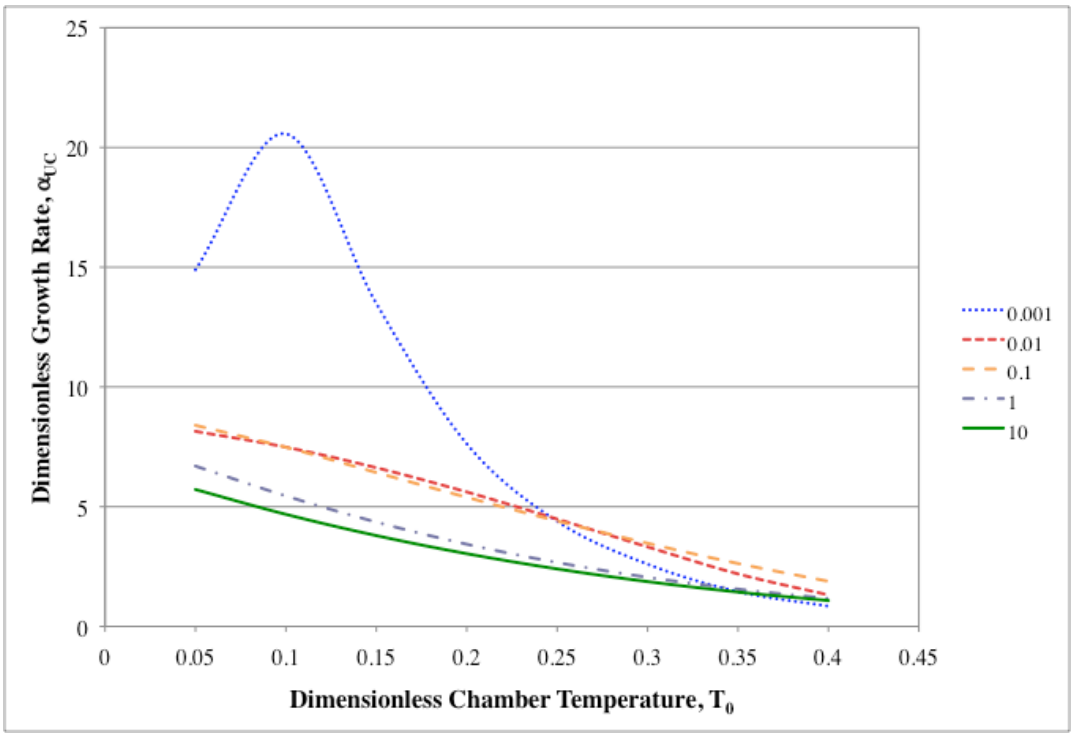

Figure A-26. Comparison of Dimensionless Growth Rate for Different Chamber Frequency Over Initial Temperature (γ=1.3)

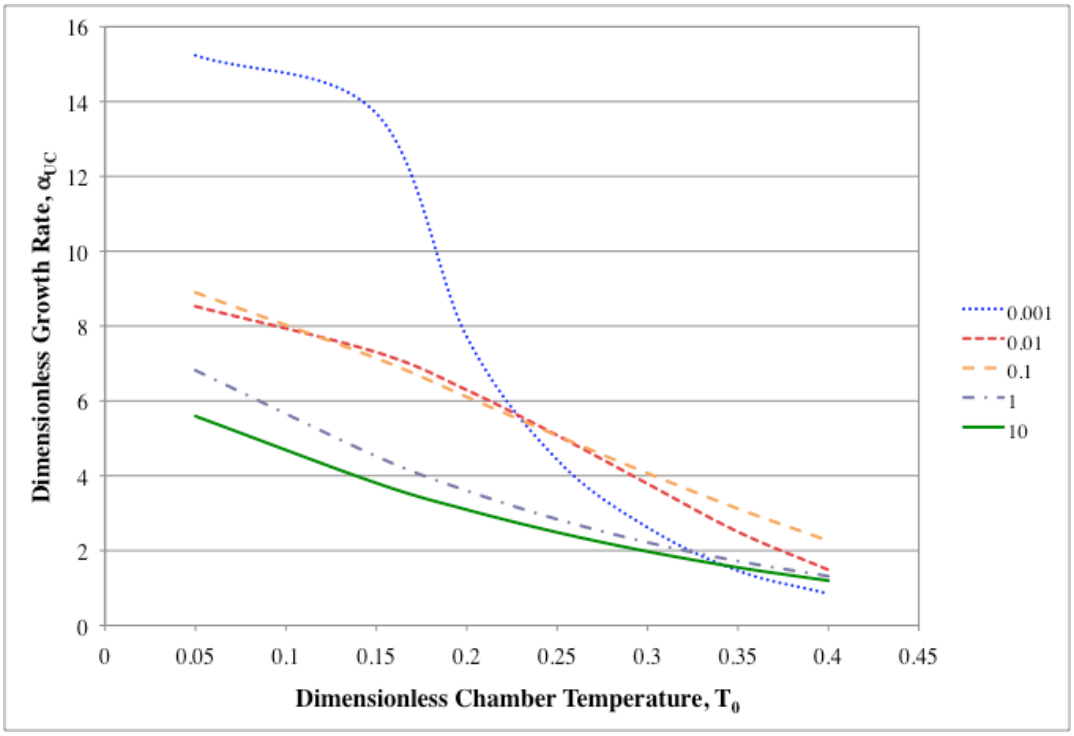

Figure A-27. Comparison of Dimensionless Growth Rate for Different Chamber Frequency Over Initial Temperature (γ=1.4)

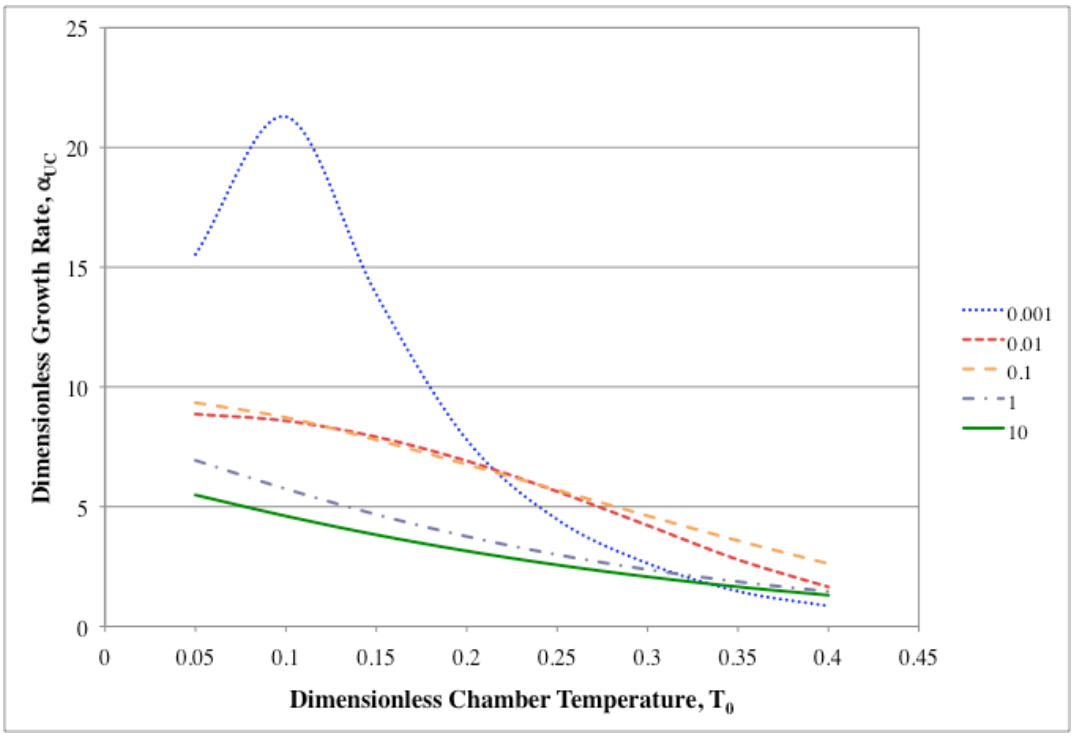

Figure A-28. Comparison of Dimensionless Growth Rate for Different Chamber Frequency Over Initial Temperature (γ=1.5)

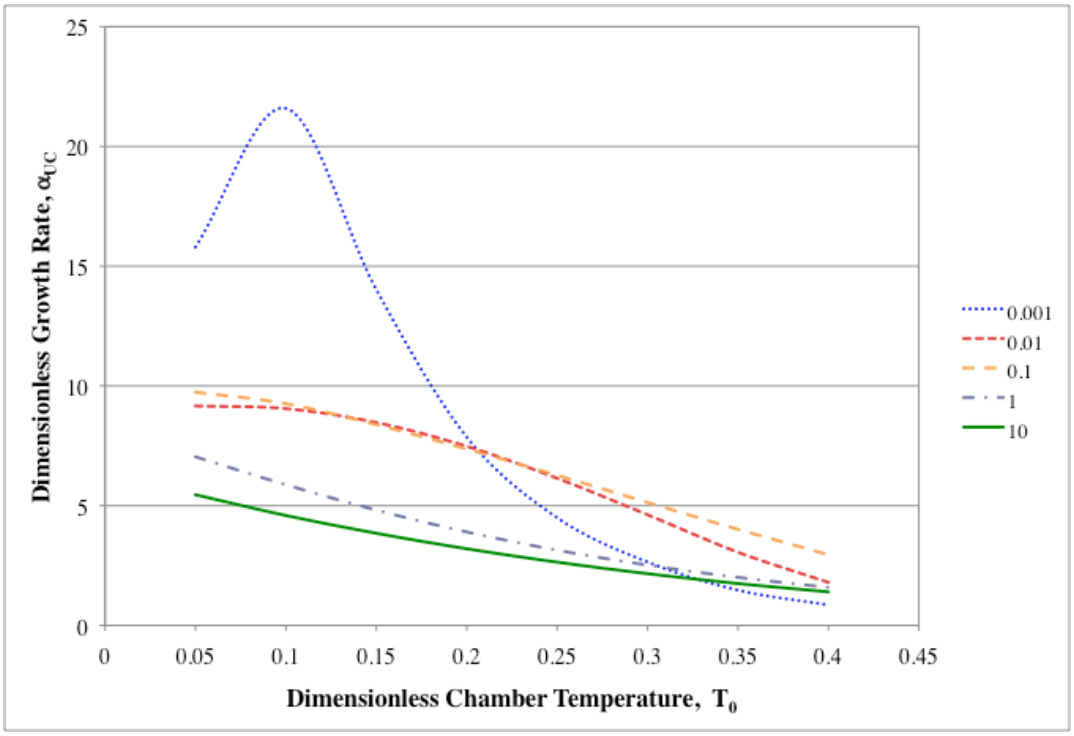

Figure A-29. Comparison of Dimensionless Growth Rate for Different Chamber Frequency Over Initial Temperature (γ=1.6)

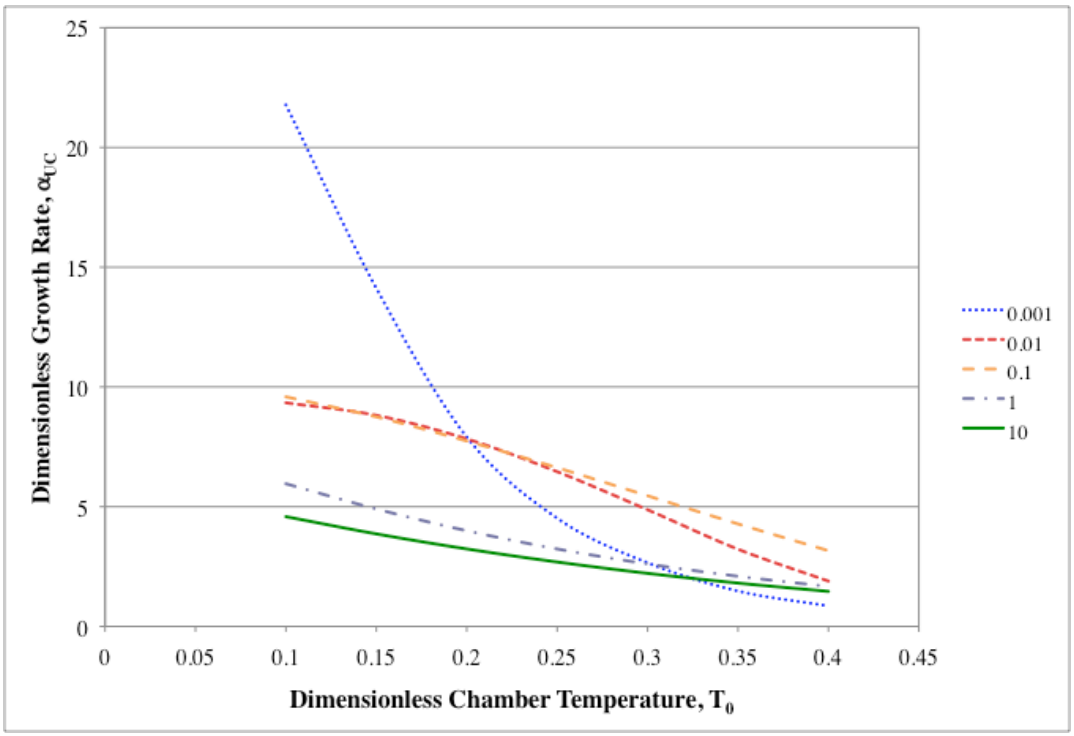

Figure A-30. Comparison of Dimensionless Growth Rate for Different Chamber Frequency Over Initial Temperature (γ=1.667)

APPENDIX C

This appendix presents a more detailed discussion of the numerical technique used in solving for the unsteady components of the temperature, τ, velocity, ν, and fuel species concentration, Y_f, than that given in Chapter 5, Section 2, for the Matlab code presented in appendix A. This is accomplished by first explaining the steps taken in the development of the Jacobian matrix shown in equation 178. The elements of the Jacobian matrix are estimated by simple differencing. A solution vector is first computed using an initial guess for the initial condition matrix [X]. This yields the solution matrix "ybase." The values of [X] are then incremented by a small change, labeled "delx" in the computer program to provide a perturbed error estimate. This yields a new solution matrix "y_i". Then the two sets of values are differenced and divided by "delx" to provide the 16 values of the partial derivatives in the Jacobian matrix, [J].

Beginning at code line number 196 (appendix A), the unsteady solving technique begins a loop chosen to run 25 times to ensure convergence. Until line 232, a solution is calculated based upon the initial conditions in the [X] matrix. This matrix includes the initial conditions of x=0 for the four unknown derivative conditions for temperature and species, $\frac{d\tau^{(r)}}{dx}$, $\frac{d\tau^{(i)}}{dx}$, $\frac{dY^{(r)}}{dx}$, and $\frac{dY^{(i)}}{dx}$.

A [Z] matrix is then created based upon the solution for the temperature and species derivatives in lines 234 to 241 assigned the name "ybase". An error condition in lines 242 to 256 is then checked to ensure that the error is decreasing and the solution is converging for use as the loop repeats the specified 25 times. If the error is increasing instead of decreasing, the program automatically terminates because it is unable to obtain

a solution; this does not occur for the range of conditions used in the calculations presented in this thesis.

A new solution set is then computed using a value of initial conditions plus "delx" to determine the unknown variables in lines 258 to 292. Upon calculation of the solution, another [Z] matrix is created consisting of the solutions of the unknown derivative values in lines 294 to 300 and is assigned the name "y_i".

The 'for' loop in lines 302 to 304 then computes an approximation to the Jacobian matrix using the secant method as discussed in section 5.2. Taking the difference between the two solutions across the difference of their x values, each of the derivative terms in the Jacobian matrix is created. For example, the first derivative term consisting of the difference of the first values of each of the two [Z] matrices with respect to the difference of their x values is constructed as shown.

$$\frac{\partial z[1]}{\partial x[1]} = \frac{z[1]_n - z[1]_{(n-1)}}{x[1]_n - x[1]_{(n-1)}}$$

Next, lines 311 to 335 consist of a process of solving the linear system of equations (consisting of the Jacobian and "ybase" matrix)

$$[J][\Delta X] = [Z]$$

simultaneously to arrive at a value for the $[\Delta X]$ matrix. This approach is known as the multivariable Newton-Raphson method for nonlinear systems. As analogous to the fixed-point one-dimensional approach for this multivariable case, and assuming a nonsingular matrix of partial derivatives, [J], near a fixed point p of G(x), the following expression,

$$G(x) = x - J(x)^{-1}F(x)$$

represents a quadratic convergence to the solution of F(x)=0. In this expression F(x) represents [Z] and x represents $[X]$. The values of the initial conditions [X] are determined from the relationship

$$[X]^n = [X]^{n-1} - J(x)^{-1}F(x).$$

Thus, the new values of [X] are obtained from the following expression

$$[X]^n = [X]^{n-1} - [\Delta X]$$

as done in line 339. Instead of solving for the inverse of the Jacobian directly, the linear equations (represented by the expression, $[J][\Delta X] = [Z]$) are solved simultaneously for the current estimate for the correction to the boundary condition vector $[\Delta X]$. This is done through the use of a Gaussian elimination technique using upper triangulation as shown in lines 315 to 325. Backward substitution is then used to determine the solution for each $\Delta x[i]$ value, as shown in lines 328 to 333. Upon obtaining the new [X] initial conditions matrix, the loop then repeats until a suitable solution is obtained.

VITA

Tina Morina Rice was born in Dearborn, Michigan in 1982. At the age of four, she and her family moved to Gainesboro, Tennessee to return to where her father was born and raised. Tina graduated from Jackson County High School as Salutatorian in 2000. She attended Tennessee Technological University in Cookeville, Tennessee on a university valedictorian/salutatorian scholarship working in the University Library Archives. While there she took part and leadership in clubs such as ASME, AIAA, and Pi Tau Sigma. She graduated in Spring 2004 with a bachelor's degree in Mechanical Engineering. Tina completed an Aerospace Engineering Master's degree at University of Tennessee Space Institute and is currently pursuing a Ph.D. in aerospace engineering as well as another master's degree in aviation systems. Upon graduation, she will be working with Gloyer-Taylor Laboratories (GTL) to continue work in furthering the understanding of combustion instability.